



HAL
open science

Spatio-temporal coherence between spaceborne measurements of salinity and optical properties in the Amazon-Orinoco Plume Region

Séverine Fournier

► **To cite this version:**

Séverine Fournier. Spatio-temporal coherence between spaceborne measurements of salinity and optical properties in the Amazon-Orinoco Plume Region. Oceanography. Université de Bretagne occidentale - Brest, 2014. English. NNT : 2014BRES0071 . tel-02111966

HAL Id: tel-02111966

<https://theses.hal.science/tel-02111966>

Submitted on 26 Apr 2019

HAL is a multi-disciplinary open access archive for the deposit and dissemination of scientific research documents, whether they are published or not. The documents may come from teaching and research institutions in France or abroad, or from public or private research centers.

L'archive ouverte pluridisciplinaire **HAL**, est destinée au dépôt et à la diffusion de documents scientifiques de niveau recherche, publiés ou non, émanant des établissements d'enseignement et de recherche français ou étrangers, des laboratoires publics ou privés.

UBO

université de bretagne
occidentale



THÈSE / UNIVERSITÉ DE BRETAGNE OCCIDENTALE

sous le sceau de l'Université européenne de Bretagne

pour obtenir le titre de

DOCTEUR DE L'UNIVERSITÉ DE BRETAGNE OCCIDENTALE

Mention : Océanographie Physique

École Doctorale des Sciences de la Mer

présentée par

Séverine Fournier

Préparée à IFREMER

Signature des Panaches des Grands Fleuves à la Surface des Océans : Corrélation entre Salinité et Propriétés Optiques déduites de Mesures Satellite

Thèse soutenue le 6 Juin 2014

devant le jury composé de :

Xavier CARTON

Professeur, Université de Bretagne Occidentale / *président de jury*

Joe SALISBURY

PhD, University of New Hampshire, USA / *rapporteur*

Jacqueline BOUTIN

Directrice de recherche CNRS, France / *rapporteuse*

Doug VANDEMARK

PhD, University of New Hampshire, USA / *examinateur*

Michelle GIERACH

PhD, Jet Propulsion Laboratory, USA / *examinatrice*

Bertrand CHAPRON

PhD, Ifremer, France / *encadrant*

Nicolas REUL

PhD, Ifremer, France / *directeur de thèse*





PhD THESIS

Space Oceanography Department, IFREMER, Brest, France

Doctoral School of the Marine Sciences, IUEM, Brest, France

Speciality: **Oceanography**

by

Séverine FOURNIER

Spatio-Temporal Coherence between Spaceborne Measurements of Salinity and Optical Properties in the Amazon-Orinoco Plume Region

Nicolas REUL, *Ifremer, France*

Bertrand CHAPRON, *Ifremer, France*

Joe SALISBURY, *University of New Hampshire, USA*

Jacqueline BOUTIN, *CNRS, France*

Doug VANDEMARK, *University of New Hampshire, USA*

Michelle GIERACH, *Jet Propulsion Laboratory, USA*

Xavier CARTON, *Université de Bretagne Occidentale, France*

Supervisor

Supervisor

Opponent

Opponent

Examinator

Examinator

President of jury

Remerciements

Je tiens tout d'abord à remercier mon directeur de thèse Nicolas Reul, chercheur à l'Ifremer, pour la confiance qu'il m'a accordée durant ces dernières années. Je lui suis également reconnaissante pour ses conseils et son enthousiasme pour la science qui m'a toujours motivée.

Je souhaiterais également remercier mon co-encadrant de thèse et directeur de laboratoire, Bertrand Chapron de m'avoir accueillie au sein de son équipe. Je tiens à le remercier pour sa patience, sa confiance, ses conseils et pour toutes ces discussions originales. Merci de m'avoir donné les moyens d'achever ce travail dans d'excellentes conditions et de m'avoir permis de réaliser tous ces voyages enrichissants pour des conférences et des collaborations.

Un grand merci à Joe Salisbury et Doug Vandemark pour avoir suivi mon travail pendant ces quelques années et pour leur disponibilité. Je tiens également à les remercier de m'avoir accueillie pendant deux mois à l'Université du New Hampshire. Merci pour leurs conseils, le temps qu'ils ont toujours su m'accorder, leur patience et leur gentillesse. Merci également à Tim Moore et ses conseils avisés. Je tiens particulièrement à remercier Joe et sa femme Maureen pour leur accueil chez eux pendant ces deux mois et de m'avoir intégrée à leur famille.

Merci à mes deux rapporteurs Jacqueline Boutin et Joe Salisbury mais également aux autres membres de mon jury Doug Vandemark, Xavier Carton et Michelle Gierach pour avoir attentivement lu mon manuscrit et pour tous leurs commentaires constructifs.

Je tiens aussi à remercier toute l'équipe du laboratoire d'océanographie spatiale de l'Ifremer pour leur bonne humeur et la bonne ambiance qui régnait au quotidien. Merci à Emmanuelle Autret pour toutes ces discussions et son entraide particulièrement dans les moments difficiles. Merci à Elena Maksimovich avec qui j'ai partagé mon bureau pendant un bout de temps. Merci à ses conseils et à ses discours de motivation. Merci à Nicolas Rascle et Clément de Boyer Montégut pour leur bonne humeur et leur optimisme. Merci également à Olivier Archer, Mickael Accensi et Fabien Leckler pour leur soutien en informatique.

Je remercie tous mes amis qui ont été là ces dernières années pendant les bons et surtout les mauvais moments, qui ont su me motiver, me changer les idées, m'écouter et surtout me supporter. Donc un grand merci à Fabien, Carine, Laure, Cristina, Daniele, Pierre-

Marie, Quentin, Camille, Sophie, Marie-Hélène, Matthieu, Céline...

Enfin, je tiens à remercier mes parents pour leur soutien tant matériel que moral et affectif et sans qui je ne serais pas là aujourd'hui. Ils ont toujours cru en moi et m'ont toujours donné les moyens de faire ce que j'aime. Je les remercie ainsi que ma soeur Leslie d'avoir toujours été présents et de m'avoir supportée jusqu'à la fin.

Abstract

We enter now in a new era of global Sea Surface Salinity (SSS) observing systems from Space with the recent successful launches of the ESA Soil Moisture and Ocean Salinity (SMOS) mission and the NASA Aquarius/SAC-D mission. These new satellite SSS observing systems are as well complemented by an increased number of devices deployed *in situ*. Finally, ocean color products can be used as well for tracking salinity via semi-conservative tracers such as dissolved organic matter absorption coefficient at 443 nm (a_{cdm}), light attenuation at 490 nm and chlorophyll concentration. With these new methods, we are now in an excellent position to revisit the SSS observed in the warm seas of the tropical Atlantic with multi-year time series of excellent remote sensing and concurrent *in situ* observations. The seasonal cycles in the spatial extent of low surface salinity waters of the major river plumes and freshwater pools of the tropical Atlantic oceans as the Amazon and Orinoco rivers can thus be analyzed in a new and original manner. In particular, the correlation between SSS and bio-optical properties measured from Space in the plume waters can now be established and analyzed over large spatial scales. In the frame of this PhD work, different major research topics were studied. First the correlations between sea surface salinity and absorption coefficient of colored detrital matter at 443 nm in the Amazon-Orinoco plume over 2010-2013 are studied. Then the conservative mixing relationship is robustly established based on two different approaches, a regional one over the whole Amazon plume and a local one. Once the SSS/ a_{cdm} relationship established, it is used to retrieve a SSS product from 1998 to 2013 based on Ocean Color data. Finally, we attempt to explore the conservative mixing using a lagrangian approach.

Résumé

Avec les lancements réussis des missions ESA Soil Moisture and Ocean Salinity (SMOS) et NASA Aquarius/SAC-D, la salinité de surface des océans peut maintenant être déduite. De plus, les produits de couleur de l'eau, tels que les mesures d'absorption et d'atténuation de la lumière et de concentration en chlorophylle, peuvent être utilisés comme traceurs de la salinité. Les signatures des panaches des grands fleuves tropicaux tels que l'Amazone et l'Orénoque peuvent être étudiées en détail grâce à ces nouvelles méthodes. En particulier, les relations de corrélations entre SSS et propriétés optiques également déduites de mesures satellites peuvent maintenant être établies et analysées sur des échelles spatiales beaucoup plus grandes. Différents efforts de recherche sont envisagés dans le cadre de ce travail de thèse. Tout d'abord, nous étudions les corrélations entre salinité de surface et propriétés optiques dans le panache de l'Amazone durant la période 2010-2013. Ensuite, la relation de mélange est établie de façon robuste selon tout d'abord une approche régionale, puis selon une approche locale. Ensuite, une fois cette loi de dilution établie de façon robuste, nous l'utilisons pour estimer un produit de salinité de surface à partir des produits couleur de l'eau sur la période 1998-2013. Enfin, nous tentons d'envisager la relation de dilution suivant une approche lagrangienne.

Contents

Introduction	1
1 State of the Art	4
1.1 The Importance of River Plumes in Oceanography	4
1.2 Sea Surface Salinity & Ocean Color in River Plumes	6
1.2.1 Sea surface salinity	6
1.2.2 Ocean Color	7
1.3 The Conservative Mixing in River Plumes	9
1.3.1 Generalities	9
1.3.2 Conservative mixing in river plumes using Ocean Color and sea surface salinity observations	11
2 Observations	13
2.1 Sea Surface Salinity Data	13
2.1.1 <i>In situ</i> data	13
2.1.2 Sea Surface Salinity climatology	16
2.1.3 SMOS Sea Surface Salinity data	16
2.1.3.1 Remote sensing measurement of sea surface salinity	16
2.1.3.2 SMOS sea surface salinity measurement	17
2.1.3.3 SMOS SSS quality assessment in the Amazon River plume region	19
2.1.3.4 Known issues	25
2.2 Ocean Color Data	33
2.2.1 Ocean Color remote sensing	33
2.2.2 Ocean Color semi-analytic algorithms	38
2.2.3 On the use of the absorption coefficient of colored detrital matter	40
2.2.3.1 A river plume water tracer	40
2.2.3.2 Justification of the choice to use GlobColour a_{cdm}	41
2.2.4 Net Primary Production data	44
2.3 Other Geophysical Data	45
2.3.1 Discharge levels	45
2.3.2 Sea Surface Temperature estimates	45
2.3.3 Altimetric data	46
2.3.4 Wind estimates	46
2.3.5 Rain rate estimates	46

2.3.6	AMSR-E Brightness Temperatures estimates	46
3	The Northwestern Tropical Atlantic Ocean	47
3.1	Physical Oceanography of the Northwestern Tropical Atlantic Ocean	47
3.1.1	The Amazon-Orinoco discharge	47
3.1.2	Tidal and local currents	49
3.1.3	Trade winds & Inter Tropical Convergence Zone	51
3.2	The Dispersal of the Amazon Plume	56
3.2.1	Annual Amazon waters dispersal	56
3.2.2	Seasonal Amazon plume dispersal	58
3.2.3	Interannual Amazon plume dispersal	61
3.2.4	Observed Correlation between the plume extension seasonal variability and the Amazon discharge	62
3.3	Conclusions	65
4	The Relationship Between Sea Surface Salinity and Optical Properties in the Amazon Plume Region	66
4.1	Introduction	66
4.2	A Regional Approach using a Conservative Mixing model	68
4.2.1	The annual average SSS/ a_{cdm} relationship	69
4.2.2	Seasonal variabilities in the conservative mixing	73
4.2.3	Interannual variabilities in the conservative mixing	78
4.2.4	Spatial variabilities in the conservative mixing	80
4.2.5	Non conservative behaviour in a_{cdm} mixing	84
4.3	A Local Approach of the Conservative Mixing	97
4.3.1	Correlations between SSS and optical properties	97
4.3.2	SSS and optical properties correlations with the Amazon discharge .	102
4.3.3	Advection of the Amazon plume	103
4.3.4	The Conservative Mixing in the Amazon Plume	106
4.3.5	Non conservative behaviours of the conservative mixing	109
4.4	Conclusions & Perspectives	114
5	Application : Sea Surface Salinity retrieval from Ocean Color in the Amazon Plume	116
5.1	Introduction	116
5.2	Methodology	116
5.3	Sea Surface Salinity Estimates	118

Contents

5.4	Comparison with Other Sea Surface Salinity Retrieval Methods	126
5.5	Validation	130
5.5.1	Over 2010-2012	130
5.5.2	Along TSG tracks	131
5.6	Discussion & Conclusions	133
6	A Lagrangian Approach of the Relationship between Sea Surface Salinity and Light Absorption in the Amazon Plume	137
6.1	Introduction	137
6.2	Methodology	138
6.3	Virtual Drifters Examples	140
6.4	Statistical Analysis	141
6.4.1	Mixing and relaxation behaviours along the trajectory	141
6.4.2	The conservative mixing along the drifter trajectory	143
6.5	Conclusions	145
	Conclusions & Perspectives	147
	A The Northwestern Tropical Atlantic Ocean	153
	B Amazon river plume signatures in AMSR-E low-frequency brightness temperature data	157
B.1	Radiative Transfer Model	157
B.2	Sea surface salinity signal from the AMSR-E	161
B.3	Initial empirical SSS retrieval methodology	165
B.4	AMSR-E ΔT_b^v algorithm improvement	167
B.4.1	Atmospheric corrections improvement	167
B.4.2	Residual biases corrections	169
B.5	New SSS retrieval methodologies	171
B.5.1	Empirical model	171
B.5.2	Neural network model	172
B.5.3	AMSR-E SSS Validation	173
B.6	Conclusion	181
	References	183
	Publications & Conferences	195

Introduction

Earth observation science is a growing field. It provides synoptic coverage across both space and time. Spaceborne sensors gather data from sites across the world, including places too remote or otherwise inaccessible for ground-based data acquisition. In the long term, this monitoring of the Earth's environment will enable a reliable assessment of the global impact of human activity and the likely future extent of climate change. And because Earth Observation satellites remain in place for long periods of time, they can highlight environmental changes occurring gradually.

The principles of the sea surface salinity (SSS) remote sensing measurements are quite well established. It implies the precise determination of the surface seawater dielectric properties thanks to low frequency passive microwave measurements of sea surface brightness temperatures. At the end of 2009, the interferometric radiometer ESA Soil Moisture and Ocean Salinity (SMOS) has been successfully launched. Since then, this instrument acquires the first multi-angular space observations of band L (around 1.4 GHz) brightness temperatures. From these measurements, an estimation of sea surface salinity can be obtained.

In addition to being freshwater sources, the large rivers carry suspended and dissolved organic matter. As this organic matter contains organic carbon and nutrients, it modifies the light attenuation. The organic matter flux from large rivers to the open ocean can have dramatic effects on the local ecology.

The strong negative correlation between salinity and optical properties of plume waters is a remarkable and well-known property. In coastal regions, the organic matter acts as an efficient tracer of the freshwater flux, decreasing as it flows away from the river mouth, whereas the salinity increases. The linearity in the relationship between salinity and optical properties in plume areas implies the conservative mixing notion. This conservative mixing can be affected by discharge intensity, exogeneous water masses advected by currents or generated by intense precipitation/evaporation fluxes. The relationship can also be affected by external production of organic matter (primary production) or removal processes, such as photobleaching.

Our current knowledge of the dispersal patterns of the freshwater pools at the ocean surface mainly relies on *in situ* hydrographic observations, numerical models, and indirect satellite imagery through analysis of sea surface temperature (SST) fields and Ocean Color. Until the recent launches of satellite SSS missions SMOS and Aquarius, the con-

servative mixing in estuaries has only been derived from sparse *in situ* SSS observations. Being able to monitor the possible conservative mixing variability, the dispersal patterns of river plumes and their extension is however extremely important to better characterize the seasonal and interannual changes in riverine constituents concentration at the mouth of the rivers (endmembers) but also to better identify spatio-temporal variability in the different sources of non conservative mixing. While *in situ* observations are key elements of the SSS observing systems, remote sensing from Space is the only viable approach to monitor the temporal variability of the dispersal of waters from large rivers over synoptic basin scales and at sufficient spatial and temporal resolutions. Indeed, only satellite remote sensing data are known to provide means to monitor the wide surface dispersal of these fresh pools. Since these first observations, the application of Ocean Color, altimetry and sea surface temperature (SST) satellite mapping has increased in its sophistication. The satellite data are able to provide temporal information on advective processes up to certain limits that include cloud cover, SST and Ocean Color gradients, non conservative dilution processes for the Ocean Color to salinity conversions.

Since 2010, we have entered in a new era of global SSS observing systems from Space with the successful launches of the ESA Soil Moisture and Ocean Salinity (SMOS) and the NASA Aquarius/SAC-D missions. Thus, new SSS observations are now available and can further be used to monitor the spatial and temporal variability of the dispersal of Amazon-Orinoco waters over synoptic basin scales, with improved spatial and temporal resolutions. Orbiting platforms are now providing SSS data averaged over periods varying from about 10 days to 1 month and with a spatial resolution from about 50 km to 100 km. These new satellite SSS observing systems are as well complemented by an increased number of devices deployed *in situ*.

In this work, we study the relationship between sea surface salinity and dissolved organic matter in estuaries. To this aim, we use a suite of remote sensing data, including Ocean Color observations and the new satellite SSS data from the SMOS mission. It allows us to monitor river plumes dispersal with unprecedented spatial and temporal resolutions.

We decided to focus on the area of the northwestern tropical Atlantic ocean. In this region, the largest river of the world in terms of discharge : the Amazon, and the fourth one : the Orinoco river, discharge into the ocean. Both river plumes generate strong salinity gradients at the sea surface of the western tropical Atlantic that span large spa-

tial scales ($\gg 100$ km). Moreover, accuracy of the satellite SSS products are maximum in the relatively high sea surface temperature conditions encountered in that tropical ocean region (generally above 20°C). Finally, this part of the ocean has been well-documented in the literature. Our study focuses on the period 2010-2013 during which both SMOS sea surface salinity and MERIS/MODIS Ocean color observations are available.

First, in chapter 1, we establish the state of the art necessary to this study. In chapter 2, we present the data used in this thesis. An assessment of SMOS SSS data quality will be provided for the northwestern tropical Atlantic region and we will discuss the ocean color products. In chapter 3, we provide an overview of the seasonal variability of the major physical atmospheric and oceanic processes at play in the northwestern tropical Atlantic region. We first describe surface currents, winds, salinity, temperature and ocean color seasonal variabilities and their impact on the dispersal of the Amazon waters. In chapter 4, we first review our knowledge of the conservative mixing relationship in this area. Further, we present the results of our analyses on the relationship between SSS and Ocean color from spaceborne data using different methods, the first one based on a regional approach and the second one on a local approach of the conservative mixing. Finally, we explore the deviations from this conservative mixing due to biogeochemical processes. Once the conservative mixing relationship robustly established, we explore, in chapter 5, an application of this relationship. We attempt to retrieve sea surface salinity from Ocean Color based on the conservative mixing. Finally, in chapter 6, we briefly explore another method of the conservative mixing relationship analysis based on a Lagrangian approach, which should be deeply explored in the future.

Chapter 1

State of the Art

1.1 The Importance of River Plumes in Oceanography

Large rivers are key components of the global water cycle (Meybeck [2003]) which represents the freshwater storage and the exchanges between the oceans, the continents, the atmosphere and the cryosphere (Schanze et al. [2010]). The global water cycle is a crucial part of the Earth's climate system, particularly with respect to its response to changing climate and societal use (Vörösmarty et al. [2000] ; Meybeck and Vörösmarty [2005] ; Oki and Kanae [2006], Trenberth et al. [2007] ; Milliman et al. [2008]). Global warming, for instance, could accelerate the hydrological cycle (Trenberth [1999]).

The water cycle provides one of the most important resources to support human life. Continental runoff represents a major portion of freshwater resources available to organisms, including humans, and required to their survival. As the world's population grows along with increasing demands for fresh water, it is essential to ensure that adequate supplies of water are available and, thus, interannual variability and long-term changes in continental runoff are of great concern (Vörösmarty et al. [2000] ; Oki and Kanae [2006]).

The hydrological cycle can no longer be considered as being controlled by only the Earth system processes but also by social, societal and economic processes (Meybeck [2003]). Humans are simultaneously increasing the river transport of sediment through soil erosion activities and decreasing this flux to the coastal zone through sediment retention in reservoirs (Syvitski et al. [2005]). Large river estuaries are "drivers" and "recorders" of natural and anthropogenic environment change. Specifically, they can have an influence on the flux of particulate and dissolved materials from the continent to the open ocean that can have a profound impact on diverse coastal issues such as coastal eutrophication and the development of hypoxic zones (Bianchi and Allison [2009]).

Large river delta front estuaries represent important land-ocean interfaces for material fluxes that have a global impact on marine biogeochemistry (Bianchi and Allison [2009]). They provide an important amount of organic and inorganic particulates into the ocean, impacting biogeochemical and ecological activity (McKee et al. [2004] ; Hickey et al. [2010]). As the river discharges sediments into the ocean, primary production tends to increase and atmospheric CO₂ is then sequestered, causing sink for atmospheric CO₂ (Körtzinger [2003] ; Lefèvre et al. [2014]). By modifying the ocean salinity, one of the

1.1. The Importance of River Plumes in Oceanography

variables regulating CO₂ uptake and release, river plumes have an impact on the oceanic carbon cycle. Rivers have also an impact on bio-optic through the ocean optical properties (Muller-Karger et al. [1988] ; Longhurst [1995] ; Muller-Karger et al. [1995] ; Fratantoni and Glickson [2002] ; Del Vecchio and Subramaniam [2004] ; Hu et al. [2004]); ecology (fisheries, phytoplankton : see Muller-Karger et al. [1995]) and geomorphology (erosion).

Moreover, large river runoffs play important roles in several physical ocean processes. The basic components of the hydrological cycle are precipitation, evaporation, transpiration (from plants on land), riverine runoff (including generally groundwater seeps), and ice fluxes. Riverine discharge (R) into the ocean is the second most important freshwater input after oceanic precipitation, it accounts for approximately 10% of the total freshwater input to the ocean (Dai and Trenberth [2002] ; Dai et al. [2009]). Over the period 1987-2006, Schanze et al. [2010] estimated the annual mean precipitation (P) into the ocean at about 12.2 ± 1.2 Sv, the evaporative loss (E) at 13 ± 1.3 Sv. To simplify the freshwater budget to E-P-R, the iceberg/meltwater discharges from both Antarctica and Greenland were included in the total riverine runoff to augment the mean annual riverine discharge of 1.18 Sv (Dai and Trenberth [2002]) by the mean of the available iceberg/meltwater observations for Antarctica and Greenland (0.06 and 0.01 Sv, respectively) to a total value of 1.25 ± 0.1 Sv for the total freshwater input from land.

These large amounts of fresh water discharged into the open ocean modify the local sea surface salinity (SSS), and therefore the density and buoyancy of the surface layers and vertical stratification (Pailler et al. [1999] ; Masson and Delecluse [2001] ; Ferry and Reverdin [2004] ; Mignot et al. [2012]). The significant freshwater inflow forces ocean circulation regionally through these changes in density (Carton [1991]) and this may have consequences on the local ocean-atmosphere fluxes. Ffield [2007] thus demonstrated that hurricanes tend to strengthen as they pass over the Amazon plume waters because of higher SST over the plume than in surrounding open ocean waters and the presence of a barrier layer (BL) below the plume. The large-scale low salinity 'lenses', characterized by relatively small thicknesses (~ 20 -40 m) as well as by distinct and strongly seasonal spatial extents (Lentz and Limeburner [1995]), form a near-surface barrier layer. The warm and fresh surface waters within the plume indeed create thick and persistent ocean barrier layer (BL) in the northwestern tropical Atlantic (NwTA). Mixing is restricted within the shallower mixed layer and entrainment of cool thermocline water into the mixed layer is reduced during the passage of storms in presence of a BL (Anderson et al. [1996] ; Vialard and Delecluse [1998a] ; Vialard and Delecluse [1998b] ; Foltz and McPhaden [2009]). During the hurricane season the BL in the Amazon plume region is further shallowing and

thinning, but subsurface temperature maxima are getting intense (Mignot et al. [2012]). The stable plume limits the mixed layer to a very thin depth ($\sim 20\text{-}30$ m) while the intense radiative heat flux penetrates significantly below, thereby heating the subsurface waters protected from air-sea interactions. Because of combined physical processes (river discharge, plume advection, development of BL and intense radiative heat flux penetration), warm sea surface temperature anomalies (SSTAs) and higher upper ocean heat content (OHC) persist in this region. This favors hurricane intensification (Balaguru et al. [2012])

For many oceanographical processes, it is therefore important to consider and study the effects of riverine discharge plumes and the resulting mixing with the surrounding saltwater.

1.2 Sea Surface Salinity & Ocean Color in River Plumes

1.2.1 Sea surface salinity

The salinity is the total amount of dissolved materials in grams in one kilogram of seawater (Sverdrup et al. [1942]). Salinity is dimensionless. It is expressed by a practical salinity scale (pss) as the conductivity ratio of a sea water sample to a standard KCl solution. Although this quantity is dimensionless, it corresponds to grams of salt per kilogram of seawater. In the ocean, the average salinity is 35 pss. Table 1.1 presents the average composition of the major constituents in 1 litre of seawater with a salinity of 35 pss (Pawlowicz [2013]).

Constituent	Formula	Concentration (g/kg)	Percentage of salt
Chloride	Cl^-	19.35 g	55 %
Sodium	Na^{2+}	10.78 g	31 %
Sulphate	SO_4^{2-}	2.71 g	8 %
Magnesium	Mg^{2+}	1.28 g	4 %
Calcium	Ca^{2+}	0.41 g	1 %
Potassium	K^{2+}	0.39 g	1%
Other		0.00... g	0.0... %

Table 1.1: Salt composition of a sample of 1 litre of seawater with a salinity of 35 pss.

A water mass is defined by Tomczak [1999] as a body of water with common formation history, having its origin in a particular region of the ocean. Water masses are usually

1.2. Sea Surface Salinity & Ocean Color in River Plumes

seen as objective physical entities that move around the ocean at different velocities.

A conservative property is a water mass characteristic, or property, which has no sources or sinks in the ocean interior. Observed changes in conservative properties can therefore only be the result of mixing with surrounding water (Tomczak [1999]).

A nonconservative property is a water mass characteristic or property which changes during the life span of the water mass. The reasons for this change can be biochemical, as in the case of nutrients and oxygen, or physico-chemical, as in the case of radionuclides and tracers (Tomczak [1999]).

Salinity, can thus be seen as a conservative property of these water masses if ocean/atmosphere fluxes are neglected. This property only changes by mixing with nearby water masses of different properties, there is no source or sink of salinity in the ocean interior (isochemical).

1.2.2 Ocean Color

The Dissolved Organic Matter (DOM) is the largest reservoir of organic carbon in the ocean. The riverine DOM represents a link between terrestrial and oceanic DOM pools and consists of highly degraded material primarily derived from soil humic and fulvic acids (Ertel et al. [1986]). DOM has a main role in the biogeochemistry of the oceans (Duce and Duursma [1977]). It plays a number of important roles in both biogeochemical cycling of a wide variety of elements (such as carbon) and controlling coastal water optical properties (Bricaud et al. [1981] ; Green and Blough [1994]). The transport of riverine terrestrial carbon into the ocean is a major component in the global carbon cycle. The main part of this carbon is dissolved (Dissolved Organic Carbon (DOC)) and it is a part of the DOM.

Consequently, DOM and DOC represent a prominent topic of research. Ocean Color sensors permit, among other, to retrieve the materials in the ocean which interact with the light. The color of ocean, measured in full spectral detail, tells the composition and concentration of dissolved and particulate materials in seawater. Sunlight striking the ocean surface penetrates into the water column and interacts with the dissolved and particulate material in the seawater. Part of the light, not absorbed by these materials, is scattered in a backward direction and exits the surface. This reflected light represents the ocean color signature of the water. The most important components contributing to ocean color other than the water itself are 1) phytoplankton pigments (organic particles), which mainly consist of chlorophyll ; 2) inorganic particulates, non living organic particulates, bubbles and bacteria ; and 3) colored or chromophoric dissolved organic matter (CDOM) also known as yellow substances, gilvin or gelbstoff (Coble et al. [2004]). Because it can

be measured by Ocean Color sensors and because it has an important impact on the biogeochemistry of the coastal waters, we will focus on the CDOM.

Colored Dissolved Organic Matter (CDOM), also called Chromophoric Dissolved Organic Matter, is the largest fraction of DOM. It is the DOM component which absorbs ultraviolet and visible light. The term "colored" refers to the optical properties of CDOM which include the absorption of blue light and blue fluorescence (Coble [2007]). The "organic matter" term means that this material contains both carbon and hydrogen and is of biological origin. "Dissolved" refers to the opposite of particulate and is defined operationally by mechanical separation of water samples to remove particles larger than some minimal diameter (around 0.2-0.7 μm). In some cases, GF/F filters (glass fiber filters), which effective pore size is 0.7 μm , are used but in most cases, 0.2 μm polycarbonate Nuclepore filter (a filter in which holes a few micrometres in size have been created in a plastic (polycarbonate) membrane) are used to separate the dissolved and particulate fractions. Dissolved materials pass such filters whereas particulate does not. This definition persists today although it is now known that seawater contains a continuum of discrete units with no discernable break in abundance in the micrometer range (Blough and Del Vecchio [2002]).

The recent interests in CDOM has numerous origins. CDOM, such as DOM in general, can play a substantial role in the biogeochemistry of carbon, trace elements and gases and natural waters merely through its influence on the aquatic light field ; ocean optics and remote sensing ; photochemistry and photobiology ; phytoplankton ecology and physiology (CDOM can both increase primary production by blocking harmful ultraviolet radiation and limit productivity due to light limitation) ; harmful algal bloom mitigation ; and coral reef ecology (Blough and Del Vecchio [2002] ; Coble [2007] and references therein).

Colored Dissolved Organic Matter (CDOM) can come from both terrestrial and marine sources. In coastal areas, CDOM mostly comes from rivers containing organic materials leached from soils (humic substances). CDOM is also produced in the open ocean by the release of organic molecules from organisms during bacterial and viral lysis (cell breakage), excretion, and grazing (Coble et al. [1998] ; Nelson et al. [1998] ; Blough and Del Vecchio [2002]).

In regions experiencing large freshwater inputs from river and their subsequent entrainment by surface circulation, significant levels of terrestrial CDOM are not only confined to the mouth but they can extend offshore (see figure 1.1) and impact the optical prop-

1.3. The Conservative Mixing in River Plumes

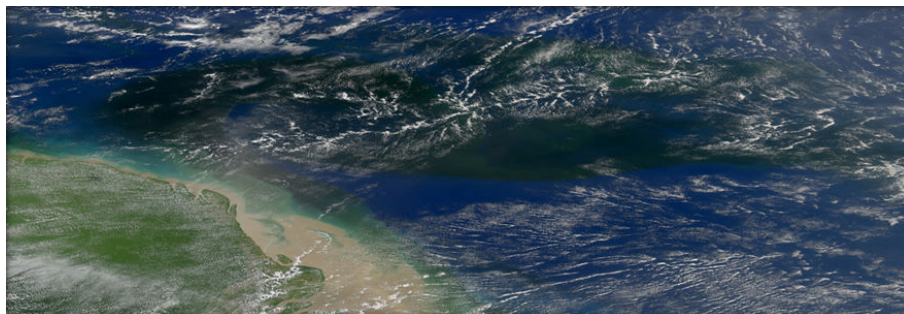


Figure 1.1: Amazon plume seen by the spaceborne MERIS sensor.

erties of oceanic waters over significant geographic areas (Muller-Karger et al. [1988] ; Del Castillo et al. [1999]).

1.3 The Conservative Mixing in River Plumes

1.3.1 Generalities

In this study, we focus on the water mass which finds its origins at the mouth of a river. This water mass is characterized in general by a low salinity and a high concentration in DOM, and thus CDOM. We are interested in the mixing of such a water mass from the mouth to the open ocean.

Salinity, being a conservative constituent, can act as a tracer of water masses, more precisely in that case, of riverine freshwater masses.

Moreover, in estuaries, because rivers are the main source of DOM, and thus CDOM, the latter can act as a tracer of these riverine waters, while they mix with the higher-salinity and lower-DOM open ocean waters (Blough and Del Vecchio [2002] ; Coble et al. [2004] ; Hu et al. [2004]). A distinction between two different water masses in the ocean has been introduced by Morel and Prieur [1977] and refined by Gordon and Morel [1983]. Case I waters are those where the optical properties are dominated by phytoplankton and their associated debris and dissolved organic matter, CDOM and chlorophyll are thus correlated. In river plumes, considered as case II waters, CDOM and chlorophyll are not correlated. This implies the indirect role of chlorophyll in CDOM production which comes from the continent through the river discharge (Hu et al. [2004]). Thus, CDOM represents a better tracer of river waters than chlorophyll (Hu et al. [2003]).

In estuaries, the salinity of riverine freshwater masses tends to increase linearly as they mix in the open ocean. DOM concentration, or more generally the riverine constituents concentration, also tends to decrease. A mixing plot, in which a dissolved constituent, such as DOM, is plotted against salinity, is commonly used to interpret conservative and non-conservative processes in estuarine systems (Loder and Reichard [1981]). Assuming that the system is at steady state (Boyle et al. [1974]) for an estuary in which constituent concentrations in the endmembers (river and ocean) remain constant over time period greater than the estuary’s flushing time (defined as the time required for river flow to replace the existing fresh waters in the estuary (Dyer [1973])), if the plotted data fall on a straight line, then the constituent is said to mix conservatively (Loder and Reichard [1981]). This is what is called a conservative mixing process (see figure 1.2).

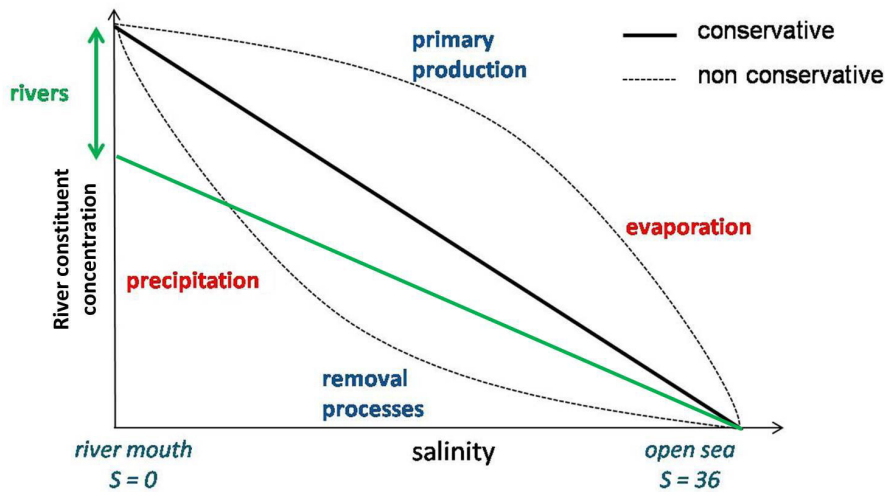


Figure 1.2: Scheme of the conservative mixing and the different potential sources of non conservative behaviours.

A non-linear dependence between SSS and the dissolved constituent concentration usually indicates a non conservative behaviour, the presence of internal sources or sinks (Loder and Reichard [1981]). Biogeochemical processes can affect the DOM concentration. Primary productivity or photobleaching can cause the creation or the destruction of DOM. Salinity is considered as a conservative property in a water mass. However, in this study, as we consider the surface layer, which is at the interface with the atmosphere, sinks and sources of salinity can exist. In presence of evaporation or precipitation, the salinity would be higher or lower, respectively, than expected for a conservative mixing process (see figure 1.2). Sea surface salinity cannot be considered as conservative and physical non conservative processes, affecting sea surface salinity, in the mixing curve have also to be taken into account.

1.3. The Conservative Mixing in River Plumes

It has been shown by [Loder and Reichard \[1981\]](#) that, in estuaries, a bend in the mixing line, generally interpreted as a non conservative behaviour, could also be the result of temporal variations in end-member (river and ocean) constituent concentrations even during a conservative mixing. In estuaries with flushing time greater than a few days, the changes in endmember concentrations could affect the shape of the observed mixing curve. As a consequence, for a conservative property, the resulting mixing curve would be a function of variability in river properties and flow, flushing time of the estuary and changes in ocean endmember properties ([Loder and Reichard \[1981\]](#)).

1.3.2 Conservative mixing in river plumes using Ocean Color and sea surface salinity observations

In this thesis, we focus our analysis on the study of the conservative mixing using remote sensing observations. The information about the constituents in the surface layer of the ocean, such as dissolved organic matter, can be recovered from Ocean Color sensors in terms of light absorption and not in terms of concentrations. Moreover, as these sensors permit to recover information on the interaction between, among others, the pigment contained in dissolved organic matter and the light, only information on the CDOM, the colored part of the dissolved organic matter, can be retrieved ([Robinson \[2004\]](#)). In our work, we thus mainly focus on the relationship between sea surface salinity and optical parameters, such as light absorption, light attenuation at precise wavelengths which mainly depend on colored dissolved organic matter, a tracer of the riverine water.

A strong negative linear correlation between sea surface salinity and bio-chemical/optical parameters has been often reported in the literature for numerous river estuaries ([Ferrari and Dowell \[1998\]](#) ; [Binding and Bowers \[2003\]](#) ; [Hu et al. \[2003\]](#) ; [Chen et al. \[2007\]](#) ; [Granskog et al. \[2007\]](#) ; [Bowers and Brett \[2008\]](#) ; [Del Castillo and Miller \[2008\]](#) ; [Urquhart et al. \[2012\]](#) ; [Bai et al. \[2013\]](#)).

The slope of the linear SSS/riverine constituents relationship can however vary significantly (see figure 1.2) as a considerable range of constituent concentration values at the river endmembers have been reported ([Blough and Del Vecchio \[2002\]](#)). The variation of the riverine constituents concentration at the river mouth is indeed a function of hydrology and land cover attributes for a given river ([Battin \[1998\]](#) ; [Salisbury \[2003\]](#) ; [Salisbury et al. \[2008\]](#) ; [Huang and Chen \[2009\]](#)). Both vary geographically and seasonally and

show time scales of variability depending on cumulated atmospheric forcings along the river upstream. In addition, departures from the linear conservative mixing may occur due to physical, bio-optical and bio-chemical processes downstream of the mouth (see figure 1.2). These include mixing with additional water masses (Blough and Del Vecchio [2002]) or *in situ* subsidies of river constituents released via net phytoplankton growth (Twardowski and Donaghay [2001] ; Yamashita and Tanoue [2004]), microbial utilization (Moran et al. [1999] ; Obernosterer and Herndl [2000]) or photochemical oxidation (Miller and Zepp [1995]).

Chapter 2

Observations

2.1 Sea Surface Salinity Data

2.1.1 *In situ* data

Our basic knowledge about the global Sea Surface Salinity (SSS) distribution prior to 2010 is derived from compilation of all the available oceanographic data collected over time (Boyer et al. [2005] ; Antonov et al. [2006]). The SSS *in situ* observing system has expanded significantly during the last 14 years. The most significant increase has come about with the full deployment of the Argo array in recent years with >3000 floats providing an average of one sample every 300-400 km square every 10 days. Already, these data are useful for documenting the changes in the large scale salinity field in recent years (Riser et al. [2008] ; Johnson and Lyman [2008]). The tropical mooring arrays (TAO, PIRATA, RAMA) are now almost completely outfitted with SSS sensors. The underway ship thermosalinograph measurement program (GOSUD) has also continued, and the data provide complementary quantitative information about SSS spatial variability. Another observing platform with the potential to substantially enhance in SSS observing capability is the surface velocity drifter program, as the technical obstacles for calibration stability are being resolved. Most *in situ* SSS observing data (TSG onboard ships, drifters, floats, moorings, equipped mammals, gliders,...) are now integrated, quality controlled and made available to the users through international Data Assembly Center (DAC). The european DAC for *in situ* ocean observations is the Coriolis center hosted by Ifremer. However, efforts have still to be conducted regarding quality controls and the availability of data in databases.

We use the 5 m depth salinity data transects acquired in the Amazon-Orinoco River plume region during 2010-2012 from the ThermoSalinoGraph (TSG) sensors onboard ships of opportunity and gathered within the Global Ocean Surface Underway Data (GOSUD) project. These include the data from 45 transects regularly acquired along a Europe-French Guiana shipping route collected by vessels Colibri and Toucan.

We also consider a collection of UnderWay TSG SSS measurements at 3 m depth collected from the R/V Knorr during several cruises in 2010 across the Amazon River plume. One has been performed in the frame of the US/NFS project Amazon iNfluence on the At-

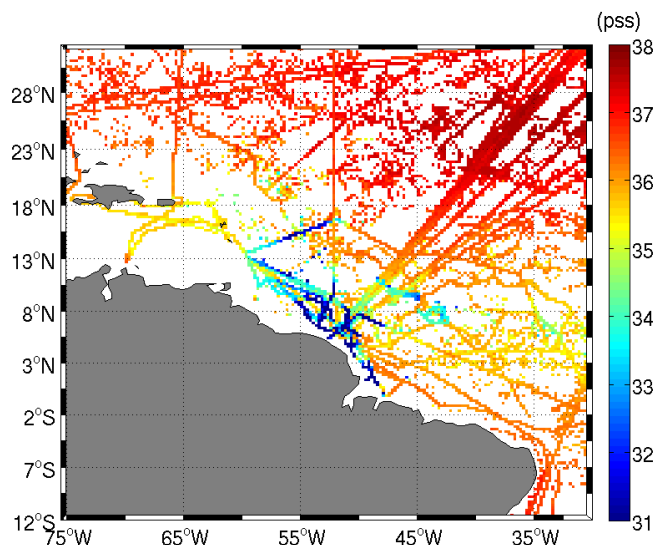


Figure 2.1: Average *in situ* sea surface salinity per 0.25° bins over the period 2010-2012.

lantic: CarbOn export from Nitrogen fixation by DiAtom Symbioses (ANACONDAS). An other one in the frame of the project Field and Laboratory Program to Evaluate Atlantic Intermediate Circulation During the Past 25,000 Years. Finally, another one has been conducted in the frame of the project Reconstruction of a continuous, high-resolution record of late Quaternary paleohydrology and paleoclimate of the Amazon basin.

We also consider TSG SSS measurements collected from the R/V Atlantis during 3 cruises in 2012 across the Amazon River plume. They have been performed in the frame of the projects ANADONDAS, Global Ocean Repeat Hydrography, Carbon, and Tracer Measurements and the project Seismicity of the Equatorial Mid-Atlantic Ridge and Its Large Offset Transforms.

In the frame of the Geotraces international program which aims to improve the understanding of biogeochemical cycles and large-scale distribution of trace elements and their isotopes in the marine environment (see <http://www.geotraces.org/>), the Geotraces West Atlantic cruise leg 2 was conducted on R/V Pelagia across the Amazon River plume. During leg 2 of the Geotraces cruise, which started the 11th of June 2010 departing from St George (Bermuda) and ended in Fortaleza (Brazil) on the 7th of July 2010, a total of 22 Conductivity-Temperature-Depth (CTD) stations were conducted.

Numerous surface drifters over various parts of the ocean have been deployed in order to measure SSS in the first 50 cm of the ocean. They were quality controlled and made available by LOCEAN laboratory. We consider data from METOCEAN and PacificGyre

2.1. Sea Surface Salinity Data

drifters, launched from 2010 to 2012.

Two other important sources of *in situ* salinity data in the northwestern tropical Atlantic are the upper level measurements from Argo profiling floats and from the Pirata mooring array. We consider here the daily mean 1 m depth mooring salinity data from the Pirata moorings. For the period 2010-2012, we also collect an ensemble of ~ 6500 Argo samples acquired in the top 10 meters and within the spatial domain defined by $[5^{\circ}\text{S}-30^{\circ}\text{N}, 70^{\circ}\text{W}-30^{\circ}\text{W}]$. At each location, Argo data are computed as the mean of salinity data available between 10 meters deep and the surface.

All *in situ* data listed above for the period 2010-2012 are shown in figure 2.1. The map represents all the *in situ* data averaged per 0.25° bins over 2010-2012.

Profiles from the World Ocean Database 2009 (WOD09) distributed by the National Oceanographic Data Center (NODC) of the National Oceanic and Atmospheric Administration (NOAA) are also used. In figure 2.2, the number of SSS data available from the World Ocean Atlas 2009 per bin of the grid is shown.

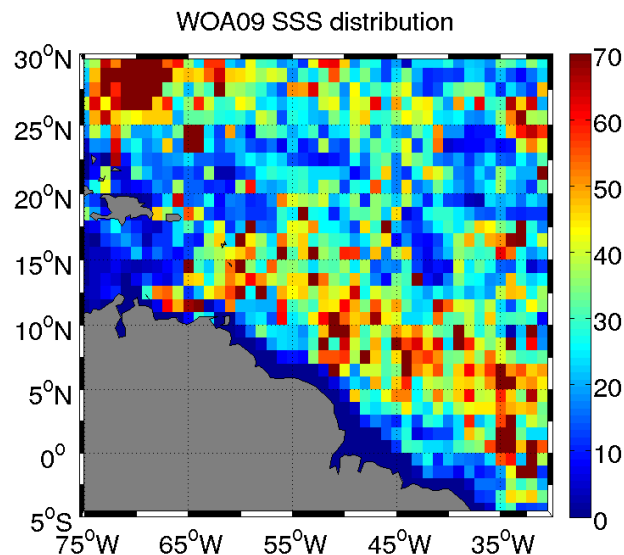


Figure 2.2: Number of sea surface salinity data (from 0 to 10 m deep) from World Ocean Atlas 2009 (WOA09) available averaged per bin of $1 \times 1^{\circ}$.

The SeaBASS system, originally developed by the SeaWiFS Project, catalogs radiometric and phytoplankton pigment data used for ocean color satellite product calibration and validation. Archived data include measurements of apparent and inherent optical properties,

phytoplankton pigment concentrations, and other related oceanographic and atmospheric data, such as water temperature, salinity, stimulated fluorescence, and aerosol optical thickness. Data are collected using a number of different instrument packages, such as profilers, buoys, hand-held instruments on a variety of platforms, including ships and moorings (<http://seabass.gsfc.nasa.gov>). In this study, *in situ* measurements of total sea water absorption from the SeaBASS system are used, especially measurements from the cruises apr03atl from the 19th of April 2003 to the 20th of May 2003, jan01sj from the 8th of January 2001 to the 20th of February 2001 and jun01kn from the 26th of June 2001 to the 15th of August 2001.

2.1.2 Sea Surface Salinity climatology

The monthly sea surface salinity climatology of the tropical Atlantic ocean developed by [Reverdin et al. \[2007\]](#) is also used in this work. These products are generated at a spatial resolution of 1x1 degrees.

2.1.3 SMOS Sea Surface Salinity data

2.1.3.1 Remote sensing measurement of sea surface salinity

The emissivity of a material (usually written ε or e) is the relative ability of its surface to emit energy by radiation. It is the ratio of energy radiated by a particular material to energy radiated by a black body at the same temperature. A true black body would have an $\varepsilon = 1$ while any real (grey body) object would have $\varepsilon < 1$. Emissivity is a dimensionless quantity. ([Sharkov \[2003\]](#)).

The emissivity of the ocean surface is a function of the complex dielectric constant of sea water constant also called permittivity and the roughness state of the sea surface. Thus, a precise knowledge of the sea water complex dielectric constant is required to study the radiative transfer of microwave radiation emitted by the ocean surface. The dielectric constant depends on electromagnetic frequency, temperature and salinity. It is therefore possible to retrieve sea surface salinity estimates from passive microwave measurements, as long as other geophysical variables influencing the brightness temperature signal can be accounted for (sea surface temperature, surface roughness, ionospheric effects, cosmic background radiation, atmosphere).

Radiometers operating at an L-band and more precisely at a frequency of 1.4 GHz, are

2.1. Sea Surface Salinity Data

usually chosen for SSS remote sensing as a trade-off between good sensitivity to SSS, reasonable spatial resolution from Space, but also because L-band is a protected band. However, sensitivity of brightness temperature to SSS at such frequency remains low (0.5 K per pss for a SST of 20°C, decreasing to 0.25 K per pss for a SST of 0°C). Furthermore, the best-case radiometric sensitivity of currently available radiometers (0.1 to 1-2 K) limits the accuracy for salinity estimates from a single pass, which makes temporal and spatial averaging necessary (Kerr et al. [2000] ; Berger et al. [2002] ; Font et al. [2010] ; Kerr et al. [2010]).

2.1.3.2 SMOS sea surface salinity measurement

Notwithstanding the gains of the past decade regarding the *in situ* data available, the *in situ* sample density remains sparse compared to the sampling capabilities to be achieved by the satellites. The absolute accuracy of the satellite SSS measurements is however commensurately less than automated *in situ* sensors. Moreover, they are not sensing the same layers of the upper ocean. Whereas L-band sensors measure the first 20 cm of the ocean, *in situ* instruments can measure salinity from few meters to several hundred meters depth. Therefore, the satellite and *in situ* observing systems are complementing each other when their respective merits are put to use. Two satellite missions are currently co-flying with the aim of measuring salinity from Space : SMOS and Aquarius missions.



Figure 2.3: MIRAS instrument onboard the SMOS satellite.

The Soil Moisture Ocean Salinity (SMOS) Mission : Developed by the European Space Agency (ESA) in cooperation with the space agencies of France and Spain. The SMOS

mission was launched in late 2009. As the name implies, SMOS is a dual science mission, with the engineering design driven primarily by acquiring high spatial resolution over land. The radiometric signals associated with SSS variability are small relative to the SMOS radiometer sensitivity, and the data require careful calibration and considerable spatio-temporal averaging to reduce measurement noise (Font et al. [2004]). The sensor consists of three radial arms with 69 small microwave (1.413 GHz) detectors that form a phased array (see figure 2.3). From the interferometric inter-correlations and considerable ground processing, a two-dimensional image is reconstructed with an average pixel size of 43 km. The field of view is about 1000 km wide, and the maximum revisit time interval at the equator is about 3 days. The SMOS orbit is near polar, sun-synchronous (6 am/6 pm local time at the equator).

The official SMOS ESA mission delivers data up to Level 2 (along swath geo-located retrieved salinity per orbit), with an additional Near Real Time processing chain implemented for operational applications by meteorological centers (mainly for soil moisture). The spatio-temporal averaged and analyzed products (Level 3), as well as other value added products including external information (Level 4), are generated and distributed by dedicated processing centers in France (CATDS, developed by CNES and operated by Ifremer) and the Barcelone Expertise Center in Spain (CP34).

Aquarius/SAC-D Mission : Launched in summer 2011, the NASA/CONAE Aquarius/SAC-D mission primary scientific measurement goal is to estimate SSS from space (Lagerloef et al. [2008]). The Aquarius instrument includes a set of 3 precisely calibrated real-aperture satellite microwave radiometers operated at L-band, as well as a radar backscatter sensor to correct for the surface roughness effect (Le Vine et al. [2007]). The Aquarius/SAC-D orbit is also near polar, sun-synchronous, crossing the equator at 6 am/6 pm local time but with opposite ascending/descending times from SMOS. The orbit repeats the ground track every 7 days. SSS is retrieved along 3-beam swaths, ranging from 90 to 150 km beam widths. The science data files include Level 1a (unprocessed raw data), Level 2b (swath format science data file, including retrieved SSS calibrated and validated with *in situ* SSS observing network, calibrated brightness temperature, radar backscatter, and all other ancillary geophysical data and corrections), and Level 3b (1°x1° gridded SSS, error covariance and gradient fields objectively analyzed every 7 and every 30 days). For both missions, higher-level data products such as blended satellite and *in situ* data fields, blended Aquarius-SMOS analyses and data assimilation products are still being addressed by the science teams and the broader science community.

2.1. Sea Surface Salinity Data

For this study, we used the Centre Aval de Traitement des Données SMOS (CATDS, www.catds.fr) Expertise Center-Ocean Salinity (CEC-OS) SMOS SSS (IFREMER V02) products (Reul and Tenerelli [2011]). Data were first processed to provide a Level 3 daily-mean gridded SSS field at a resolution of $0.25^\circ \times 0.25^\circ$ for the complete period 2010-2013. Composite L4 products were then generated using a running mean having a temporal and a spatial window of ± 5.5 days and $\pm 0.25^\circ$, respectively. Regarding our region of interest, the precision of this product is about 0.5 pss.

Our first objective in this study is to analyze the relationship between satellite SSS and ocean color. At the time this work was conducted, the maturity of SMOS products was more advanced than the Aquarius. While it would have been interesting to compare results obtained using either SMOS or Aquarius SSS, as first step, we choose here to consider only SMOS data.

2.1.3.3 SMOS SSS quality assessment in the Amazon River plume region

To validate SMOS satellite SSS retrievals in the region of the Amazon plume over 2010-2012, sets of *in situ* measurements from several sensors (ThermoSalinoGraph (TSG), Conductivity-Temperature-Depth (CTD), TAO moorings and Argo profiling floats) acquired routinely or during dedicated scientific campaigns were gathered and analyzed.

Validation with ThermoSalinoGraph data

The open ocean salinity in the northwestern tropical Atlantic region is 36-37 pss. The Amazon River plume can induce very strong surface salinity drops of more than 3-4 pss with respect to the open ocean conditions. This is illustrated in figure 2.4, where we show underway ship measurements. The Amazon river plume was crossed many times by the several Voluntary Observing Ships from the GOSUD and from the US/NFS ANACONDAS projects from January 2010 to November 2012. Satellite SSS were compared to the thermosalinograph (TSG) samples by averaging SMOS data in space and time considering all satellite swath data acquired within ± 25 km and ± 5 days from the TSG samples along each vessel track. The histogram of the SSS differences between these SMOS products and the TSG data is shown in figure 2.5 and is found to be quasi Gaussian with a near zero pss mean and a standard deviation of ~ 0.3 pss.

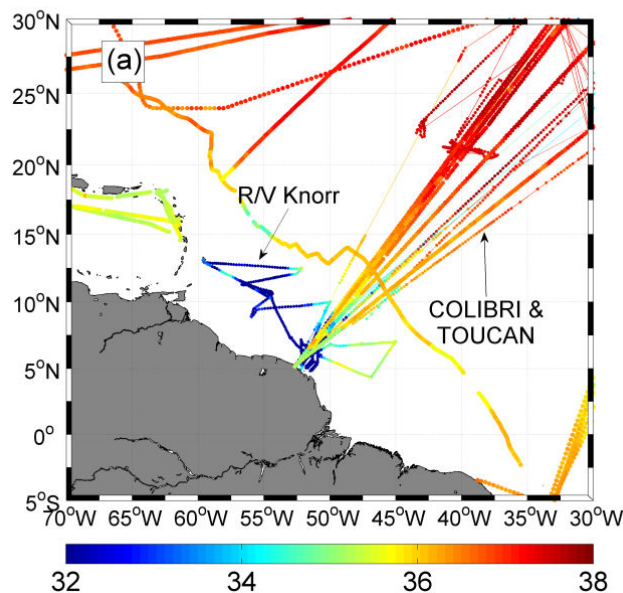


Figure 2.4: Ensemble of ship tracks collected for years 2010, 2011 and 2012 onboard which salinity measurements were conducted from TSG at 3 or 5 m depth (color indicates value of salinity).

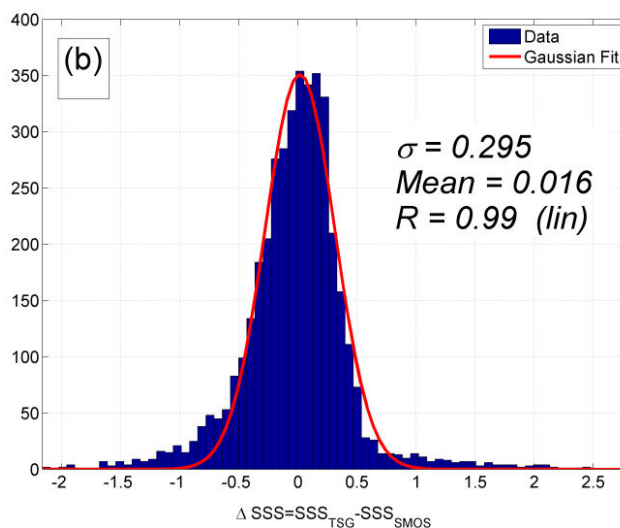


Figure 2.5: Histogram of the salinity differences between TSG data and collocated 10-day running mean SMOS SSS.

Figure 2.6 shows representative examples of the collocated satellite SSS together with the *in situ* TSG data acquired at depth between 3 and 5 meters along the ship tracks for different seasons and years. Comparisons with TSG data show that in general, SMOS detected the river plume freshwater surface signal as observed by the ship measurements regardless of the season or year. As expected, the ± 25 km and 10-day averaging of SMOS

2.1. Sea Surface Salinity Data

data appears to yield smoother SSS gradients than the localized space and time ship observations. This is particularly evident for the ANACONDAS R/V Knorr 2010 cruise datasets (bottom panel).

If not carefully validated, ship SSS measurements can be afflicted with several pss biases. In the northwestern tropical Atlantic ocean, these biases are weak (0.1 pss for Toucan and Colibri cruises, up to 0.5 pss for the Knorr cruise in 2010) in comparison with the SSS variations studied here.

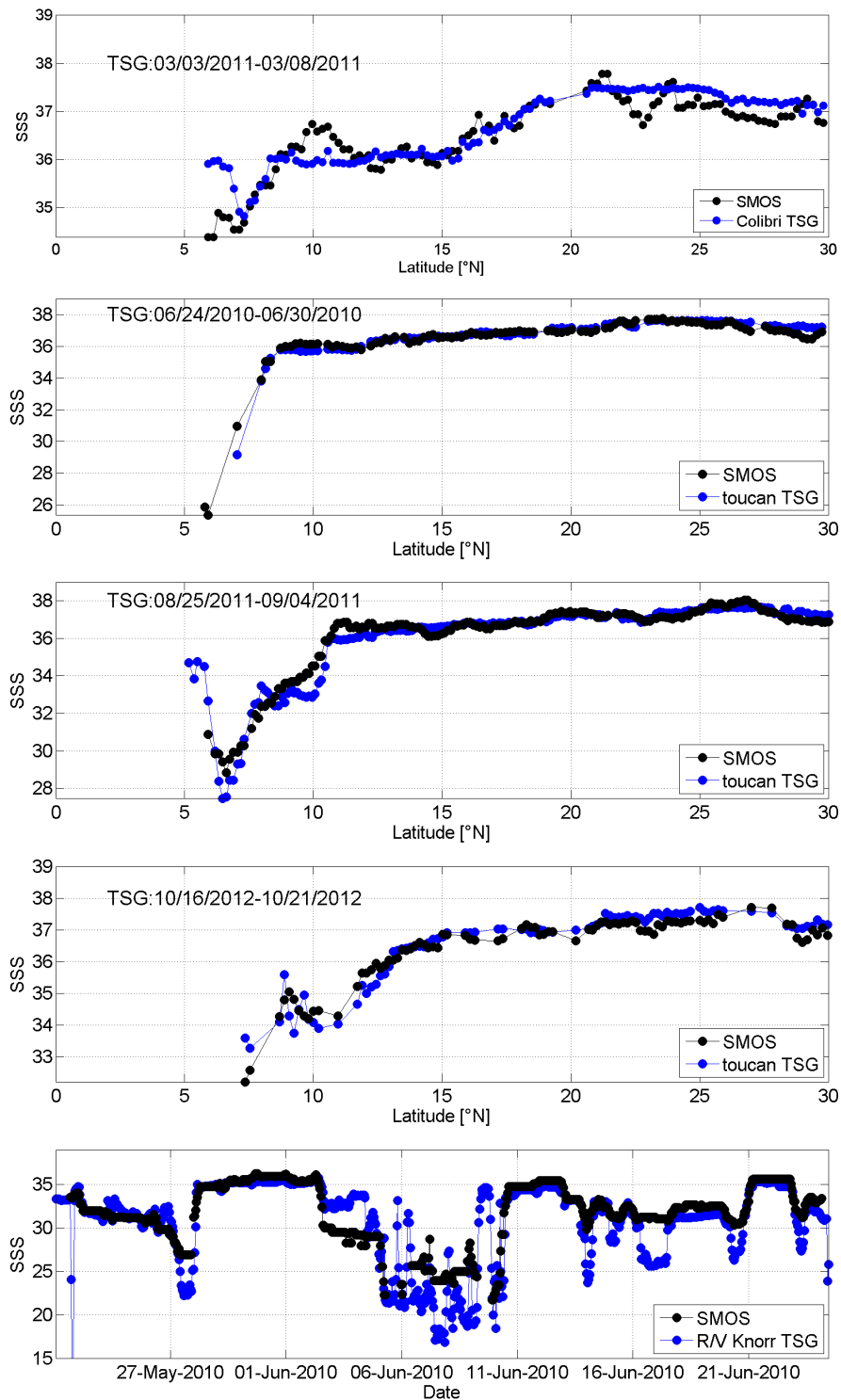


Figure 2.6: Examples of TSG data (blue dots) with collocated 10-day running mean SMOS SSS (black dots) as a function of latitude along several ship tracks (for the top four panels, the date is indicated in the inset) and as function of date during the Anaconda R/V Knorr 2010 cruise (bottom panel).

2.1. Sea Surface Salinity Data

Validation with CTD data

Comparisons between collocated SMOS SSS and *in situ* conductivity-temperature-depth (CTD) measurements acquired during the Geotraces West Atlantic cruise leg 2 across the Amazon River plume in June 2010 (see figure 2.7) illustrate the ability of the satellite data to monitor the freshwater Amazon-Orinoco plume signal. This campaign was conducted on RV Pelagia in the frame of the Geotraces international program (see <http://www.geotraces.org/>). As shown in figure 2.8, the comparison between collocated SMOS SSS and the upper depth CTD data again reveals an overall good agreement with a standard deviation of the difference $SSS_{SMOS} - SSS_{CTD} \sim 0.45$ pss. There is a nice agreement over ~ 4 pss gradient. In particular, the strong SSS gradient and ~ 3 pss drop detected *in situ* as the R/V Pelagia crossed the Amazon River plume at the end of June 2010 is well reproduced by the satellite observations.

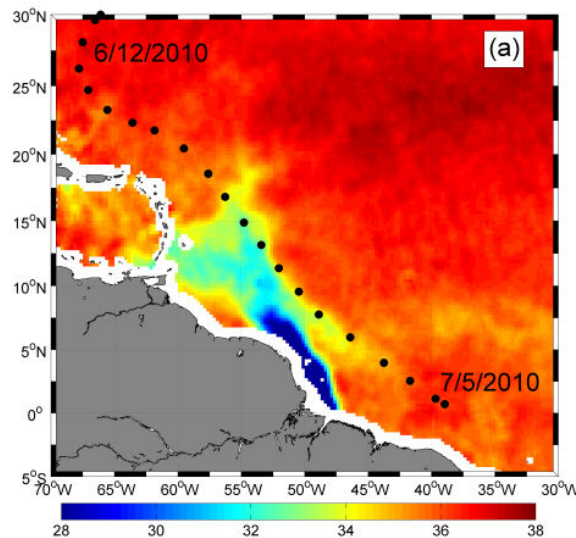


Figure 2.7: Black dots: location of the CTD stations conducted during the Geotraces West Atlantic cruise leg 2 (RV Pelagia) superimposed on the SMOS averaged SSS from June 12th to July 5th 2010.

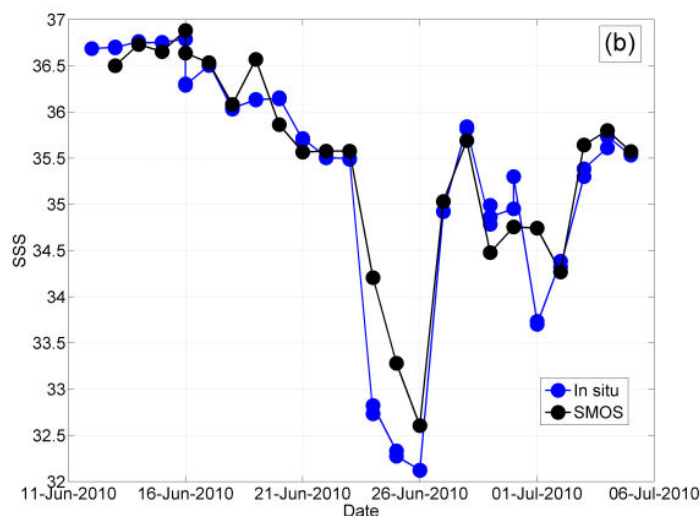


Figure 2.8: Collocated surface salinity between SMOS and *in situ* data along the leg. SMOS data have been averaged at 50 km resolution with a ± 5 day running temporal window.

Validation with Argo and TAO Mooring data

As illustrated in figures 2.9 and 2.1, the density of Argo and TAO Moorings surface observations available during 2010-2012 is significantly higher in the northern and western parts of the domain. Almost no *in situ* data are found in the Caribbean sea and a small amount of the ensemble of Argo floats sampled the Amazon-Orinoco plume, as defined using SMOS SSS as SSS fresher than ~ 35.5 pss.

Differences $\Delta SSS = SSS_{SMOS} - SSS_{in\ situ}$ between the satellite SSS and the *in situ* data including both Argo and Pirata observations exhibit an overall about zero mean and a standard deviation of ~ 0.3 pss, consistent with the results found with the TSG data (see figure 2.10). Apparently, the dispersion is nevertheless higher within the plume fresh waters and SMOS SSS are systematically saltier by ~ 0.5 -1 pss than the *in situ* measurements as SSS drops below 35 pss.

2.1. Sea Surface Salinity Data

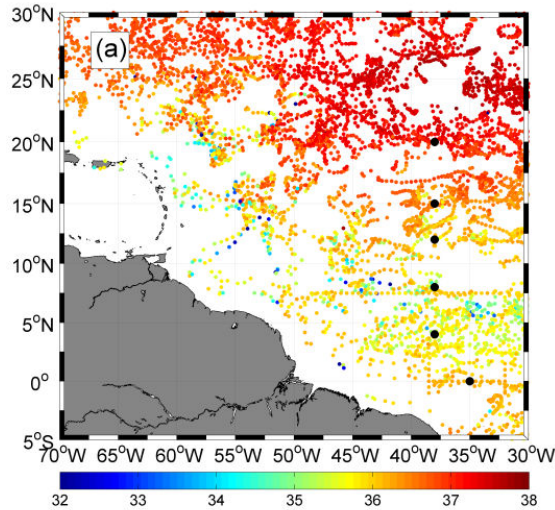


Figure 2.9: Ensemble of Argo floats SSS measurements collected in the top 10 meters during the period 2010-2012 within the spatial domain defined by $[5^{\circ}\text{S}-30^{\circ}\text{N}, 70^{\circ}\text{W}-30^{\circ}\text{W}]$ (color indicates the salinity value). The location of the Pirata moorings is indicated by black dots.

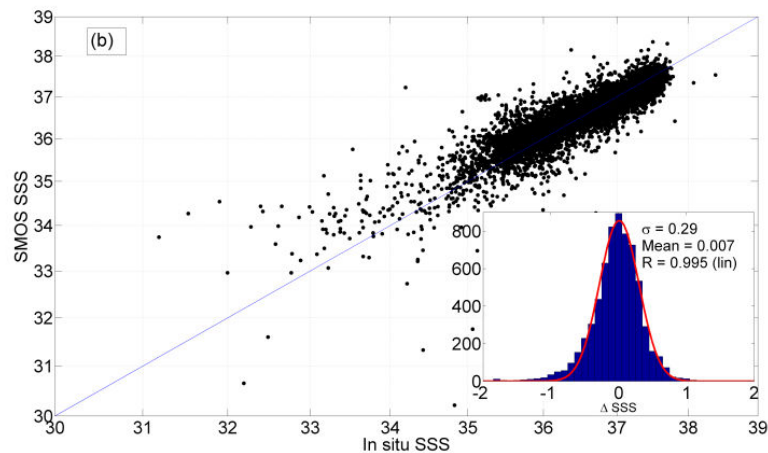


Figure 2.10: Comparison of the 10-1 m depth tropical salinity data and collocated, 10 days averaged SMOS SSS. The inset in (b) shows the histogram of the salinity differences $\Delta\text{SSS} = \text{SSS}_{\text{SMOS}} - \text{SSS}_{\text{in situ}}$ (blue) and a Gaussian curve fit (red) through that histogram.

2.1.3.4 Known issues

In the previous section, by comparing SMOS SSS data to various *in situ* surface measurements collected in the northwestern tropical Atlantic ocean from 2010 to 2012, the satellite SSS products were shown to well reproduce the observed strong SSS gradients found in the region of the Amazon plume. Overall, the standard deviation of the differences $\Delta\text{SSS} = \text{SSS}_{\text{SMOS}} - \text{SSS}_{\text{in situ}}$ is on the order of $\sim 0.3-0.5$ pss, considering 10 day averaged satellite

products at 50 km resolution. This is at least a factor 10 smaller than the SSS signal spatio-temporal variability encountered in this region. Nevertheless, a generally higher standard deviation of the satellite/*in situ* SSS differences is found in the plume waters as well as a salty bias in the satellite data, than the *in situ* ones, mostly at low sea surface salinity (see figure 2.11). These discrepancies can be attributed to either (i) differences in the respective spatio-temporal sampling characteristics of the space and *in situ* sensors, (ii) to the high spatio-temporal variability of the SSS within the plume waters (horizontal and vertical variability), (iii) to potential errors in the satellite products in the proximity of land masses, (iv) to potential errors when the radiometer data are contaminated by radio-frequency interferences (RFI), (v) to potential errors in the dielectric constant model used in the SSS retrieval algorithm, (vi) to eventual issues in the L3 SMOS SSS product correction based on climatological SSS data.

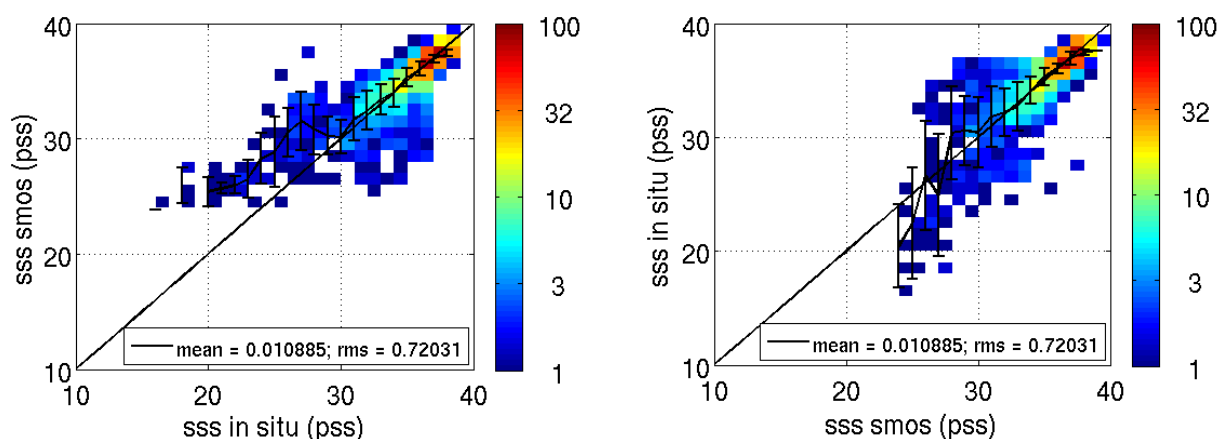


Figure 2.11: (Left) Mean SMOS SSS per bin of 1 pss of 2010-2012 *in situ* SSS ± 1 standard deviation. (Right) Mean 2010-2012 *in situ* SSS per bin of 1 pss of SMOS SSS ± 1 standard deviation. In z-axis is represented the number of data per bin of 1x1 pss.

SSS variability in the Amazon plume

Largest disagreement between satellite and *in situ* observations are found when the sampled plume is the closest to the river mouth. There is a high natural variability of horizontal and vertical salinity in the Amazon plume region considering time scales lower than the satellite revisit time (around 3 days). Salinity variations within the Amazon plume can reach 10 pss on timescales of days to weeks (Lentz and Limeburner [1995] ; Reverdin et al. [2007]). This can potentially explain the discrepancies found in the validation of SMOS data against *in situ* data in this region. On figure 2.12, the *in situ* climatological SSS, from World Ocean Atlas 2009 data, and its RMS are represented, showing the vari-

2.1. Sea Surface Salinity Data

ability of SSS in the Amazon plume region.

As seen in figure 2.6, for the shown ANACONDAS's campaign track, SMOS SSS is successively fresher and saltier than the one measured from the ship at 3 m depth, between the 2nd and 11th of June 2010. As revealed by the CTD casts conducted during that period in the stations 10 to 16 (see figure 2.13), very strong vertical SSS gradients are found here (sometimes reaching 20 pss in the upper 15 m). A high temporal variability is found in the vertical salinity structure from one profile to the other at the same location on the same day (e.g. station 11), probably indicating tidal impacts on the vertical plume structure.

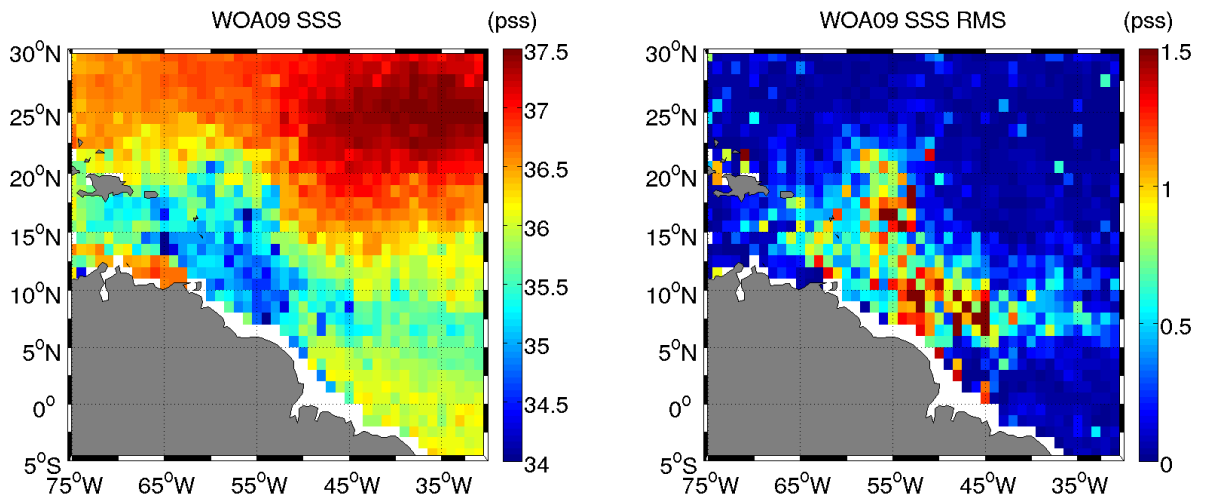


Figure 2.12: (Right) 0-10 m deep salinity from World Ocean Atlas 2009 (WOA09) and (left) its RMS averaged per bin of $1 \times 1^\circ$.

The fact that there is a systematic positive bias between SMOS and *in situ* SSS at low salinity (see figure 2.11) shows that the natural variability of horizontal and vertical salinity in the region is not the only source of the observed offsets between SMOS and *in situ* SSS data. In that case, there would be random biases. Therefore, the errors source comparing SMOS and *in situ* SSS is a mix between several different causes listed below.

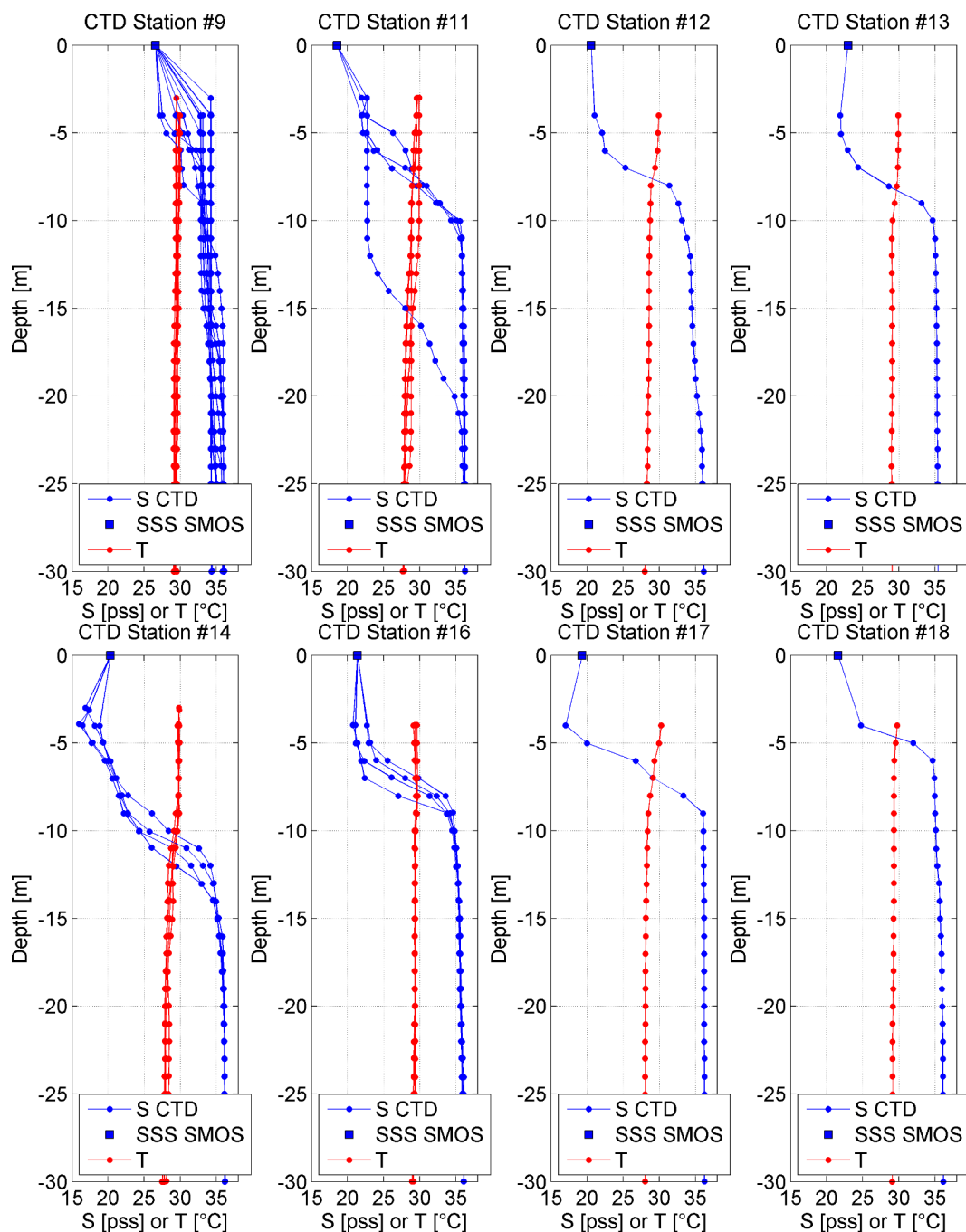


Figure 2.13: Temperature (red) and Salinity (blue) profiles in the upper 30 m of the ocean at some CTD stations shown in figure 2.6. SMOS SSS interpolated at the station location and time are shown by the blue squares.

Spatio-temporal sampling characteristics

In the Amazon plume region, where there are a strong horizontal and vertical natural SSS variability, SMOS spatial and temporal sampling characteristics can act as a main

2.1. Sea Surface Salinity Data

limitation in the SSS retrieval and in the validation of such products against *in situ* data. *In situ* data used are sampled at 3 to 5 meters depth whereas SMOS measures salinity in the first centimeters of the surface layer. Vertical SSS gradients being strong in this area (see figure 2.13), important bias can be found in the comparison between SMOS and *in situ* data.

Moreover, SMOS estimates sea surface salinity inside a footprint of about 50-100 km of diameter whereas an *in situ* instrument measures SSS at a precise location. In an area of strong horizontal SSS gradients, such as the Amazon plume river, this can thus bring lots of discrepancies when comparing SMOS and *in situ* data.

The high temporal variability also found in the vertical salinity structure (e.g. station 11 on figure 2.13) can impact the comparison with SMOS SSS products which are daily products +/- 5 days.

The combination of the horizontal, vertical and temporal plume structure variability and of the SMOS versus *in situ* sampling specificities may therefore explain these differences observed locally.

Level-3 SSS product correction

In the SMOS SSS retrieval algorithm, Level-3 products are corrected based on a SSS climatology in order to correct systematic biases. A high-pass filter is applied on SMOS data using a monthly $5 \times 5^\circ$ climatological SSS. The climatology is computed using World Ocean Atlas 2005 data (<http://www.nodc.noaa.gov/OC5/WOA05.html>). This climatology is then spatially interpolated on a $0.25 \times 0.25^\circ$ grid and temporally linearly interpolated every day. The interannual variability on the phenomena studied here can also be affected, attenuated. Indeed, compared with *in situ* data, biases can be higher than 1 pss in coastal regions (see figure 2.14). Climatological SSS tends to overestimate low SSS (below 28 pss). Consequently, this correction can have an impact on large-scale phenomena (500 km).

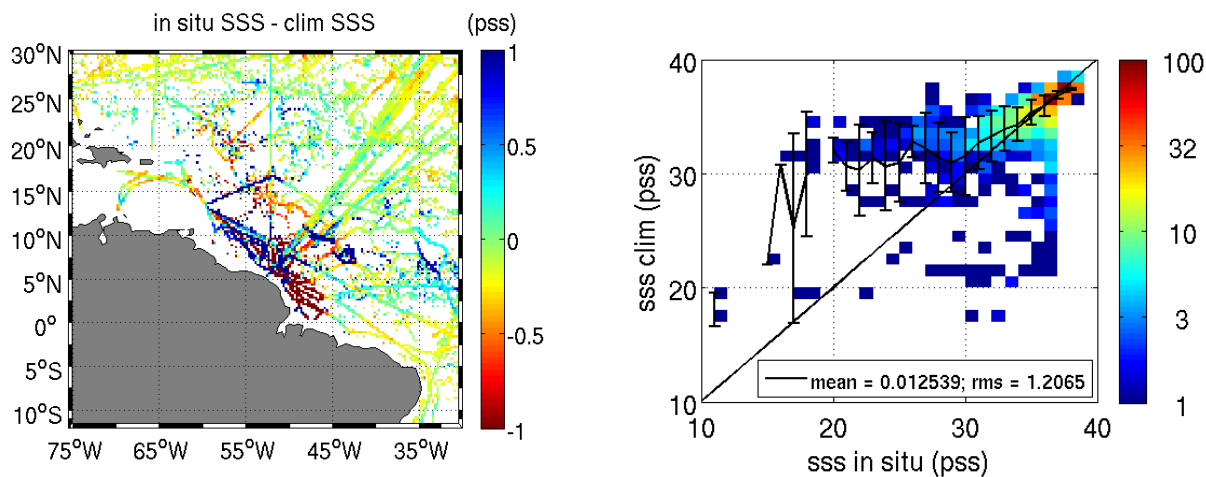


Figure 2.14: (Left) 0.25° map of the differences between climatological and 2010-2012 *in situ* SSS. (Right) Mean climatological SSS per bin of 1 pss of 2010-2012 *in situ* SSS ± 1 standard deviation. In z-axis is represented the number of data per bin of 1×1 pss.

Land contamination

The presence of land masses in the satellite footprint can affect the estimation of sea surface salinity close to the coast. In figure 2.15, we can notice that closer to the coast, the higher the anomaly between *in situ* and SMOS and the higher the standard deviation of the anomaly.

In order to attempt to get rid of land contamination in this analysis we don't consider the first three pixels from the coast which correspond to a distance of about 150 km off the coast.

2.1. Sea Surface Salinity Data

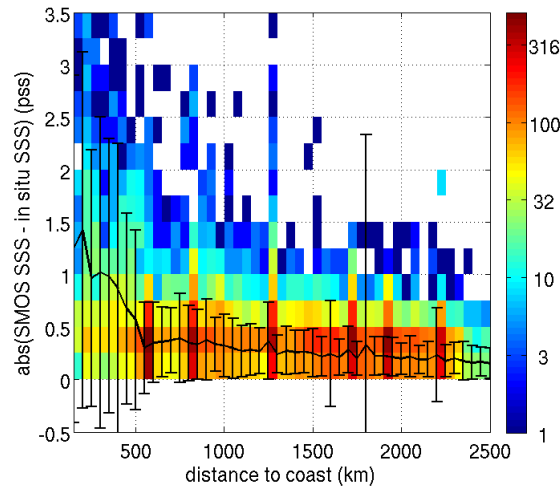


Figure 2.15: Mean differences between SMOS sea surface salinity and *in situ* salinity per bin of 50 km from the coast ± 1 standard deviation. In z-axis are represented the number of data per bin of 1x1 pss.

Radio-frequency interferences

Active radar sources emitting in some specific spectral bands cause the degradation of SMOS brightness temperature observations. In figure 2.16, the annual mean RFI percentage estimated in each $0.25 \times 0.25^\circ$ pixel is represented over 2010, 2011, 2012 and 2013. Important RFI contamination is present in the Caribbean sea and the contamination is more and more important over the years along the Brazilian shelf south of the Amazon river mouth. From 2013, it seems that the contamination next to the Amazon mouth becomes less important.

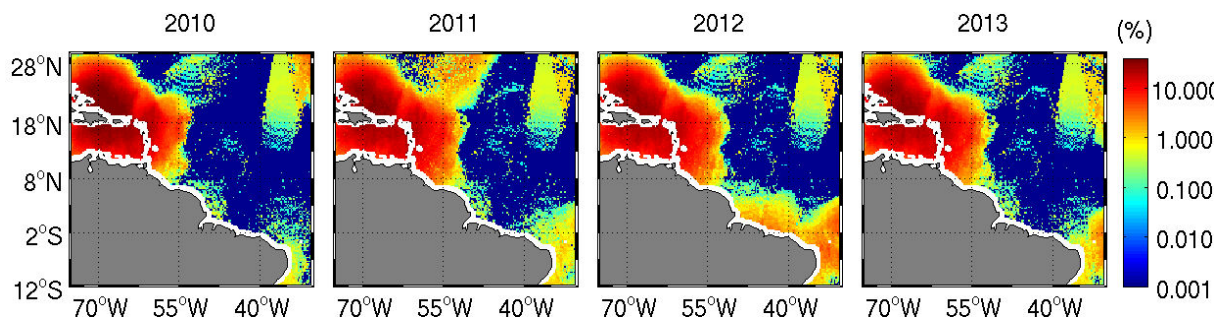


Figure 2.16: Maps of the mean Radio Frequency Interference percentage estimates in each $0.25 \times 0.25^\circ$ pixel over, from left to right, 2010, 2011, 2012 and 2013, represented using a logarithmic scale.

The seawater dielectric constant model

In the SMOS SSS retrieval algorithm, the dielectric constant model used is the [Klein and Swift \[1977\]](#) model computed for waters containing exclusively sodium and chloride. However, the Amazon river discharges waters highly concentrated in suspended and dissolved organic matter. These brackish waters affect the ionic concentration of seawater in the northwestern tropical Atlantic ocean. The dissolved and suspended particles could modify the local dielectric constant and the model used here could not be well-adjusted to this region.

Moreover, the dielectric constant model used here was developed for waters which temperature is lower than 25-28°C. However in this tropical region, waters can reach temperatures of 29-30°C during late summer.

2.2 Ocean Color Data

2.2.1 Ocean Color remote sensing

Ocean Color remote sensing refers to the scientific principles of a passive radiometer operating in the visible and near-infrared (IR) wavelengths. It is a remote sensing method which penetrates beneath the surface skin of the ocean down to a depth of several meters or more. The presence of living plant cells, dissolved organic matter and particulates in the upper ocean influences the color of sunlight scattered out of the sea. Accordingly, when the light leaving the water is measured, it can be interpreted to recover the information about the constituents in the surface layers of the sea. (Robinson [2004])

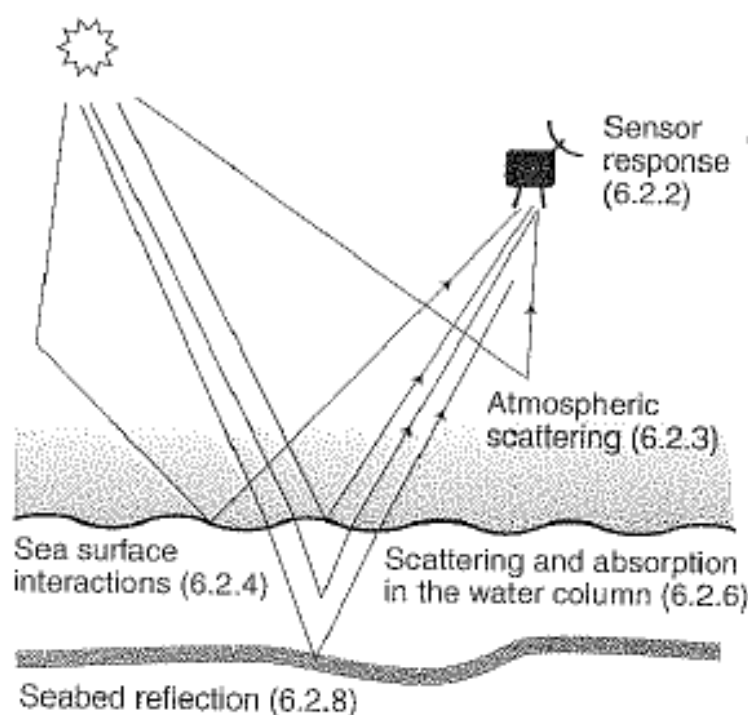


Figure 2.17: Scheme of the interactions of sunlight in the marine environment (Robinson [2004]).

Light from the sun, in the visible and near-IR wavelengths, after passing through or being reflected on the sea surface, can reach a sensor in space by several different routes (see figure 2.17). Part of this light is reflected directly at the sea surface, or within the atmosphere without entering into the sea. Another part enters into the sea and is reflected within the water column or at the seabed. (Robinson [2004])

Interactions that can occur between a photon and a molecule of seawater, the pigment contained in dissolved organic matter or in a phytoplankton cell, or a particle in suspen-

sion, are absorption, scattering and fluorescence (Robinson [2004]), which represent the inherent optical properties (IOPs) of seawater. Some constituents in the water cannot be measured in terms of concentration (number of molecules per volume solution) : they are measured based on the intensity of absorption of light or fluorescence emission.

The backscattering coefficient takes into account the scattering of the water (b_{bw}) and of the particulates (b_{bp}), a portion of which returns towards the sensor (see equation 2.1). The total absorption is the sum of the absorption of water (a_w), CDOM (a_g), inorganic particulates, non living organic particulates, bubbles and bacteria (a_d) and phytoplankton (a_{ph}) (see equation 2.2). (Maritorena et al. [2002])

$$b_b(\lambda) = b_{bw}(\lambda) + b_{bp}(\lambda) \quad (2.1)$$

$$a(\lambda) = a_w(\lambda) + a_g(\lambda) + a_d(\lambda) + a_{ph}(\lambda) \quad (2.2)$$

Because of their similar spectral shapes (Maritorena et al. [2002]), satellite instruments are not able to differentiate between CDOM and inorganic particulates, non living organic particulates, bubbles and bacteria, whereas, laboratory methods can separate these components. Consequently, Ocean Color algorithms measure the combined pool (see equation 2.3), called colored detrital matter (cdm).

$$a_{cdm}(\lambda) = a_g(\lambda) + a_d(\lambda) \quad (2.3)$$

A passive radiometer operating in the visible and near-IR wavelengths measures the reflectance, or water-leaving radiance exiting the ocean surface (in $\text{mW}/\text{cm}^2/\mu\text{m}/\text{sr}$), at different wavelengths. It represents the portion of downwelling sunlight leaving the surface of the ocean to the sensor, that has not been absorbed or scattered by seawater components. The reflectance depends on the IOPs : the total absorption and the backscattering coefficients of all constituents in the water including living plant cells, dissolved organic matter such as CDOM and particulates, and the water itself (Coble et al. [2004] ; Robinson [2004]). In the open ocean, there is almost no absorption in the blue region, it is bright thus the blue light backscattered to the satellite is high. In an area where a bloom occurs, the concentration in chlorophyll-a increases, there are more pigments which absorb light, thus the signal backscattered to the satellite is weak.

Thus, from the reflectance, several Ocean Color parameters can be estimated, depending

2.2. Ocean Color Data

on the wavelength considered. Corrections must be made for absorption and scattering by the atmosphere (Gordon [1997]). Radiances used to retrieve Ocean Color parameters from the MERIS sensor are :

- 412 nm : the radiance is usually the highest signal in the open ocean, it is backscattered out more efficiently in the open ocean. When CDOM becomes prominent, it affects this band the most (extremely low 412 nm radiance).
- 443 nm : the absorption of chlorophyll-a is maximum and the absorption of CDOM is also very high (very low 443 nm radiance).
- 490 nm : the absorption of CDOM, inorganic particulates, non living organic particulates, bubbles and bacteria and chlorophyll-a is almost equal so these components are hard to discriminate at such wavelength. K490 represents the attenuation of the light at 490 nm. If CDOM increases and chlorophyll-a decreases or the opposite, the K490 parameters wouldn't vary.
- 555, 670 and 709 nm : the radiances are dominated by backscattering, they thus permit to distinguish turbid and non turbid water.

In figure 2.18, the distributions of 412, 443, 555 and 709 nm water leaving radiances in the northwest tropical Atlantic ocean are represented for the 12th of January 2011 and the 15th of July 2011. We can notice that during the high discharge (in July), while the Amazon waters are travelling further and further from the mouth, two different schemes are noticeable in the radiance distributions at 412 and 443 nm especially, whereas only one is highlighted during the low flow.

In figure 2.19 are represented the corresponding daily radiances maps for these two particular days. We can notice that thanks to the 412 and 443 nm water leaving radiance, the Amazon plume could be isolated. Moreover, we could isolate very turbid waters using the 555 and 709 nm radiances. Indeed, the magenta contour next to the coast in figure 2.19, isolates waters with very high 555 and 709 nm radiances (higher than $0.4 \text{ mW/cm}^2/\mu\text{m/sr}$ for the 555 nm radiance and $0.08 \text{ mW/cm}^2/\mu\text{m/sr}$ for the 709 radiance), which correspond to very turbid waters.

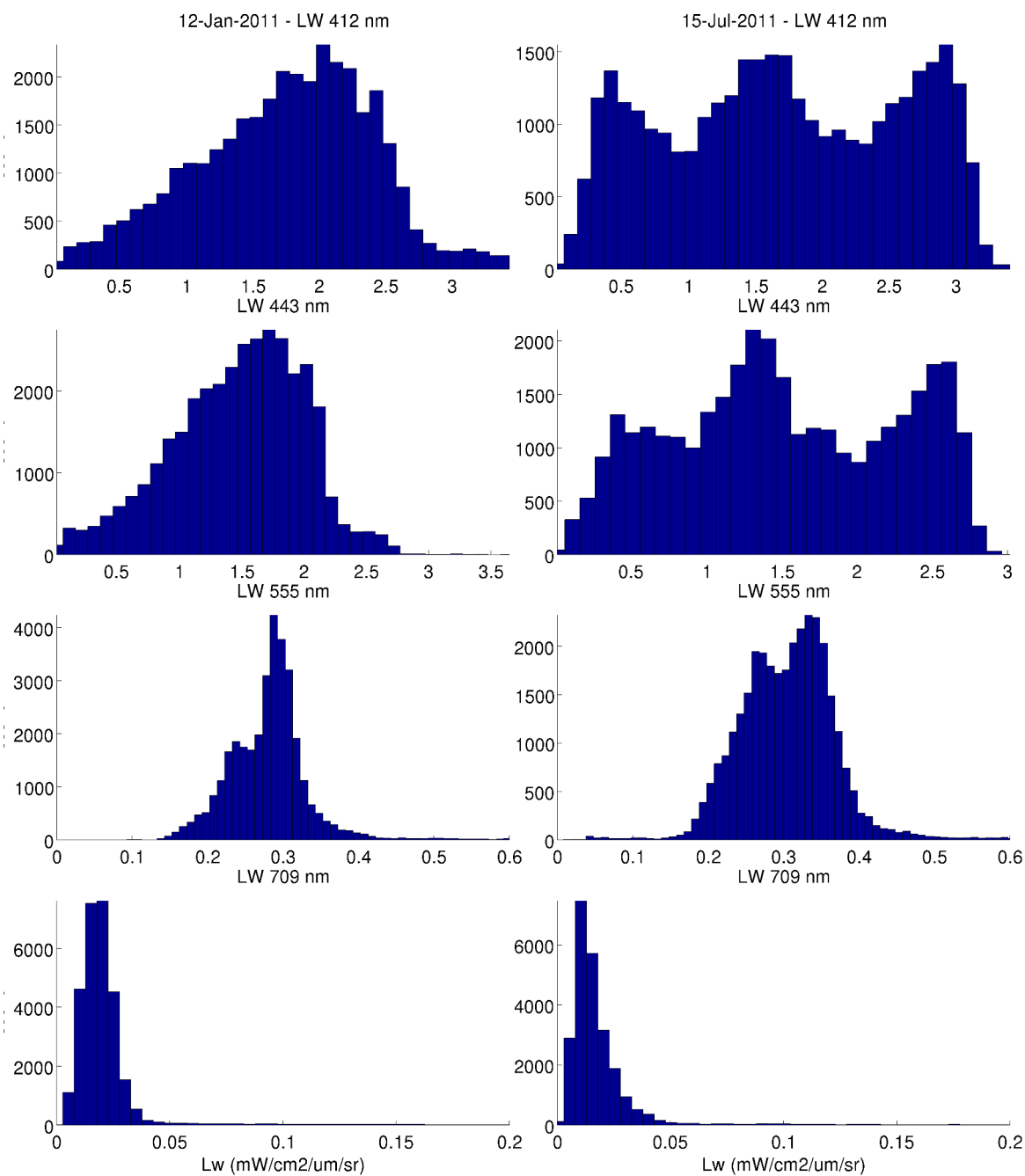


Figure 2.18: Distributions of, from top to bottom, 412, 443, 555 and 709 nm water leaving radiances for the 12th of January 2011 (left) and for the 15th of July 2011 (right).

2.2. Ocean Color Data

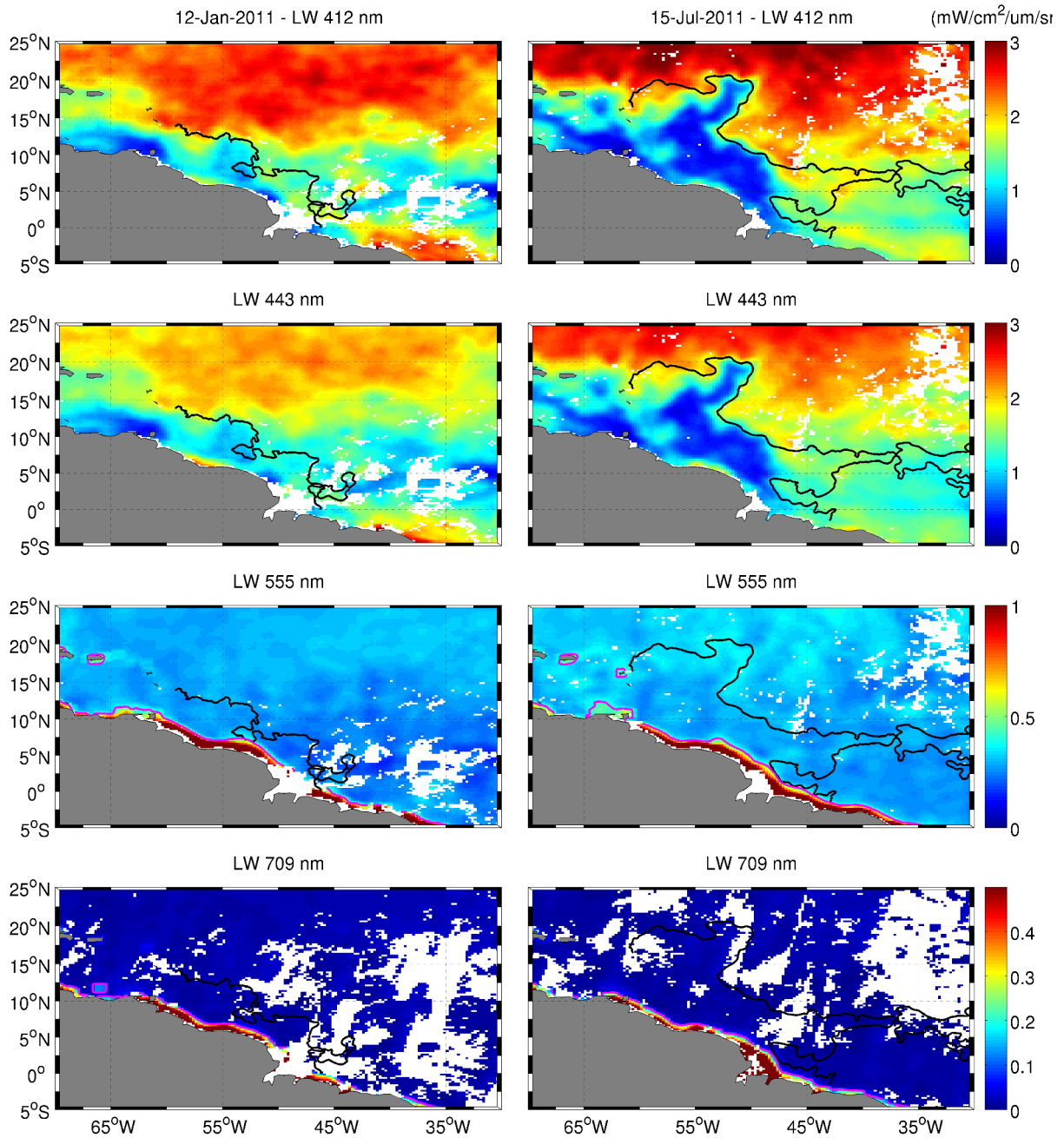


Figure 2.19: Daily maps of, from top to bottom, 412, 443, 555 and 709 nm water leaving radiances for the 12th of January 2011 (left) and for the 15th of July 2011 (right), on top of which is drawn the averaged 35.5 pss January and July plume contour (solid black line). For the 555 nm radiances maps, the 0.4 mW/cm²/μm/sr contour is added on top and for the 709 nm radiances, the 0.08 mW/cm²/μm/sr contour is added (magenta solid line).

2.2.2 Ocean Color semi-analytic algorithms

Information on IOPs can be derived from Ocean Color data using semi-analytic algorithms (Maritorena et al. [2002]). These algorithms relate reflectance (or water-leaving radiance) spectra to inherent optical properties of seawater : the backscattering and the absorption coefficients. The colored detrital matter (cdm) absorption coefficient, but also the phytoplankton absorption (a_{ph}) and the particulate backscatter (b_{bp}), can be estimated by the inversion of these models (Maritorena et al. [2002]). Corrections have to be made for absorption and scattering by the atmosphere (Gordon [1997]). The products used in this study are based on the Garver, Siegel and Maritorena (GSM) model (Garver and Siegel [1997] ; Maritorena et al. [2002]). Particularly, we used the level 3 daily, 4-km resolution estimates of different parameters processed and distributed by ACRI-ST GlobColour service (<http://www.globcolour.info/>), using ESA ENVISAT MERIS data, NASA MODIS and SeaWiFS data. We specifically used the following products, averaged at the SMOS product 0.25 degree resolution, with a 10-day running mean :

- the absorption coefficient of colored detrital matter at 443 nm (a_{cdm}), in m^{-1}
- the diffuse attenuation coefficient at 490 nm (K490), in m^{-1} . It is an indicator of the turbidity of the water column.
- the Total Suspended Matter (TSM) in g/m^3 .
- the particulate backscattering coefficient at 443 nm (b_{bp}), in m^{-1} , from the MODIS, SeaWiFS and MERIS instruments.
- the chlorophyll-a concentration (chla), in mg/m^3 , for case II water, is only available from the MERIS instrument.

In this study, we mainly focus on the cdm absorption coefficient. The cdm absorption coefficient absorbance spectrum is modeled as an exponential toward shorter wavelength increase :

$$a_{cdm}(\lambda) = a_{cdm}(\lambda_0)e^{-S(\lambda-\lambda_0)} \quad (2.4)$$

where $a_{cdm}(\lambda)$ is the absorption coefficient at wavelength λ , $a_{cdm}(\lambda_0)$ is the absorption coefficient at a reference wavelength and S is the spectral slope parameter. Differences in spectral slopes have been proposed as an indicative of cdm origin, with generally lower slopes in freshwater and coastal environments than in marine environments.

In figure 2.20 are represented the daily maps of a_{cdm} , b_{bp} , chla (chlorophyll-a concentration) and npp (net primary productivity) for the 12th of January 2011 and the 15th of July 2011.

2.2. Ocean Color Data

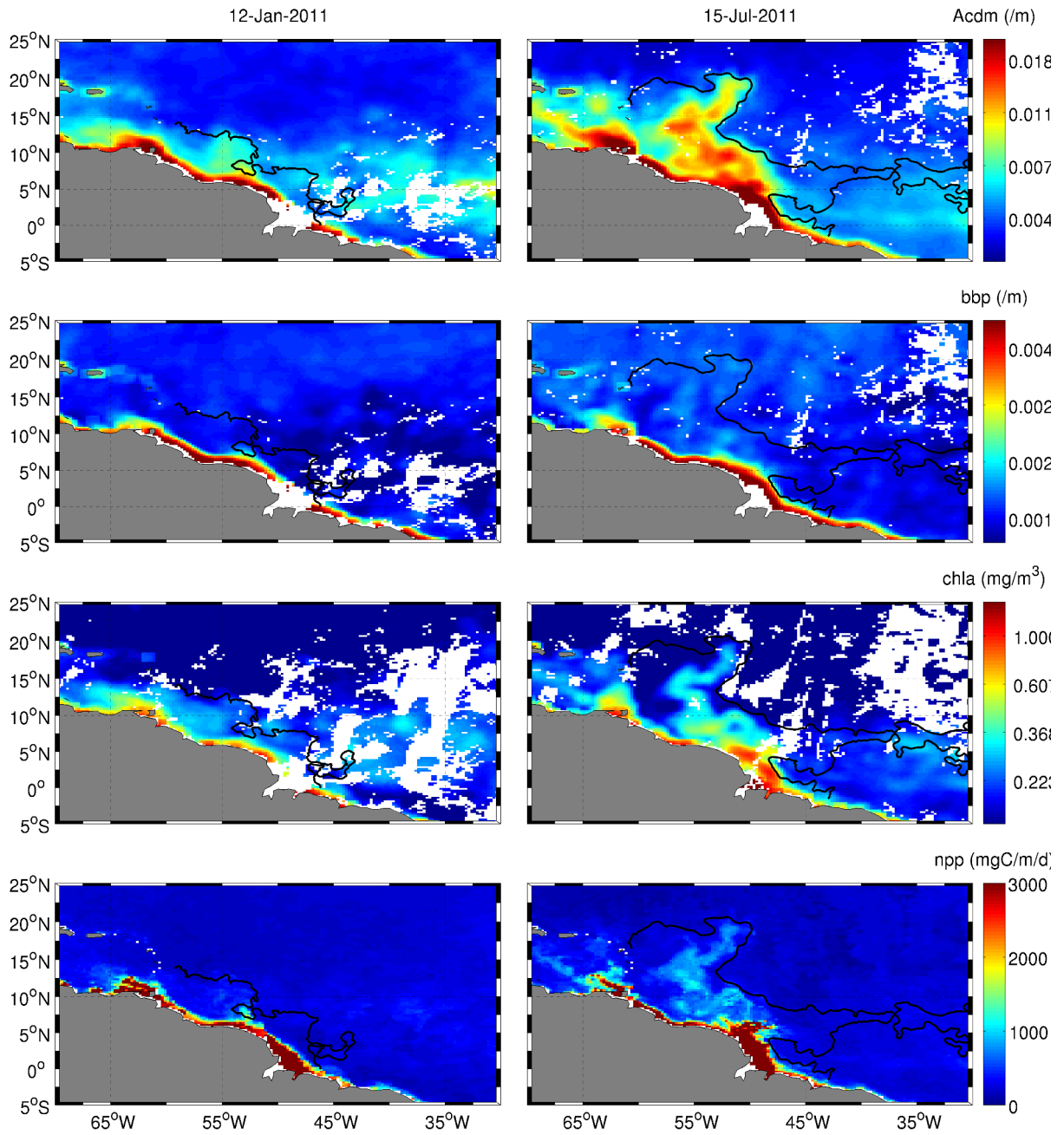


Figure 2.20: Daily maps of, from top to bottom, a_{cdm} , b_{bp} , chl_a and npp for the 12th of January 2011 (left) and for the 15th of July 2011, on top of which is drawn the averaged 35.5 pss January plume contour (solid black line).

2.2.3 On the use of the absorption coefficient of colored detrital matter

2.2.3.1 A river plume water tracer

In this study, we focus on the use of the a_{cdm} absorption coefficient. Indeed, it has been shown that Colored Dissolved Organic Matter (CDOM) and its proxy a_{cdm} represent better tracers for the Amazon waters, our area of study, than the chlorophyll-a concentration (Hu et al. [2004]). In Amazon waters, as highlighted by Hu et al. [2004], CDOM absorption and chl-a concentration are not always correlated (see figure 2.21 which shows the mean anomalies between chl-a and a_{cdm}), it implies the indirect role of chl-a in CDOM production which comes from terrestrial sources. In the Amazon Plume, the light attenuation by suspended materials is the main limitation to phytoplankton growth. Near shore, CDOM absorption dominates, at about 440 nm, which is also a main region of phytoplankton absorption. Thus, it interferes in the retrieval of phytoplankton concentration. Away from this area, absorption attributable to organic substances begins to dominate the attenuation of light in surface waters, as mineral detritus is removed by sinking. Indeed, in figure 2.21, there are strong anomalies between chlorophyll-a absorption and a_{cdm} in the plume (a_{cdm} being higher than chl-a absorption). Away from the plume, chl-a and a_{cdm} covary (i.e. case II like waters). East of the plume, there are strong positive anomalies (chl-a absorption being higher than a_{cdm}).

2.2. Ocean Color Data

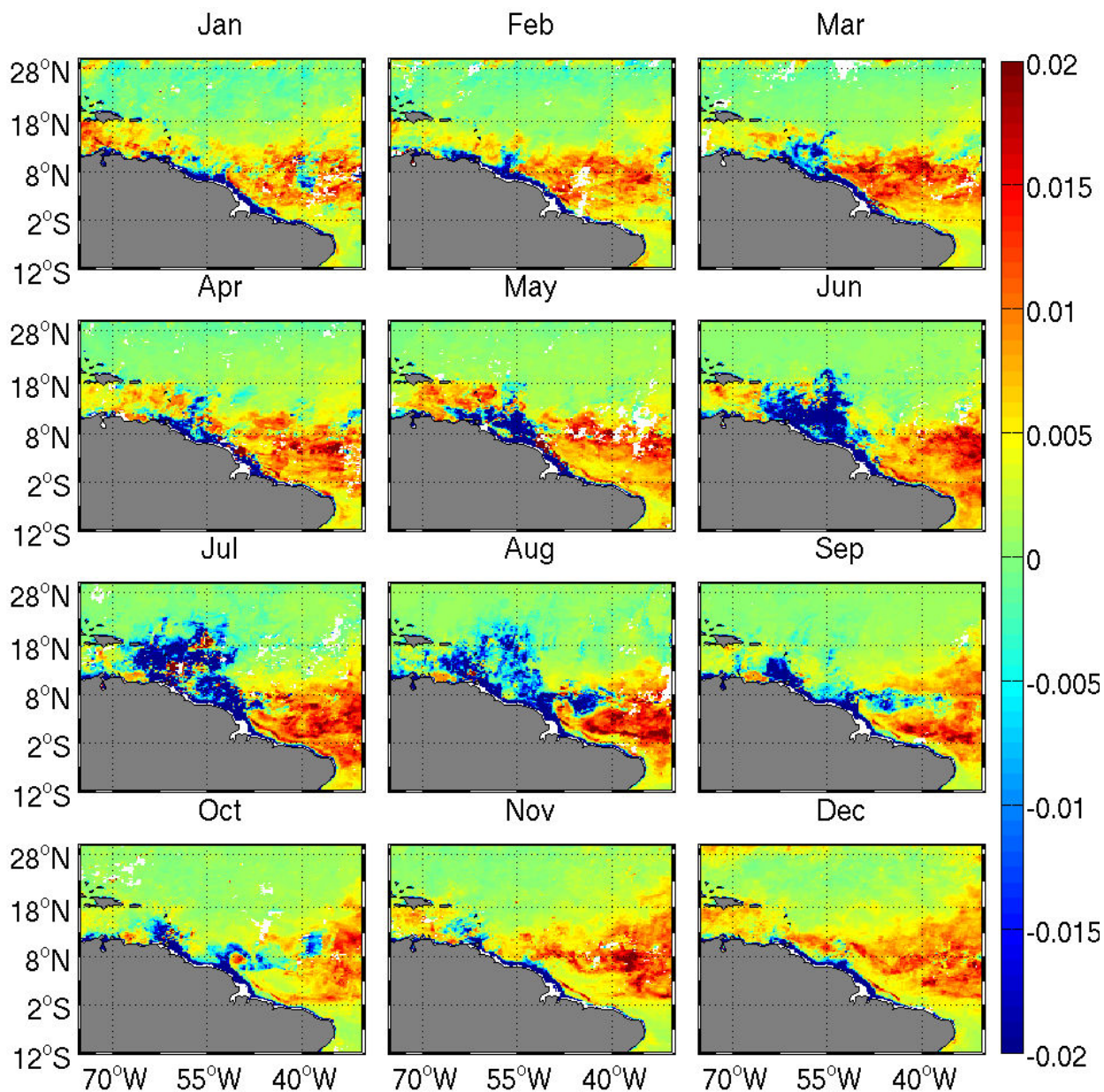


Figure 2.21: 2010 monthly anomaly between chlorophyll-a absorption and a_{cdm} .

2.2.3.2 Justification of the choice to use GlobColour a_{cdm}

Ocean color algorithms begin to break down in very turbid waters especially in the north-western part of the tropical Atlantic ocean, a tricky area regarding ocean color products. Thus, potential errors in the retrieval of Ocean Color products are expected.

However, the choice to use the GlobColour a_{cdm} product is justified for the following reasons : The total absorption represents the sum of the absorption due to phytoplankton and the absorption due to colored detrital matter ; these two components are hard to discriminate especially in river plume areas as the Amazon plume. The total absorption

is the Ocean Color product the most reliable, it has the least error compared to the 2 sub-components and a_{cdm} , in theory, represents most of the total absorption (see figures 2.22 and 2.23).

The a_{cdm} versus total absorption ratio is computed from 4-km 10-day running mean Ocean Color satellite data. As GlobColour doesn't provide the total absorption, this parameter has been computed by the formula 2.5 (see Maritorena et al. [2002]), depending on the wavelength λ :

$$a(\lambda) = a_{cdm}(\lambda) + a_{ph}(\lambda) \quad (2.5)$$

with :

$$a_{ph}(\lambda) = a_{ph} * .chla \quad (2.6)$$

chla being the chlorophyll-a concentration and :

$$a_{ph}^* = \begin{cases} 0.00665, & \text{for } \lambda = 412nm \\ 0.05582, & \text{for } \lambda = 443nm \\ 0.02055, & \text{for } \lambda = 490nm \\ 0.01910, & \text{for } \lambda = 510nm \\ 0.01015, & \text{for } \lambda = 555nm \\ 0.01424, & \text{for } \lambda = 670nm \end{cases} \quad (2.7)$$

This satellite ratio has then been compared to the equivalent ratio using *in situ* a_{cdm} from the SeaBASS *insitu* database and total absorption data (see figure 2.22).

The distribution of these ratios for several months and over the whole months and years considered here have then been computed (see figure 2.23).

Using the SeaBASS *in situ* a_{cdm} and total absorption measurements of January, February, June, July and August 2001 and April, May 2003 in the Amazon plume (381 measurements), it turns out that in average, this ratio is about 0.68 with a standard deviation of about 0.24. Thus, a_{cdm} represents the most of the total absorption, the most reliable Ocean Color product. Moreover, *in situ* and satellite ratios' histograms fall, in general, in the same range (see figure 2.23). So, even though Ocean Color products are not very reliable and error free, especially in the Amazon plume area, the use of a_{cdm} satellite product is justified, satellite a_{cdm} distributions match *in situ* distributions.

2.2. Ocean Color Data

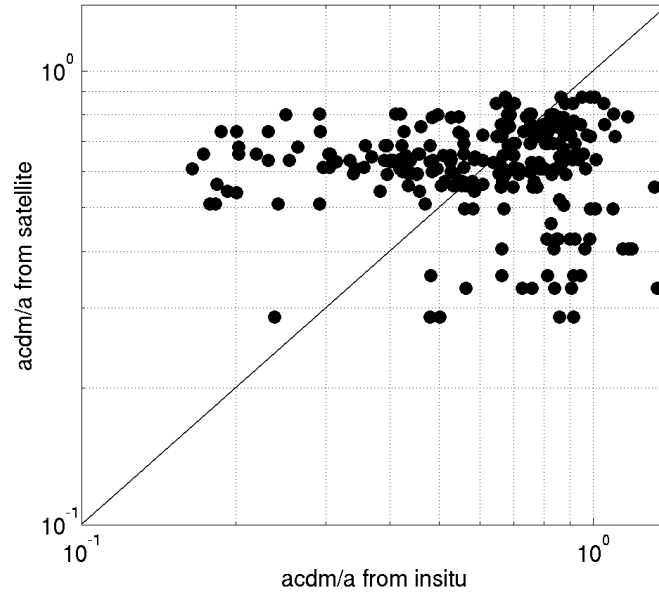


Figure 2.22: SeaBASS *in situ* a_{cdm} versus total absorption as a function of satellite a_{cdm} versus total absorption.

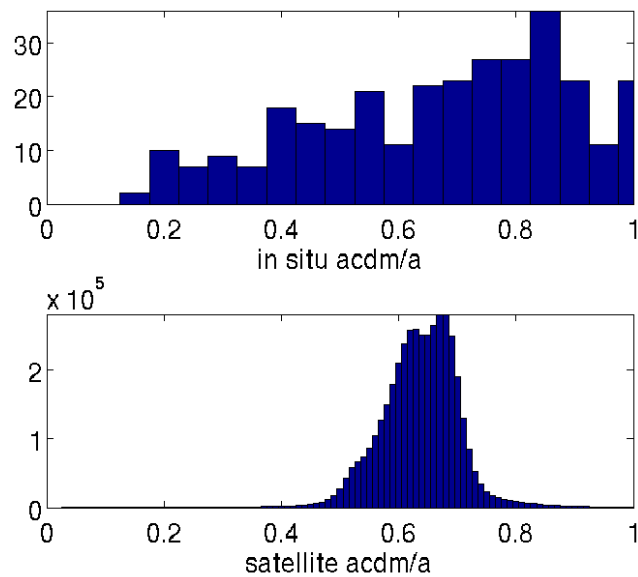


Figure 2.23: Distributions of the SeaBASS *in situ* ratio a_{cdm} versus total absorption (top panel) and the satellite ratio a_{cdm} versus total absorption (bottom panel) for January, February, June, July and August 2001 and April and May 2003.

2.2.4 Net Primary Production data

16-km 8-day Carbon based Production Model (CbPM) Net Primary Productivity (NPP) products from Ocean Productivity were used. Such data is available on their website (<http://www.science.oregonstate.edu/ocean.productivity/>). These products have been averaged at the SMOS product 0.25 degree resolution. CbPM data used here are based on the updated model by [Westberry et al. \[2008\]](#).

The traditional Net Primary Productivity models are "chlorophyll-a based" algorithms, NPP is commonly modeled as a function of chlorophyll-a concentration (chl_a). The problem is that the phytoplankton cellular chlorophyll-a concentrations (chl_a) are extremely plastic, responding to changes in growth irradiance (photoacclimation), nutrient status and other environmental stressors. The chlorophyll-a concentration we see from space is not simply a reflection of how many phytoplankton are present in a given location, but also of the effect of light and nutrient conditions on the chlorophyll-a concentration in each phytoplankton individual. Because of this, chl_a is often a poor proxy for phytoplankton biomass whereas the phytoplankton carbon biomass (C) represents a better proxy ([Westberry et al. \[2008\]](#)).

The Carbon based Production Model relates the Net Primary Productivity to phytoplankton carbon biomass and growth rate (see the water column integrated NPP expression in the equation 2.8) :

$$NPP = carbon * growth\ rate * volume\ function \quad (2.8)$$

The phytoplankton carbon biomass can be estimated from satellite estimates of particulate backscattering coefficients and phytoplankton growth rates can be estimated from chlorophyll-a-to-carbon ratios.

However, getting growth rates from satellite chlorophyll-a-to-carbon ratios does require an understanding of how light and nutrient effects influence phytoplankton pigmentation levels which in turn requires an estimate of the light level to which surface mixed layer phytoplankton are acclimated. CbPM thus includes information on the subsurface light field and nitracline depths to parametrize photoacclimation and nutrient stress throughout the water column. Three inputs are required to calculate mixed layer light conditions : surface Photosynthetically Available Radiation (PAR), attenuation coefficients for PAR (KPAR) and mixed layer depth (MLD). [Westberry et al. \[2008\]](#)

2.3. Other Geophysical Data

2.3 Other Geophysical Data

2.3.1 Discharge levels

Daily and monthly discharge data of the Amazon and Orinoco rivers were obtained from the Environmental Research Observatory Geodynamical, hydrological and biogeochemical control of erosion/alteration and material transport in the Amazon basin (ORE-HYBAM) available at <http://www.ore-hybam.org/>.

Monthly Amazon tributaries discharge estimates were derived from the University of New Hampshire (UNH) Water Balance Model (PDL-WBM), driven by climate fields from the Modern Era Retrospective-Analysis For Research And Applications (MERRA) (<http://gmao.gsfc.nasa.gov/merra>).

2.3.2 Sea Surface Temperature estimates

Two similar sea surface temperature products are used here. First, the High Resolution Sea Surface Temperature (GHRSST) Level 4 sea surface temperature analysis is produced daily on an operational basis at the UK Met Office using optimal interpolation (OI) on a global 0.054 degree grid (Donlon et al. [2012]). The Operational Sea Surface Temperature and Sea Ice Analysis (OSTIA) analysis uses satellite data from sensors that include the Advanced Very High Resolution Radiometer (AVHRR), the Advanced Along Track Scanning Radiometer (AATSR), the Spinning Enhanced Visible and Infrared Imager (SEVIRI), the Advanced Microwave Scanning Radiometer-EOS (AMSRE), the Tropical Rainfall Measuring Mission Microwave Imager (TMI), and *in situ* data from drifting and moored buoys. This analysis has a highly smoothed SST field and was specifically produced to support SST data assimilation into Numerical Weather Prediction (NWP) models.

The other SST product used is the high resolution sea surface temperature (SST) analysis product which has been developed using optimum interpolation (OI) (Reynolds et al. [2002]). The analyses have a spatial grid resolution of 0.25° and temporal resolution of 1 day. The product uses Advanced Very High Resolution Radiometer (AVHRR) infrared satellite SST data and Advanced Microwave Scanning Radiometer (AMSR) on the NASA Earth Observing System satellite SST data. It also uses *in situ* data from ships and buoys and include a large-scale adjustment of satellite biases with respect to the *in situ* data.

2.3.3 Altimetric data

In the present study, we used the 1/3 degree resolution global surface current products from Ocean Surface Current Analyses Real time (OSCAR) (<http://www.oscar.noaa.gov> ; Bonjean and Lagerloef [2002]). The OSCAR products are calculated from sea surface velocities from satellite altimetry (AVISO), vector wind fields (QuikSCAT) and from sea surface temperature (Reynolds-Smith) using quasi-steady geostrophic, local wind-driven, and thermal wind dynamics. Near real-time velocities are calculated on a 1/3x1/3 degree grid and on a 5-day time base over the global ocean.

2.3.4 Wind estimates

Daily 0.25° wind products from the Advanced SCATerometer (ASCAT) instrument are used in this work. These products, obtained from the Centre de Recherche et d'Exploitation Satellitaire (CERSAT), at IFREMER, Plouzané (France), have been averaged at 0.25 degree resolution with a 10-day running mean.

2.3.5 Rain rate estimates

Rain rate estimates used here are the Tropical Rainfall Measurement Mission Project (TRMM) and Other Satellites Precipitation Product (3B42). The 3B42 estimates are 3hourly at 0.25° resolution. The major inputs into the 3B42 algorithm are Infra Red (IR) data from geostationary satellites and Passive Microwave data from the TRMM microwave imager (TMI), special sensor microwave imager (SSM/I), Advanced Microwave Sounding Unit (AMSU), and Advanced Microwave Sounding Radiometer-Earth Observing System (AMSR-E). These estimates are obtained through the NASA/Giovanni server (<http://reason.gsfc.nasa.gov/OPS/Giovanni>).

2.3.6 AMSR-E Brightness Temperatures estimates

We used the data from the 6.9 and 10.7 GHz frequency bands of the Advanced Microwave Scanning Radiometer-EOS (AMSR-E) onboard NASA EOS Aqua satellite. We specifically used the L2A and L2B brightness temperature products resampled at 56 km spatial resolution from the National Snow and Ice Data Center (NSIDC) available on NSIDC website (<http://nsidc.org/data/>).

Chapter 3

The Northwestern Tropical Atlantic Ocean

3.1 Physical Oceanography of the Northwestern Tropical Atlantic Ocean

The Amazon shelf and more generally, the northwestern tropical Atlantic ocean, is subject to forcings from various sources, including large buoyancy flux from the Amazon river discharge, local currents, tidal currents, trade winds and precipitation.

3.1.1 The Amazon-Orinoco discharge

The Amazon river watershed, extending across the Amazon rain forest to the crest of the Andes with an area of about 7.10^6 km², is the largest drainage basin in the world (Geyer et al. [1996]). Moreover, it is the largest river on the planet in terms of runoff, as it discharges about 15% of the global freshwater run-off (Baumgartner and Reichel [1975]). The Amazon river enters into the Atlantic ocean at the equator through two channels, the north one and the south one. These channels debouch on a broad, shallow inner shelf with a water depth of about 15 m extending 100-200 km off the coast (Geyer et al. [1996]).

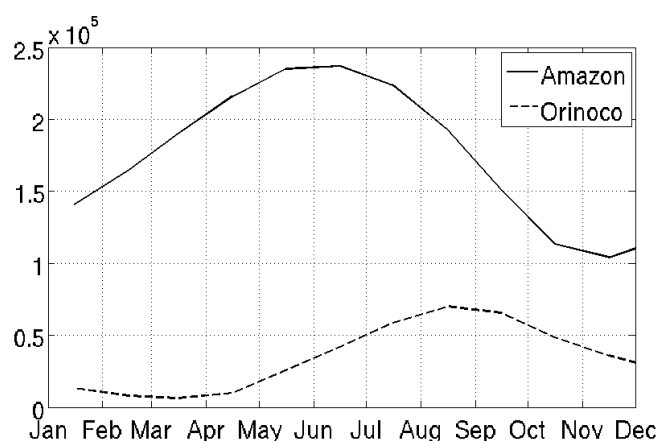


Figure 3.1: Average Amazon river cycle (m³/s) computed from 1968 to 2013 (solid black line) and Orinoco average discharge computed from 2003 to 2013 (dashed black line).

The Amazon discharge has a strong seasonal variation reaching a maximum of about

$2.4 \cdot 10^5 \text{ m}^3/\text{s}$ in mid-May and a minimum of $0.8 \cdot 10^5 \text{ m}^3/\text{s}$ in mid-November (Lentz [1995]) (see figure 3.1). It also supplies the largest riverine flux of suspended (1200 Mt.y^{-1}) and dissolved matter (287 Mt.y^{-1}) to the global ocean, which includes Colored Dissolved Organic Matter (CDOM) (Meybeck and Ragu [1997]), also known as gelbstoff or yellow substances (see figure 1.1).

The Orinoco river exhibits the fourth highest river discharge of the planet (Hu et al. [2004]). Its discharge peak occurs in August (see figure 3.1). Combined with the Amazon, these rivers discharge 20% of the global freshwater run-off into the northwestern tropical Atlantic (NWTA).

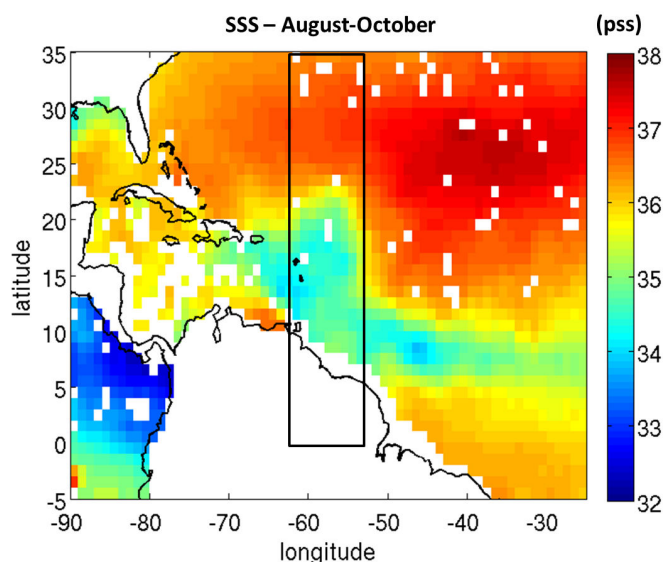


Figure 3.2: Average salinity from NODC profiles in the first 5 m depth in each $1 \times 1^\circ$ pixel over the August-October period. As a solid black line is represented the box in which the hovmueller plot in figure 3.3 is computed.

The Amazon and Orinoco rivers, discharging such an amount of fresh water, are responsible for a large part of the low sea surface salinity in this area (Masson and Delecluse [2001]). These fresh waters play an important role in the formation of barrier layers, inducing a strong halocline in the 3-30 m depth range and accordingly, a pycnocline that acts as a barrier for mixing between the surface and the subsurface waters (Pailler et al. [1999]). A thick barrier layer (more than 40 m) is present every summer from July to September north of the Amazon mouth (Masson and Delecluse [2001]). Using the NODC database, an average salinity profile north of the Amazon plume has been computed (see figures 3.2 and 3.3) showing the presence of the barrier layer of about 40 m depth up to 20°N .

3.1. Physical Oceanography of the Northwestern Tropical Atlantic Ocean

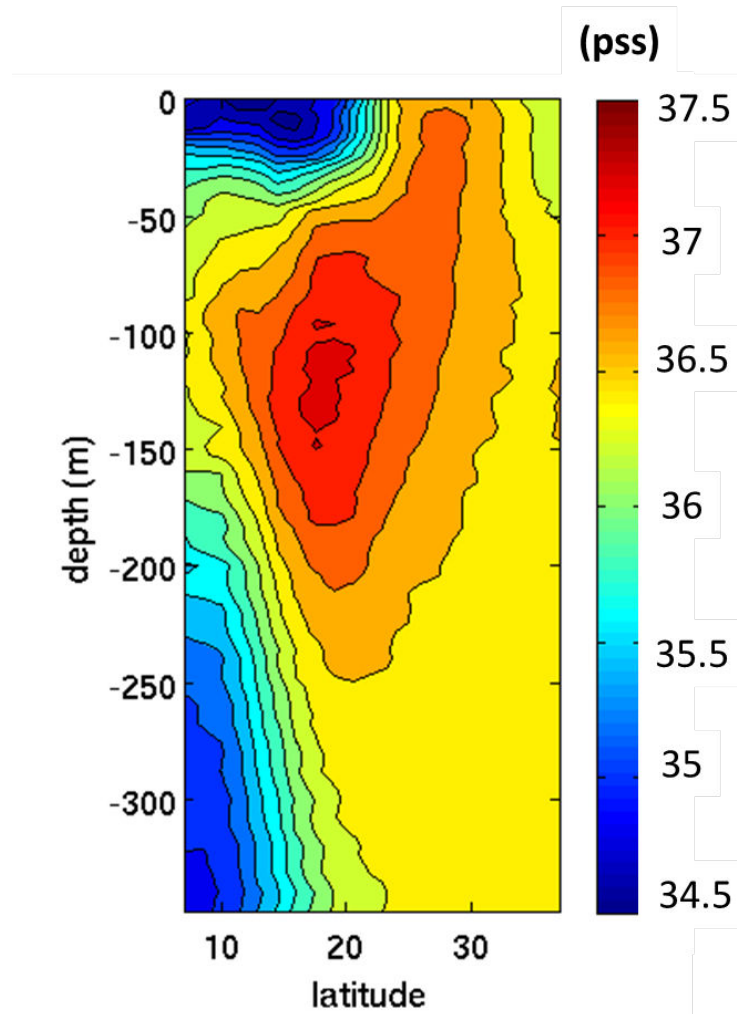


Figure 3.3: Mean salinity profile for longitude from 61°W to 53.5°W as a function of latitude, based on NODC profiles over the period August-October.

3.1.2 Tidal and local currents

The north and south hemispheres subtropical gyres are the boundaries of the tropical Atlantic surface circulation. This Atlantic equatorial gyre (see figure 3.4) is composed of the North Brazilian Current (NBC), its retroflexion, the North Equatorial Counter Current (NECC), the Guinea Current and the several branches of the South Equatorial Current (SEC) (Lumpkin and Garzoli [2005]).

The South Equatorial Current (SEC) flows westward to the Brazilian coast and feed the North Brazilian Current (NBC) northwestward, and the Brazilian Current (BC) southward. The NBC is the western boundary of the tropical Atlantic gyre. It carries waters northwestward across the Equator along the Brazilian shelf. Important seasonal varia-

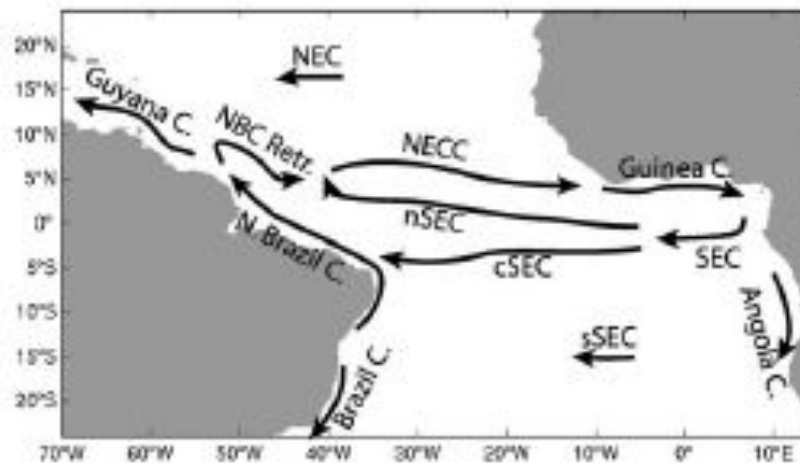


Figure 3.4: Scheme of sea surface currents calculated from drifter observations by Lumpkin and Garzoli [2005].

tions affect the North Equatorial Counter Current (NECC) which carries waters eastward to the African coasts (Garzoli and Katz [1983] ; Richardson and Walsh [1986]). The NECC strengthens during boreal fall, a retroflection appears in the NBC around 5-10°N carrying waters mainly eastward instead of northwestward (Richardson and Walsh [1986] ; Richardson and Reverdin [1987]). The NECC weakens or even reverses in early spring, waters are then carried northwestward by the NBC. These seasonal variations are clearly visible in figure 3.5 which represents the 2010 monthly maps of current speed and direction.

Occasionally, rings, of about 200 to 300 kms of diameter, shed off the NBC retroflection and propagate along the shelf towards the Caribbean sea (Fratantoni and Glickson [2002] ; Goni and Johns [2003] ; Johns et al. [2003]). Approximately 8-9 eddies are formed each year (Johns et al. [2003]). These rings play an important role as they carry waters influenced by the Amazon plume from the south Atlantic ocean toward the north, with relatively warm (cold) sea surface temperature anomalies of up to 1°C in the first (second) part of the year (Ffield [2005]).

The strongest currents over the shelf are due to semi-diurnal tides which range up to 6 m in some areas, with current speeds reaching 200 cm.s⁻¹ (Gibbs [1982]). Tidal currents are generally oriented cross-shelf.

3.1. Physical Oceanography of the Northwestern Tropical Atlantic Ocean

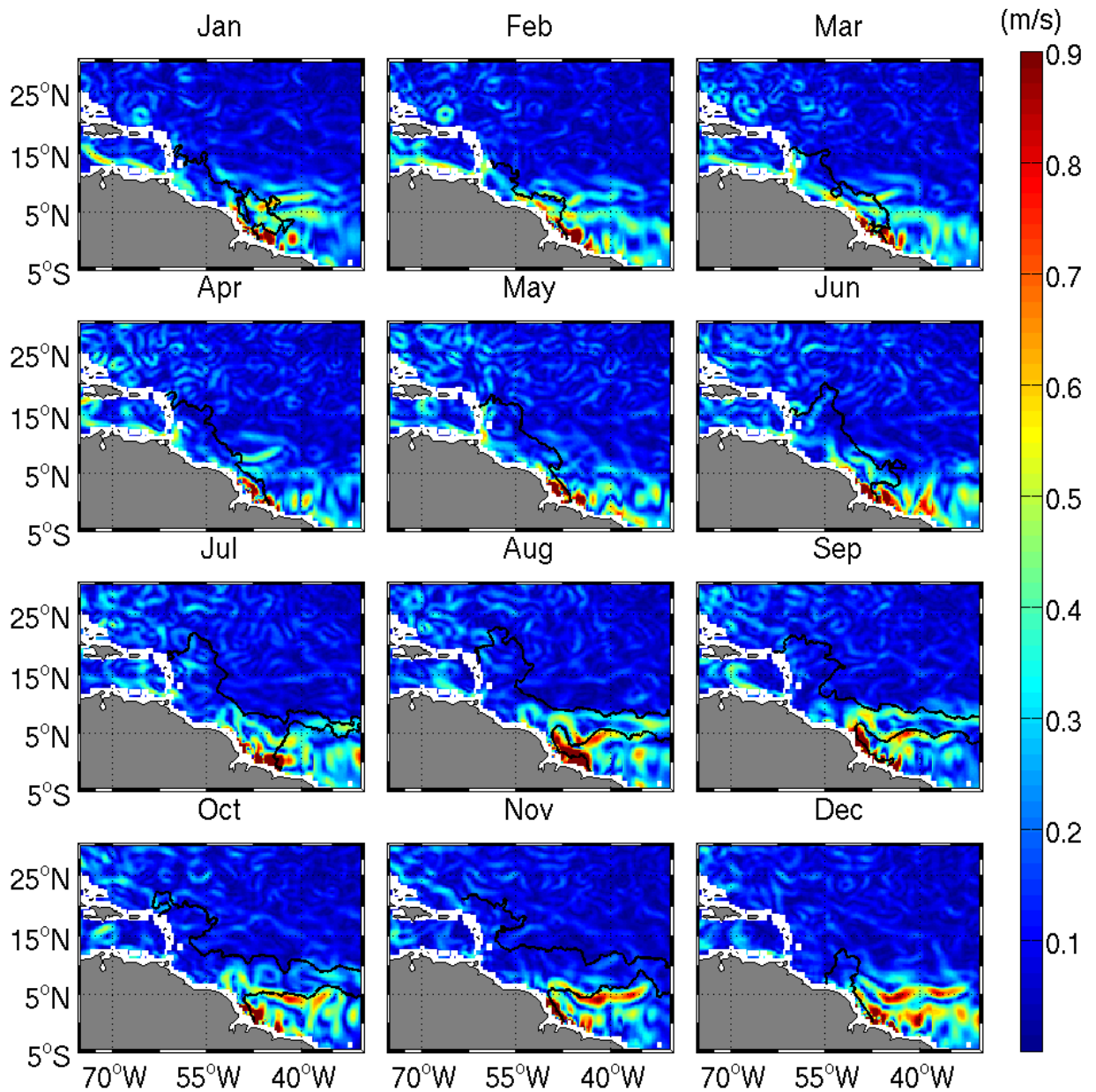


Figure 3.5: Monthly OSCAR currents from January to December 2010, on top of which is represented the 2010 monthly 35.5 pss contour.

3.1.3 Trade winds & Inter Tropical Convergence Zone

The climate variability of the tropical Atlantic ocean is strongly dependent on the location of the Inter Tropical Convergence Zone (ITCZ) which oscillates through the year (see figure 3.6). From boreal winter to boreal summer, the ITCZ goes from south to north as do the high SST patterns which follow the ITCZ.

The atmospheric forcing over the Amazon shelf region is dominated by the trade winds.

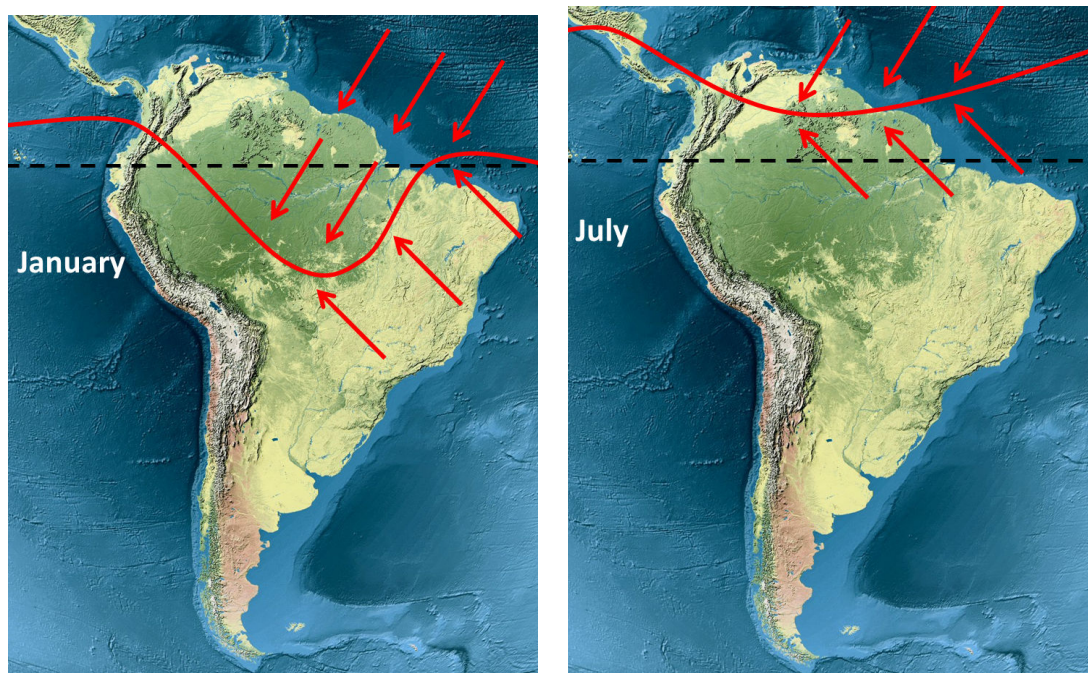


Figure 3.6: Scheme representing, as a solid red line, the position of the Inter Tropical Convergence Zone (ITCZ) in January (left) and in July (right). The location and direction of trade winds for each month are represented as solid red arrows.

The Inter Tropical Convergence Zone (ITCZ) is a wind field convergence zone in the tropics (see figure 3.6). In boreal winter over December-April, the ITCZ being low, the area undergoes a maximum wind stress corresponding to the northeast trade winds (see figures 3.6 and 3.7). During this period, trade winds are oriented roughly perpendicular to the coast (Geyer et al. [1996]). The rest of the year, wind stress over this area relaxes. In boreal summer, wind stress intensifies south of the Amazon mouth, due to southeast trade winds (see figures 3.6 and 3.7).

Besides trade winds, the ITCZ is also associated with a band of clouds and rain. Precipitation and evaporation represent other freshwater sources and sinks in the northwestern tropical Atlantic ocean. During the boreal summer, it mainly influences the west tropical Atlantic ocean area and during boreal winter, it influences the east tropical Atlantic ocean area (see figure 3.8).

The ITCZ is related to the sea surface temperature (SST) patterns (see figures 3.6 and 3.9). The local sea surface temperature is also influenced, to a lesser extent, by the presence of the Amazon plume. The Amazon plume form a near-surface barrier layer that reduces exchange with the cooler and saltier water below and thus keeps the SST high.

3.1. Physical Oceanography of the Northwestern Tropical Atlantic Ocean

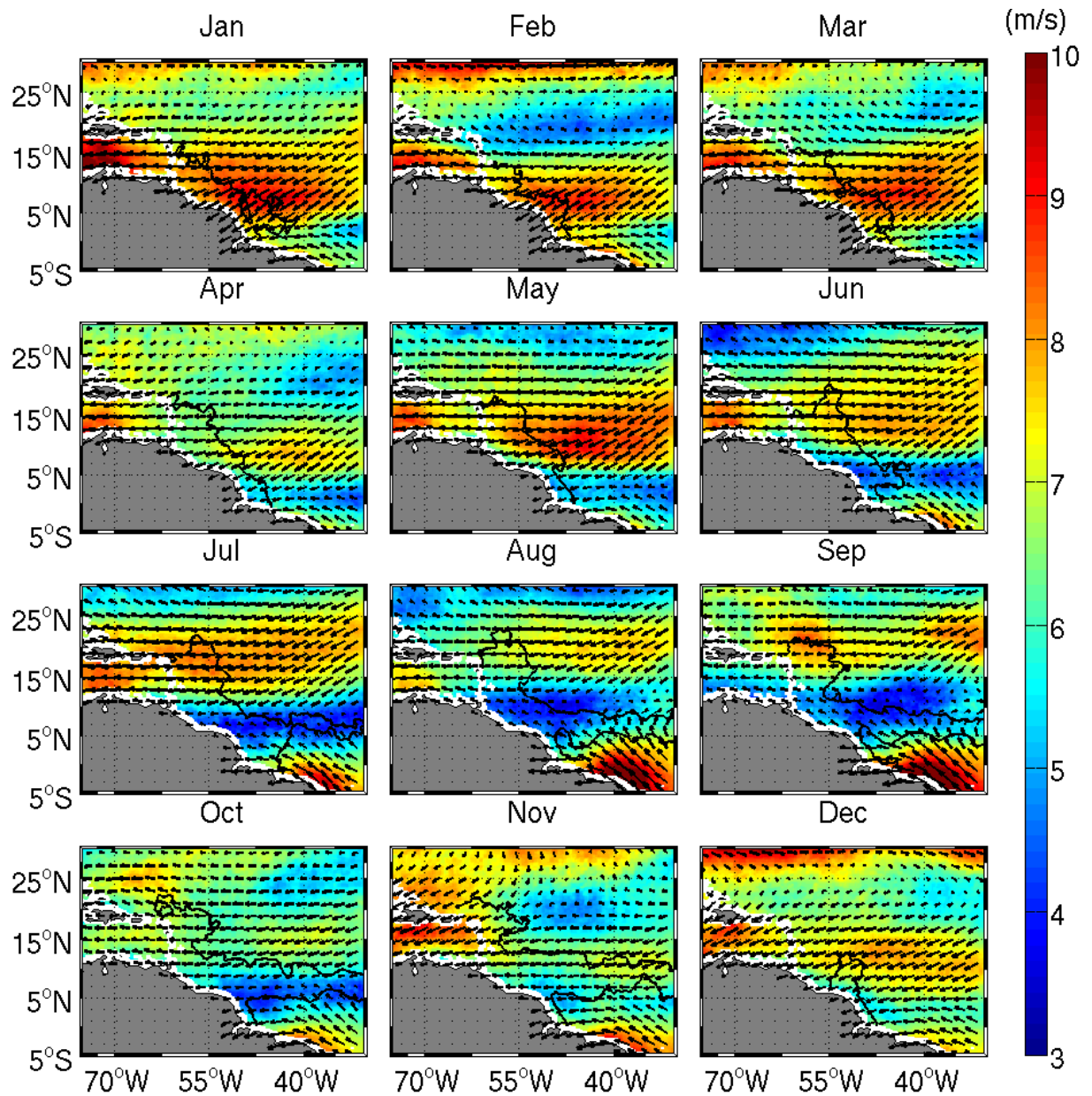


Figure 3.7: Monthly ASCAT wind speed from January to December 2010, on top of which is represented the 2010 monthly 35.5 pss contour.

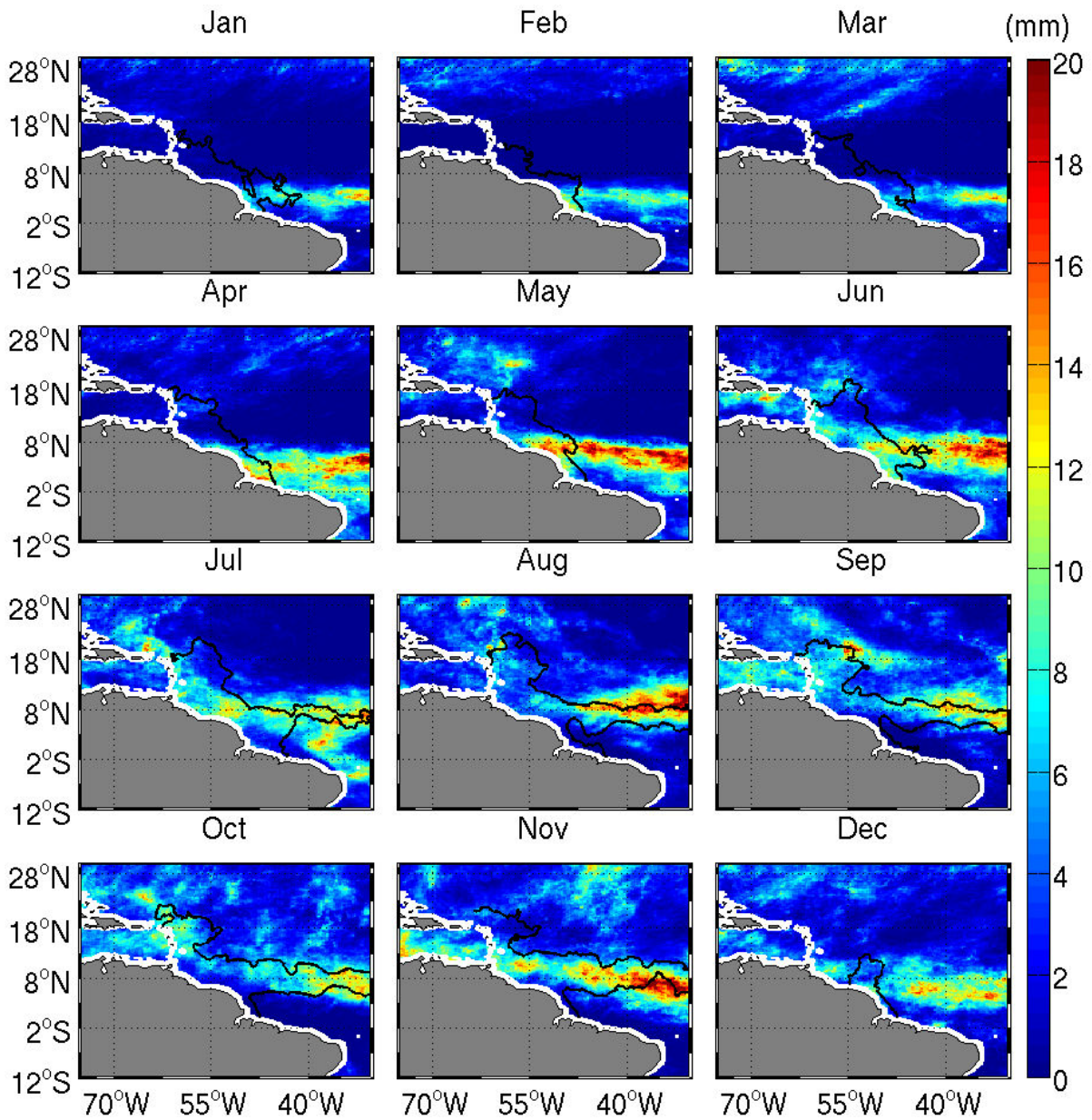


Figure 3.8: Monthly precipitations from January to December 2010, on top of which is represented the 2010 monthly 35.5 pss contour.

3.1. Physical Oceanography of the Northwestern Tropical Atlantic Ocean

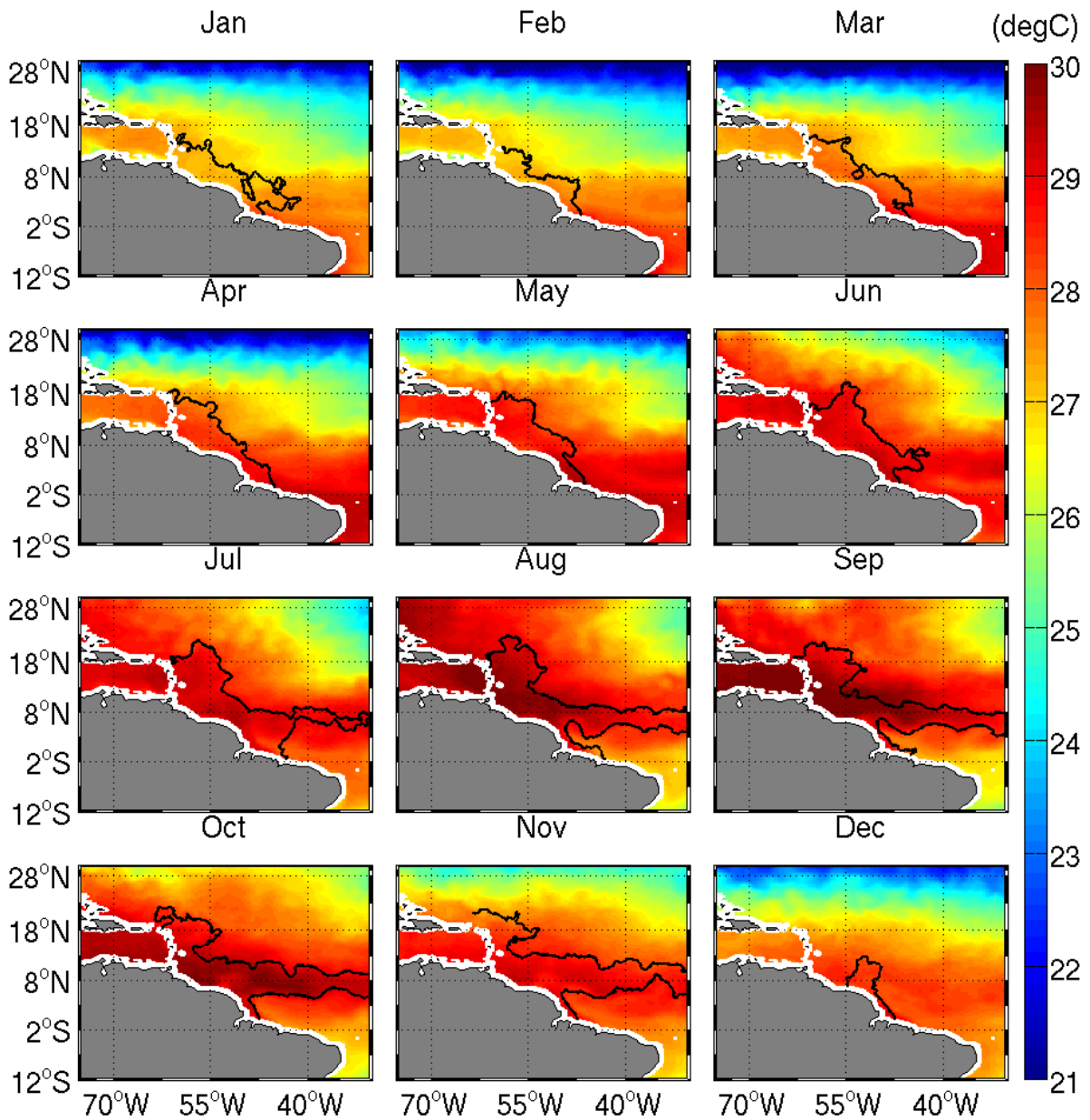


Figure 3.9: Monthly OSTIA sea surface temperature from January to December 2010, on top of which is represented the 2010 monthly 35.5 pss contour.

3.2 The Dispersal of the Amazon Plume

3.2.1 Annual Amazon waters dispersal

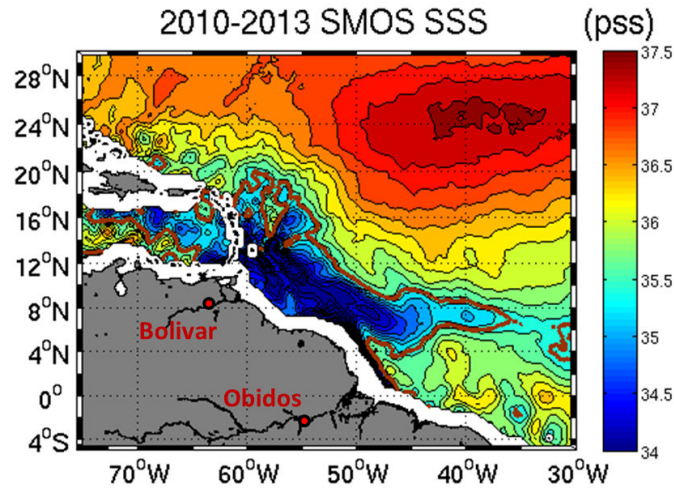


Figure 3.10: 2010-2013 SMOS SSS average. Contours from 32 to 38 pss are represented, every 0.2 pss. The brown thick line represents the 35.5 pss contour. The Amazon and Orinoco gauges at Obidos and Bolivar, respectively, are pointed out by red dots.

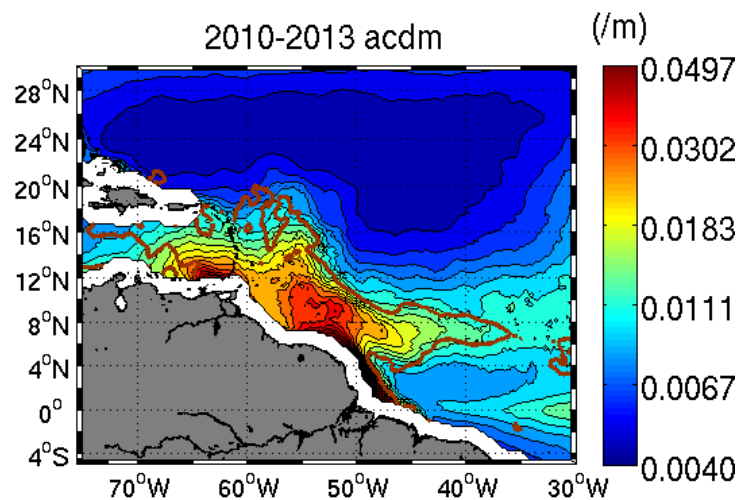


Figure 3.11: 2010-2013 GlobColour a_{cdm} mean. Contours from 0 to 1 /m are represented, every 0.005 /m. The brown thick line represents the 35.5 pss contour.

The riverine fresh waters discharged by the Amazon and Orinoco rivers have a large influence on the northwestern tropical Atlantic ocean discharging an important amount of

3.2. The Dispersal of the Amazon Plume

fresh waters highly concentrated in organic matter. These water masses thus affect the local sea surface salinity and optical properties such as the light absorption. On figures 3.10 and 3.11, the 2010-2013 mean SSS and light absorption at 443 nm are represented. It shows a large area of the northwestern tropical Atlantic ocean, over which light absorption and salinity properties are influenced by the Amazon waters. Waters can be fresher than 20 pss close to the mouth and become gradually saltier northwestward and eastward to reach 36 pss and above, the mean common open ocean value. The average pattern of a_{cdm} over 2010-2013 is close to the SSS map. A_{cdm} water values close to the mouth are above 0.05 /m, gradually decreasing to reach a value close to zero in the open ocean. The precipitation rate represents less than 10% of the fresh waters supplied by the Amazon river during this period. Thus, it is not a dominant factor in the observed plume salinity variability (Lentz and Limeburner [1995]).

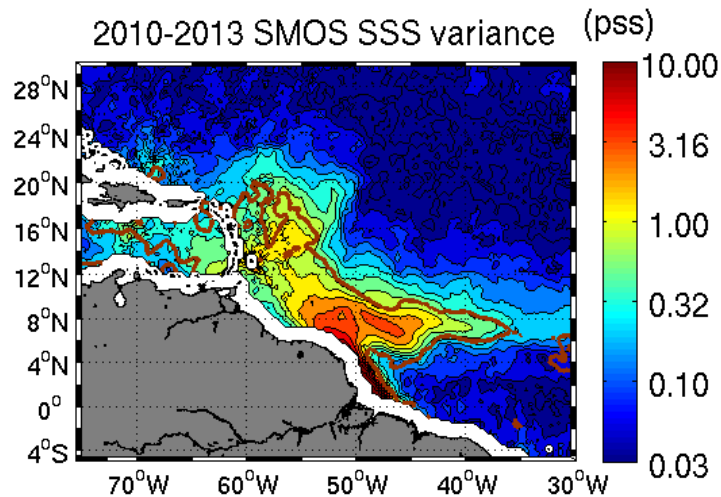


Figure 3.12: 2010-2013 SMOS SSS variance. Contours from 0 to 10 pss are represented every 1.5 pss. The brown thick line represents the 35.5 pss contour.

On figures 3.12 and 3.13, the 2010-2013 SSS and light absorption at 443 nm variances are represented showing the seasonal and interannual variabilities of the influence of Amazon waters on the northwestern tropical Atlantic ocean. We can notice that the SSS is more variable than a_{cdm} in the eastern part of the plume (eastern than 48°W).

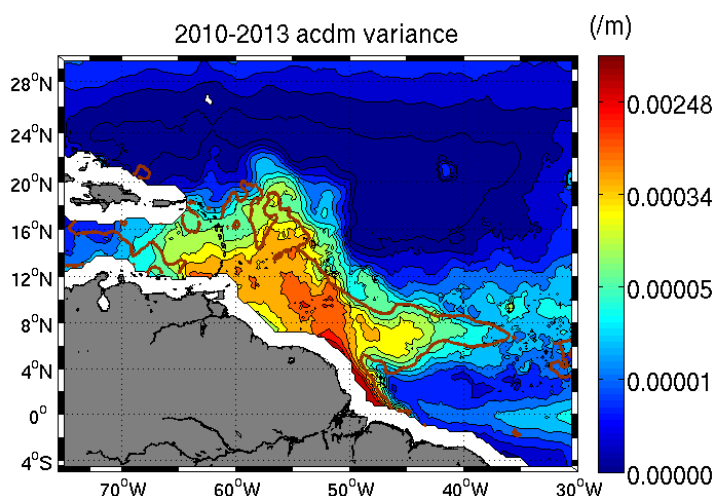


Figure 3.13: 2010-2013 GlobColour a_{cdm} variance. Contours from 0 to 0.01 /m are represented every 0.005 /m. The brown thick line represents the 35.5 pss contour.

3.2.2 Seasonal Amazon plume dispersal

On figures 3.14 and 3.15, representing the average 2010-2013 monthly maps of sea surface salinity from SMOS and the monthly Reverdin et al. [2007] climatologic SSS, respectively, the Amazon plume waters can be identified as the freshwater mass spreading from the mouth to the open ocean. The Amazon plume waters can then be tracked from the mouth to the open ocean using sea surface salinity observations. The seasonal variability of the Amazon plume waters dispersal is clearly visible on these SSS monthly maps.

During the boreal winter and spring seasons, as the discharge level is low, the Amazon plume waters accumulate in the vicinity of the mouth due to northeastern trade wind events (see figure 3.7). These winds consequently block the normally northwestward flow along the NBC current (see figure 3.5) (Muller-Karger et al. [1988] ; Muller-Karger et al. [1995] ; Paluszkiwicz et al. [1995] ; Da Silva [2007]).

In late spring, as the discharge level gets high, Amazon waters flow northwestward along the Brazilian shelf up to the Caribbean sea (see figure 3.5) when the wind relaxes and then reverses (see figure 3.7).

In summer/early fall, when the North Equatorial Counter Current develops, the river plume is carried eastward through the North Brazilian Current retroflexion (Muller-Karger et al. [1988] ; Muller-Karger et al. [1995]).

In general, according to figures 3.14 and 3.15, SMOS permits to improve the spatial res-

3.2. The Dispersal of the Amazon Plume

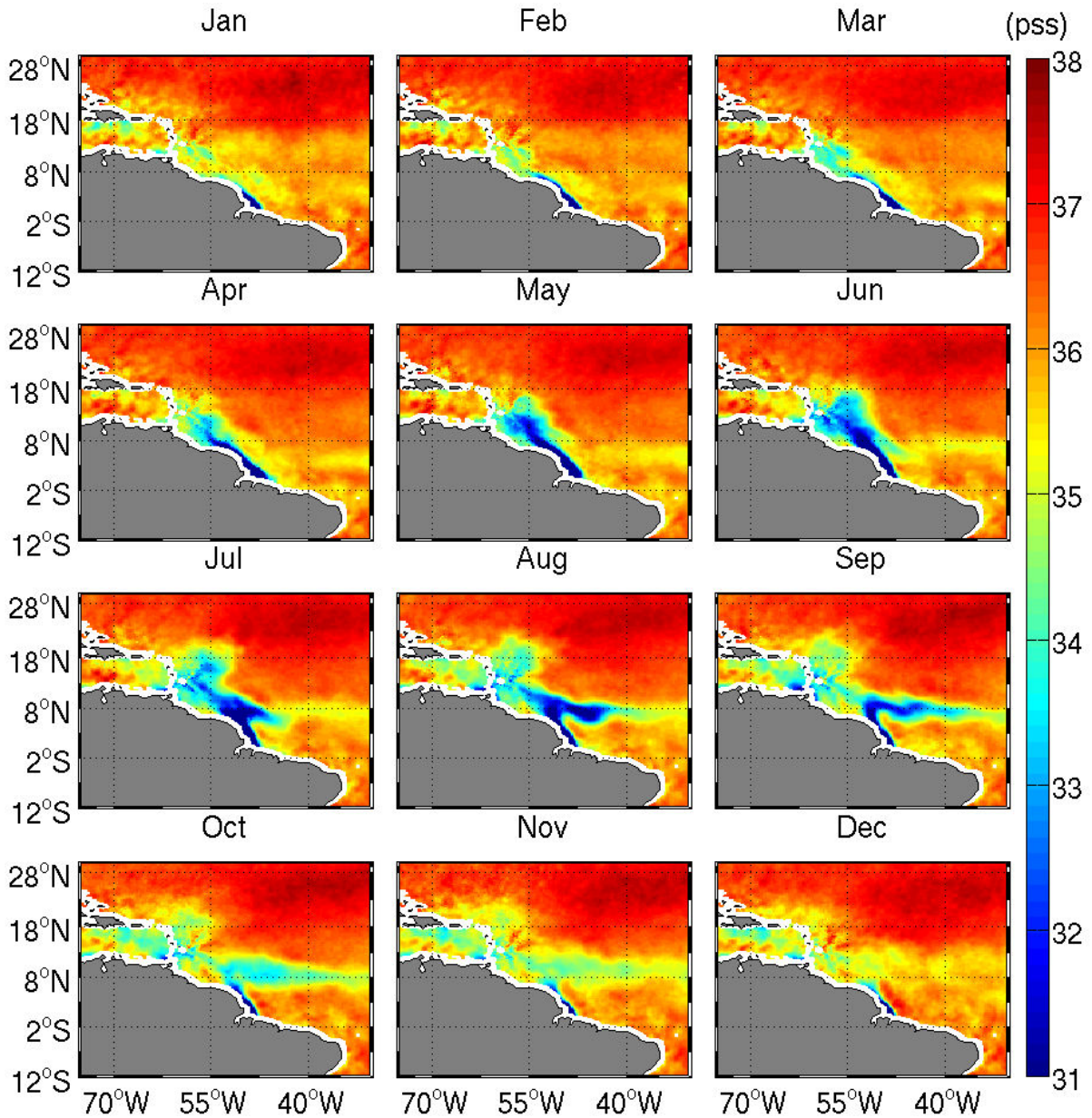


Figure 3.14: Monthly 2010-2013 SMOS sea surface salinity from January to December.

olution in SSS fields, in comparison with the climatology. Climatologic SSS is smoother and thus, SSS fronts are badly positioned. Indeed, in February, the plume waters only correspond to a limited pool at the mouth of the river. SMOS traces these waters more precisely at the mouth and northwestward along the coast. On figure 3.16, are represented the monthly anomalies between 2010-2013 SMOS and [Reverdin et al. \[2007\]](#) climatologic SSS. Important differences are noticeable in the Amazon plume region. At the mouth, there are positive SSS anomalies due to the SSS fronts misplacement of the climatology. When the plume extension is large, from May to September, SMOS tends to underesti-

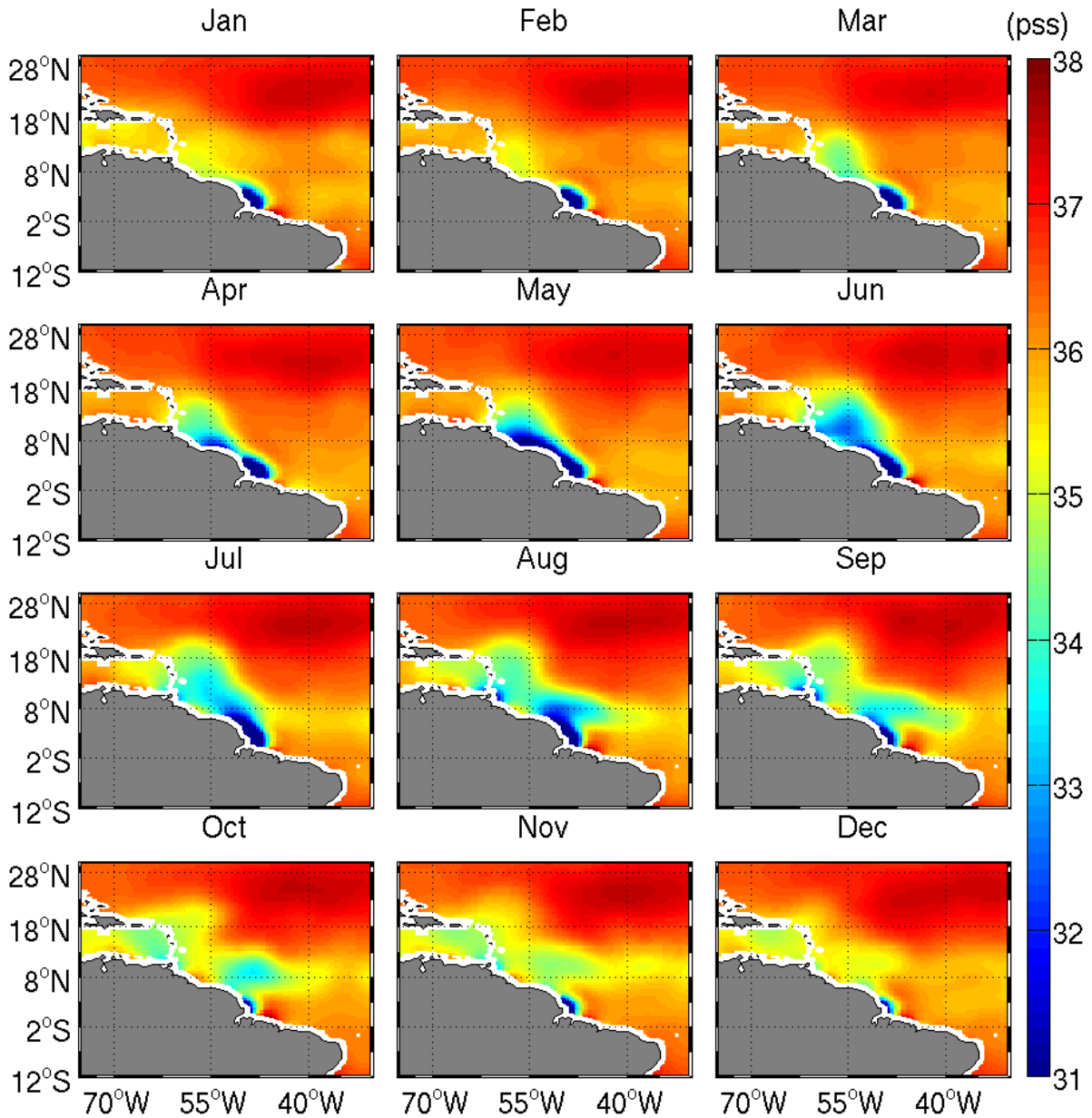


Figure 3.15: Monthly 2010-2013 Reverdin et al. [2007] climatologic sea surface salinity from January to December.

mate SSS in the plume. This is in conflict with the fact that SMOS tends to overestimate SSS near the coast in comparison with *in situ* data (see figure 2.11).

3.2. The Dispersal of the Amazon Plume

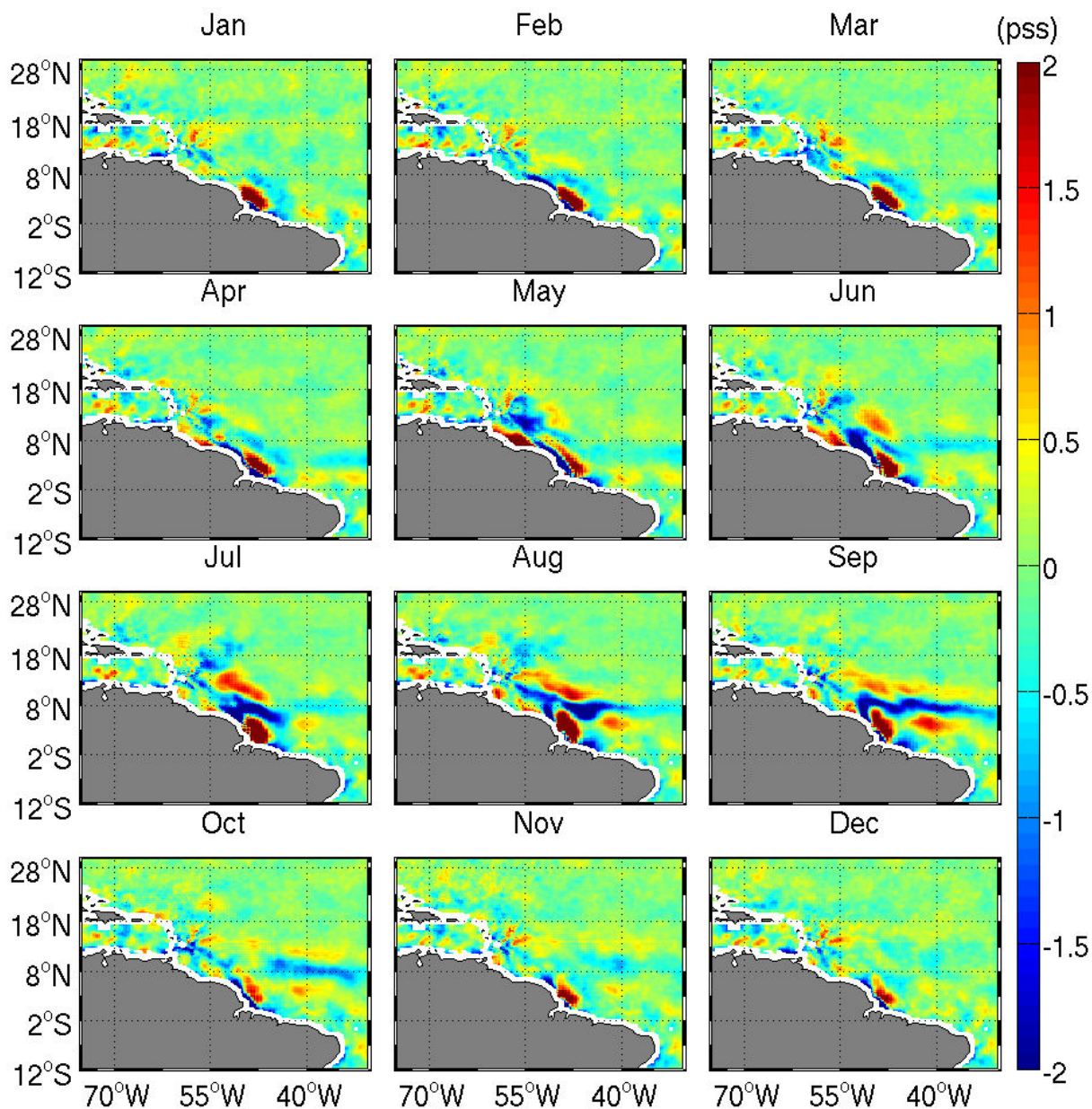


Figure 3.16: Monthly maps of differences between 2010-2013 SMOS SSS and [Reverdin et al. \[2007\]](#) climatologic SSS.

3.2.3 Interannual Amazon plume dispersal

In figures A.1, A.2, A.3 and A.4, in the appendix A, the 2010, 2011, 2012 and 2013 monthly maps are also represented. From one year to another the dispersal of the Amazon waters is in general identical but the plume extension can vary, being more important one year from another. Thus, an interannual variability is noticeable even though SMOS data L3 products were corrected based on the climatology.

On figure 3.17, 2010, 2011, 2012 and 2013 SMOS SSS maps are represented for the month

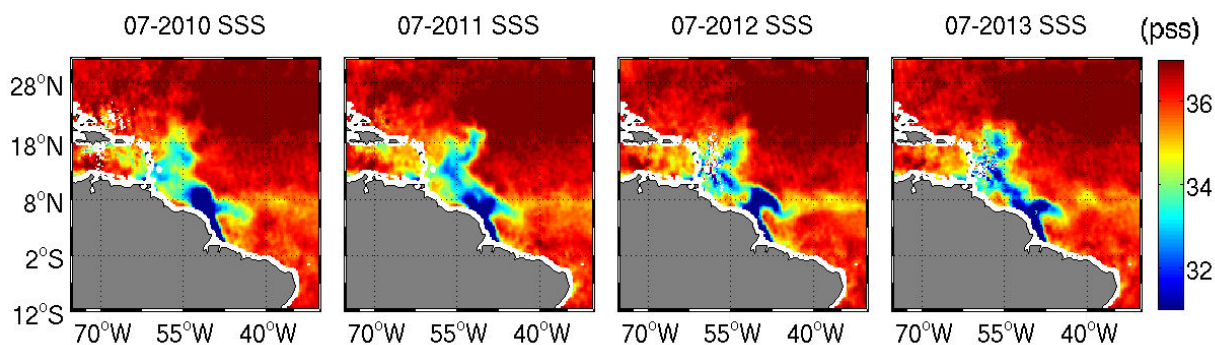


Figure 3.17: From left to right, 2010, 2011, 2012 and 2013 July SMOS sea surface salinity.

of July. As the average plume extension seem coherent from one year to another, some disparities are noticeable. In July 2012 and 2013, fresh waters are already trapped in the retroflexion and carried eastward whereas they are still carried northwestward in 2010 and 2011. Moreover, in 2011 the northwestward dispersal of the plume extends further east, reaching 50°W against only 55°W during other years.

3.2.4 Observed Correlation between the plume extension seasonal variability and the Amazon discharge

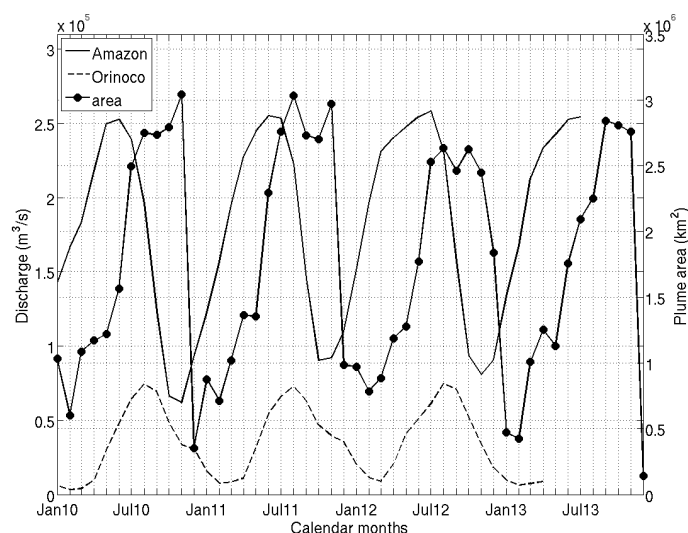


Figure 3.18: Time series of the Amazon (solid line) and Orinoco (dotted line) discharges at Obidos and Bolivar gauges, respectively. The time serie of the plume area computed from the 35.5 pss contour is shown as a solid black line with circles.

3.2. The Dispersal of the Amazon Plume

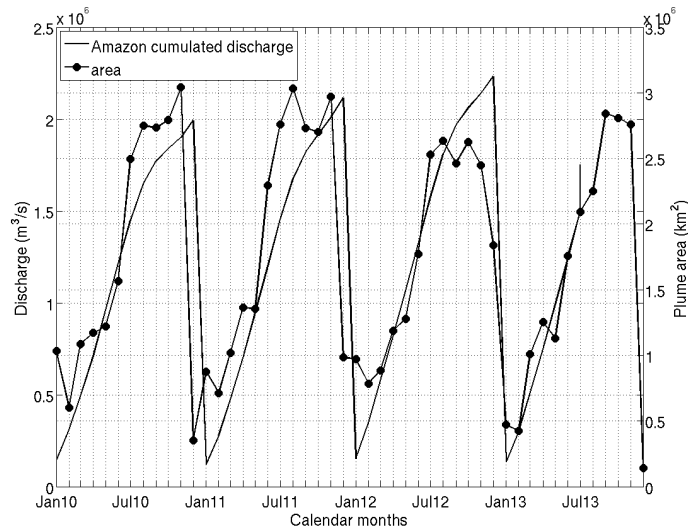


Figure 3.19: Time series of the Amazon (solid line) cumulated discharges at Obidos gauge. The time series of the plume area computed from the 35.5 pss contour is shown as a solid black line with circles.

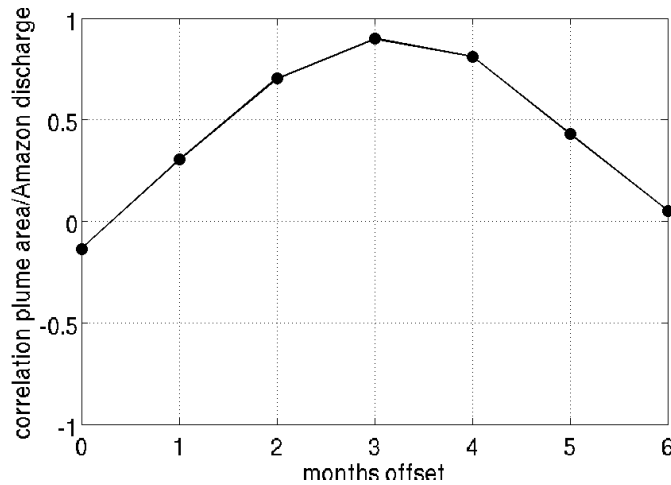


Figure 3.20: Correlations between the time series of the Amazon Plume area, computed from the determination of the 35.5 pss contour, and the Amazon discharge at Obidos, considering an offset from +0 to +6 months on the discharge signal.

The monthly area covered by the plume over 2010-2013, the plume area, is computed as the area inside the 35.5 pss contour. In figures 3.18 and 3.19, we can notice that this extension has a seasonal cycle, it is maximum in late summer (August in 2011 and 2012 and October in 2010) and it is minimum in December-January.

This extension is first related to the Amazon discharge cycle (see figure 3.18, 3.19 and 3.20). The plume extension is maximum about 2-3 months after the Amazon discharge level, depending on the year, around 1 month before the maximum of cumulated discharge level. Indeed, the correlation between the time series of the Amazon discharge and the

plume area is maximum (approximately 0.9) considering a time lag of about 3 months on the Amazon discharge signal. This relationship between plume area and Amazon discharge is robust and follows lags suggested by [Hu et al. \[2004\]](#) and [Muller-Karger et al. \[1988\]](#).

Then a linear relationship can be computed between the monthly plume area and the monthly Amazon discharge considering a 3-month lag (see figure 3.21) which shows that the discharge can be directly deduced from the plume area.

In figures 3.18 and 3.19, we can notice that in 2012, the plume extension is lower comparing to other years. However, the discharge and cumulated discharge in 2012 are not lower, on the contrary. More needs to be done to explain this anomaly in the plume extension. Other physical processes such as precipitation, evaporation, wind, currents could explain this anomaly in 2012.

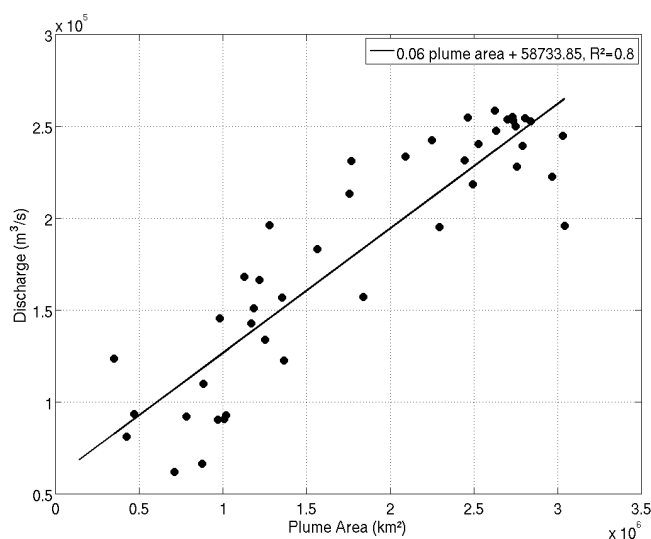


Figure 3.21: Monthly discharge levels over 2010-2013 plotted as a function of the plume area computed from the determination of the 35.5 pss contour, considering a 3-month lag.

As we have seen before, the Amazon discharge is not the only physical process affecting the Amazon plume dispersal and thus its extension in the open ocean. The monthly average wind speed is computed along the plume contour over 2010-2013 and related to the Amazon plume area (see figure 3.22). The wind speed along the plume contour is maximum every year in February corresponding to the trade wind associated with the ITCZ. As the wind stress decreases during spring and early summer, the Amazon plume extension increases to reach its maximum around August-September when the wind stress is minimum ([Geyer et al. \[1996\]](#)).

3.3. Conclusions

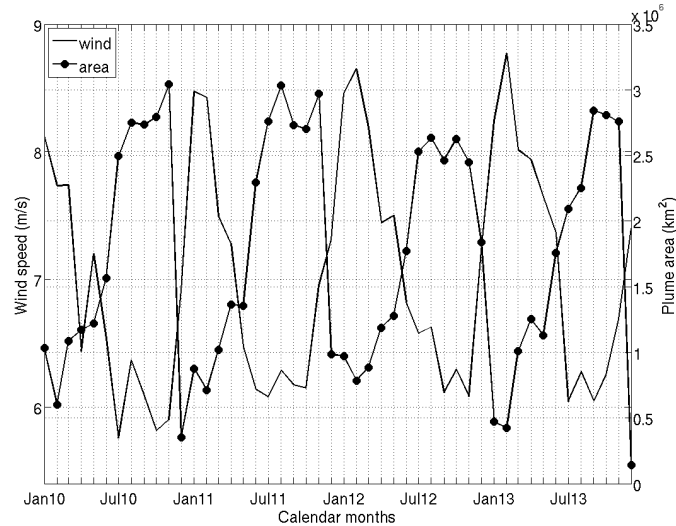


Figure 3.22: Time series of the plume area computed from the 35.5 pss contour is shown as a solid black line with circles. Time series of the average wind speed on the plume contour.

3.3 Conclusions

Our study in the frame of this PhD work focuses on the northwestern tropical Atlantic ocean. This region is subject to many major forcing processes.

The Amazon river, a main player of the land/sea interactions, discharges large amount of fresh waters highly concentrated in dissolved and suspended organic matter into the ocean. This can have an important impact on the local biogeochemistry and physics.

The area is also subject to local and tidal currents, trade winds and precipitations, all being physical forcings having an important impact on the local area.

All these forcings have a seasonal variability which influences the dispersal of the Amazon fresh waters. We demonstrate for the first time that the Amazon discharge is the main player in the Amazon plume extension. Indeed, there is a linear relationship between the Amazon discharge levels and the plume extension considering a 3-month lag. Moreover, it has been shown that the seasonal cycle of trade winds affecting the region can be inversely related to the seasonal variability of the Amazon plume extension.

Chapter 4

The Relationship Between Sea Surface Salinity and Optical Properties in the Amazon Plume Region

4.1 Introduction

Conservative mixing of bio-optical proxies have been extensively studied especially in the region of the Amazon and Orinoco plumes (Del Vecchio and Subramaniam [2004] ; Hu et al. [2004] ; Molleri et al. [2010] ; Salisbury et al. [2011]). It has been analyzed in terms of correlations between SSS data and optical properties measurements (Del Vecchio and Subramaniam [2004] ; Hu et al. [2004] ; Molleri et al. [2010]). In these studies, authors relied on *in situ* SSS data and optical properties within the plume waters estimated either from spaceborne or *in situ* sensors (absorption coefficient of colored detrital matter (a_{cdm}), at several wavelengths (355, 400, 443 nm), the diffuse attenuation coefficient at 490 nm (K490) or chlorophyll concentration) (see figures 4.1 and 4.2). Clear negative correlations between SSS and these optical parameters have been well captured based on limited numbers of colocalized observations.

For example, Hu et al. [2004] found $SSS = 38.18 - 118.24 a_{CDOM}(400 \text{ nm})$, based on about 40 samples of colocalized S-PALACE floats SSS measurements and satellite CDOM values, acquired during 2 winter months in 1999.

Based on CTD and *in situ* optical measurements along several ship transects, Del Vecchio and Subramaniam [2004] found different linear relationships between SSS and a_{CDOM} at 355 nm depending on the location within the plume (proximity of the Amazon mouth or ~ 1000 km north west off the latter). They were not able to find any seasonal variability in this relationship. Note that most of their data were however acquired during the high flow period of the river discharge (May to August).

Combining *in situ* SSS and SeaWiFS optical data, Molleri et al. [2010] found $SSS = -126.03 a_{cdm}(443 \text{ nm}) + 37.259$. This averaged relationship was derived from 30 colocalized samples at oceanographic stations in the proximity of the Amazon mouth, and were acquired at different periods of the seasonal cycle between 1999 and 2003.

For the first time, Salisbury et al. [2011] studied the spatial coherence between the Amazon discharge, the cdm absorption and SSS, and the nature of the SSS- a_{cdm} relationship

4.1. Introduction

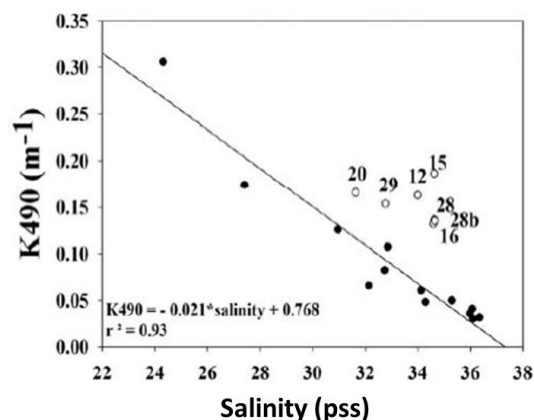


Figure 4.1: Relationship between the diffuse attenuation coefficient at 490 nm and *in situ* salinity computed by Del Vecchio and Subramaniam [2004].

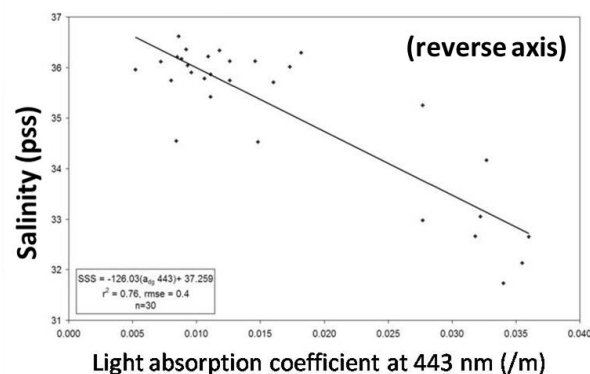


Figure 4.2: Relationship between the absorption coefficient for dissolved organic and detritus material and *in situ* salinity computed by Moller et al. [2010].

using spaceborne measurements of sea surface salinity deduced from the AMSR-E instrument (Reul et al. [2009]). However, due to a lack of precision in the SSS estimations, climatological AMSR-E SSS estimates have been used to carry on this study.

Today, more accurate satellite sea surface salinity (SSS) observations are now available from the ESA Soil Moisture and Ocean Salinity (SMOS) and the NASA Aquarius/SAC-D missions. SMOS and Aquarius measurements now provide unprecedented mapping capabilities at improved temporal resolution. This enables a more in depth examination of the spatio-temporal behaviour of coincident colored detrital matter and salinity over the Amazon plume. Indeed, whereas *in situ* data are sparse in terms of space and time, SMOS and Aquarius satellites permit acquisition SSS data with a temporal resolution of about 10 days and a spatial resolution of about 50 km and 100 km, respectively. Figure 4.3 shows the *in situ* SSS observations available in June 2010, which are few, whereas, figure 4.4 shows a map of the monthly SSS from SMOS for this same month. A more robust conservative mixing relationship from microwave SSS space measurements can now be deduced and studied in terms of temporal and spatial variabilities.

In this chapter we discuss the relationship between sea surface salinity and ocean color properties using two different approaches.

In section 4.2, we discuss the regional relationship between colored detrital matter (cdm) and sea surface salinity over the whole Amazon plume from 2010 to 2013 at unprecedented time and space scales, using the new remote sensing datasets available. In this section we particularly investigate the eventual temporal variabilities of the conservative mixing

Chapter 4. The Relationship Between Sea Surface Salinity and Optical Properties in the Amazon Plume Region

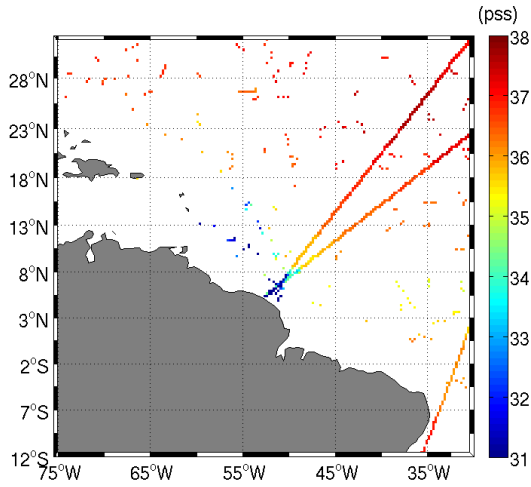


Figure 4.3: June 2010 map of *in situ* SSS observations available, averaged per $0.25 \times 0.25^\circ$ pixels.

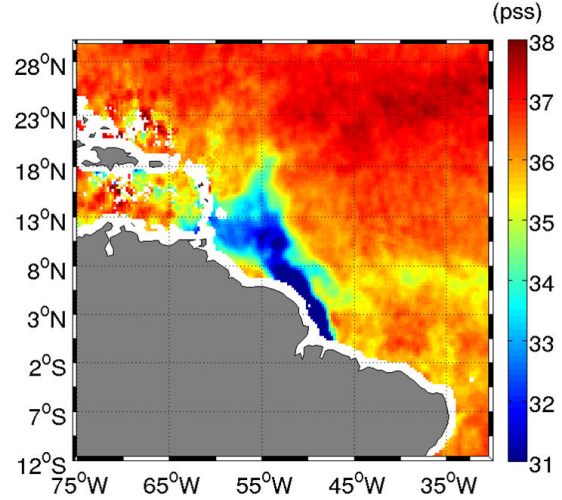


Figure 4.4: June 2010 map of the 10-day running mean 25-km SMOS SSS.

relationship and we finally investigate possible non conservative behaviours of this relationship.

In section 4.3, we first document the correlations between SSS, optical properties and the Amazon discharge over the Amazon plume region. We then discuss plume advection under a conservative mixing model based on a local approach, a spatial analysis using spaceborne measurements of sea surface salinity, and ocean color data.

4.2 A Regional Approach using a Conservative Mixing model

We use remote sensing SSS and optical properties data to reinvestigate the conservative mixing over the whole Amazon plume area, previously studied by [Del Vecchio and Subramaniam \[2004\]](#), [Hu et al. \[2004\]](#), [Molleri et al. \[2010\]](#) and [Salisbury et al. \[2011\]](#). We particularly investigate the relationship between the absorption coefficient of colored detrital matter at 443 nm (a_{cdm}) and the light absorption coefficient at 490 nm (K490) from Ocean Color sensors and SMOS sea surface salinity in the Amazon plume, over 2010-2013. First, we investigate the SSS/ a_{cdm} relationship regionally over the whole Amazon plume region from 2010 to 2013. Then, we explore the temporal and spatial variabilities of this regional relationship. Finally, possible non conservative behaviours of the relationship between SSS and optical properties are investigated.

4.2. A Regional Approach using a Conservative Mixing model

4.2.1 The annual average SSS/ a_{cdm} relationship

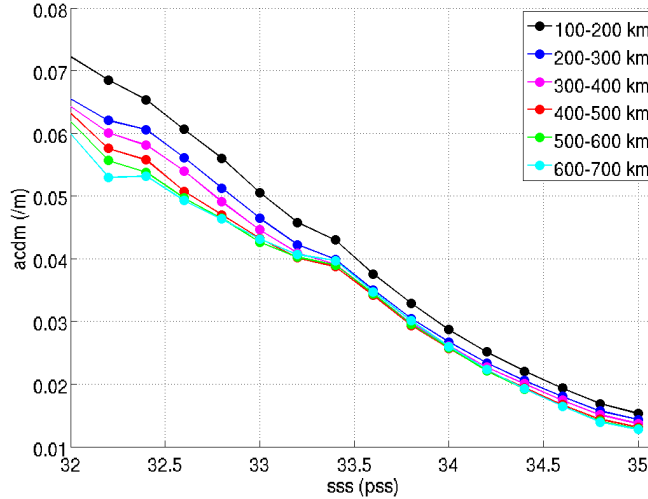


Figure 4.5: 2010-2013 mean a_{cdm} per bin of 0.2 pss depending on the distance to the coast (100 to 200 km, 200 to 300 km, 300 to 400 km, 400 to 500 km, 500 to 600 km and 600 to 700 km).

To compute the SSS/ a_{cdm} relationship, we use the 10-day running mean data over 2010-2013 and we average a_{cdm} per bin of 0.2 pss. In figure 4.5, the mean relationship between SSS and a_{cdm} over 2010-2013 is represented. We attempt to investigate the impact of the distance from the coast in order to get rid of the land contamination in SMOS data and of turbid waters in Ocean Color data, which can affect a_{cdm} retrievals. Each relationship is established depending on the distance from the coast (from 100 km to 700 km by range of 100 km). The 6 different relationships have the same behaviour, above 33.5 pss, all the relationships computed considering pixels further than 200 km from the coast are identical. Below, they have the same evolution considering an offset. The relationship computed within 200 km from the coast is detached from the others with a greater offset. As we get closer to the coast, for one a_{cdm} value, the corresponding SSS value (taking into account the conservative mixing) is higher. This is coherent with the discussion on the known issues of SMOS products discussed in the section 2.1.3.4.

In the end, in the following, in our SSS/ a_{cdm} relationship study, we choose to only consider pixels further than 200 km from the coast.

To compute the mean 2010-2013 SSS/ a_{cdm} relationship, we average the 10-day running mean a_{cdm} and K490 per bin of 0.2 pss ± 1 standard deviation (see figures 4.6 and 4.7). As seen above, in order to get rid of land contamination in SMOS data and turbid waters, only data further than 200 km from the coast are considered. As expected, a negative lin-

Chapter 4. The Relationship Between Sea Surface Salinity and Optical Properties in the Amazon Plume Region

ear correlation is found between these optical property parameters and sea surface salinity. The standard deviation of these relationships at each SSS bin is quite large and can be partly explained by the temporal variability of the relationship, discussed in the following section. The standard deviation becomes lower when sea surface salinity increases, which corresponds to the open ocean area, where SSS is higher and light attenuation and absorption lower.

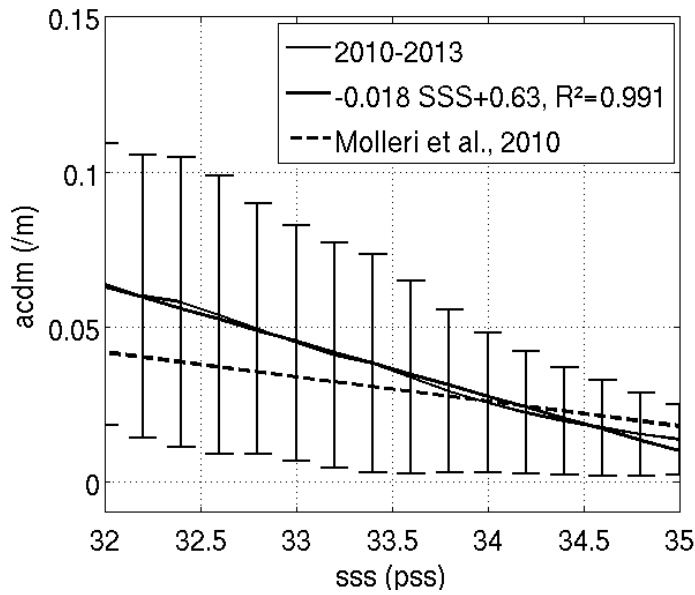


Figure 4.6: 2010-2013 average a_{cdm} per bin of $0.2 \text{ pss} \pm 1$ standard deviation and its linear interpolation (thick black solid line). As a black dotted line is represented the relationship found by Molleri et al. [2010] ($a_{cdm} = -0.008 \text{ SSS} + 0.29$).

These quasi-linear relationships can be linearly interpolated by the equations :

$$a_{cdm} = -0.018 \text{ SSS} + 0.63 \quad \text{and} \quad K490 = -0.012 \text{ SSS} + 0.47 \quad (4.1)$$

These relationships are compared with those found by Molleri et al. [2010] and Del Vecchio and Subramaniam [2004], $a_{cdm} = -0.008 \text{ SSS} + 0.29$ and $K490 = -0.021 \text{ SSS} + 0.77$, respectively. The average regional relationships found in this study using remote sensing data, are consistent with those found in these previous studies, based on *in situ* observations. The discrepancies can be explained by the fact that Del Vecchio and Subramaniam [2004] and Molleri et al. [2010] relationships have been computed using *in situ* data, where sampling in space and time is sparse.

The linear SSS/a_{cdm} relationship is not bijective. Indeed, the distribution inside each

4.2. A Regional Approach using a Conservative Mixing model

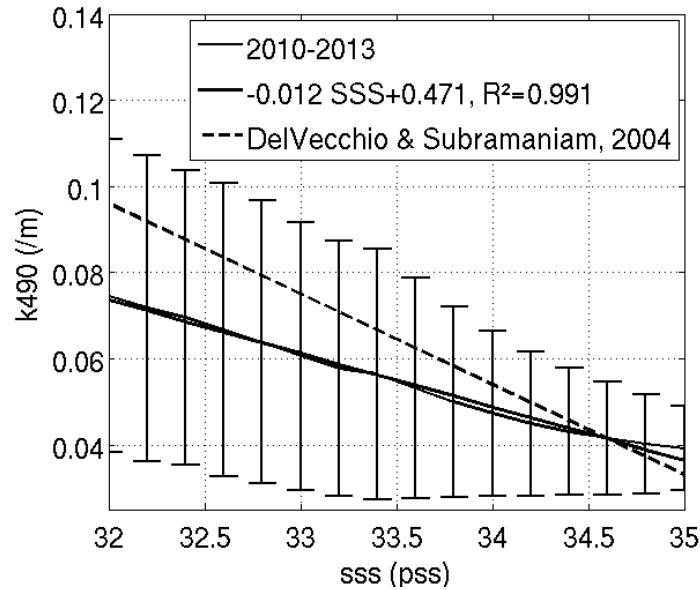


Figure 4.7: 2010-2013 average K490 per bin of $0.2 \text{ pss} \pm 1$ standard deviation and its linear interpolation (thick black solid line). As a black dotted line is represented the relationship found by [Del Vecchio and Subramaniam \[2004\]](#) ($K490 = -0.021 \text{ SSS} + 0.77$).

0.2 pss bin is not Gaussian (see figure 4.8), there is an important skewness as a_{cdm} values increase. Moreover, the mean and the median of a bin distribution are different, which induces errors in the calculation of the average a_{cdm} value in each SSS bin, and thus, in the computation of the SSS/a_{cdm} relationship.

To validate our SSS/a_{cdm} relationship, we compare it to the relationship found using spaceborne a_{cdm} and *in situ* SSS observations over 2010-2012. From these observations, we compute the average a_{cdm} per bin of 0.2 pss (see figure 4.9). The "*in situ* relationship" is consistent with the 2010-2013 relationship found using spaceborne measurements. As SSS decreases, fewer *in situ* observations are available and there are more disparities in the observations. However, two groups of observations are noticeable, one with a_{cdm} values higher than 0.05 /m and the other one with a_{cdm} values lower than 0.05 /m , whatever the salinity range. [Molleri et al. \[2010\]](#) relationship is in accordance with the second group of *in situ* data. In figure 4.10, the locations of the first group of *in situ* data are mapped. These data belong almost all to the same area, near the coast just north off the Amazon mouth. This may highlight a different behaviour of the SSS/a_{cdm} relationship in this part of the Amazon plume implying that *in situ* data acquired at precise and limited location and time may not well-represent the behaviour of the conservative mixing in the whole Amazon plume region.

Chapter 4. The Relationship Between Sea Surface Salinity and Optical Properties in the Amazon Plume Region

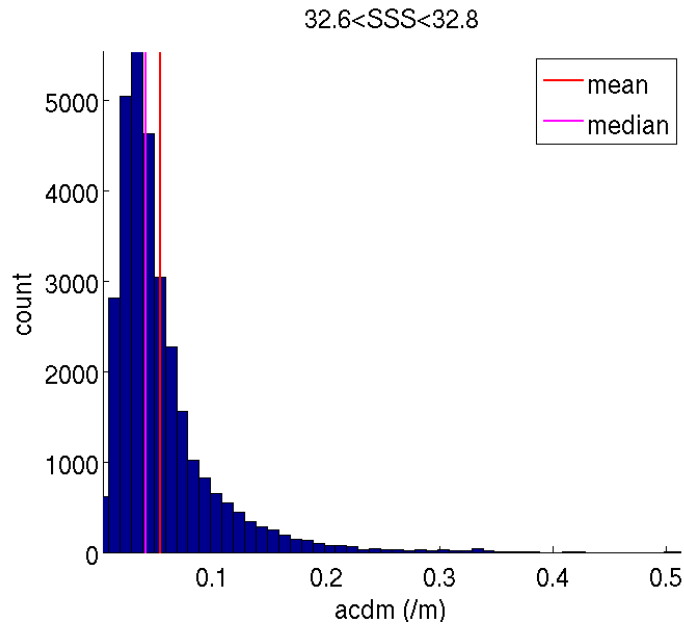


Figure 4.8: Distribution of SSS per bin of 0.1 /m, for SSS values between 32.6 and 32.8 pss.

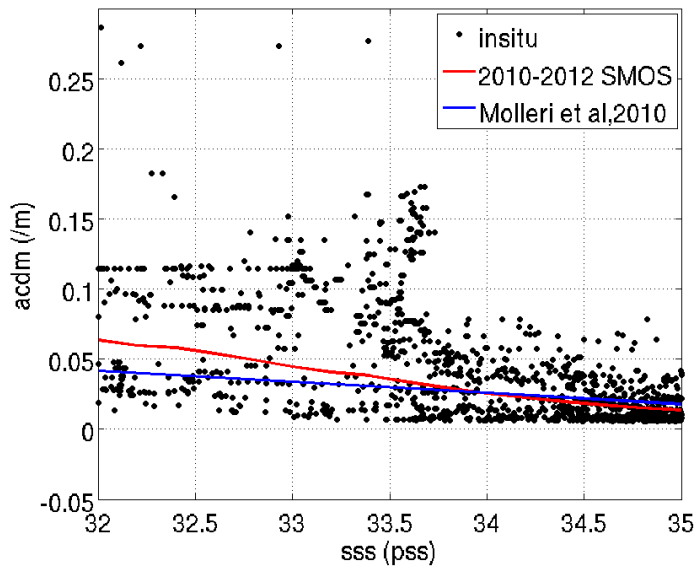


Figure 4.9: A_{cdm} as a function of *in situ* SSS over 2010-2012 (black dots) ; 2010-2012 average a_{cdm} per bin of 0.2 pss \pm 1 standard deviation (blue line) and the average 2010-2013 relationship found using spaceborne measurements (red line).

4.2. A Regional Approach using a Conservative Mixing model

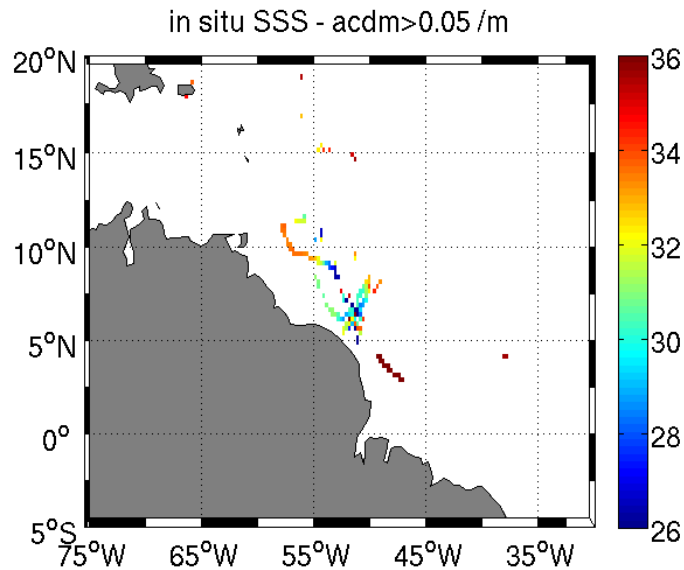


Figure 4.10: Map of locations of *in situ* data with a a_{cdm} value higher than 0.05 /m.

4.2.2 Seasonal variabilities in the conservative mixing

Thanks to spaceborne measurements and their unprecedented space and time resolutions, it is now possible to study the eventual temporal variation of SSS/optical properties relationships at scales of months-to-years.

The seasonal cycle of the Amazon discharge has a direct impact on the Amazon fresh waters transport in the north tropical Atlantic ocean. Depending on the season, two major pathways for the Amazon-Orinoco plume waters are detected by SMOS. The Amazon waters flow northward or eastward up to a certain distance (see figure 3 in Reul et al. [2013], illustrating the seasonal cycle of the plume extension). On figure 4.11, average maps of SSS (left panel) and a_{cdm} (right panel) over each season in 2010 are represented. The seasons are determined based on the Amazon river seasonal cycle (see figure 4.12), four periods are distinguished : the low flow, the ascending flow, the high flow and the descending flow (Salisbury et al. [2011]). During the low flow period (from November to January), the Amazon plume is contained in the vicinity of the river mouth. During the ascending period (from February to April), the plume starts to flow northward to reach its maximal extension during the high flow (from May to July). Finally, at the end of the high flow, the retroreflection appears and waters are carried eastward during the descending flow (from August to October) (see figure 4.11).

It is then legitimate to wonder if the seasonal variability of the Amazon river discharge,

Chapter 4. The Relationship Between Sea Surface Salinity and Optical Properties in the Amazon Plume Region

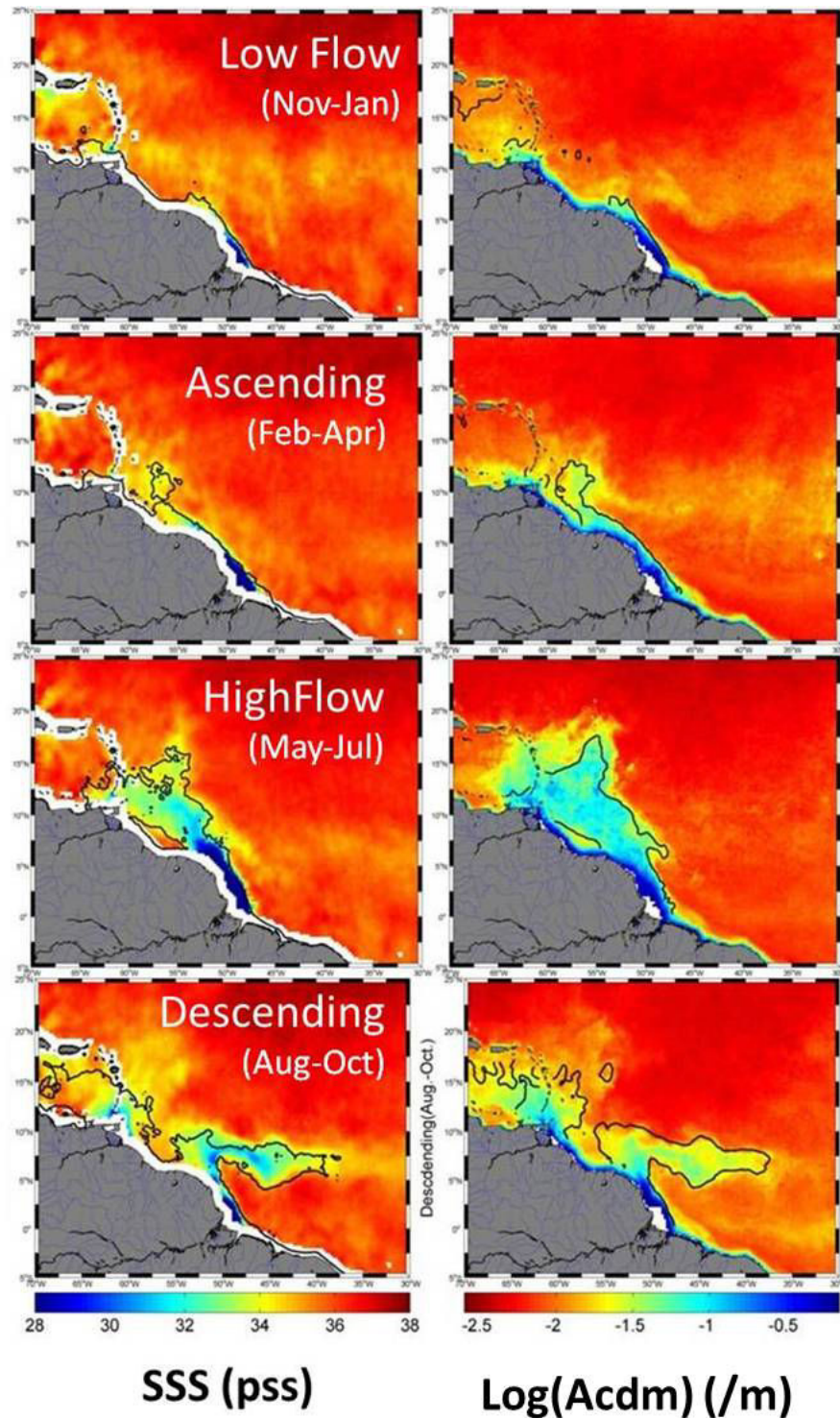


Figure 4.11: Averaged SSS from SMOS (left panel) and averaged a_{cdm} (right panel) for each period (from top to bottom) : low, ascending, high and descending flows, on top of which are represented the average Amazon plume contour computed over each period from a_{cdm} and SSS, respectively.

4.2. A Regional Approach using a Conservative Mixing model

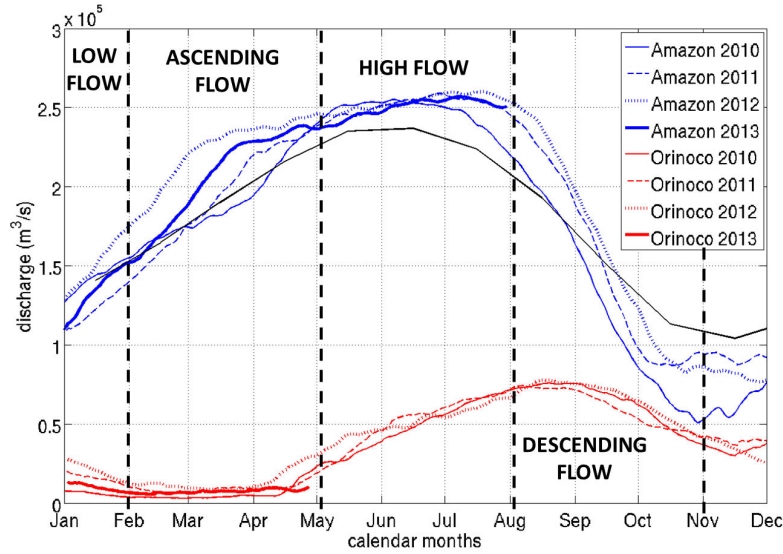


Figure 4.12: Amazon discharge in 2010 (solid blue line), 2011 (dashed blue line), 2012 (dotted blue line), 2013 (thick blue line) and the average river cycle computed from 1968 to 2013 (solid black line). Orinoco discharge in 2010 (solid red line), 2011 (dashed red line), 2012 (dotted red line) and 2013 (thick red line). Four periods are distinguished based on the seasonal cycle of the Amazon river : the low, ascending, high and descending flows.

the plume extension and the river water trajectory, have an impact on the dilution process of the Amazon waters in the open ocean. For each season, the average SSS and a_{cdm} signals are consistent with each other (see figure 4.11). On the a_{cdm} map, the average 35.5 pss contour is represented and on the SSS map, the average a_{cdm} plume contour, which threshold is computed as the mean a_{cdm} value along the 35.5 pss contour. The Amazon plume extension seen by SMOS data is very consistent with the one seen by an optical instrument along the year, except in few areas. For example during the high flow period in 2010, northwest of the plume, there is an area of high SSS and high a_{cdm} values. What seems to be a deviation from the conservative mixing will be discussed in 4.2.5 section.

We next derive and assess conservative mixing model for each month over 2010-2013 to view a possible seasonal cycle in the relationship. Monthly 10-day running mean a_{cdm} composites over the 4 years are averaged per bin of 0.2 pss in the northwestern part of the tropical Atlantic ocean. The 2010-2013 monthly relationships are represented as solid black lines in figure 4.13 ± 1 standard deviation.

The seasonal consistency between SSS and a_{cdm} is also highlighted in figure 4.13, where the monthly 2010-2013 relationships are represented. We can notice that whatever the month, there is a quasi linear relationship between the two parameters. The standard

Chapter 4. The Relationship Between Sea Surface Salinity and Optical Properties in the Amazon Plume Region

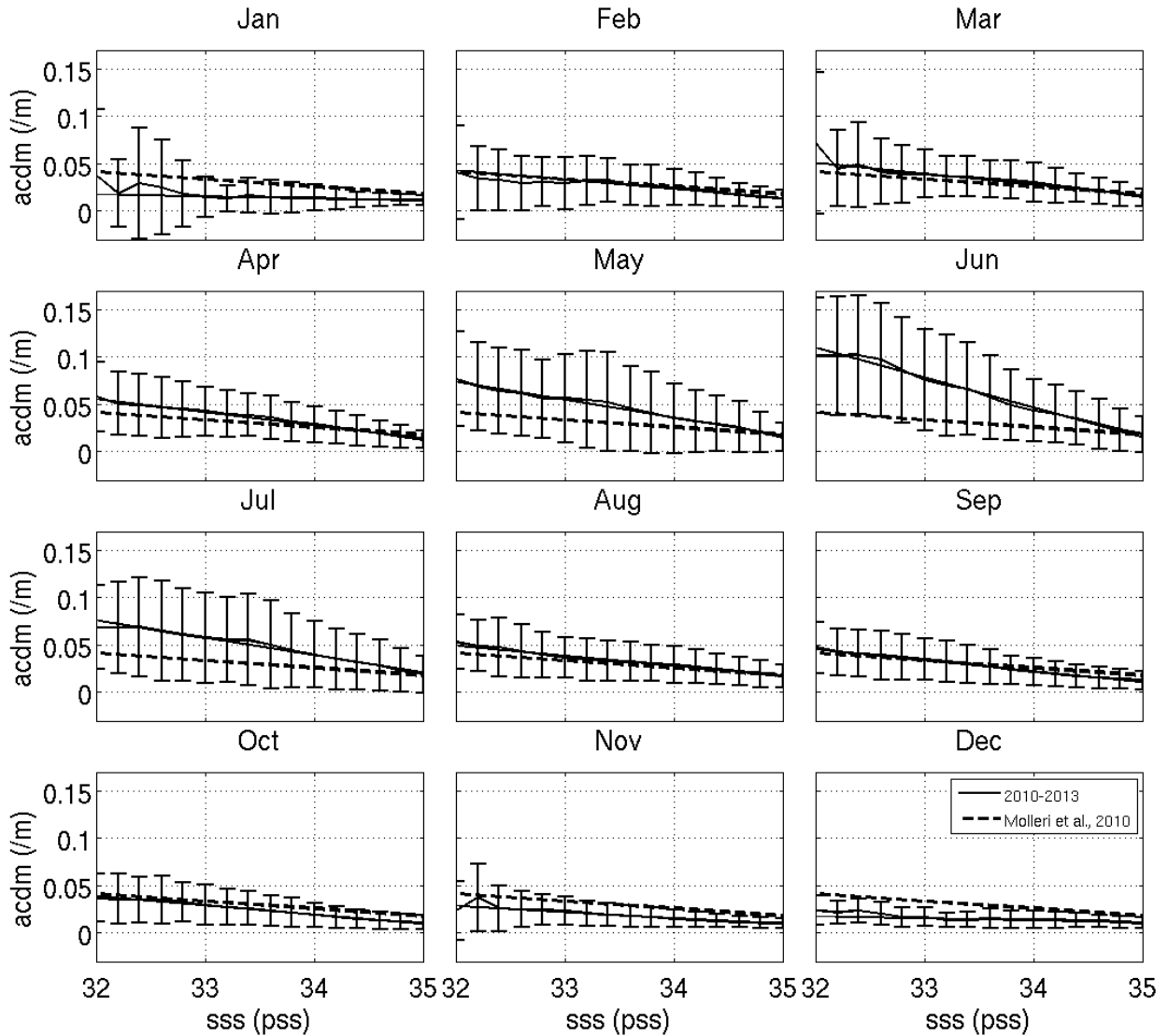


Figure 4.13: Monthly average a_{cdm} per bin of 0.2 pss over 2010-2013 (black). As a dotted line is represented the relationship found by Molleri et al. [2010].

deviation of the May through July relationships is higher, especially at low salinity, than the other months' relationships. This might be due to interannual variabilities, which will be discussed in the following section.

Moreover, the monthly relationships are compared to the relationship found by Molleri et al. [2010]. They are coherent half the year, but during the low flow (November to January) and the high flow (May to July), there are important discrepancies between the two relationships. This might be due to the fact that the relationship found by Molleri et al. [2010] has been computed using *in situ* SSS observations, sparse in time and space.

A seasonal cycle in the relationship is highlighted. All along the year, the slope and

4.2. A Regional Approach using a Conservative Mixing model

the endmember values of the relationships (the a_{cdm} values at the mouth of the river, for a SSS equal to zero) increase to reach a maximum around June, and then decrease to finally reach a minimum around December-January. We then demonstrate that the seasonality of the relationship can be related to the seasonal variability of the endmember which ensues from the river discharge cycle. We compute the linear interpolation of each 2010-2013 monthly SSS/ a_{cdm} relationships represented in figure 4.13 as solid black lines. For the linear interpolation computation, we only take into account the SSS bins in which there are at least 500 valid a_{cdm} values. From these linear relationships, we find the endmember value, which is the a_{cdm} value at the mouth of the river (where SSS is equal to zero). This is illustrated in figure 4.14. As expected from figure 4.13, there is a seasonal variability in the endmember value in accordance with the seasonal cycle of the Amazon discharge (see figure 4.15). The endmember value is maximum in June, when the discharge peak occurs, and minimum in December, 1 month after the minimum discharge level. Thus, the seasonal cycle of the Amazon discharge could be the main source of the seasonal variability in the conservative mixing.

Accordingly, using spaceborne measurements of SSS and optical properties in the Amazon plume from hundred kilometers off the coast and the existing relationship between these parameters, we can deduce an information on optical properties at the mouth of the river, assuming that the Amazon fresh waters mix into the open ocean conservatively, from the mouth to the open ocean.

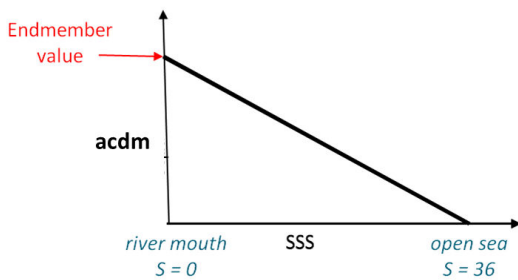


Figure 4.14: Scheme of the computation of the endmember value of the conservative mixing.

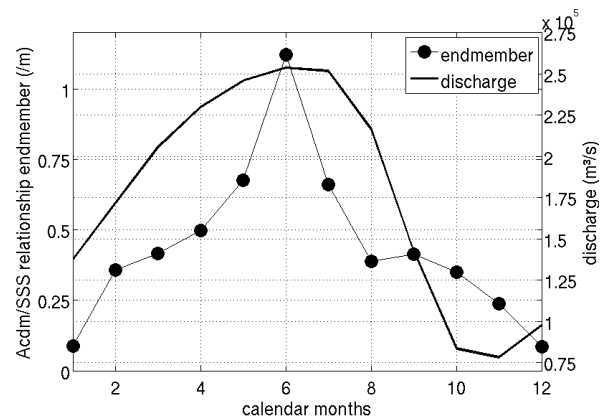


Figure 4.15: Temporal series of the 2010-2013 monthly Amazon discharge and of the 2010-2013 monthly SSS/ a_{cdm} relationship's endmember.

Besides the Amazon discharge, the Amazon tributaries can affect the optical properties of the Amazon plume and thus the conservative mixing, especially because northern and southern tributaries carry different sediments and have their own discharge seasonal cycles

Chapter 4. The Relationship Between Sea Surface Salinity and Optical Properties in the Amazon Plume Region

(see figures 4.16 and 4.17). Southern tributaries are mostly composed of "white waters" and have a peak discharge around February (see figure 4.16), whereas, northern tributaries, composed mostly of "black waters", have a peak discharge, around April-May (see figure 4.17).

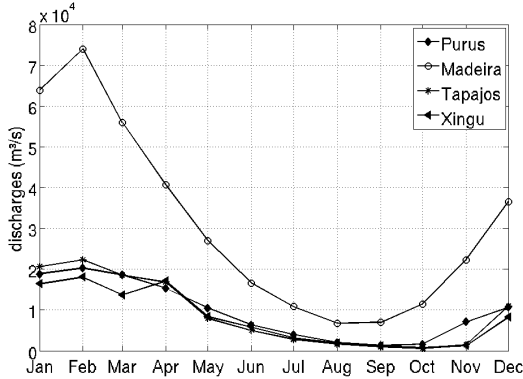


Figure 4.16: Southern Amazon's tributaries monthly discharge in 2010.

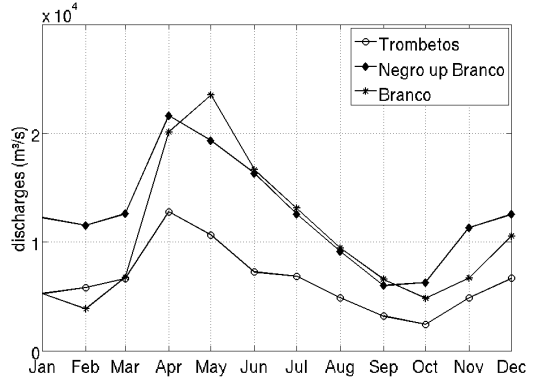


Figure 4.17: Northern Amazon's tributaries monthly discharge in 2010.

4.2.3 Interannual variabilities in the conservative mixing

In figure 4.18, the monthly SSS/a_{cdm} relationships are represented each year from 2010 to 2013. No interannual variability is noticeable in the relationship most of the months. Indeed, from August to April, the 2010, 2011, 2012 and 2013 monthly relationships are consistent. However, in May, June and July, the high flow period, months for which the relationship's standard deviation is higher (see figure 4.13), as the 2011, 2012 and 2013 relationships are coherent with each other, the 2010 relationship has a different behaviour, whatever the sea surface salinity range. For an equivalent SSS value, the a_{cdm} value is, on average, in May, June and July 2010, greater. This might be explained by a non conservative behaviour of the relationship which will be discussed in the section 4.2.5.

In figure 4.19, as in the previous section, we compare the discharge and monthly conservative mixing relationships' endmember time series, each year in that case. As shown previously, the seasonal cycle of the endmember time serie is coherent with the discharge cycle but the amplitudes are not. This tends to imply that there are other sources than the discharge which influence the seasonal variability of the relationship. In summer 2010, the endmember seems abnormally high in comparison with other years' endmembers in summer whereas the discharge maximum is not. This is coherent with a possible non con-

4.2. A Regional Approach using a Conservative Mixing model

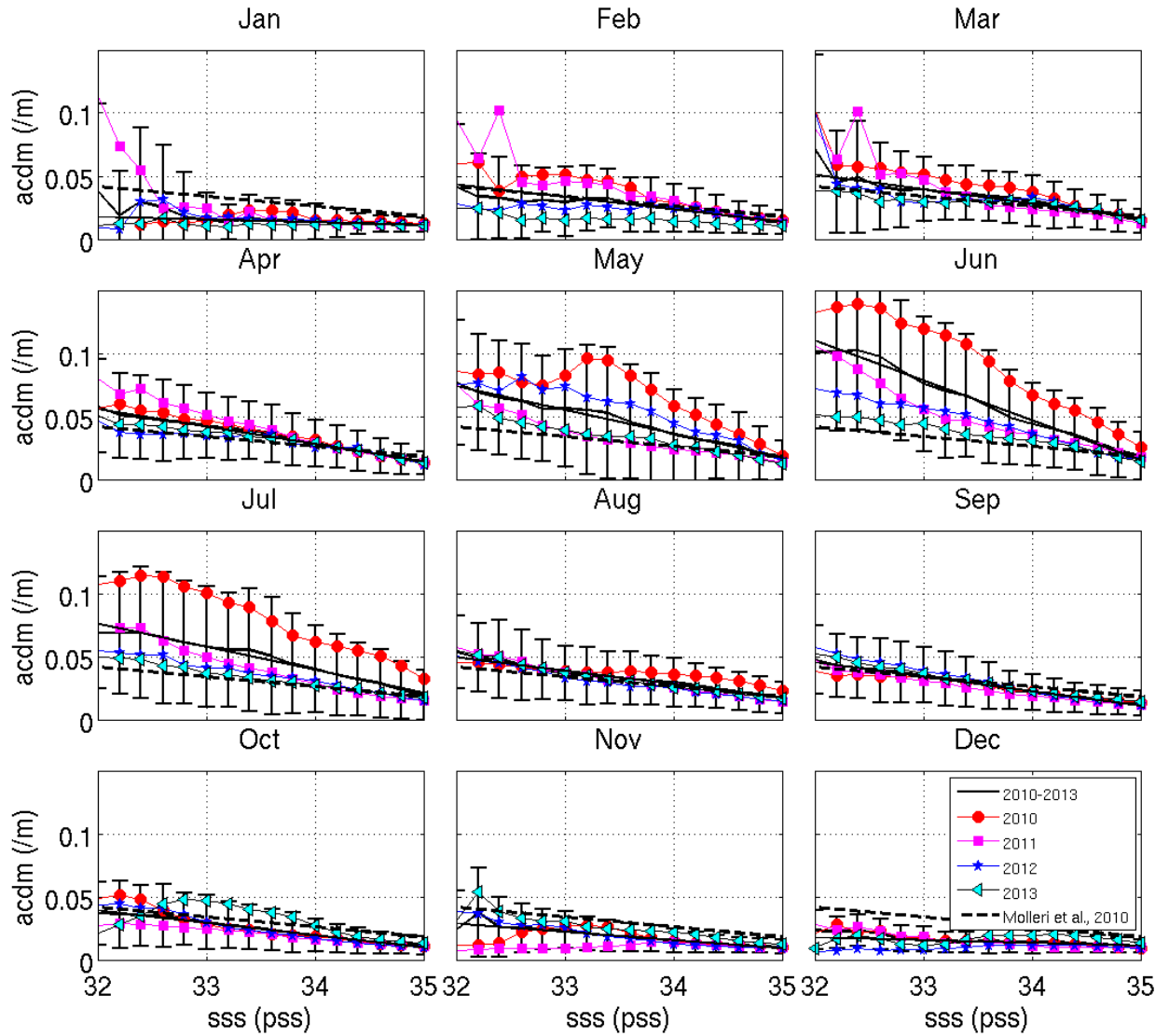


Figure 4.18: Monthly average a_{cdm} per bin of 0.2 pss in 2010 (red), 2011 (magenta), 2012 (blue), 2013 (cyan and black) and over 2010-2013 (black). As a dotted line is represented the relationship found by Molleri et al. [2010].

servative process affecting the relationship between sea surface salinity and ocean color properties during summer 2010.

Chapter 4. The Relationship Between Sea Surface Salinity and Optical Properties in the Amazon Plume Region

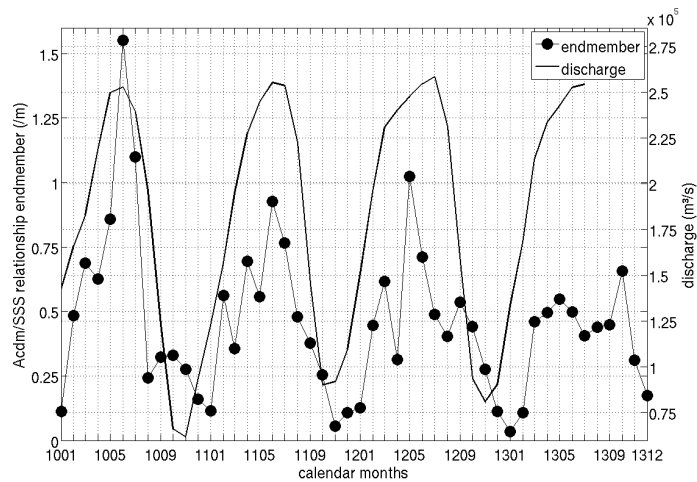


Figure 4.19: Time series of the monthly Amazon discharge and of the monthly SSS/ a_{cdm} relationship's endmember.

4.2.4 Spatial variabilities in the conservative mixing

Besides the temporal variability of the SSS/ a_{cdm} relationship, we wonder if there is a spatial variability in the conservative mixing. Indeed, as two main pathways of the Amazon fresh waters have been highlighted (Reul et al. [2013]), northwestward and eastward, one can wonder if the mixing process is identical in each direction. We thus attempt to study the relationship at a smaller scale.

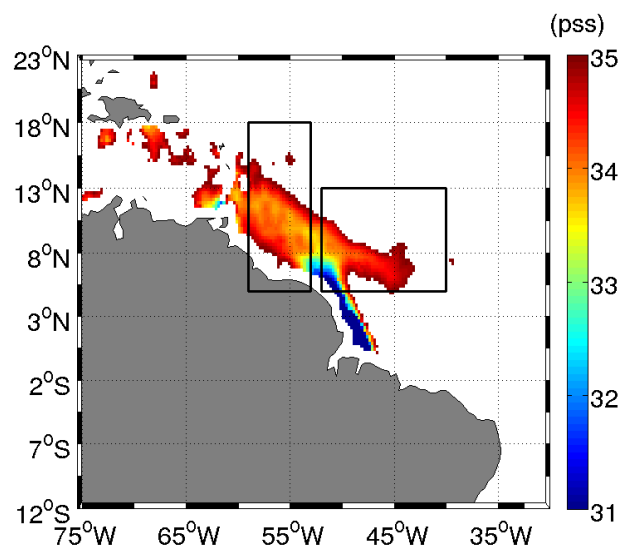


Figure 4.20: 2010 average SMOS SSS. Only pixels which are in average lower than 35 pss are shown here. The 2 boxes, the northwestern one and the eastern one are delimited as black solid lines.

4.2. A Regional Approach using a Conservative Mixing model

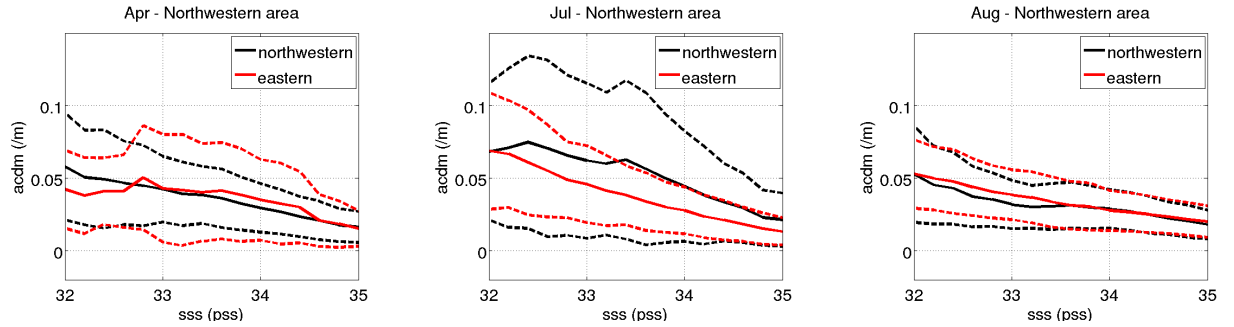


Figure 4.21: 2010-2013 monthly average a_{cdm} per bin of 0.2 pss and the dotted lines represent the 2010-2013 monthly relationships standard deviation. In black, are represented the relationships found in the northwestern box and in red, those found in the eastern part of the plume. From left to right are represented the April, July and August relationships.

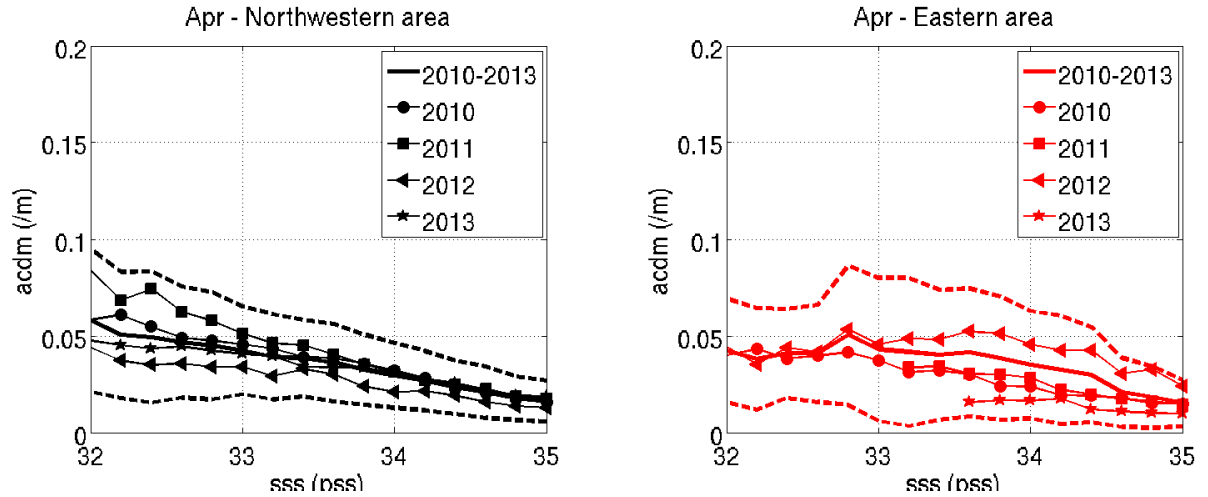


Figure 4.22: Monthly average a_{cdm} per bin of 0.2 pss in 2010 (circles), 2011 (squares), 2012 (triangles), 2013 (pentagrams) and 2010-2013 (solid lines) in April (ascending flow). In black, are represented the relationships found in the northwestern box and in red, those found in the eastern part of the plume. The dotted lines represent the 2010-2013 monthly relationships standard deviation.

To study an evolving spatial variability in the SSS/a_{cdm} relationship, two separate domains were considered (see figure 4.20). The first domain is chosen in the northwestern part of the Amazon plume, away from the mouth of the Orinoco plume which could have an impact on the relationship. This first domain is delimited by the coordinates [59°W 53°W 5°N 18°N]. The second domain is chosen in the eastern part of the plume and is delimited by the coordinates [52°W 40°W 5°N 13°N].

In each domain, a_{cdm} is averaged per bin of 0.2 pss each month from 2010 to 2013 and over 2010-2013. In figures 4.21 to 4.24, the 2010, 2011, 2012, 2013 and over 2010-2013 conservative mixing relationships in each domain are shown for several months. One monthly

Chapter 4. The Relationship Between Sea Surface Salinity and Optical Properties in the Amazon Plume Region

relationship per period is shown : April for the ascending flow (figure 4.21 on the left and figure 4.22), July for the high flow (figure 4.21 on the middle and figure 4.23), August for the descending flow (figure 4.21 on the right and figure 4.24) and no relationship during the low flow is shown here.

In figure 4.21 are compared, in April, July and August the northwestern and eastern 2010-2013 relationships between SSS and a_{cdm} . During the low flow, ascending flow and descending flow, there is no noticeable differences between the northwestern and eastern relationships. Indeed, in April and August, the northwestern and eastern relationships are similar, their standard deviation too. During the high flow period (from May to July), the northwestern and eastern 2010-2013 relationships show some disparities (see figure 4.21 in the middle). Moreover, the standard deviation of the northwestern relationship is higher than the one of the eastern relationship, whatever the salinity range. We will show in the following that these disparities are due to interannual variabilities occurring in the northwestern part of the plume.

In general, in the eastern part of the plume, the interannual variability each month is quasi non existent. Indeed, every month, the 2010, 2011, 2012 and 2013 relationships are consistent and the 2010-2013 relationships' standard deviations are lower than in the northwestern part of the plume and increase as SSS decreases.

In April, during the ascending flow, (see figure 4.22), the mean 2010-2013 relationship's standard deviations are consistent from one region to the other. It is around 0.01 /m at 35 pss and around 0.04 /m in the eastern area and 0.03 /m in the northwestern area at 33 pss. The conservative mixing relationships in both regions considered here are consistent with each other whatever the year.

During the high flow period (May through July), as we discussed earlier, the 2010 relationship has a noticeable different behaviour in the northwestern part of the Amazon plume (see figure 4.23 on the right panel). This behaviour of the relationship which will be related to a non conservative process will be discussed further in the following section. This behaviour induces a higher 2010-2013 relationship's standard deviation in the northwestern part of the plume. The standard deviation is around 0.03 /m at 35 pss and up to 0.1 /m at 33 pss. In the eastern part of the plume, the standard deviation is about 0.02 /m at 35 pss and 0.07 /m at 33 pss. Besides the unusual behaviour in 2010 next to the Caribbean Sea, the conservative mixing in the northwestern and the eastern parts of the plume are consistent whatever the year, taking into account the standard deviation

4.2. A Regional Approach using a Conservative Mixing model

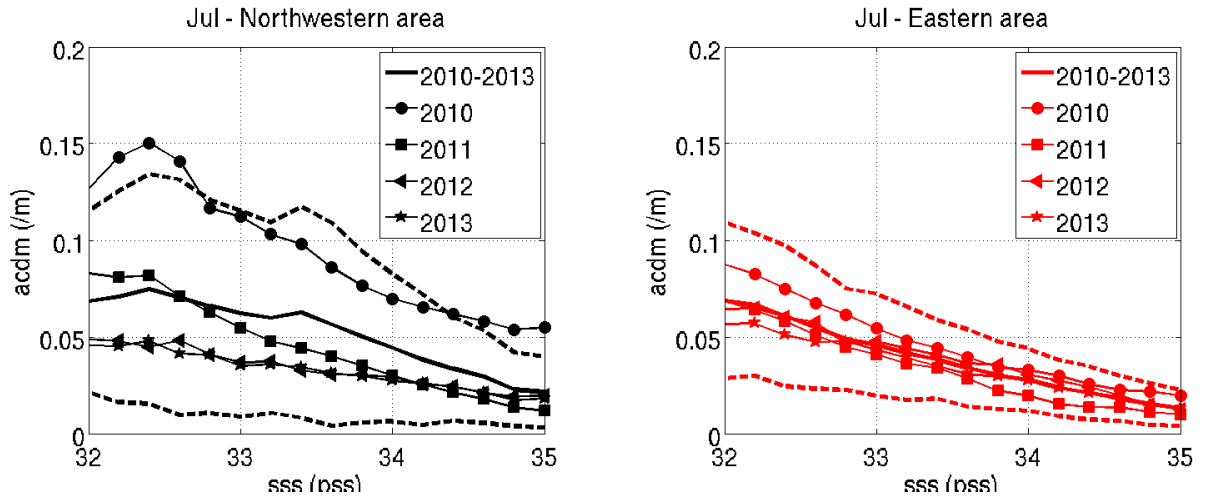


Figure 4.23: Monthly average a_{cdm} per bin of 0.2 pss in 2010 (circles), 2011 (squares), 2012 (triangles), 2013 (pentagrams) and 2010-2013 (solid lines) in July (high flow). In black, are represented the relationships found in the northwestern box and in red, those found in the eastern part of the plume. The dotted lines represent the 2010-2013 monthly relationships standard deviation.

of the average 2010-2013 relationships.

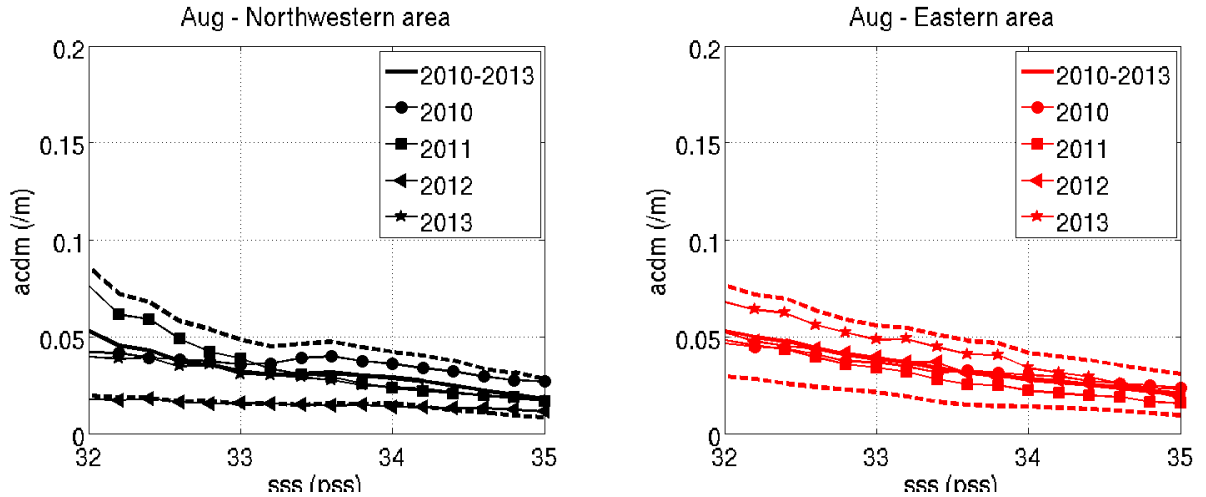


Figure 4.24: Monthly average a_{cdm} per bin of 0.2 pss in 2010 (circles), 2011 (squares), 2012 (triangles), 2013 (pentagrams) and 2010-2013 (solid lines) in August (descending flow). In black, are represented the relationships found in the northwestern box and in red, those found in the eastern part of the plume. The dotted lines represent the 2010-2013 monthly relationships standard deviation.

In August (see figure 4.24), the relationships computed in both regions are consistent with each other except in 2012 in the northwestern part of the plume. This year in the northwestern part of the plume, in August, for a same SSS value, the a_{cdm} value is lower, it might be due to a removal process such as photobleaching.

Chapter 4. The Relationship Between Sea Surface Salinity and Optical Properties in the Amazon Plume Region

During the low flow, from November to January, while the plume extension is minimum, there are only few low SSS observations, below 33.5-34 pss, in both areas (not shown here). The behaviour of the relationships below 33.5 pss are thus non relevant and cannot be used to demonstrate an eventual spatial variability in the relationship during that period.

As a conclusion, we can say that no spatial variability in the SSS/a_{cdm} relationship can be inferred from this analysis, at these scales. Indeed, no systematic variability in the relationships computed in both areas has been highlighted. The most important variability in the relationships computed in both areas of the plume is due to a non conservative behaviour of the relationship occurring in an area at a precise time, the high flow period in 2010. This will be discussed in the section 4.2.5.

4.2.5 Non conservative behaviour in a_{cdm} mixing

Despite the spatial, seasonal and interannual variabilities of the SSS/a_{cdm} relationship, deviations from the conservative mixing can occur due to biogeochemical processes such as primary production and removal processes (photobleaching, flocculation...). In the following, we attempt to study such non conservative behaviour.

In previous sections, we highlighted an evolving non conservative behaviour during the 2010 high flow period (from May to July 2010). Indeed, in figure 4.11, during the high flow period in 2010, northwest to the plume, there is an area with high SSS and high a_{cdm} values. This is corroborated by the May to July relationships in figure 4.13 and especially by the July relationship computed in the northwestern part of the plume (see figure 4.23). During those months in 2010, only in the northwestern part of the plume, for an equivalent SSS value, the a_{cdm} value is greater, on average, in May, June and July 2010. This might be explained by a non conservative behaviour of the relationship due to biogeochemical processes next to the Caribbean Sea. Primary productivity could represent another source of cdm than a terrestrial source and affect the conservative mixing. Indeed, in summer, the arrival of the Amazon river nutrient-rich (silicates, phosphorus, nitrogen) waters stimulates the primary production and thus, induces an increase of dissolved matter next to the Caribbean Sea (Beers et al. [1968]). Moreover, on figure 4.25, we can notice that in 2010 there are important net primary productivity values next to the Caribbean Sea in particular. This biological activity in 2010 next to the Caribbean

4.2. A Regional Approach using a Conservative Mixing model

Sea may explain the different behaviour of the relationship in May through July 2010, in comparison with the years 2011, 2012 and 2013.

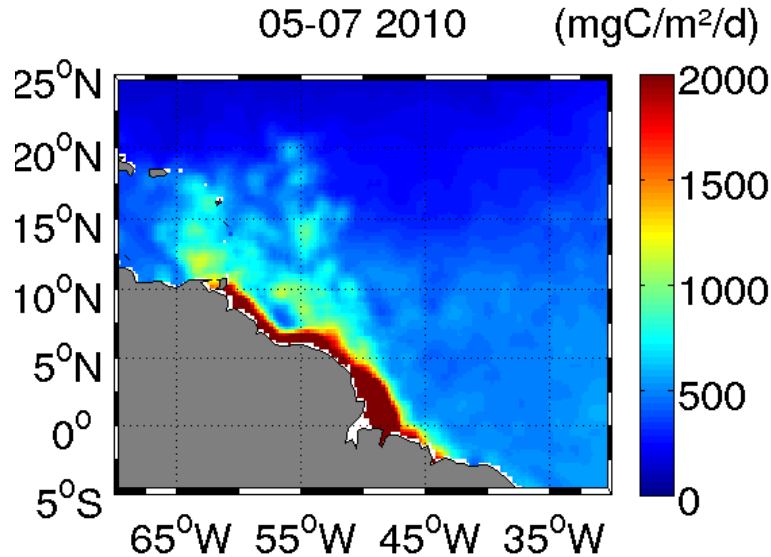


Figure 4.25: Average net primary productivity over the high flow period (May to July) in 2010.

In the following, we will study such non conservative behaviours in terms of anomalies to the conservative mixing. To do that, a reference has to be chosen and we decided to use the average 2010-2013 monthly SSS/a_{cdm} relationships as references for each month. This reference can be discussed as these average 2010-2013 monthly relationships can be tainted with errors.

We just highlighted a non conservative behaviour of the relationship during the high flow period (May to July) in 2010. Thus, computing the average 2010-2013 May, June and July relationships, taking into account the year 2010 may falsify the average monthly relationship (see figure 4.13 from May to July). In order to get rid of outlier behaviours of the relationship, the 2010 May, June and July data are not used in the computation of the 2010-2013 monthly relationships (see figure 4.26).

To study the anomalies from the conservative mixing, 2010-2013 monthly relationships are linearly interpolated (see figure 4.26). A linear interpolation is computed on 2010-2013 the monthly binned relationships between SSS and a_{cdm} . Only bins between 32 and 35 pss with at least 500 data inside are considered for the interpolation. These resulting monthly empirical relationships are then used to compute the 25-km monthly a_{cdm} estimates from 2010 to 2013 based on the 25-km monthly SMOS SSS products (see figure 4.27 for an explanatory scheme). Only for pixels where SSS is lower than 35 pss (the salinity range for which the monthly SSS/a_{cdm} relationships are valid), an a_{cdm} value is estimated.

Chapter 4. The Relationship Between Sea Surface Salinity and Optical Properties in the Amazon Plume Region

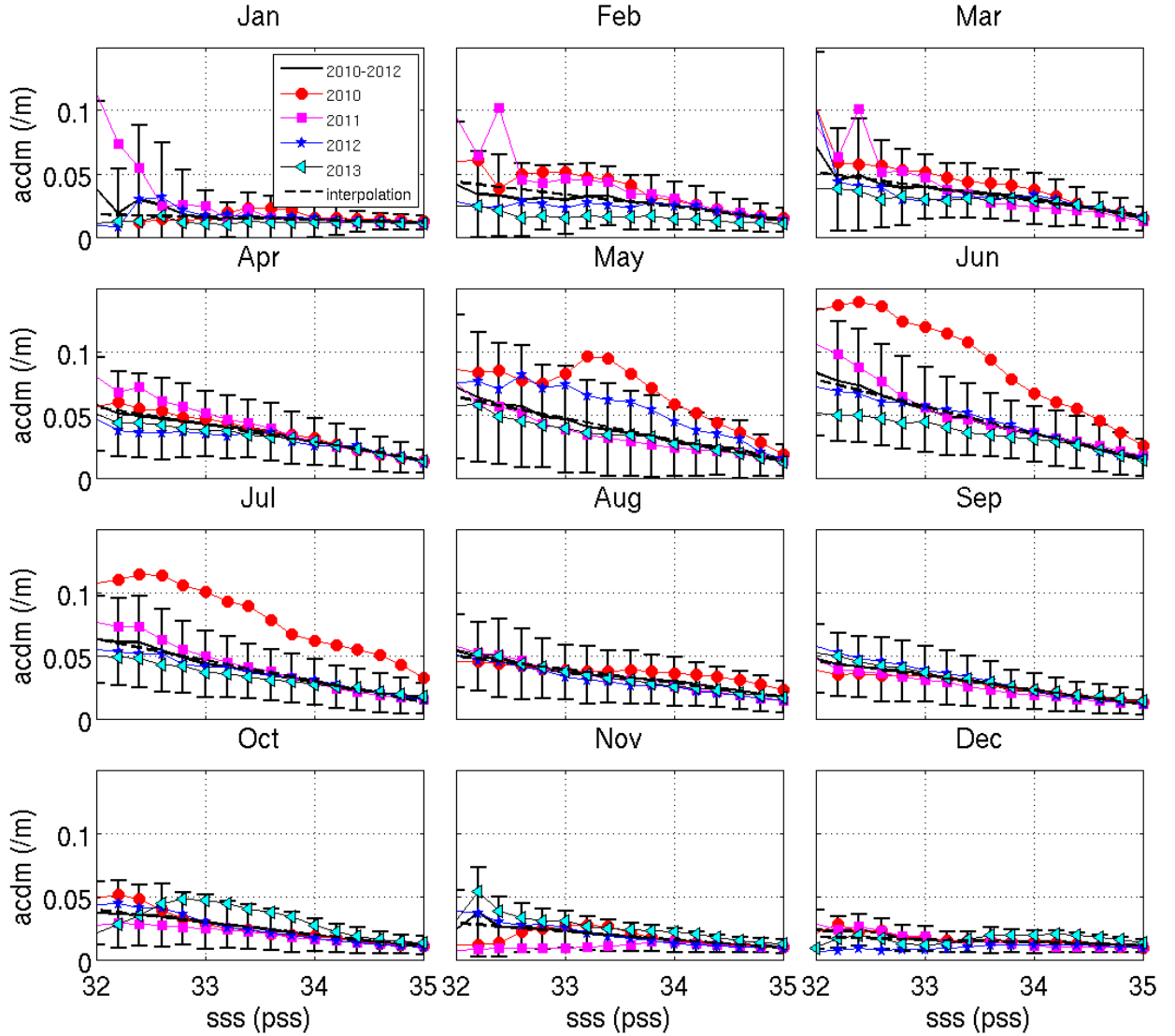


Figure 4.26: Monthly average a_{cdm} per bin of 0.2 pss in 2010 (red), 2011 (magenta), 2012 (blue), 2013 (cyan and black) and over 2010-2013 (black). As a dotted line are represented the linear interpolation of the 2010-2013 monthly relationship. In the computation of the May, June and July relationships, 2010 data are ignored.

We study then the monthly anomalies between these estimates and the GlobColour a_{cdm} products from 2010 to 2013 (estimated a_{cdm} - observed a_{cdm}). A negative anomaly would mean that the estimated a_{cdm} value is lower than the effective observed a_{cdm} value (see figure 4.28). That would mean that there is another source of cdm beyond.

Next, we compute, monthly maps of anomalies between estimated and observed a_{cdm} (see figures 4.29, 4.30, 4.31 and 4.32). We compare these monthly anomaly maps to the monthly maps of net primary productivity (see figures 4.33, 4.34, 4.35 and 4.36).

We can notice 4 different behaviours in the monthly anomaly patterns. During winter

4.2. A Regional Approach using a Conservative Mixing model

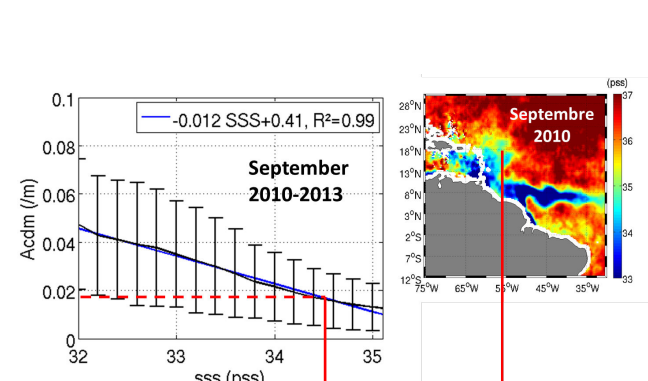


Figure 4.27: Scheme of the computation of a_{cdm} estimates from SMOS SSS and the monthly 2010-2013 SSS/ a_{cdm} relationship.

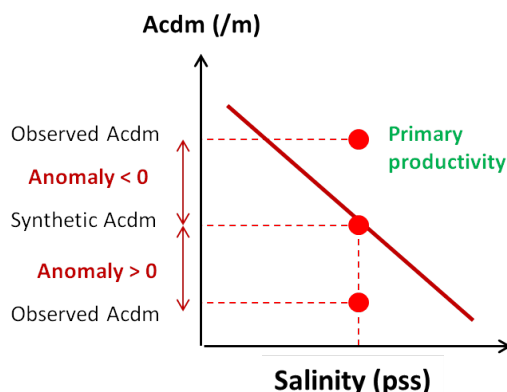


Figure 4.28: Scheme of the anomalies in the conservative mixing.

and early spring, from November to March included, negative anomalies are present next to the Amazon mouth and northwestward along the coast. In February 2013, a slightly different behaviour is noticeable with an area of positive anomalies at the river mouth.

In April, negative anomalies are also noticeable at the mouth and along the coast and few positive anomalies along the coast are also present. In April 2012, next to the Caribbean sea, important positive anomalies are noticeable which might be due to the presence of RFI in SMOS data.

From May to July, there are positive anomalies patterns at the river mouth except in 2012. Positive anomalies are also obtained in the northwestern part except in 2010. Indeed, during this period in 2010, an important negative anomaly (up to -0.1 /m) is noticeable in the whole northwestern part of the Amazon plume. It is consistent with the unusual behaviour of the SSS/ a_{cdm} relationship discussed earlier and seen in figures 4.13, 4.26 and on the top panel of figure 4.23. During these 3 months, next to the Caribbean Sea, these negative anomaly areas are associated with areas of intense net primary productivity (higher than 1500 mgC/ m^2 /d), in comparison with the years 2011, 2012 and 2013 (see figures 4.33, 4.34, 4.35 and 4.36 in May through July).

From August to October, there are negative anomalies patterns at the mouth of the river and in the retroflexion. Few positive anomalies are also present next to the Caribbean sea, as in April 2012.

Investigating the monthly net primary productivity maps from 2010 to 2013, we can notice that generally, strong net primary productivity patterns are associated with negative anomaly patterns : at the mouth of the river all year long, in the retroflexion during late summer and from May to July 2010 in the northwestern part of the plume. In 2013, strong primary productivity patterns are noticeable in May and June in the northwestern

Chapter 4. The Relationship Between Sea Surface Salinity and Optical Properties in the Amazon Plume Region

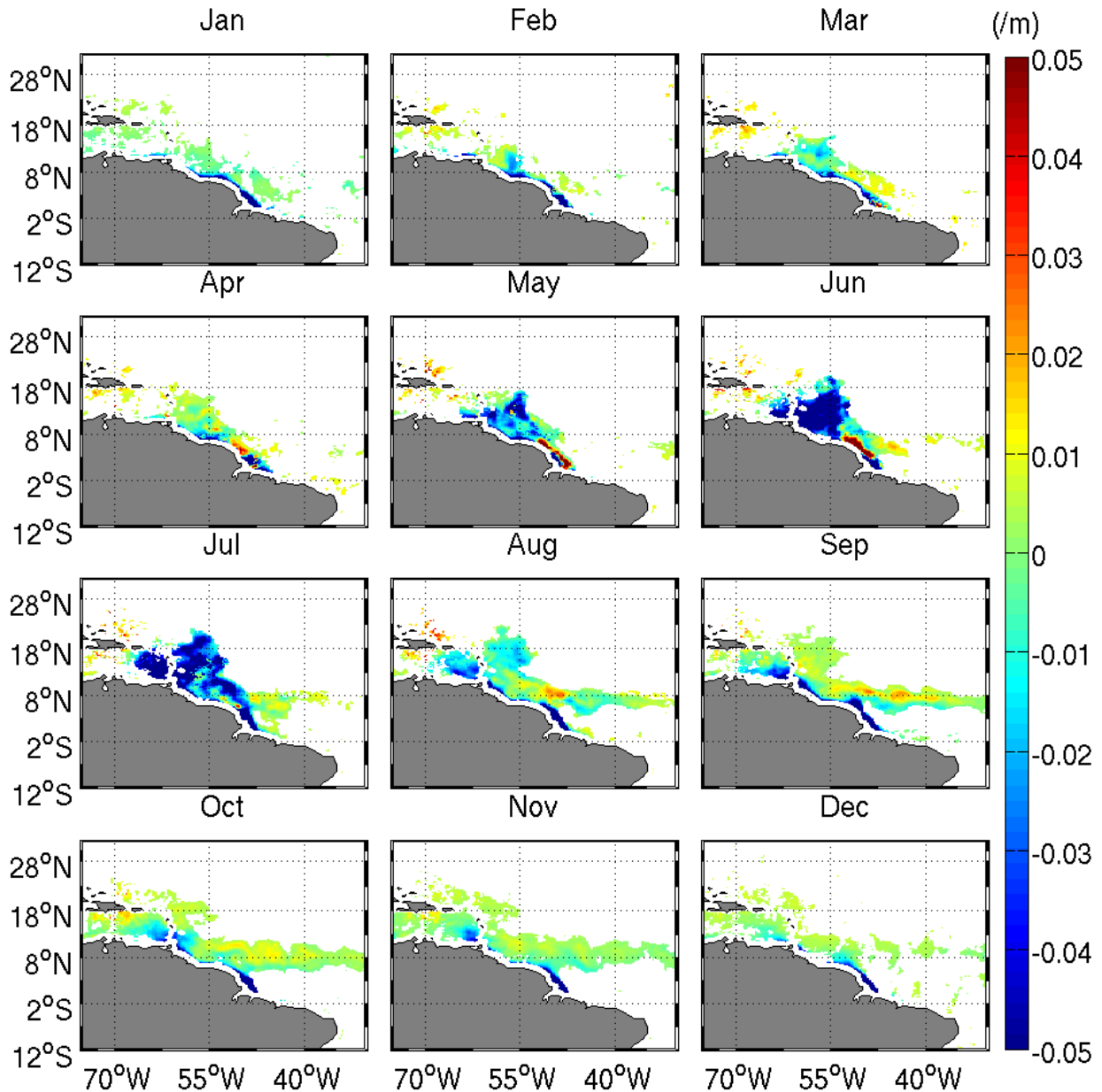


Figure 4.29: 2010 monthly maps of 25-km differences between a_{cdm} estimated from the monthly 2010-2013 SSS/a_{cdm} relationship and GlobColour a_{cdm} in the Amazon plume.

part of the plume whereas no obvious negative anomalies between estimated and observed a_{cdm} can be noticed.

The anomalies between estimated and observed a_{cdm} are plotted against chlorophyll-a concentration and the particulate backscattering coefficient at 443 nm (see figure 4.37). The larger the chlorophyll-a concentration and the backscattering coefficient, the larger the anomalies. Chlorophyll-a is a proxy of primary productivity, it shows that the anomalies between estimated and observed a_{cdm} are directly related to a possible local biological

4.2. A Regional Approach using a Conservative Mixing model

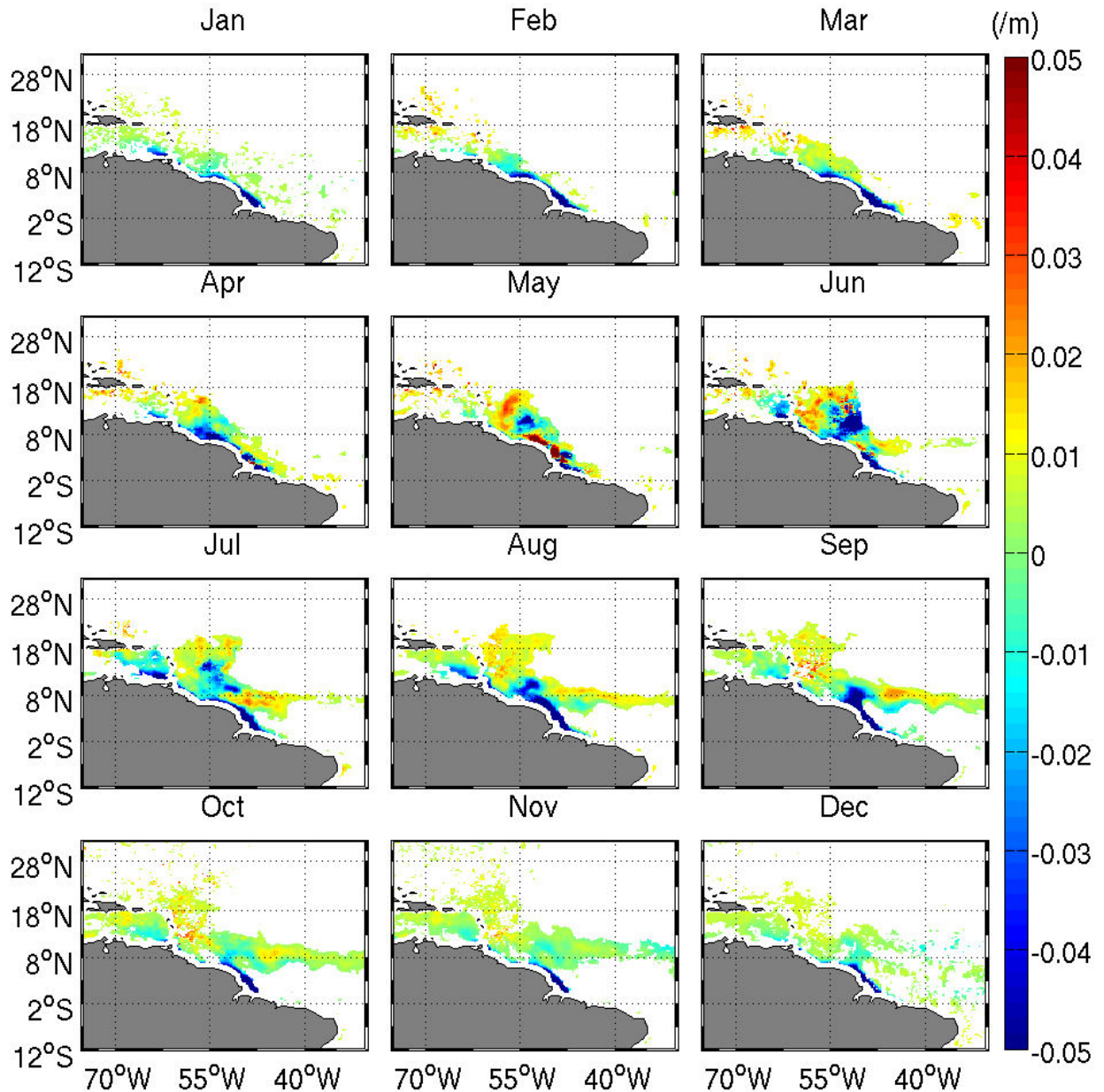


Figure 4.30: 2011 monthly maps of 25-km differences between a_{cdm} estimated from the monthly 2010-2013 SSS/ a_{cdm} relationship and GlobColour a_{cdm} in the Amazon plume.

activity. Moreover, the particulate backscattering coefficient can also be seen as an indicator of primary productivity. It represents the scattering partially due to phytoplankton which produces detrital matter.

Positive anomaly patterns noticed in figures 4.29, 4.30, 4.31 and 4.32 mean that the observed a_{cdm} is lower than the predicted one, this could be due to photobleaching (degradation of the cdm mainly due to the availability of light) or other removal processes. Indeed, during boreal summer, at the edges of the plume, where the riverine materials become

Chapter 4. The Relationship Between Sea Surface Salinity and Optical Properties in the Amazon Plume Region

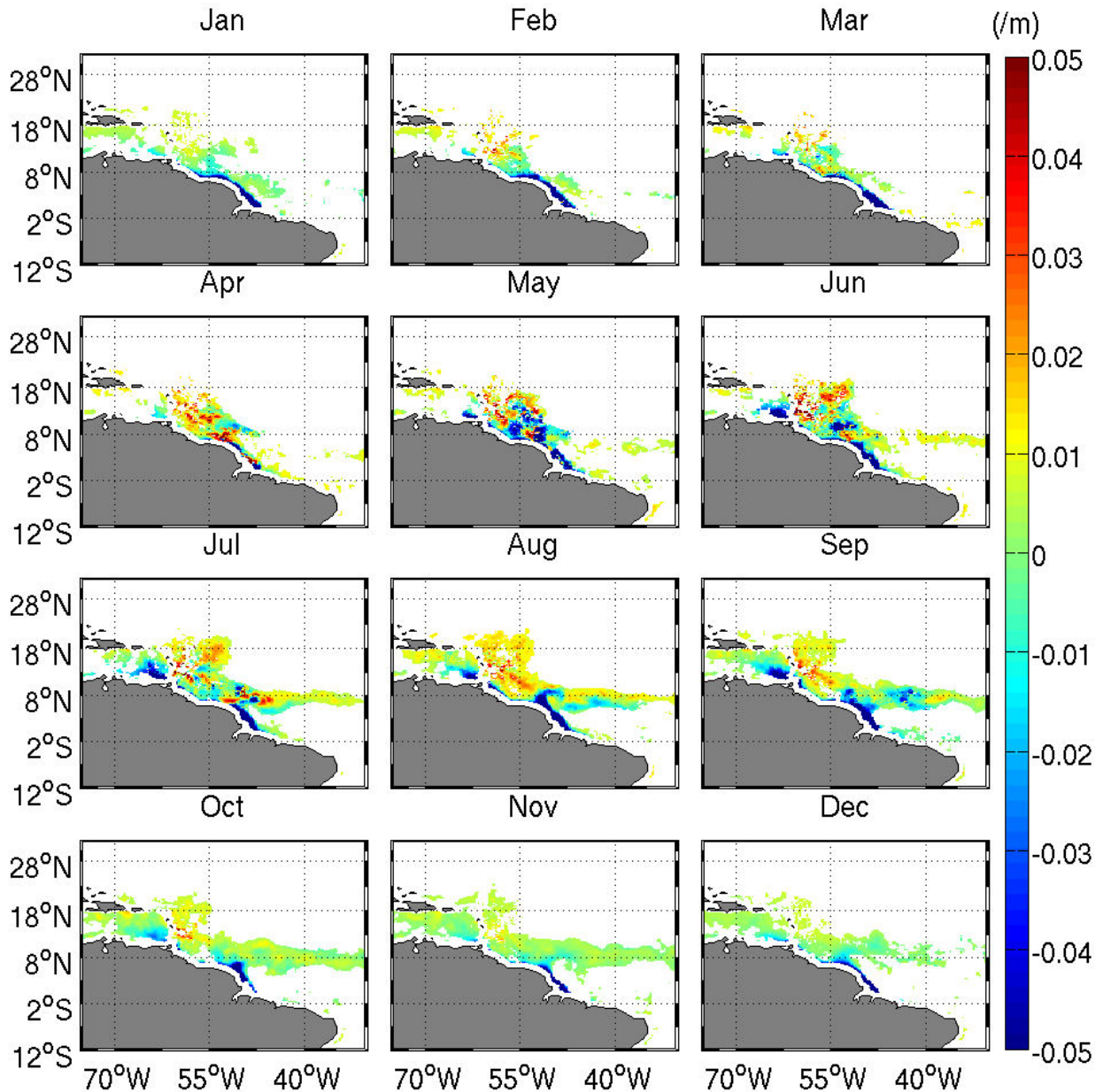


Figure 4.31: 2012 monthly maps of 25-km differences between a_{cdm} estimated from the monthly 2010-2013 SSS/ a_{cdm} relationship and GlobColour a_{cdm} in the Amazon plume.

less and less important, light is more available in the first meters of the surface layer. We won't go deeper in this topic which is beyond the scope of this study.

4.2. A Regional Approach using a Conservative Mixing model

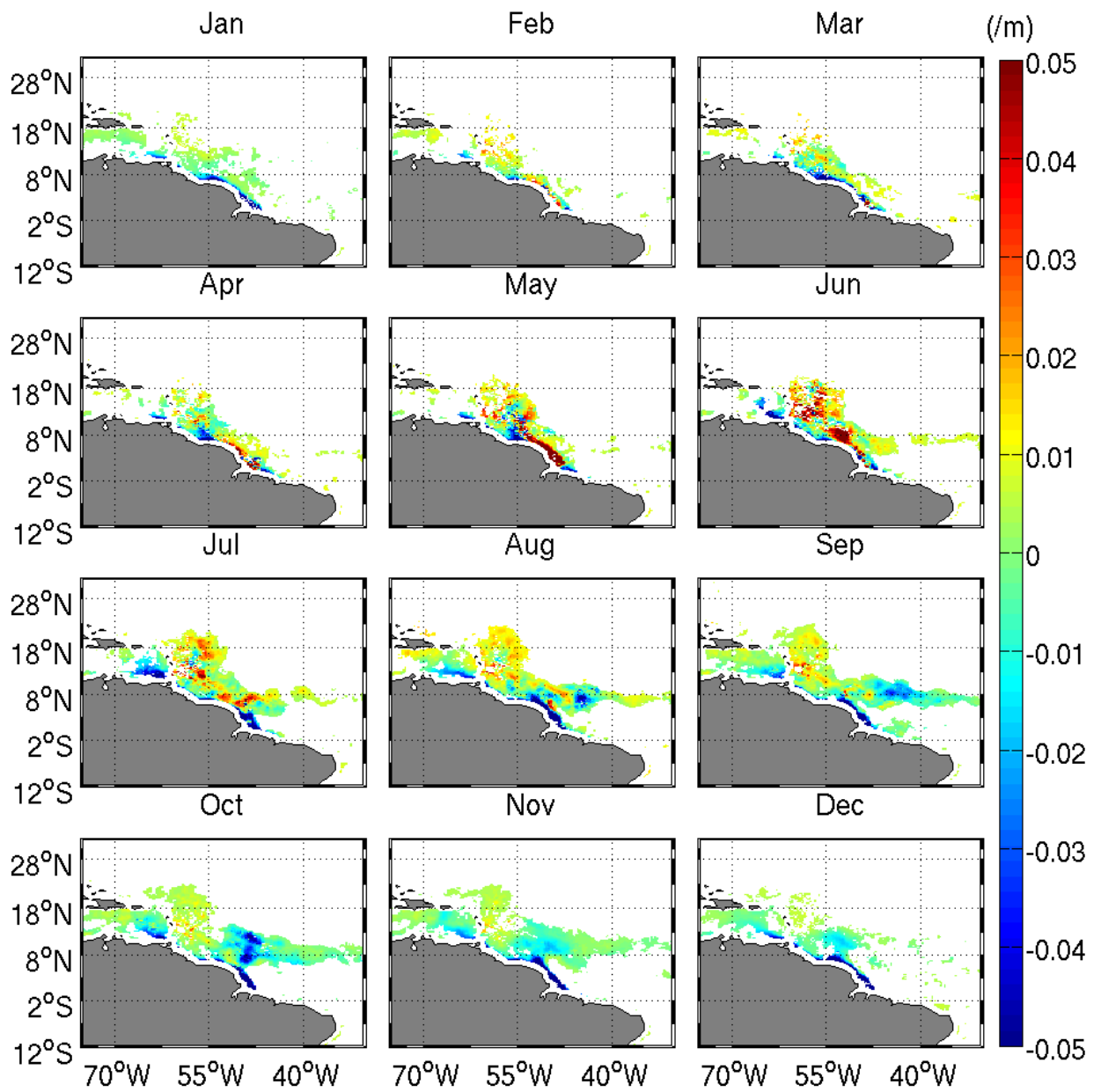


Figure 4.32: 2013 monthly maps of 25-km differences between a_{cdm} estimated from the monthly 2010-2013 SSS/ a_{cdm} relationship and GlobColour a_{cdm} in the Amazon plume.

Chapter 4. The Relationship Between Sea Surface Salinity and Optical Properties in the Amazon Plume Region

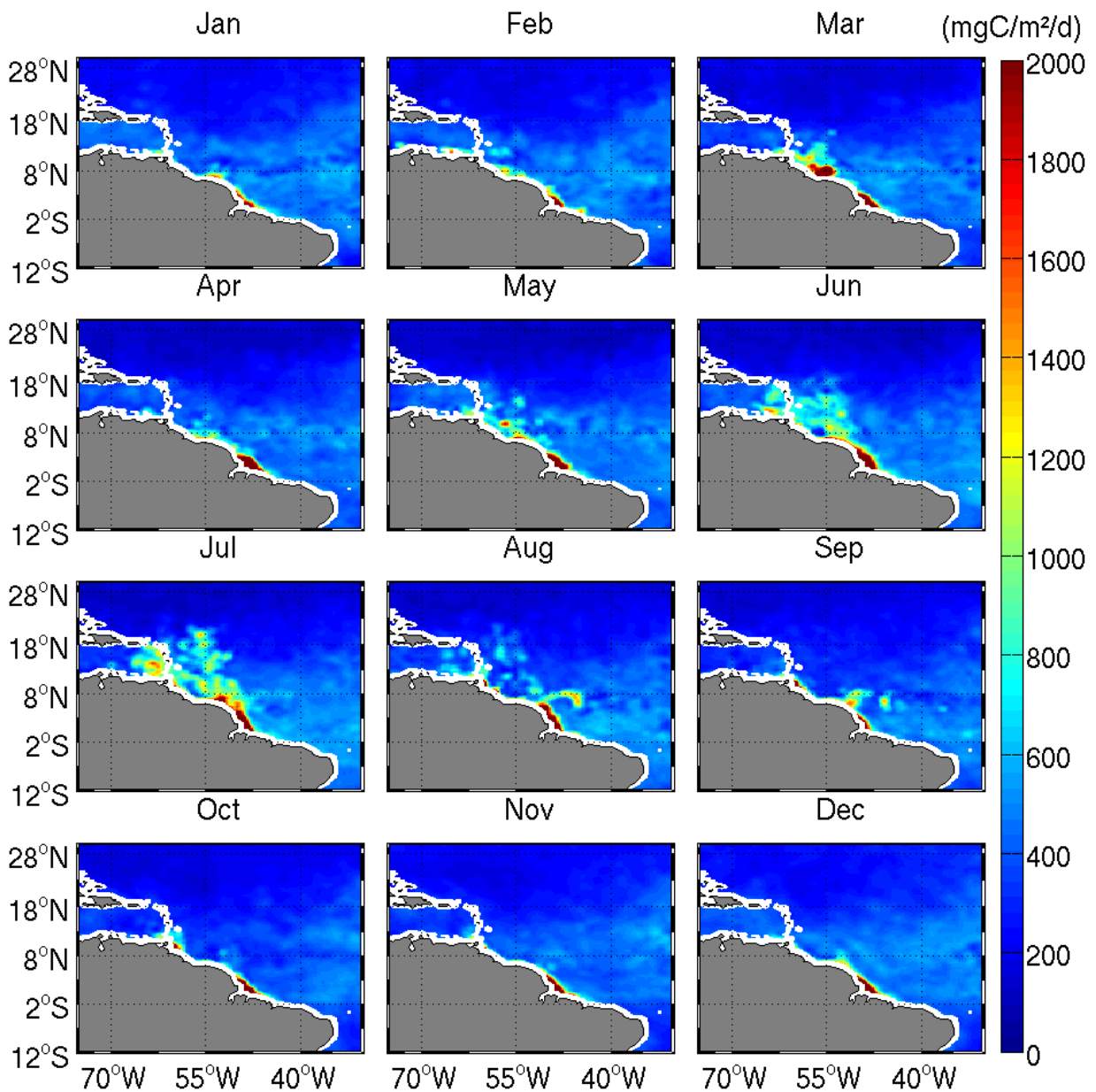


Figure 4.33: 2010 monthly maps of 25-km net primary productivity in the Amazon plume.

4.2. A Regional Approach using a Conservative Mixing model

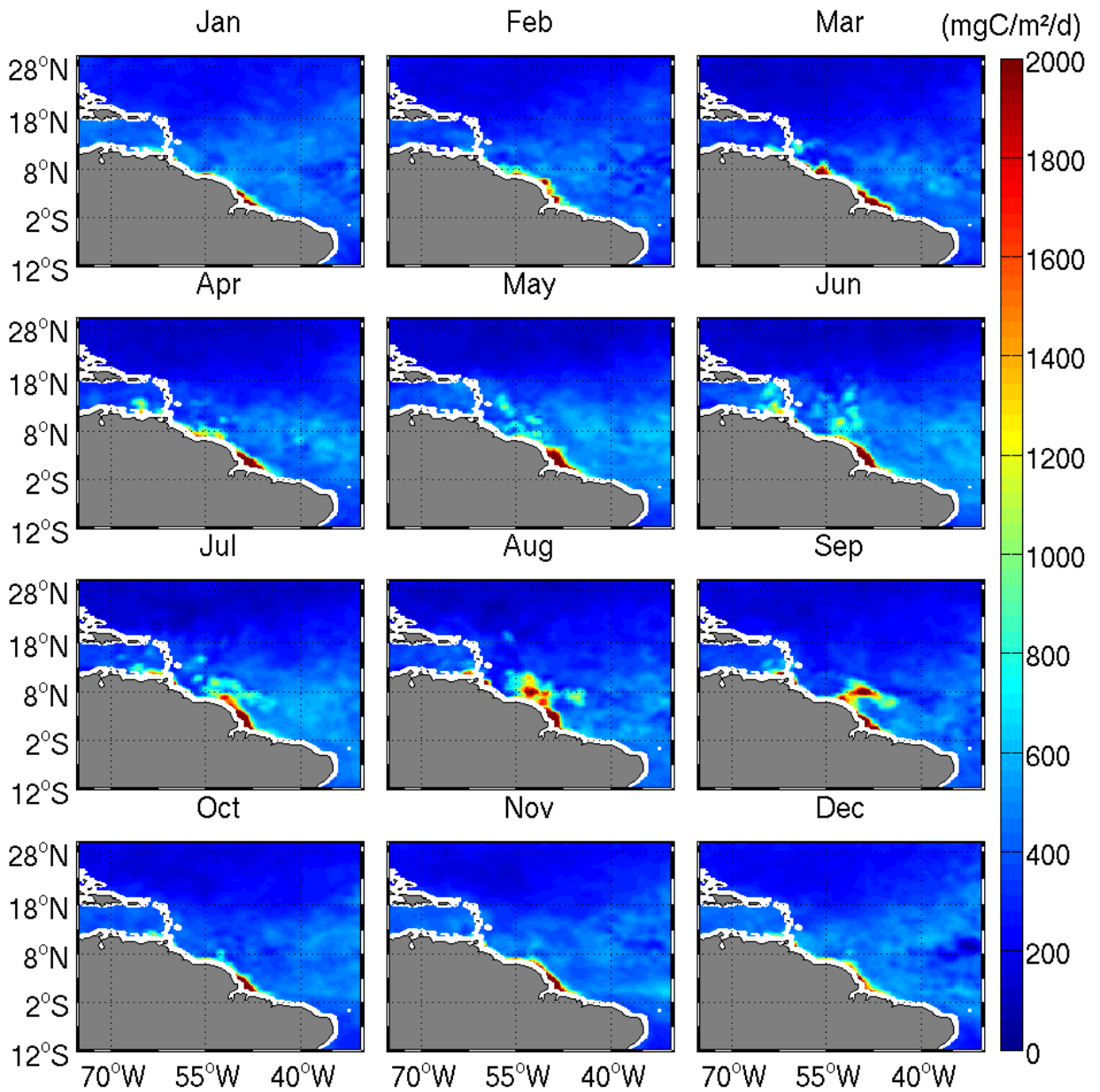


Figure 4.34: 2011 monthly maps of 25-km net primary productivity in the Amazon plume.

Chapter 4. The Relationship Between Sea Surface Salinity and Optical Properties in the Amazon Plume Region

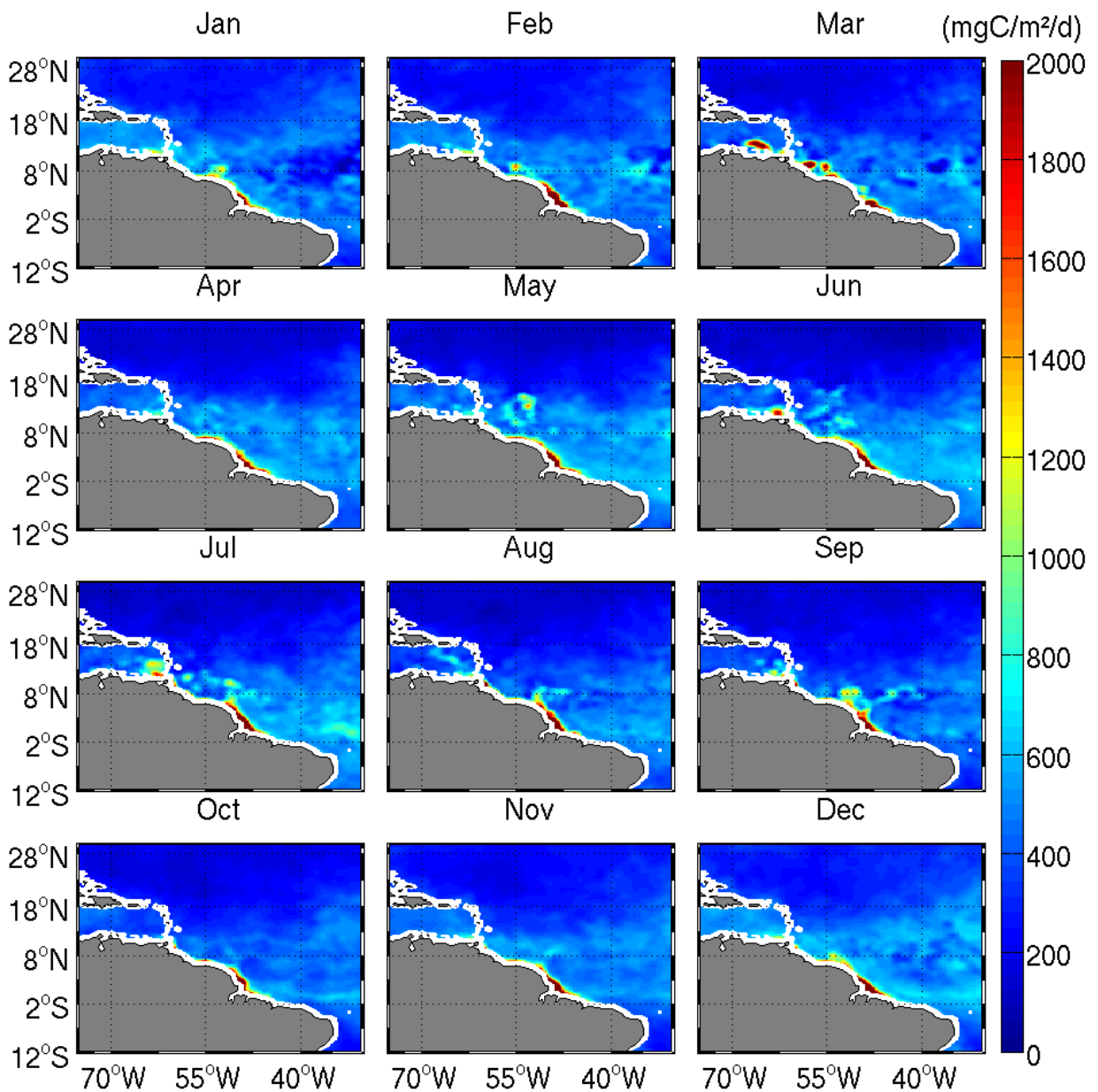


Figure 4.35: 2012 monthly maps of 25-km net primary productivity in the Amazon plume.

4.2. A Regional Approach using a Conservative Mixing model

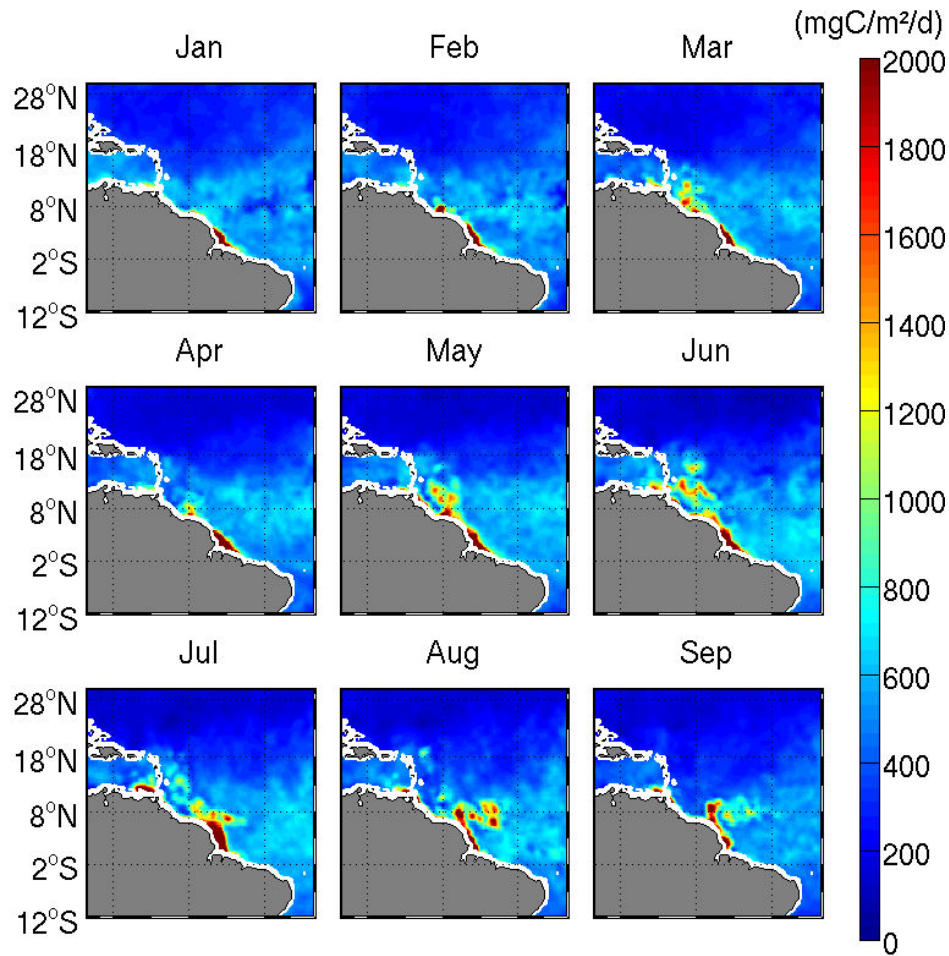


Figure 4.36: 2013 monthly maps of 25-km net primary productivity in the Amazon plume (data are only available until September 2013).

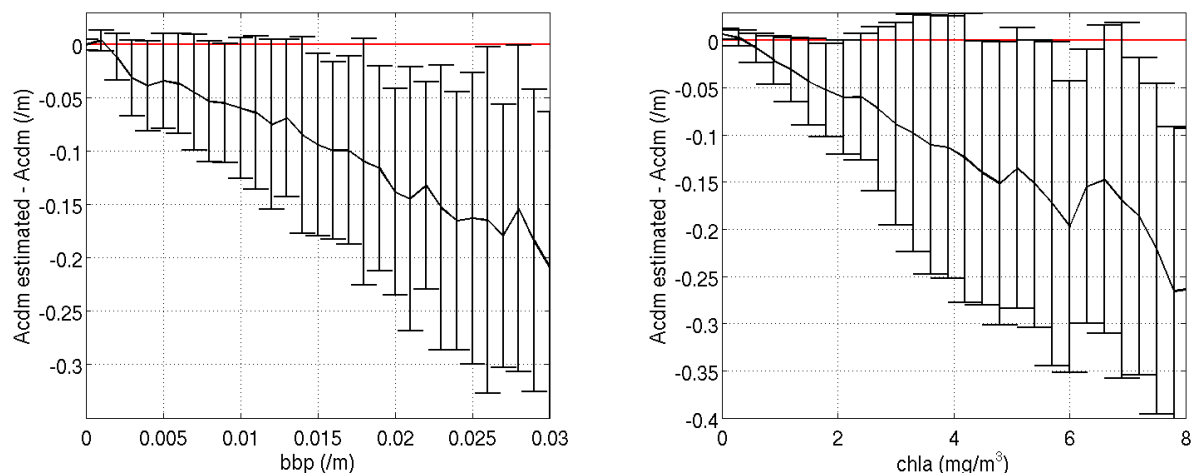


Figure 4.37: Anomalies between estimates of a_{cdm} from the 2010-2013 monthly SSS/ a_{cdm} relationships and GlobColour a_{cdm} per bins of 0.001 /m of particulate backscattering coefficient (left) and of 0.3 mg/m³ of chlorophyll-a (right).

Chapter 4. The Relationship Between Sea Surface Salinity and Optical Properties in the Amazon Plume Region

Conclusions :

- Regional coherence between sea surface salinity and a_{cdm}
- Seasonal variabilities in the conservative mixing
- No noticeable spatial variabilities in the conservative mixing
- Non conservative behaviours in the relationship highlighted at a precise time and location (northwestern part of the plume in summer 2010)

4.3 A Local Approach of the Conservative Mixing

The previous approach of the conservative mixing, a regional approach, can be discussed. This large scale vision of the relationship between SSS and a_{cdm} implies the mixing of plume waters discharged at different periods of the year and which were advected along different pathways. These water masses, thus, may have different original characteristics and they may have encountered different water masses. Accordingly, they may undergo different dilution processes ones from the others.

In this section, we decided to analyze the SSS/ a_{cdm} relationship locally, at each pixel. We first study the correlations between time series of SSS and a_{cdm} over 2010-2013, locally. We then attempt to establish a local relationship between SSS and a_{cdm} for each $0.25 \times 0.25^\circ$ pixel in the Amazon plume.

4.3.1 Correlations between SSS and optical properties

As often reported, sea surface salinity and optical properties in the Amazon plume are strongly negatively correlated. The annual correlations over 2010-2013 between SSS and ocean color parameters, such as a_{cdm} , the light attenuation at 490 nm (K490), particulate backscattering coefficient (b_{bp}), total suspended matter (TSM), chlorophyll-a (chl_a) and net primary productivity (npp) are represented in figure 4.38. For each node of the $0.25 \times 0.25^\circ$ grid, the correlation between SSS and ocean color time series is computed. On the right, only pixels for which the p-value (significance of the SSS/ a_{cdm} correlation) is below 0.01 are shown. As expected, a strong negative correlation (below -0.5) between SSS and a_{cdm} is obtained inside the river plume delimited by the average 35.5 pss contour. The largest negative correlations between SSS and a_{cdm} (below -0.95) are found in the eastern part of the plume, area delimited by a black solid line. Strong negative correlations (below -0.85) are also found outside of the average plume contour, delimited by a black solid line. As the extension of the plume varies from year to year, these strong negative correlations can indeed occur outside the average plume contour. In figure 4.39, are represented the July 2010, 2011, 2012 and 2013 monthly maps of SSS and a_{cdm} on top of which is drawn the -0.85 correlation contour computed outside the average plume between SSS and a_{cdm} . Only during summer 2011, the plume reaches this area, which has also been observed by Aquarius (Grotsky et al. [2014]). On figure 4.40, from Grotsky et al. [2014], are represented the SSS anomaly patterns between September 2011 and September 2012, from Aquarius and SMOS. These observations confirm the salinity increase over the plume area located northwest off the NBC retroreflection from 2011 to 2012.

Chapter 4. The Relationship Between Sea Surface Salinity and Optical Properties in the Amazon Plume Region

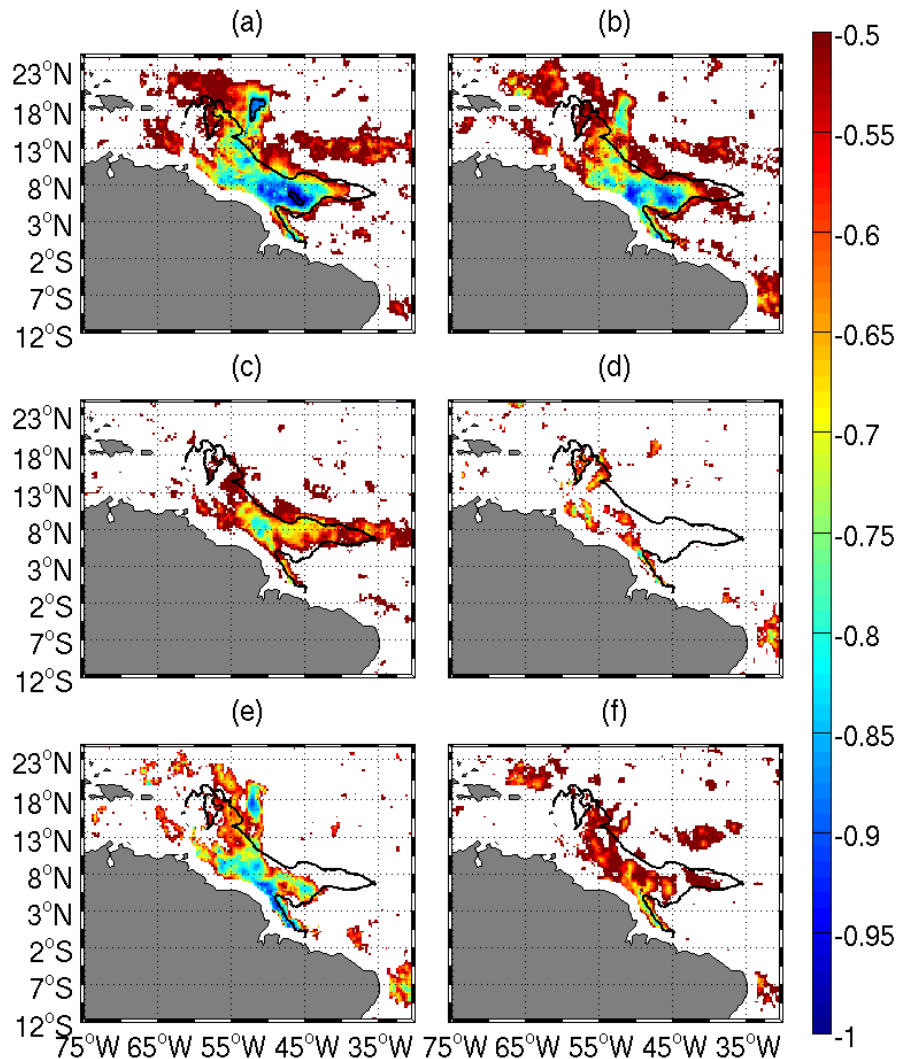


Figure 4.38: Correlations between SSS and (a) a_{cdm} ; (b) K490 ; (c) b_{bp} ; (d) TSM ; (e) chl_a ; (f) npp over 2010-2013 for each 0.25x0.25° pixel. Only pixels for which the p-value is below 0.01 are shown. Areas with highest correlations (below -0.95 and below -0.85) are delimited by black solid lines in the eastern part of the plume and north of the plume, in a, respectively. 2010-2013 average 35.5 pss contour is represented as a solid black line.

Inside the plume, negative correlations are also found between SSS and b_{bp} (around -0.3). Between SSS and TSM, few correlations around -0.3 are obtained but not in the eastern part of the plume, where there shouldn't be suspended matter from the Amazon river anymore, they already sank. No noticeable negative correlations are obtained between SSS and net primary productivity in the plume area.

Negative correlations are obtained between SSS and chl_a inside the Amazon plume (up to -0.75), correlations lower than with a_{cdm} . It is consistent with the fact that CDOM is a better indicator than chlorophyll to trace sea surface dilution by river plumes, which

4.3. A Local Approach of the Conservative Mixing

has been shown by [Hu et al. \[2003\]](#) and discussed in the previous chapter.

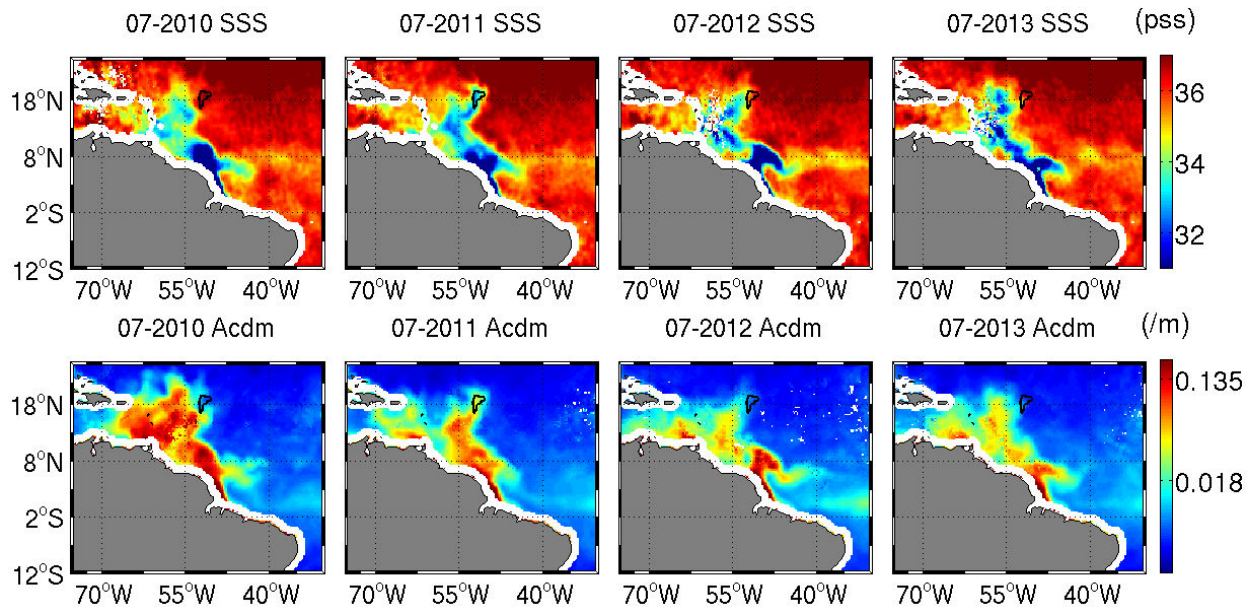


Figure 4.39: From left to right 2010, 2011, 2012 and 2013 July SSS (top) and a_{cdm} (bottom). As a black solid line is represented the area of high correlation found in the north outside of the plume

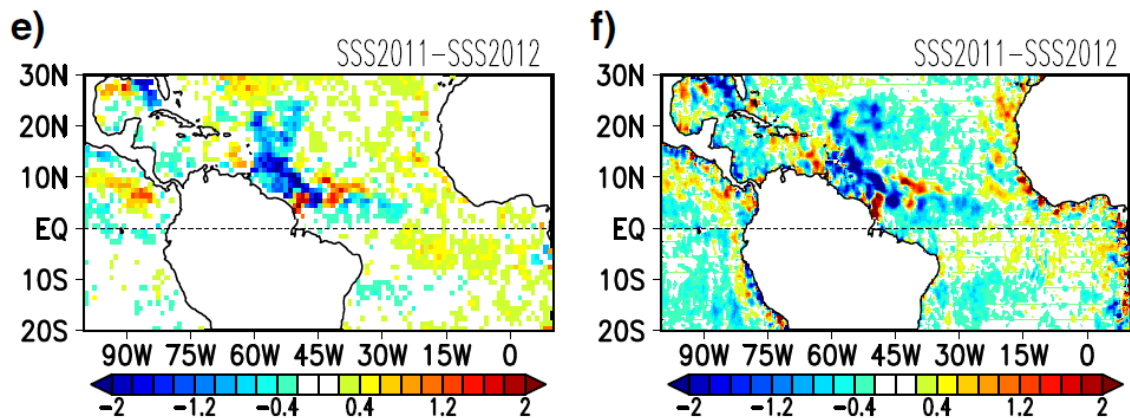


Figure 4.40: Aquarius (e) and SMOS (f) differences between averaged SSS over September 2011 and 2012. Figure from [Grotsky et al. \[2014\]](#).

In the Amazon plume area, sea surface salinity and optical properties further exhibit a seasonal cycle in accordance with the Amazon river discharge cycle. Once per year, as Amazon waters reach a given ocean area, SSS locally drops below 35.5 ps and the a_{cdm} increases. Monthly time series of sea surface salinity and a_{cdm} at locations [6.5°N 46°W], [14°N 55°W] and [19°N 51.5°W] are shown, in figure 4.42.a .b and .c. The [6.5°N 46°W] pixel (marked as a black dot) belongs to the eastern area of high correlation between SSS

Chapter 4. The Relationship Between Sea Surface Salinity and Optical Properties in the Amazon Plume Region

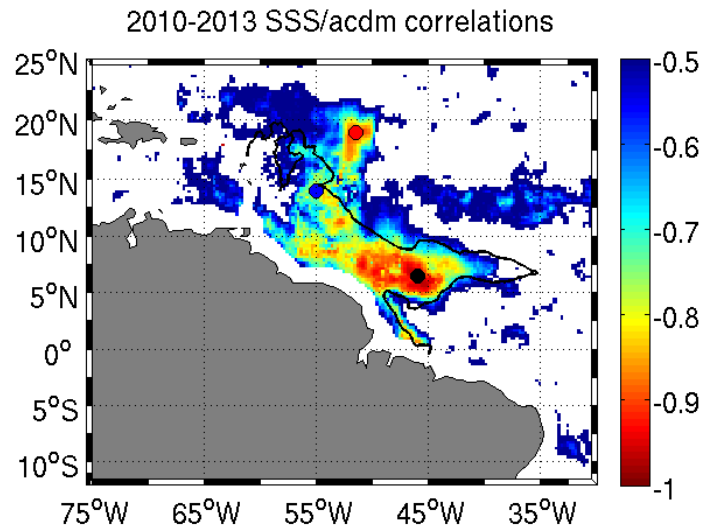


Figure 4.41: Correlations between SSS and a_{cdm} for each $0.25 \times 0.25^\circ$ pixel. Only pixels for which the p-value is below 0.01 are shown. The black, blue and red dots are representing the pixels with coordinates : $[6.5^\circ\text{N } 46^\circ\text{W}]$, $[14^\circ\text{N } 55^\circ\text{W}]$ and $[19^\circ\text{N } 51.5^\circ\text{W}]$, respectively. The black thick line represents the average plume contour delimited by the 35.5 pss contour.

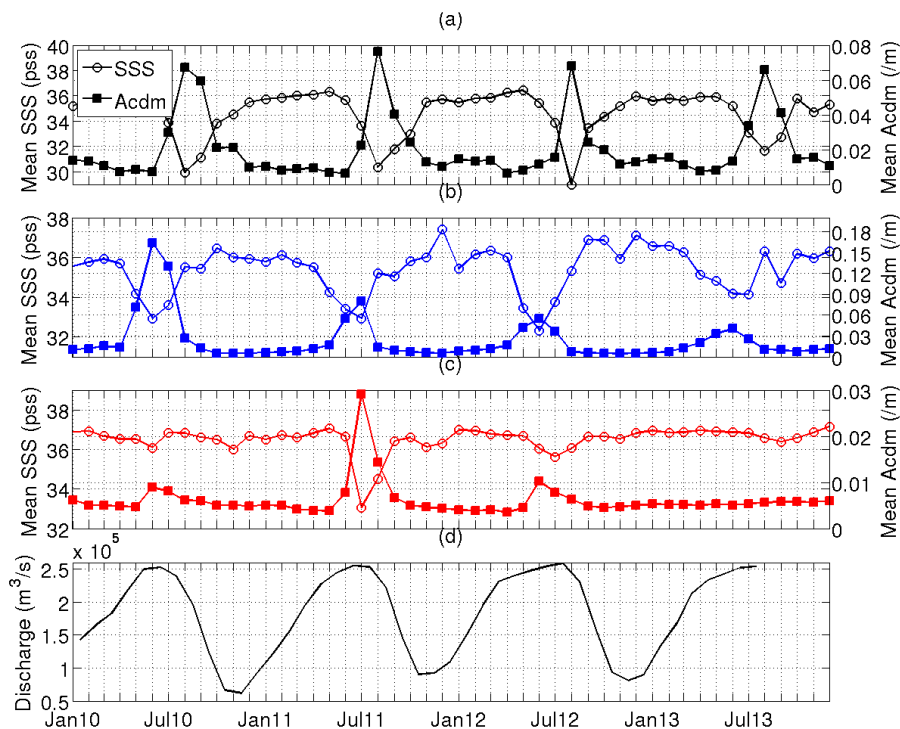


Figure 4.42: Time series of the monthly mean SSS (circles) and the monthly mean a_{cdm} (squares) computed at locations (a) $[6.5^\circ\text{N } 46^\circ\text{W}]$, (b) $[14^\circ\text{N } 55^\circ\text{W}]$ and (c) $[19^\circ\text{N } 51.5^\circ\text{W}]$ shown by the black, blue and red dots, respectively, in figure 4.41 ; (d) time series of the monthly Amazon discharge at Obidos gauge.

4.3. A Local Approach of the Conservative Mixing

and a_{cdm} over 2010-2013 (below -0.95). The [14°N 55°W] pixel (marked as a blue dot) belongs to the northwestern part of the plume. The [19°N 51.5°W] pixel (marked as a red dot) belongs to the area outside of the average plume exhibiting a strong negative correlation between SSS and a_{cdm} (below -0.85).

As shown in figure 4.42.a, the monthly SSS and a_{cdm} in the eastern part of the plume, exhibit a marked seasonal cycle. The SSS evolves between approximately 30-31 pss, in August, and 36 pss, from February to May. The monthly mean a_{cdm} , in this area, evolves between 0.01 /m, during winter and spring, and 0.06-0.08 /m, in August.

In the northwestern part of the plume, the SSS evolves between approximately 32-33 pss, in June-July, and 36-37 pss, from October to April (see figure 4.42.b). The monthly mean a_{cdm} peaks in June-July when the minimum SSS is reached.

Outside the average plume, there is no seasonal cycle (see figure 4.42.c). SSS is quasi constant, around 36-37 pss and a_{cdm} , around 0.005-0.01 /m. Only one event in July 2011 occurs, during which SSS drops to 33 pss while a_{cdm} increases to 0.03 /m.

For the three locations studied here, the time phase (in months) between SSS and a_{cdm} corresponds to zero. In figure 4.43, the correlations between SSS and a_{cdm} over 2010-2013 at the three locations are represented as black, blue and red lines, respectively, applying a time lag of -6 to +6 months on the a_{cdm} signal. The correlation is maximum (around -0.8) considering a time lag of zero between both signals. Globally, figure 4.44 indicates time phase between SSS and a_{cdm} for each 0.25x0.25° pixel. The time lag corresponds to zero for the whole area reached by the plume.

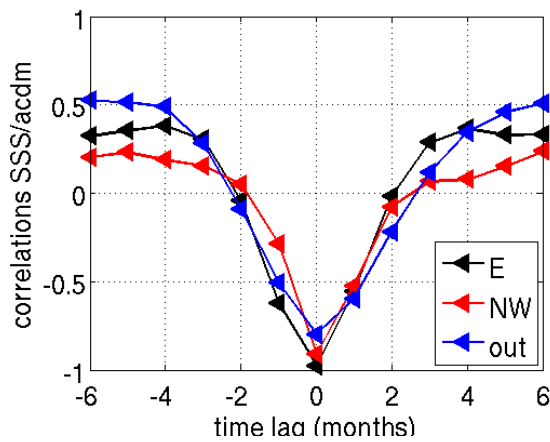


Figure 4.43: Correlations between the time series of the mean SSS and a_{cdm} considering an offset from -6 to +6 months on the a_{cdm} signal, at locations (black) [6.5°N 46°W], (blue) [14°N 55°W] and (red) [19°N 51.5°W], pointed out by dots in figure 4.41.

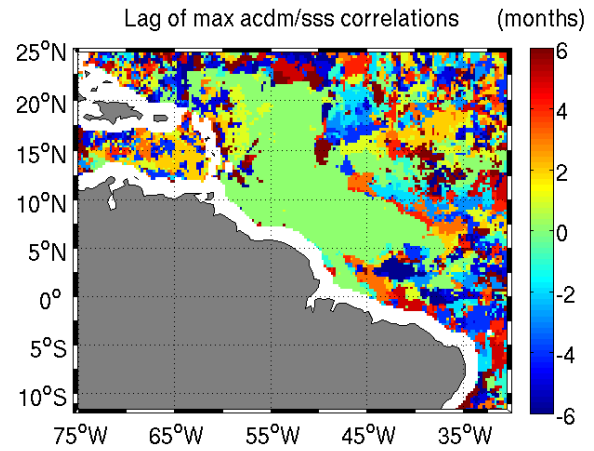


Figure 4.44: Time phase in months between SSS and a_{cdm} over 2010-2013 for each 0.25x0.25° pixel.

4.3.2 SSS and optical properties correlations with the Amazon discharge

At the Obidos gauge, the Amazon discharge is maximum around June-July with a discharge of about $2.5 \cdot 10^5 \text{ m}^3/\text{s}$, and it is minimum around October-November with a discharge of approximately $0.5\text{-}1 \cdot 10^5 \text{ m}^3/\text{s}$ (see figure 4.42.d). Both SSS and a_{cdm} signals are correlated to the Amazon discharge cycle. The time lag between the Amazon discharge maximum and the SSS minimum or a_{cdm} maximum, depends on the area of the Amazon plume. Figure 4.45 represents the correlation between SSS and the Amazon discharge (figure 4.45.a) and a_{cdm} and the Amazon discharge (figure 4.45.b) considering a time lag from 0 to 6 months on the discharge signal.

In the eastern area of the plume, lags of about 2-3 months are found between the maximum discharge level and the minimum SSS or the maximum a_{cdm} (see figure 4.42.a and .d). As found (see figure 4.45), the correlations are maximum, around -0.7, for a time lag of 3 months.

In the northwestern part of the plume, the signals are correlated, around -0.6, with no time lag (see figure 4.42.b and .d and figure 4.45). The Amazon fresh waters must rapidly reach this area to influence the ambient sea surface properties.

4.3. A Local Approach of the Conservative Mixing

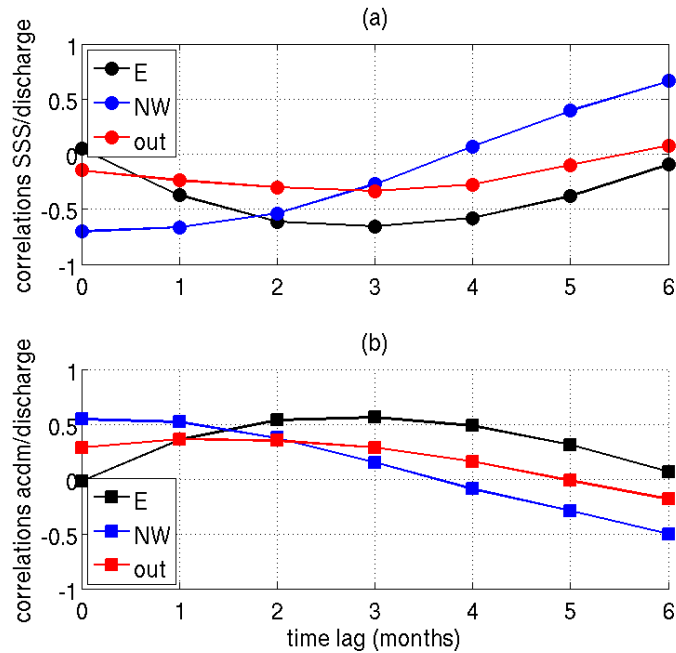


Figure 4.45: Correlations between (a) the time series of the mean SSS and the Amazon discharge at Obidos ; (b) between the time series of the mean a_{cdm} and the Amazon discharge at Obidos, considering an offset from +0 to +6 months on the discharge signal, at locations (black) [6.5°N 46°W], (blue) [14°N 55°W] and (red) [19°N 51.5°W], pointed out by dots in figure 4.41.

4.3.3 Advection of the Amazon plume

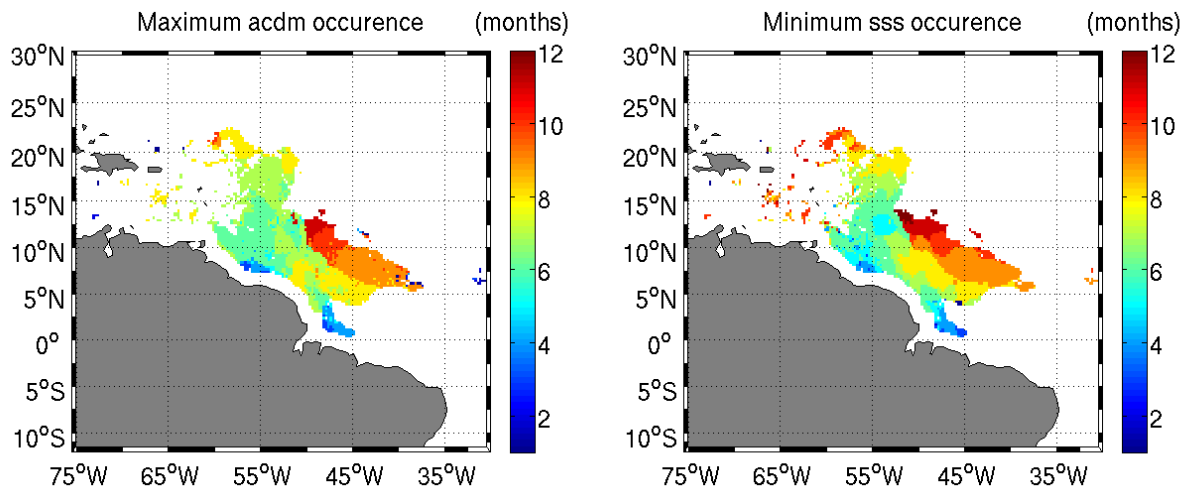


Figure 4.46: Time of the year in months for which the a_{cdm} maximum (left) and the SSS minimum (right) occur for each $0.25 \times 0.25^\circ$ pixel. Only pixels in the plume for which the p-value is below 0.01 and the time lag between the SSS minimum and a_{cdm} maximum is zero are shown.

In the eastern part of the plume, the a_{cdm} maximum and SSS minimum occur in August,

Chapter 4. The Relationship Between Sea Surface Salinity and Optical Properties in the Amazon Plume Region

they occur in June in the northwestern part of the plume (see figure 4.42.a and .b). More generally (see figure 4.46), the signal extrema occur around April next to the Amazon mouth, as soon as the Amazon discharge gets high, around June-July in the northwestern part of the plume and up to August-October in the northern areas. In the retroreflection region of the North Brazilian Current (NBC), they occur in August and up to September-October in the northeastern part of the plume. The dispersal of the Amazon plume varies along the year principally due to the external physical forcing sources. During the boreal winter and spring seasons, as the discharge level is low, the Amazon plume waters accumulate in the vicinity of the mouth due to northeastern trade wind events (Muller-Karger et al. [1988] ; Muller-Karger et al. [1995]). In late spring, as the discharge level gets high, Amazon waters flow northwestward along the Brazilian shelf up to the Caribbean sea when the wind relaxes and then reverses. In summer-early fall, when the North Equatorial Counter Current develops, the river plume is carried eastward through the North Brazilian Current retroreflection (Muller-Karger et al. [1988] ; Muller-Karger et al. [1995]).

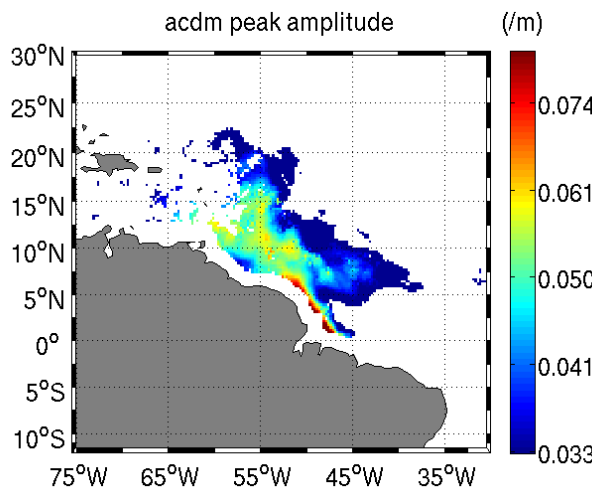


Figure 4.47: Amplitude of the a_{cdm} maximum for each $0.25 \times 0.25^\circ$ pixel. Only pixels in the plume for which the p-value is below 0.01 and the time lag between the SSS minimum and a_{cdm} maximum is zero are shown.

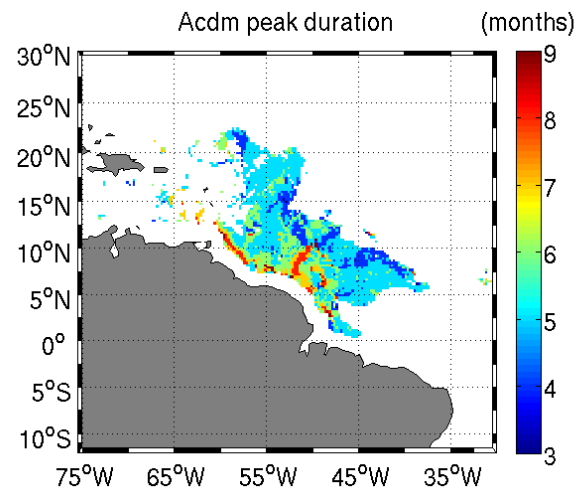


Figure 4.48: Duration of the a_{cdm} maximum for each $0.25 \times 0.25^\circ$ pixel. Only pixels in the plume for which the p-value is below 0.01 and the time lag between the SSS minimum and a_{cdm} maximum is zero are shown.

The amplitude of the SSS minimum and a_{cdm} maximum relative to the "open ocean" SSS and a_{cdm} values varies from a region to another. In figure 4.47, the amplitude of the maximum of the 2010-2013 monthly a_{cdm} time series are computed for each pixel. This amplitude is higher next to the Amazon mouth, around 0.5 /m and lower at the edges of the plume, where it drops to around 0.003 /m.

4.3. A Local Approach of the Conservative Mixing

The event duration time (in months) has also been computed around the month for which the a_{cdm} maximum occurs (see figure 4.48). To compute this duration time, from the maximum month occurrence in each pixel, backward and forward, we found the time for which a_{cdm} decreases below 80 per cent of the amplitude of the maximum. The event duration is defined as the maximum between the backward and forward duration times. Next to the mouth and northward along the Brazilian shelf, the duration is almost continuous between 10 and 12 months, as the plume is present in these areas almost all year long. The plume is only detected less than 6 months per year in general at the northern edges of the domain exhibiting high correlation between SSS and a_{cdm} .

Once the month of the year for which the maximum a_{cdm} occurs and the duration of this peak are found for each pixel, it gives the information of the period of the year during which the plume is present for each pixel (the month for which there is the a_{cdm} maximum \pm half the duration time in months). We can then map the evolution of the extension of the plume (see figure 4.49). For each pixel, months during which plume waters are present have been determined, accordingly, the seasonal variability of the plume presence in the northwestern tropical Atlantic ocean can be mapped. At the beginning of the year, as the Amazon discharge is low and northeastern trade winds are strong, plume waters stay in the vicinity of the mouth. As trade winds relax, plume waters extend along the Brazilian shelf northward to spread largely northward in May. In June, as the North Equatorial Counter Current strengthens and as the retroreflection appears, the plume extends eastward. The plume starts to vanish northward in September and eastward in November. This is in accordance with the well-known Amazon plume waters seasonal extension, often reported.

Chapter 4. The Relationship Between Sea Surface Salinity and Optical Properties in the Amazon Plume Region

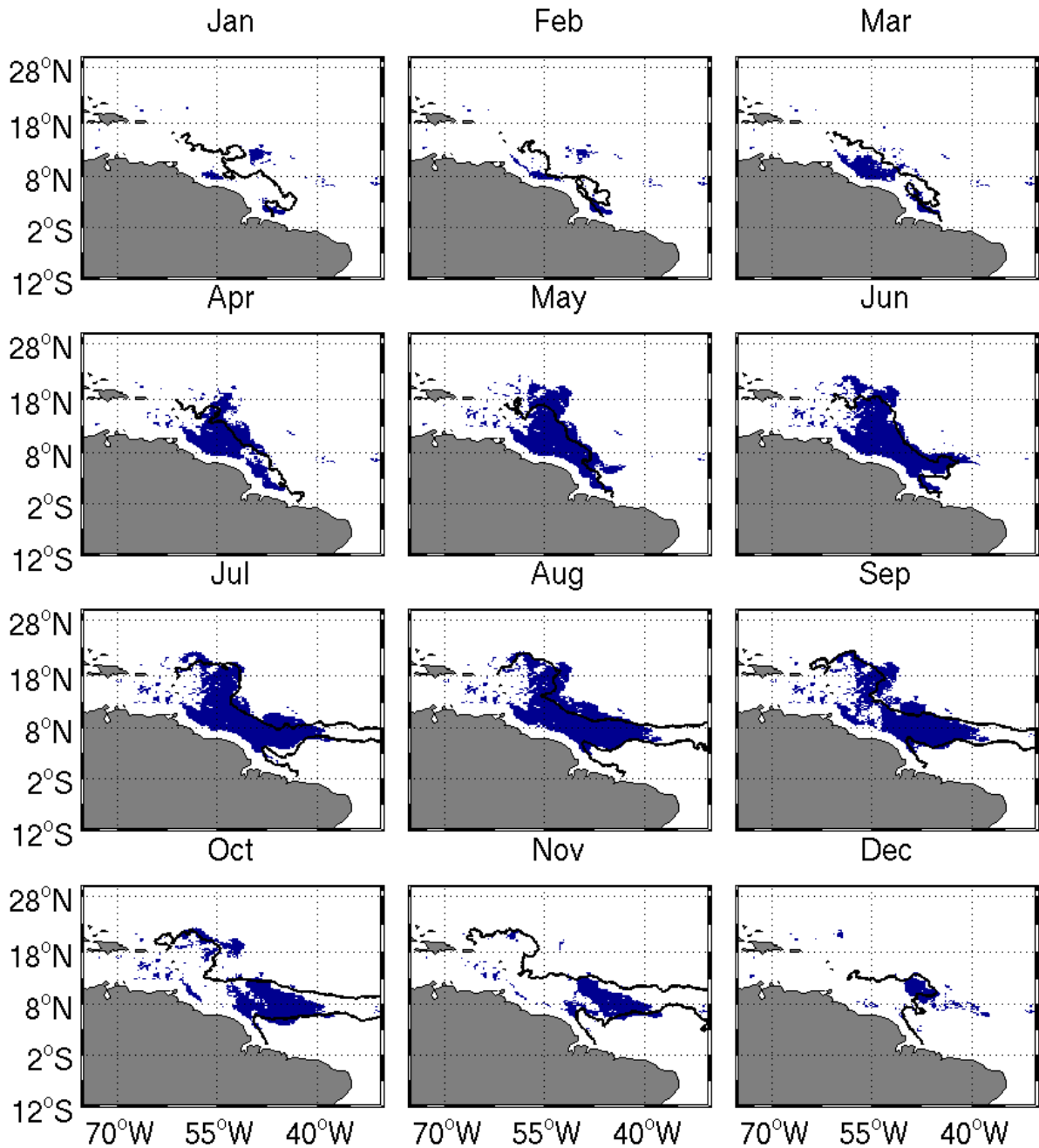


Figure 4.49: Seasonal evolution of the Amazon plume extension. Every month, the $0.25 \times 0.25^\circ$ pixels reached by the plume (months during which the a_{cdm} peak occurs for each pixel) are colored in blue. As a black solid line is represented the average 2010-2013 plume contour.

4.3.4 The Conservative Mixing in the Amazon Plume

Given the temporal and spatial coherence between SSS and a_{cdm} in the Amazon plume, we can reinvestigate the local conservative mixing dependencies.

4.3. A Local Approach of the Conservative Mixing

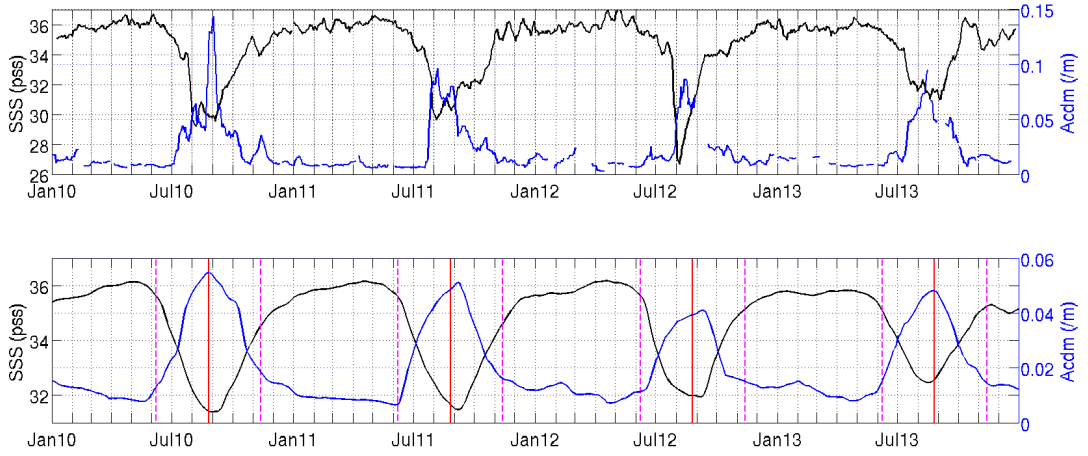


Figure 4.50: Time series of a_{cdm} (black) and SSS (blue) over 2010-2013 at location [6.5°N 46°W] (marked by a black dot in figure 4.41). On the top panel are represented the series at 10 days daily running mean temporal resolution and on the bottom panel, the time series filtered using a daily ± 45 days. As a red line is marked the occurrence of the maximum of a_{cdm} and the magenta dotted lines delimit the duration of the a_{cdm} peak.

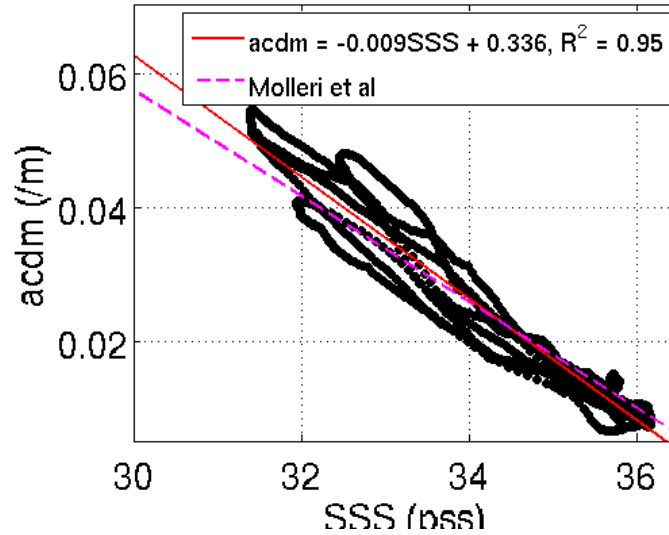


Figure 4.51: 25-km 90-day running mean a_{cdm} as a function of 25-km 90-day running mean SMOS SSS over 2010-2013 at location [6.5°N 46°W], marked by a black dot in figure 4.41. As a red solid line is represented the linear regression computed for that pixel over 2010-2013. As a magenta dotted line is represented the [Molleri et al. \[2010\]](#) linear model.

For each $0.25 \times 0.25^\circ$ pixel, the 2010-2013 25-km 10-day running mean a_{cdm} signal being noisy, both SSS and a_{cdm} signals are filtered using a daily ± 45 -day running mean. In figure 4.50, the unfiltered (top panel) and filtered (bottom panel) time series are represented for the pixel [6.5°N 46°W], corresponding to the black dot in figure 4.41. The

Chapter 4. The Relationship Between Sea Surface Salinity and Optical Properties in the Amazon Plume Region

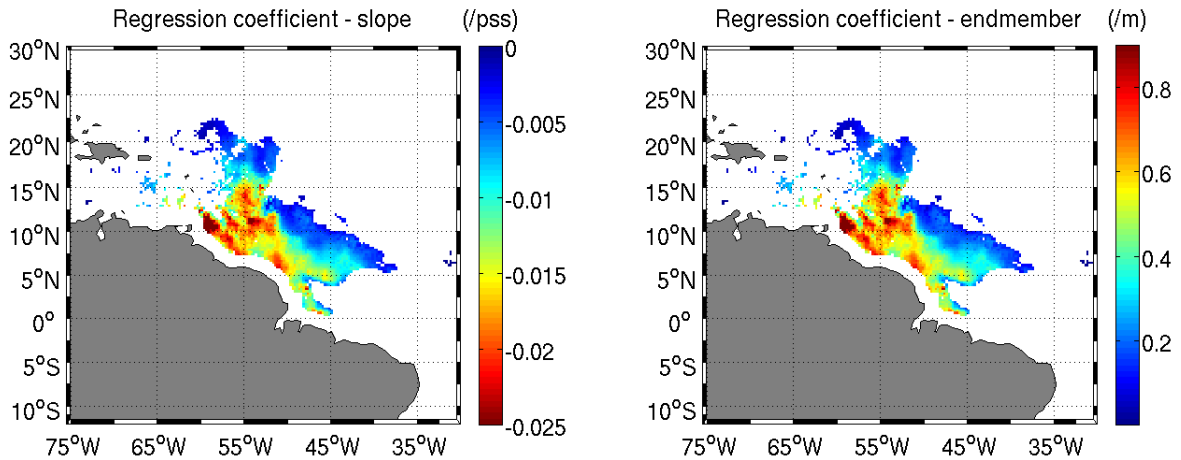


Figure 4.52: Slope (left) and endmember (right) of the linear regression between the time series of filtered SSS and a_{cdm} for each $0.25 \times 0.25^\circ$ pixel over 2010-2013.

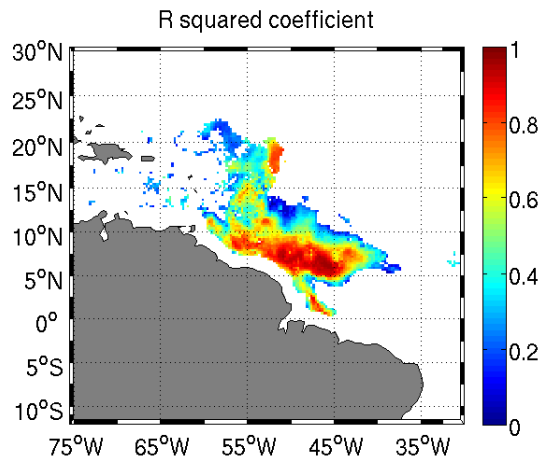


Figure 4.53: R squared coefficient of the linear regression between the time series of filtered SSS and a_{cdm} for each $0.25 \times 0.25^\circ$ pixel over 2010-2013.

linear regression is then evaluated for each pixel between SSS and a_{cdm} over 2010-2013. The regression is computed only for pixels in the plume for which the p-value (significance of the SSS/ a_{cdm} correlation) is below 0.01 and the time lag between the SSS minimum and a_{cdm} maximum is zero (see figure 4.44). In figure 4.51, the linear regression over the filtered SSS and a_{cdm} time series is represented. On this figure is also represented the linear model computed by Molleri et al. [2010] which doesn't retrieve well the linear correlation between SSS and a_{cdm} in this pixel. Figure 4.52, on the left, provides the map of the slope coefficient. The endmember map (see figure 4.52, on the right) displays the same patterns than the slope one. Over the whole region, the slope, and thus the endmember can significantly vary, as high in the northwestern part of the plume, around -0.02 for

4.3. A Local Approach of the Conservative Mixing

the slope and 0.7 for the endmember values, to low in the eastern part of the plume and next to the mouth, around -0.01 for the slope and 0.4 for the endmember values. In other words, in the eastern part of the plume and next to the mouth, for a given SSS value, a_{cdm} is lower and decreases slower. Amazon waters reaching the eastern part are still fresh but apparently clearer than those reaching the northwestern part of the plume. These waters have generally been exposed to air-sea exchanges over longer periods, as advected over larger distances from the source.

Amazon waters apparently keep homogeneously their identity over the whole basin for the entire year. Yet, as demonstrated, the conservative mixing relationship evolves as a space-time mapping of the seasonal circulation.

Figure 4.53, represents the R squared coefficient of the linear regression. Close to the coast and in the eastern part of the plume, the R-squared coefficient is high, thus there is a strong linear correlation between SSS and a_{cdm} . However, in the northwestern part of the plume, SSS and a_{cdm} are highly correlated but the R-squared coefficient of the linear regression is quite low. In this part of the plume, SSS and a_{cdm} are not linearly well-correlated.

4.3.5 Non conservative behaviours of the conservative mixing

We have seen that deviations from the conservative mixing can occur due to biogeochemical processes such as primary productivity, photobleaching, flocculation... As in the section 4.2, we attempt here to study such non conservative behaviours, using the local conservative mixing relationships established as a reference here.

The reconstruction of an a_{cdm} product based on SMOS SSS can now be straightforwardly applied using these local conservative mixing relationships established in the Amazon plume region. 25-km monthly SMOS SSS composites are used to obtain 25-km monthly maps of a_{cdm} . These retrieved composites are then used to obtain anomalies from the conservative mixing computed as the monthly differences between the retrieved a_{cdm} and the GlobColour a_{cdm} products.

Figures 4.54 to 4.57 represent the monthly maps of the anomalies between GlobColour and retrieved a_{cdm} in 2010, 2011, 2012 and 2013. As a comparison with the method established in the section 4.2, the anomalies are lower (see figures 4.29 to 4.32).

During half the year, from October to March, anomalies are quite low (<0.01 in absolute value) over the whole plume area. As an overall, significant anomaly patterns are only noticeable during May through July 2010, as already highlighted in the section 4.2. Indeed, important negative anomalies (<-0.05) are found in the northwestern part of the

Chapter 4. The Relationship Between Sea Surface Salinity and Optical Properties in the Amazon Plume Region

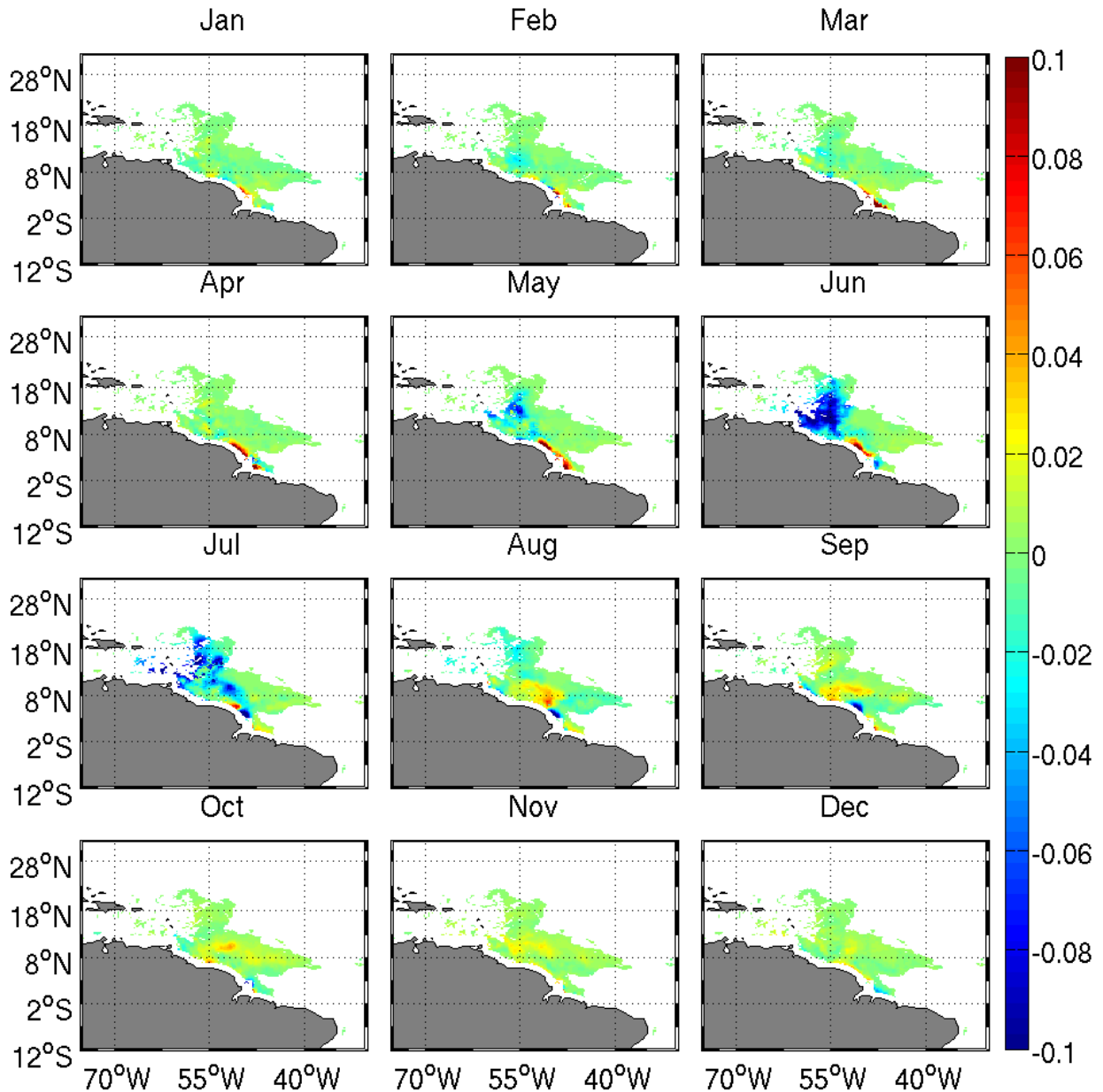


Figure 4.54: 2010 monthly maps of 25-km differences between a_{cdm} estimated from the monthly 2010-2013 SSS/a_{cdm} relationship and GlobColour a_{cdm} in the Amazon plume.

plume. As done in the section 4.2, these negative anomaly patterns can be set against highly productive areas (see figure 4.33). In June 2011, in the northwestern part of the plume, negative anomalies are also found in the northwestern part of the plume, to a lesser extent, and can also be set against productive areas (see figure 4.34).

4.3. A Local Approach of the Conservative Mixing

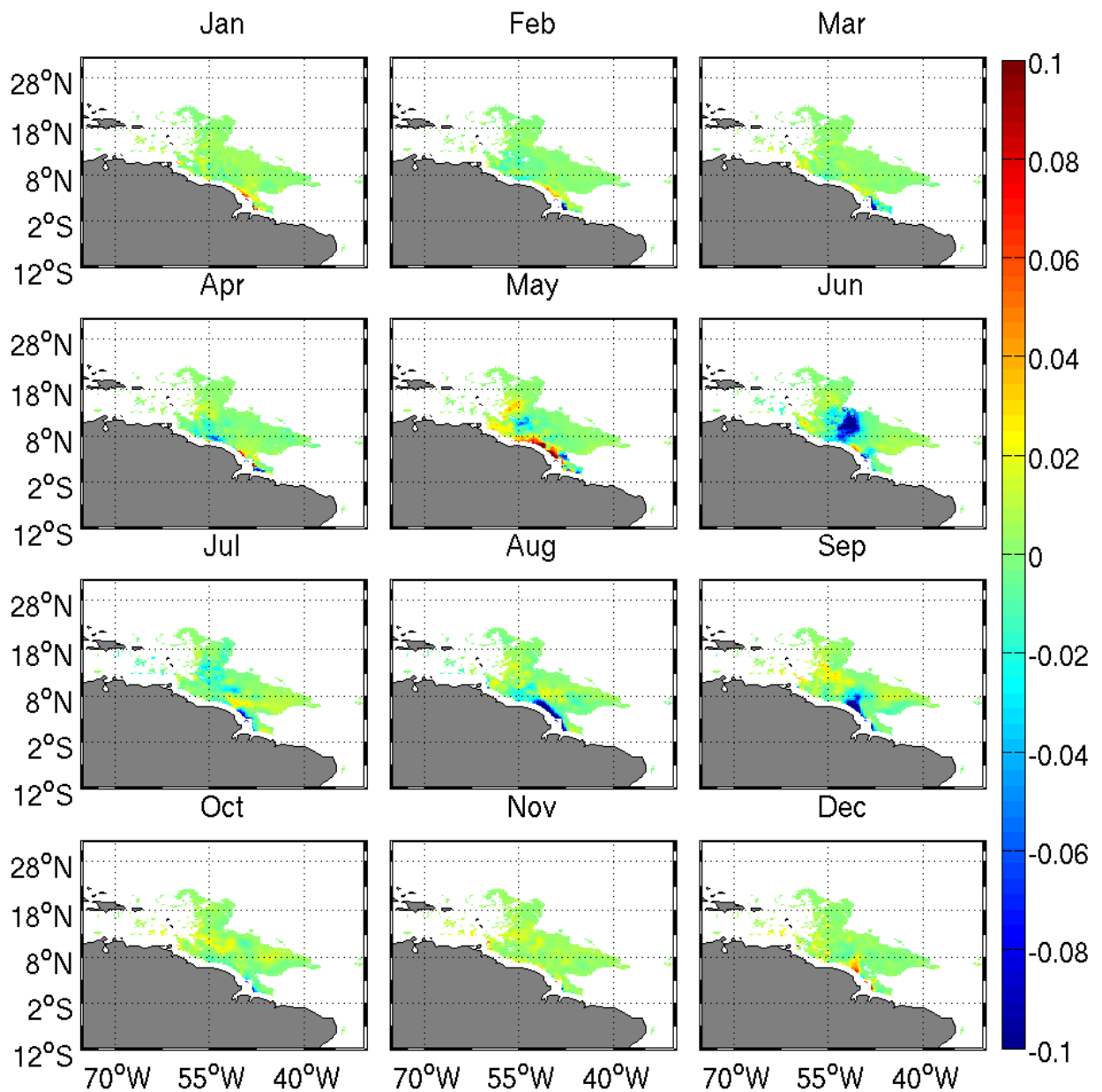


Figure 4.55: 2011 monthly maps of 25-km differences between a_{cdm} estimated from the monthly 2010-2013 SSS/ a_{cdm} relationship and GlobColour a_{cdm} in the Amazon plume.

Chapter 4. The Relationship Between Sea Surface Salinity and Optical Properties in the Amazon Plume Region

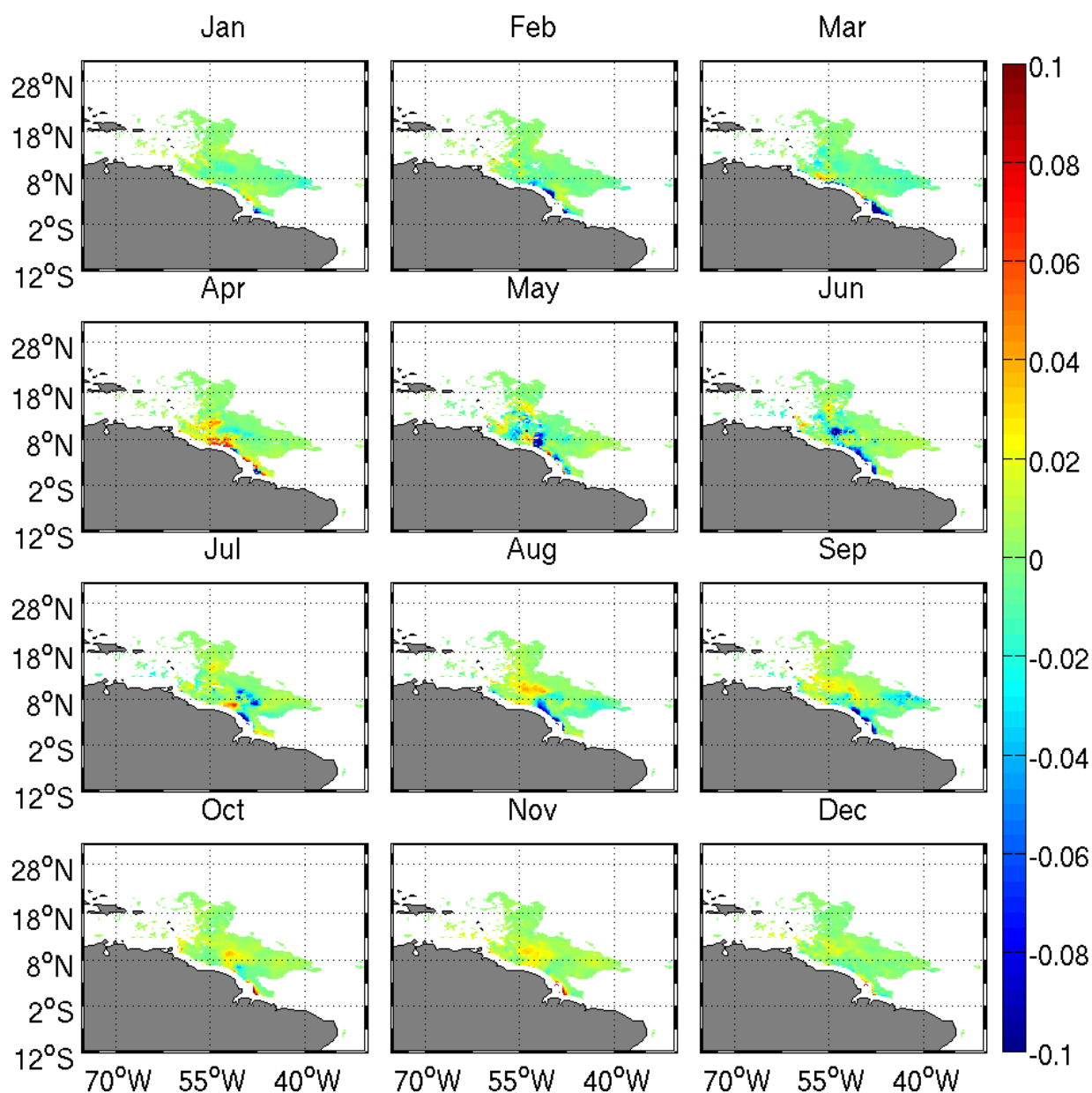


Figure 4.56: 2012 monthly maps of 25-km differences between a_{cdm} estimated from the monthly 2010-2013 SSS/ a_{cdm} relationship and GlobColour a_{cdm} in the Amazon plume.

4.3. A Local Approach of the Conservative Mixing

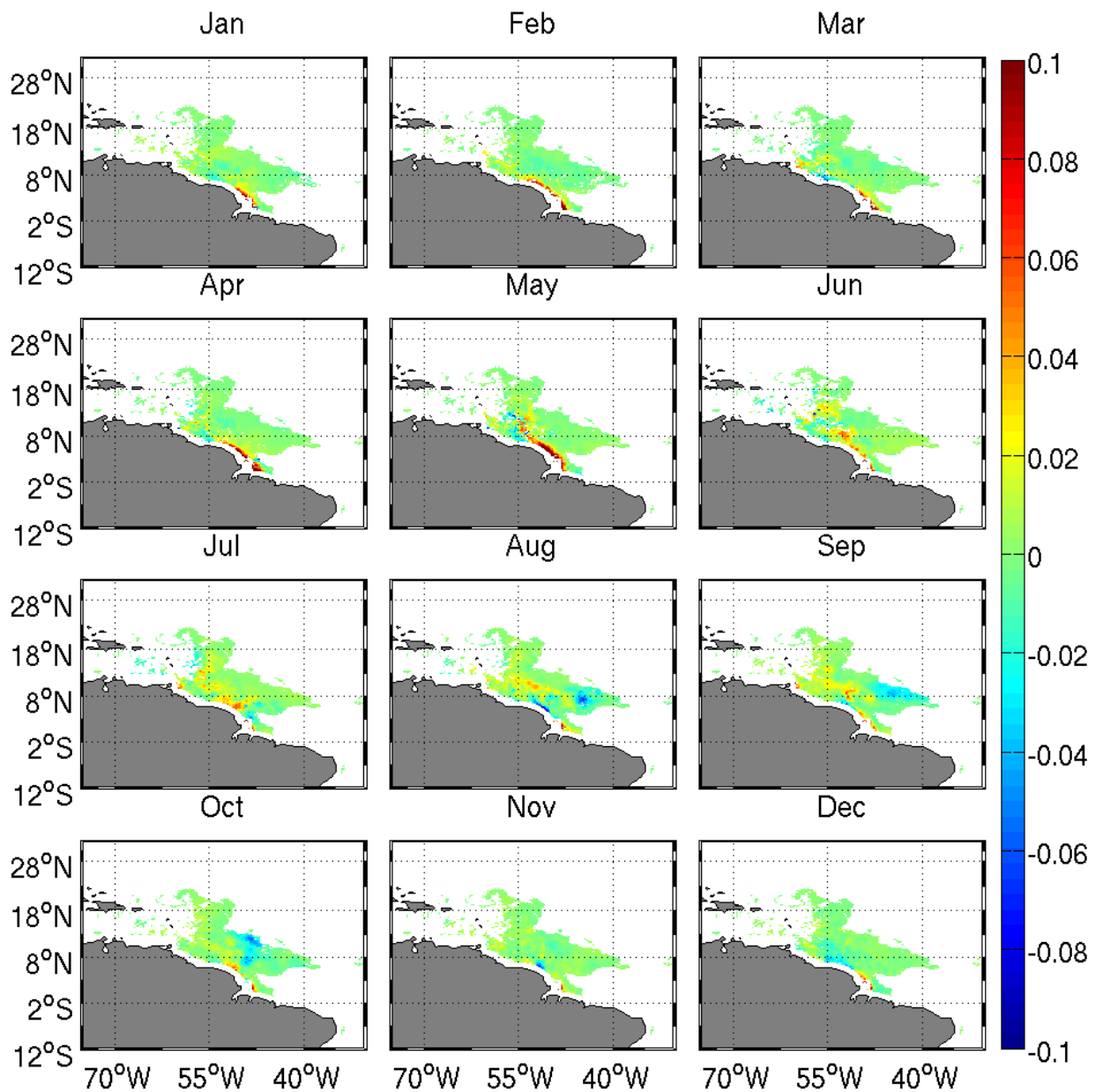


Figure 4.57: 2013 monthly maps of 25-km differences between a_{cdm} estimated from the monthly 2010-2013 SSS/a_{cdm} relationship and GlobColour a_{cdm} in the Amazon plume.

Conclusions :

- Local coherence between sea surface salinity and a_{cdm}
- Spatial variabilities in the conservative mixing
- Non conservative behaviours in the relationship highlighted in the northwestern part of the plume in summer 2010

4.4 Conclusions & Perspectives

We documented the well-known relationship between sea surface salinity and optical parameters using spaceborne SSS and Ocean Color data in the Amazon plume. Thus, we demonstrated the consistency between a microwave instrument and optical instruments. Thanks to remote sensing, this represents a new approach of the SSS/ a_{cdm} relationship with a largely improve spatio-temporal monitoring.

Two different approaches of the conservative mixing were explored. In our first analysis, as done in previous studies, the conservative mixing in the Amazon plume has been studied regionally. Thanks to the new remote sensing sea surface salinity data available, we were able to study this relationship at unprecedented space and time scales. This analysis shows the regional coherence between sea surface salinity and a_{cdm} . We attempt then to explore eventual temporal and spatial variabilities of the regional relationship. For the first time, we were then able to highlight seasonal variabilities in the relationship, a clear seasonal cycle in the relationship slope has been highlighted and related to the Amazon river discharge cycle. No spatial variability in the relationship could be inferred from this analysis. At the end, any noticeable eventual spatial or interannual variability in the relationship is related to non conservative processes affecting the relationship between SSS and a_{cdm} , at a precise period and location (in the northwestern part of the plume during 2010 high flow period). The origins of high a_{cdm} concentration in the Amazon plume area seen by ocean color sensors have been debated for a long time (Longhurst [1993] ; Muller-Karger et al. [1995]). Longhurst [1993] attributed the high a_{cdm} concentrations to phytoplankton blooms stimulated by nutrients supplied via eddy upwelling. On another hand, Muller-Karger et al. [1995] attributed it to the Amazon river. This method can help to better characterize the origins of plume waters, distinguishing non conservative behaviours in the relationship between sea surface salinity and ocean color properties. Moreover, all these conclusions call into question the previous studies in which *in situ*

4.4. Conclusions & Perspectives

data collected at precise locations and at precise months and years are used to establish the conservative mixing.

Our second analysis of the conservative mixing is based on a local approach. SSS and a_{cdm} are well negatively correlated in the whole plume area. All year long, the Amazon waters are advected from the mouth to the open ocean and mix with the surrounding water masses, locally. Amazon waters reach each region of the plume gradually after flowing through different advection pathways and after encountering different water masses. Thus, we chose to consider the conservative mixing locally for each $0.25 \times 0.25^\circ$ pixel in the plume area. Accordingly, one conservative mixing relationship is established per pixel.

Using both methods, we investigated eventual deviations from the conservative mixing established. Through May to July 2010, in the northwestern part of the plume, a non conservative mixing behaviour is related to an intense area of net primary productivity, which represents another source of colored detrital matter than the terrestrial source.

Whatever the approach of the conservative mixing considered, SSS and ocean color properties are spatially and temporally coherent in the Amazon plume.

Chapter 5

Application : Sea Surface Salinity retrieval from Ocean Color in the Amazon Plume

5.1 Introduction

As robustly established in the chapter 4, applications of this strong identity conservation can thus now be explored. In particular, the reconstruction of a sea surface salinity product based on Ocean Color data can be straightforwardly applied. A first important benefit would be to estimate sea surface salinity back in time from 1998 to 2013, with unprecedented spatial and temporal resolutions, thanks to Ocean Color measurements, to monitor and evaluate changes in the plume. Moreover, using an adapted mean relationship can help to better reveal anomalies to be possibly associated to bio-geochemical optical properties and/or air-sea interaction changes.

Many attempts have already been reported ([Binding and Bowers \[2003\]](#) ; [Del Castillo and Miller \[2008\]](#) ; [Molleri et al. \[2010\]](#) ; [Urquhart et al. \[2012\]](#) ; [Bai et al. \[2013\]](#)). In particular, [Molleri et al. \[2010\]](#) retrieved SSS from a_{cdm} in the Amazon plume river. The established linear regression model is $SSS = -126.03 a_{cdm} + 37.25$. On another hand, [Del Vecchio and Subramaniam \[2004\]](#) retrieved SSS from light attenuation at 490 nm (K490) in the Amazon plume river. The established linear regression model is $K490 = -0.0021 SSS + 0.77$. Both models are based on a relationship between *in situ* measurements of SSS and satellite Ocean Color. The *in situ* data samples were not partitioned in both time and space, to only provide an overall mean relationship for the whole basin.

5.2 Methodology

First of all, as we discussed in the section 2.1.3.4, comparing SMOS with *in situ* data, SMOS tends to overestimate SSS for $SSS < 30$ pss (see figure 2.11 on the left panel). We thus attempt to correct SMOS data empirically based on *in situ* data. The transformation applied on SMOS SSS is :

5.2. Methodology

$$SSS_{corr} = \frac{SSS(1 + f(\frac{SSS - 25}{4}))}{2} \quad (5.1)$$

with f an error function defined as :

$$f(x) = \frac{2}{\sqrt{\pi}} \int_0^x \exp -t^2 dt \quad (5.2)$$

This transformation permits to correct essentially the SSS overestimation at low SSS values (see figure 5.1).

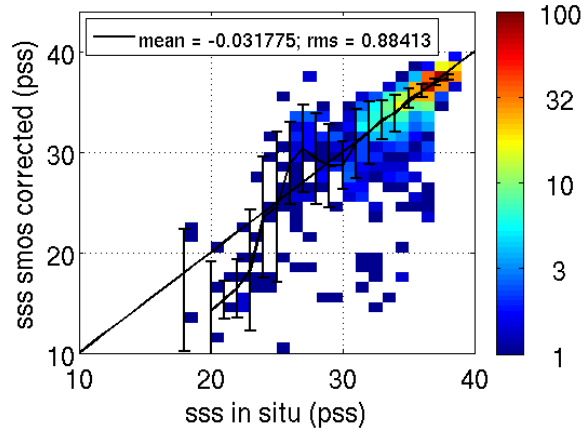


Figure 5.1: Mean SMOS SSS per bin of 1 pss of *in situ* SSS ± 1 standard deviation. In z-axis is represented the number of data per bin of 1x1 pss.

As did in the previous chapter, the linear regression was evaluated between the 25-km daily ± 45 days empirically corrected SMOS SSS and a_{cdm} computed for each $0.25 \times 0.25^\circ$ pixel in the Amazon plume over 2010-2013 (see figure 5.2). The regression were evaluated only for pixels in the plume for which the p-value (significance of the SSS/ a_{cdm} correlation) is below 0.01 and the time lag between the SSS minimum and a_{cdm} maximum is zero (see figure 4.44). Then, to 25-km daily ± 45 days a_{cdm} products, a 25-km daily ± 45 days SSS product is retrieved. In the northwestern part of the plume, as discussed in the previous chapter, SSS and a_{cdm} are highly correlated but poorly linearly well-correlated, caution has thus to be taken in that area.

In parallel, we compute 25-km daily ± 45 days SSS products retrieved using Molleri et al. [2010] and Del Vecchio and Subramaniam [2004] linear regression models, based on the 25-km daily ± 45 days a_{cdm} and K490, respectively.

Chapter 5. Application : Sea Surface Salinity retrieval from Ocean Color in the Amazon Plume

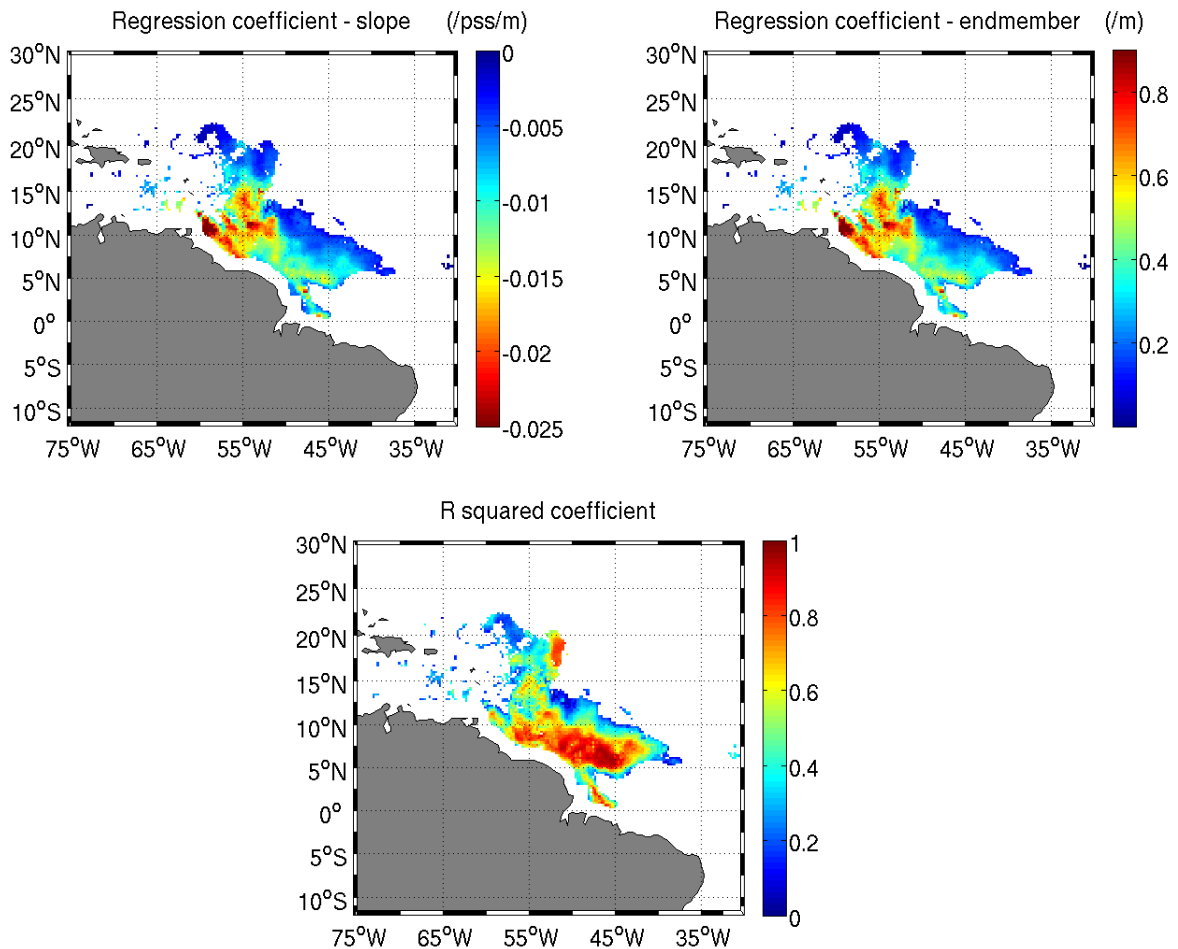


Figure 5.2: Slope (top left), endmember (top right) and R squared coefficient (bottom) of the linear regression between the time series of filtered corrected SMOS SSS and a_{cdm} for each $0.25 \times 0.25^\circ$ pixel over 2010-2013. Only pixels in the plume for which the p-value (significance of the SSS/ a_{cdm} correlation) is below 0.01 and time lag between the SSS minimum and a_{cdm} maximum is zero are shown.

5.3 Sea Surface Salinity Estimates

The 2010, 2011, 2012 and 2013 monthly maps of sea surface salinity estimates are shown in figures 5.3, 5.4, 5.5 and 5.6, respectively. These maps can be compared with the monthly maps of SMOS sea surface salinity shown in chapter 3 in figures A.1, A.2, A.3 and A.4.

5.3. Sea Surface Salinity Estimates

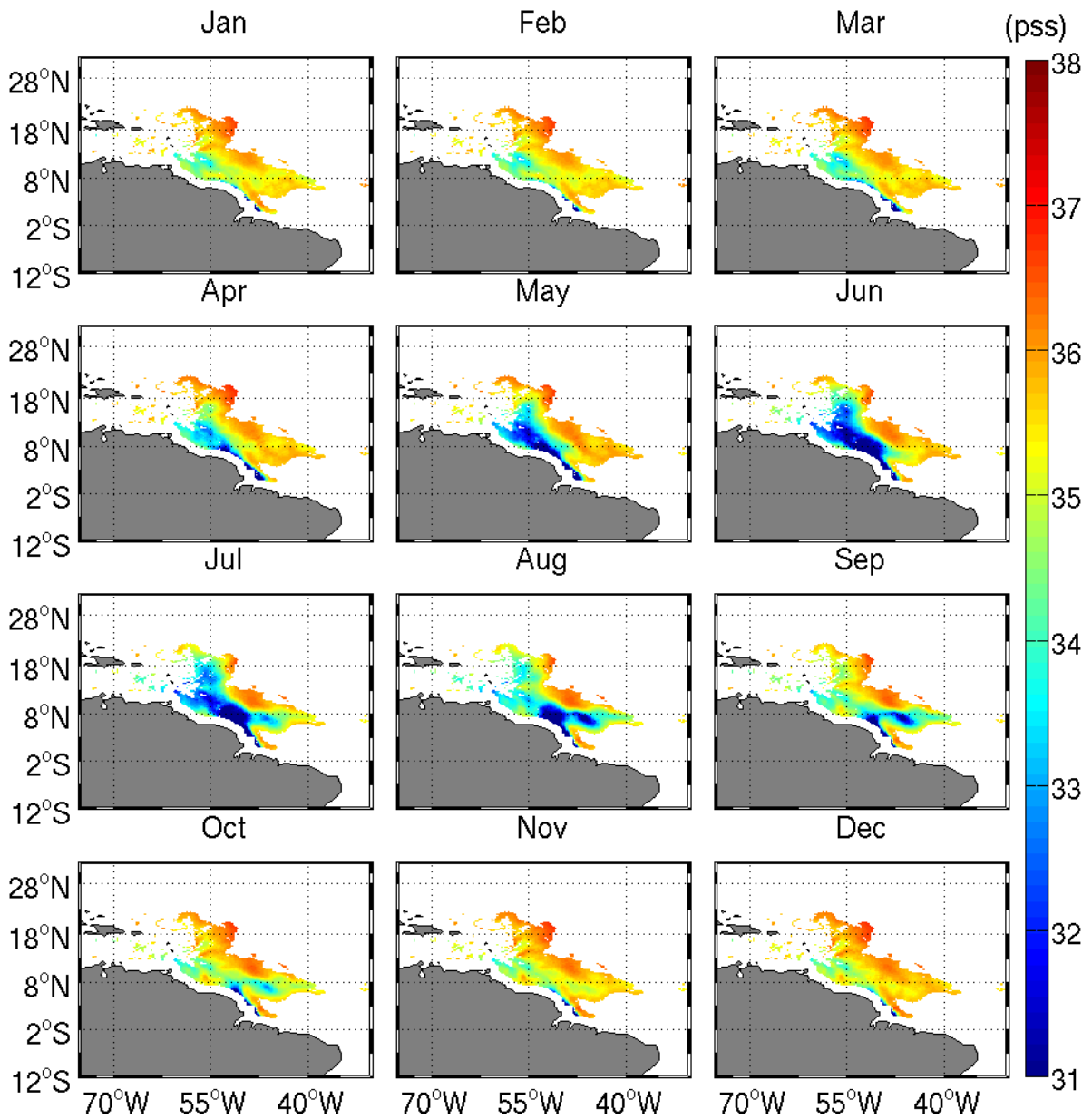


Figure 5.3: 2010 monthly maps of sea surface salinity retrieved from a_{cdm} .

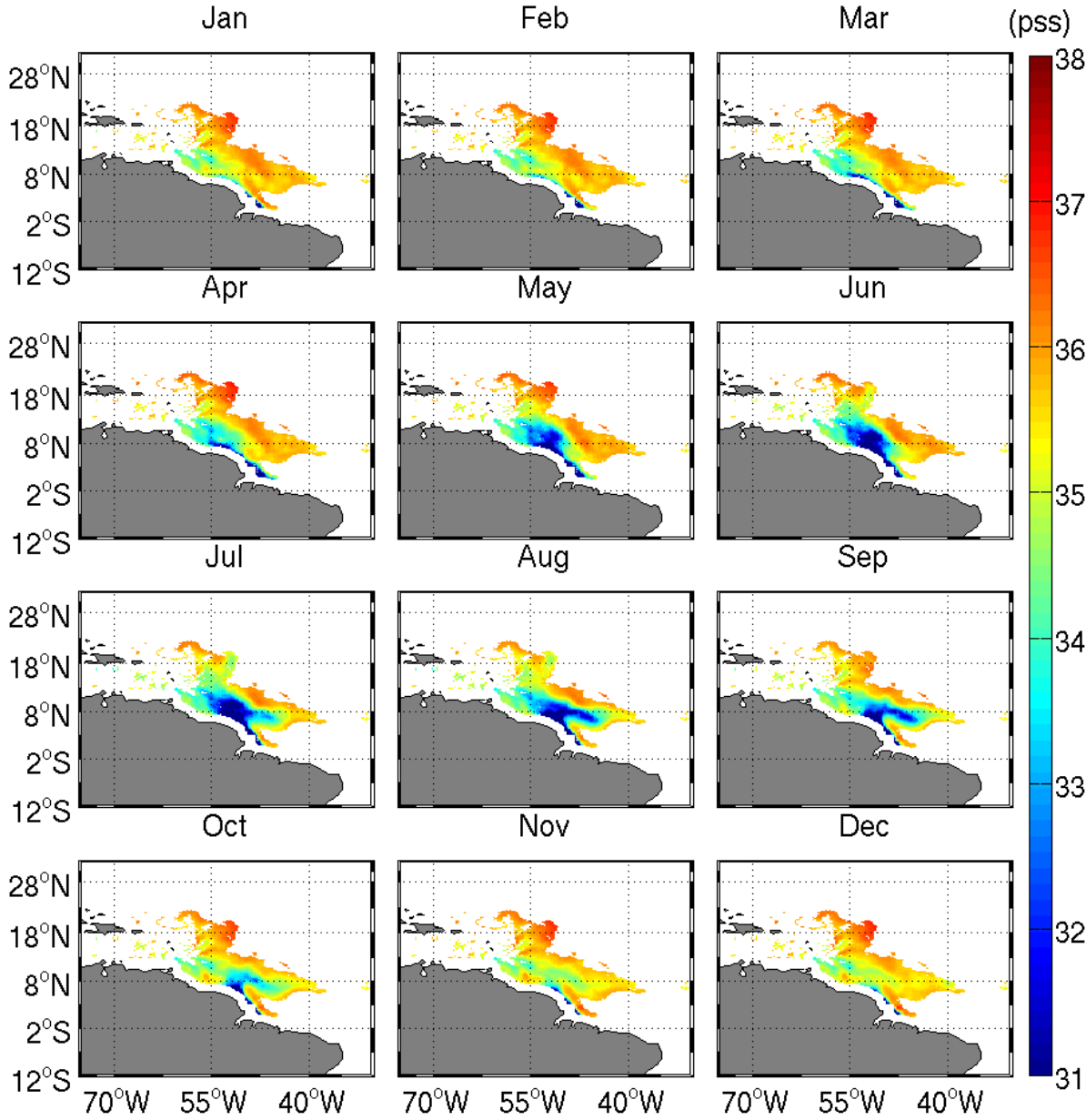


Figure 5.4: 2011 monthly maps of sea surface salinity retrieved from a_{cdm} .

5.3. Sea Surface Salinity Estimates

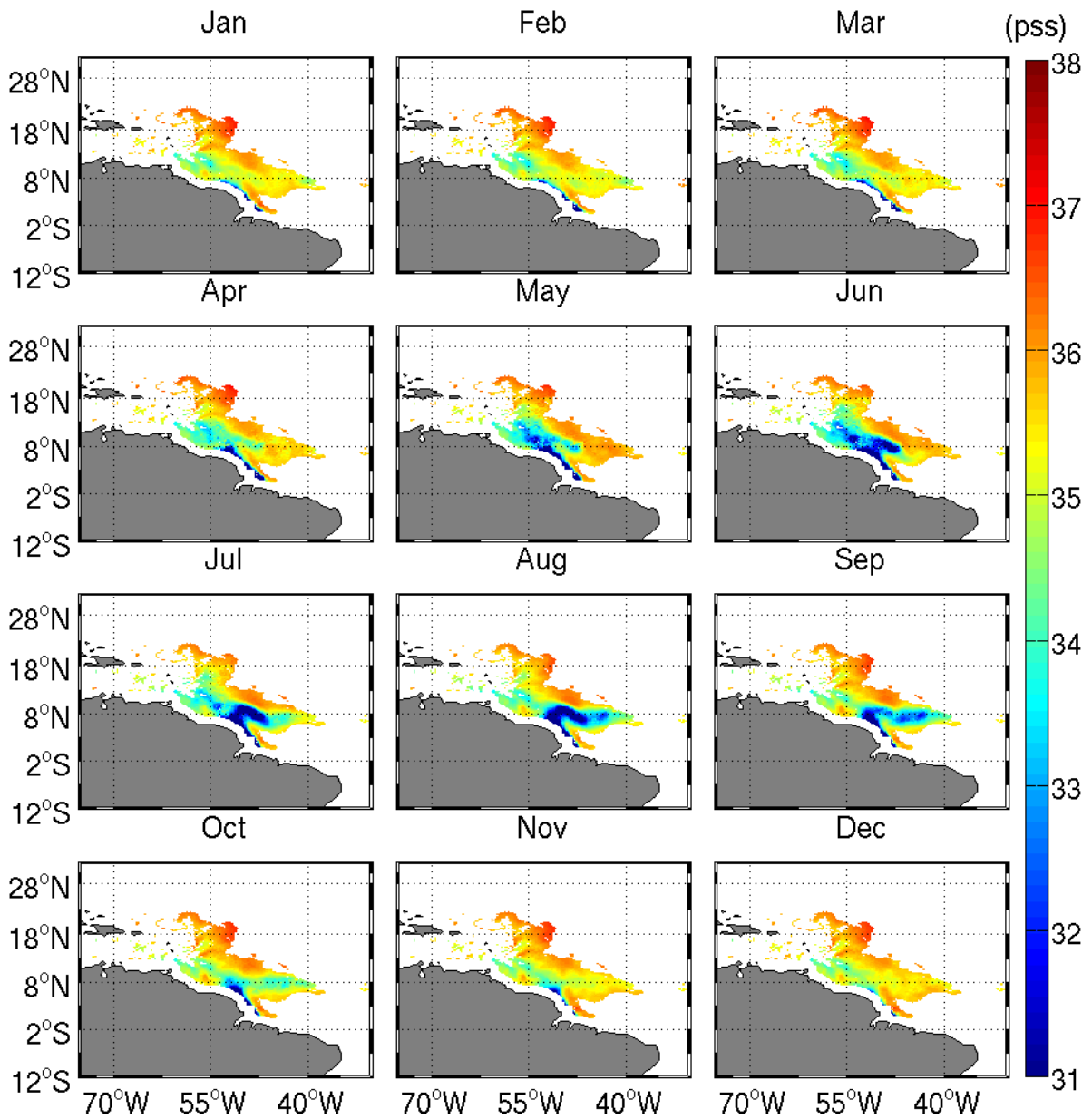


Figure 5.5: 2012 monthly maps of sea surface salinity retrieved from a_{cdm} .

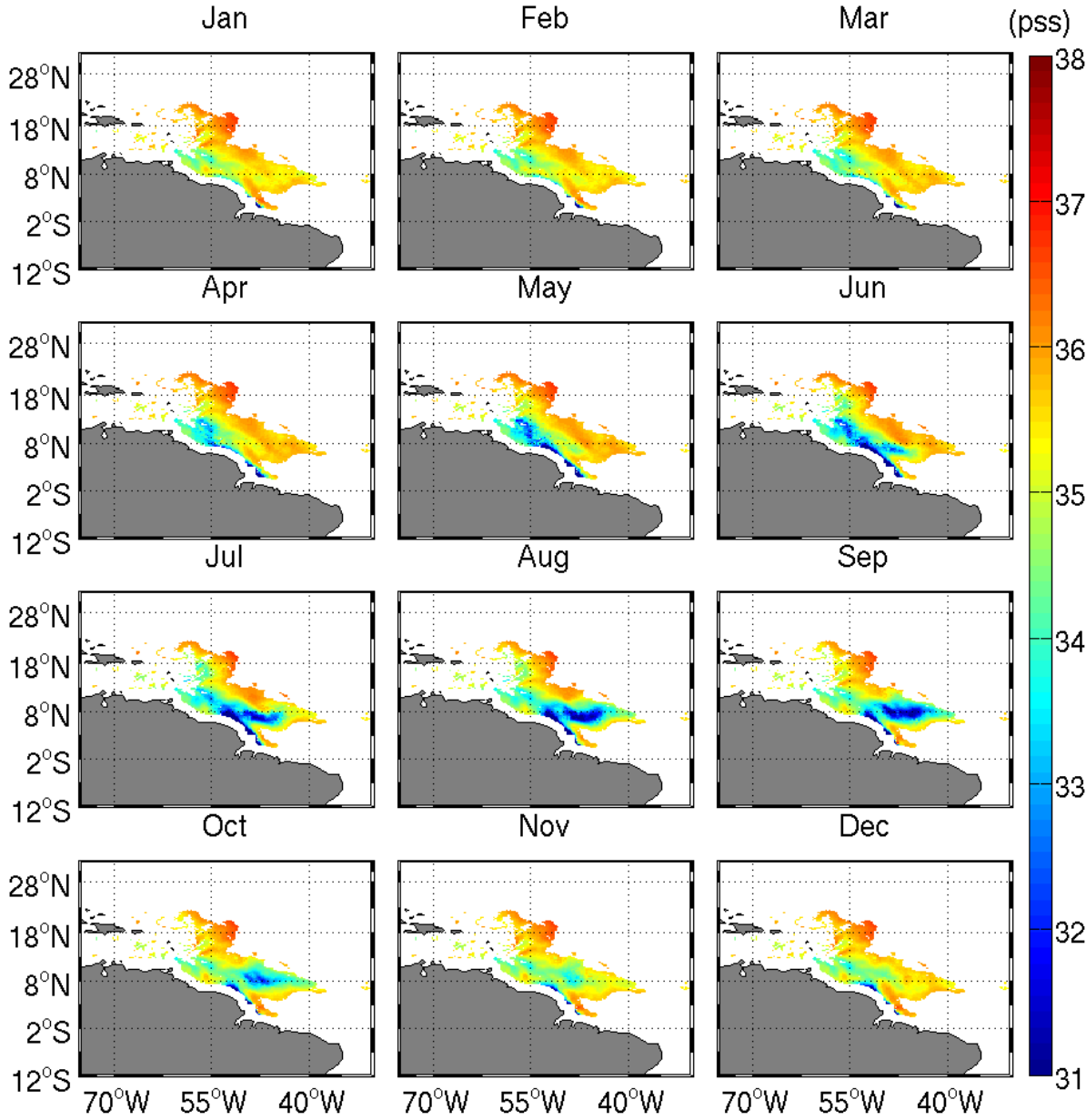


Figure 5.6: 2013 monthly maps of sea surface salinity retrieved from *a_{cdm}*.

5.3. Sea Surface Salinity Estimates

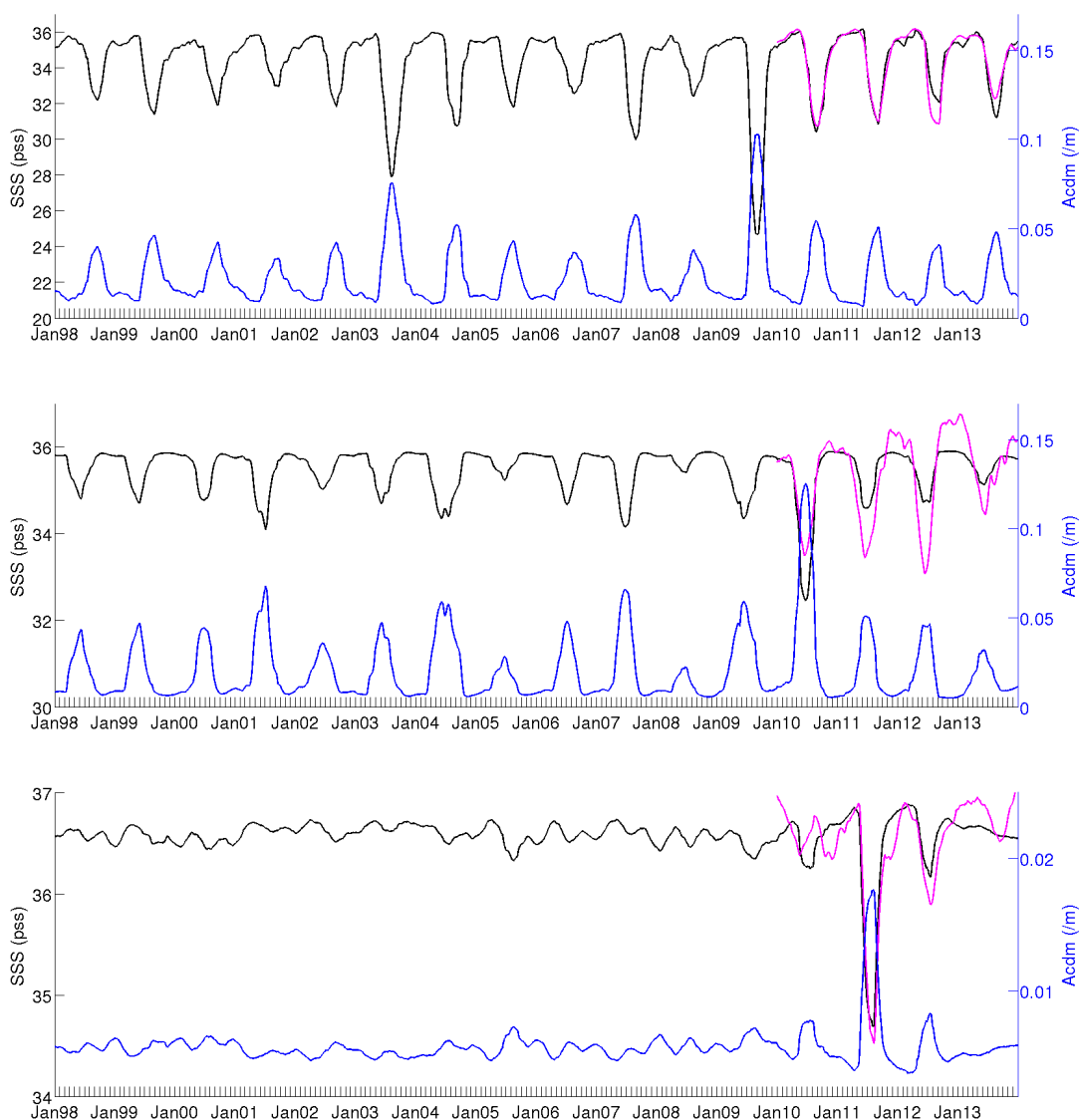


Figure 5.7: 1998-2013 time series of a_{cdm} (blue) and retrieved SSS (black) at locations $[6.5^{\circ}\text{N } 46^{\circ}\text{W}]$, $[14^{\circ}\text{N } 55^{\circ}\text{W}]$ and $[19^{\circ}\text{N } 51.5^{\circ}\text{W}]$, shown by the black, blue and red dots, respectively, on figure 5.8. As a magenta solid line is represented the 2010-2013 time serie of SMOS SSS.

Now we are able to retrieve SSS from Ocean Color data based on the conservative mixing robustly established, we are able to retrieve a SSS product back in time from 1998, year from which Ocean Color data are available. In figure 5.7, the evolution of the retrieved SSS is shown at 3 locations with coordinates $[6.5^{\circ}\text{N } 46^{\circ}\text{W}]$, $[14^{\circ}\text{N } 55^{\circ}\text{W}]$ and $[19^{\circ}\text{N } 51.5^{\circ}\text{W}]$, marked as blue, black and red dots in figure 5.8. As at $[6.5^{\circ}\text{N } 46^{\circ}\text{W}]$, in the eastern part of the plume, the SSS is well retrieved in comparison with SMOS, low SSS are not well retrieved at location $[14^{\circ}\text{N } 55^{\circ}\text{W}]$, in the northwestern part of the plume, being overestimated (this will be investigated more precisely in the section 5.6). Moreover,

Chapter 5. Application : Sea Surface Salinity retrieval from Ocean Color in the Amazon Plume

there is a saturation in the retrieved signal for SSS higher than 35.5 pss. It corresponds to the plume limit from which SSS and a_{cdm} do not covary anymore. There, at high SSS values, the a_{cdm} signal is also saturated, it has reached the open ocean value. However, SSS gradients are well retrieved. At location [19°N 51.5°W], a part which is only reached by the plume in 2011, the SSS gradients, when occur, seem well retrieved.

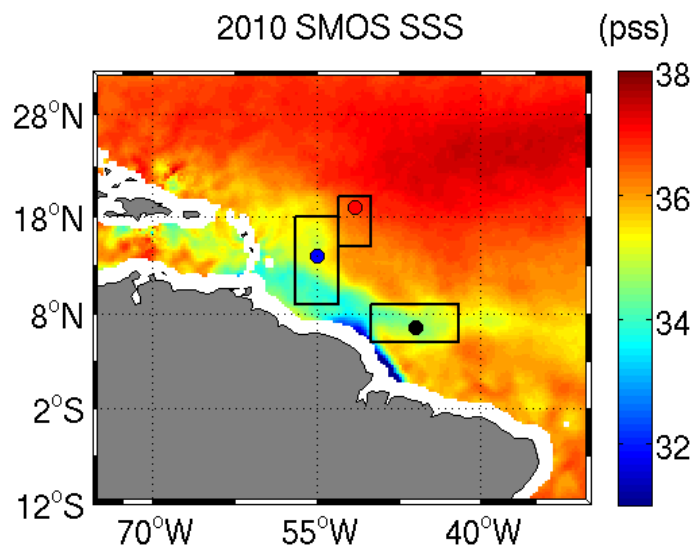


Figure 5.8: 2010-2013 mean SMOS SSS on top of which are drawn the three boxes in which hovmueller maps are computed.

Around these three locations (see figure 5.8), hovmueller maps are computed. Figure 5.9 shows, in each location, the evolution of SMOS SSS, retrieved SSS and a_{cdm} from 1998 to 2013. In each part of the plume, we can identify the arrival of plume waters every year and the variability in the extension of plume waters from a year to another. In the eastern part of the plume (see the top panel of figure 5.9), we can notice that in 2003 and 2009, the plume waters are carried further east than during other years, reaching 42°W. The bottom panel shows the northeastern extension variability of the Amazon plume. As during most years, the plume doesn't reach 15°N in that part of the ocean, in 2000, 2005 and 2010, the Amazon waters reach almost 17°N and in 2011, as noticed previously, the plume extends much more northeastward than other years, reaching more than 20°N.

5.3. Sea Surface Salinity Estimates

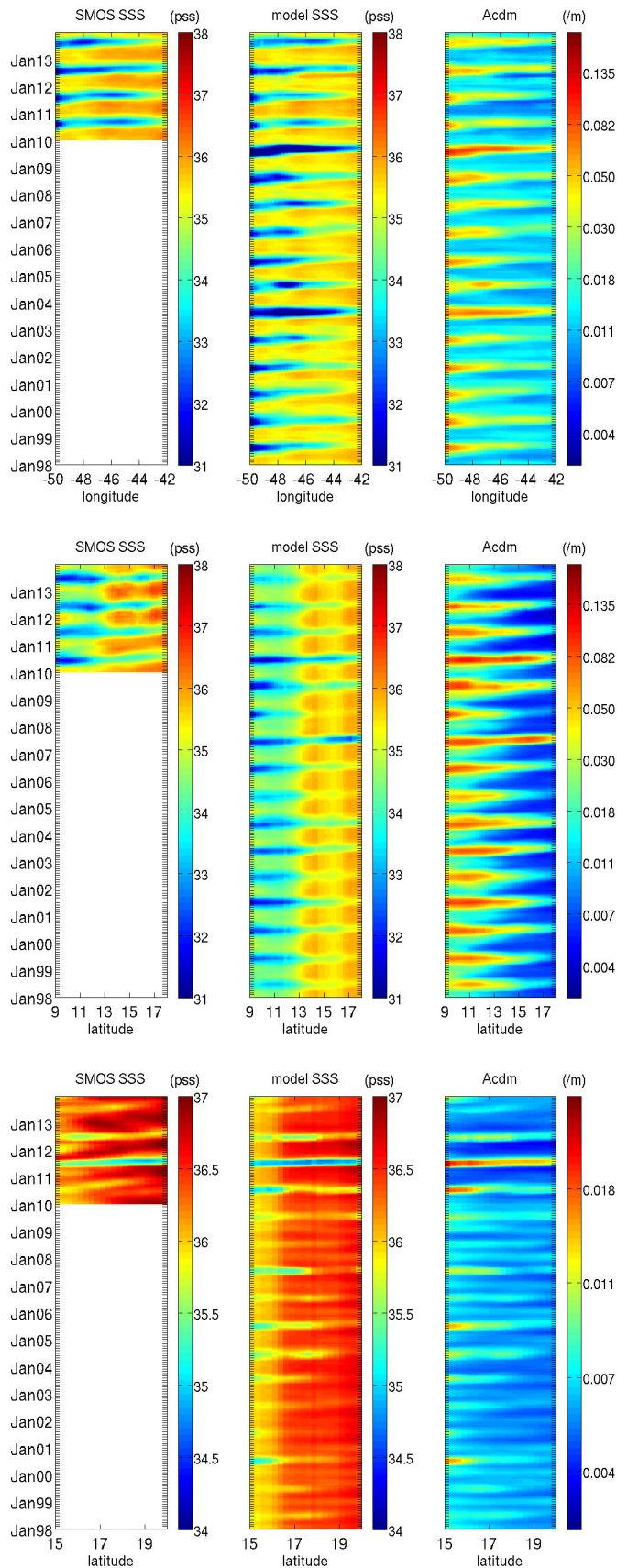


Figure 5.9: Hovmueller plot of (left) SMOS SSS, (middle) retrieved SSS and (left) a_{cdm} in each box represented in figure 5.8 from 1998 to 2013.

5.4 Comparison with Other Sea Surface Salinity Retrieval Methods

Molleri et al. [2010] and Del Vecchio and Subramaniam [2004] already attempted to retrieve sea surface salinity from a_{cdm} and K490 in the Amazon plume area using a relationship they first established using SeaWiFS a_{cdm} and K490 data and *in situ* SSS measurements. They established a linear regression model ($SSS = -126.03 a_{cdm} + 37.25$ and $K490 = -0.021 SSS + 0.77$, respectively) they applied on satellite a_{cdm} and K490, respectively. I used the models established by Molleri et al. [2010] and Del Vecchio and Subramaniam [2004] to retrieve monthly estimates of sea surface salinity in 2010, 2011, 2012 and 2013, in the Amazon plume area. On figures 5.10 and 5.11, examples of the 2010 monthly maps of the SSS retrieved using both models are shown. Concerning the Molleri et al. [2010], the plume fronts each month are well-retrieved. The sea surface salinity retrieved seems however, in overall, too low, compared to 2010 SMOS SSS monthly maps (see figure A.1). Considering the Del Vecchio and Subramaniam [2004] method, as it seems to well retrieve low SSS next to the mouth, SSS are too low at the edges of the plume.

We compare on one hand, the SSS retrieved using our method described previously with SMOS SSS and, on another hand, the SSS retrieved using Molleri et al. [2010] and Del Vecchio and Subramaniam [2004] models with SMOS SSS. In figure 5.12, are represented the 2010 monthly maps of the method exhibiting the lowest anomaly compared to SMOS SSS for each pixel. It is shown that most of the time in most areas, our method works better, however, Molleri et al. [2010] method seems to work better at the edges of the plume, especially in the northern part of the plume and Del Vecchio and Subramaniam [2004] method in the retroreflection during late summer.

5.4. Comparison with Other Sea Surface Salinity Retrieval Methods

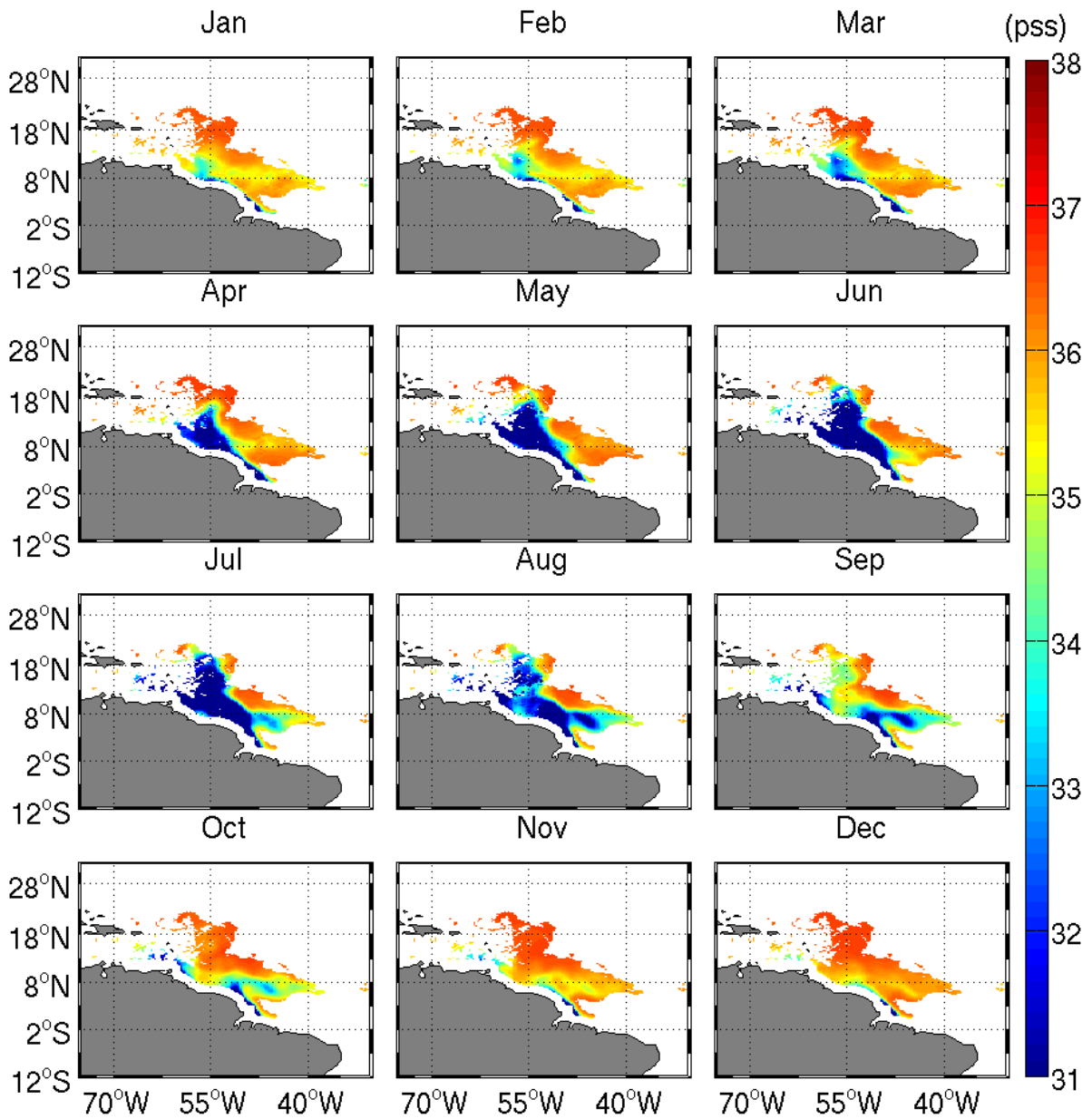


Figure 5.10: 2010 monthly maps of the SSS retrieved using the Molleri et al. [2010] model.

Chapter 5. Application : Sea Surface Salinity retrieval from Ocean Color in the Amazon Plume

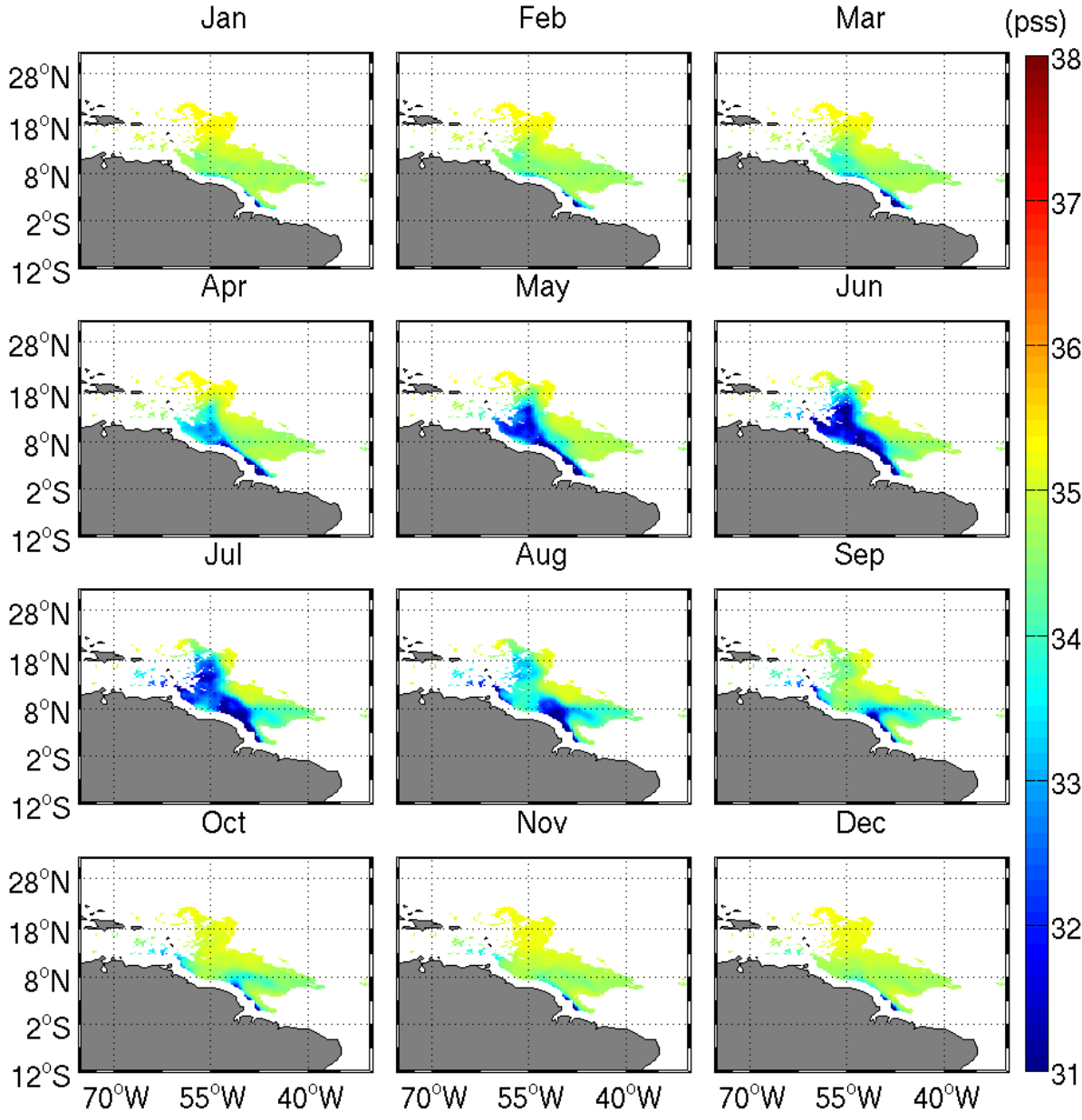


Figure 5.11: 2010 monthly maps of the SSS retrieved using the Del Vecchio and Subramaniam [2004] model.

5.4. Comparison with Other Sea Surface Salinity Retrieval Methods

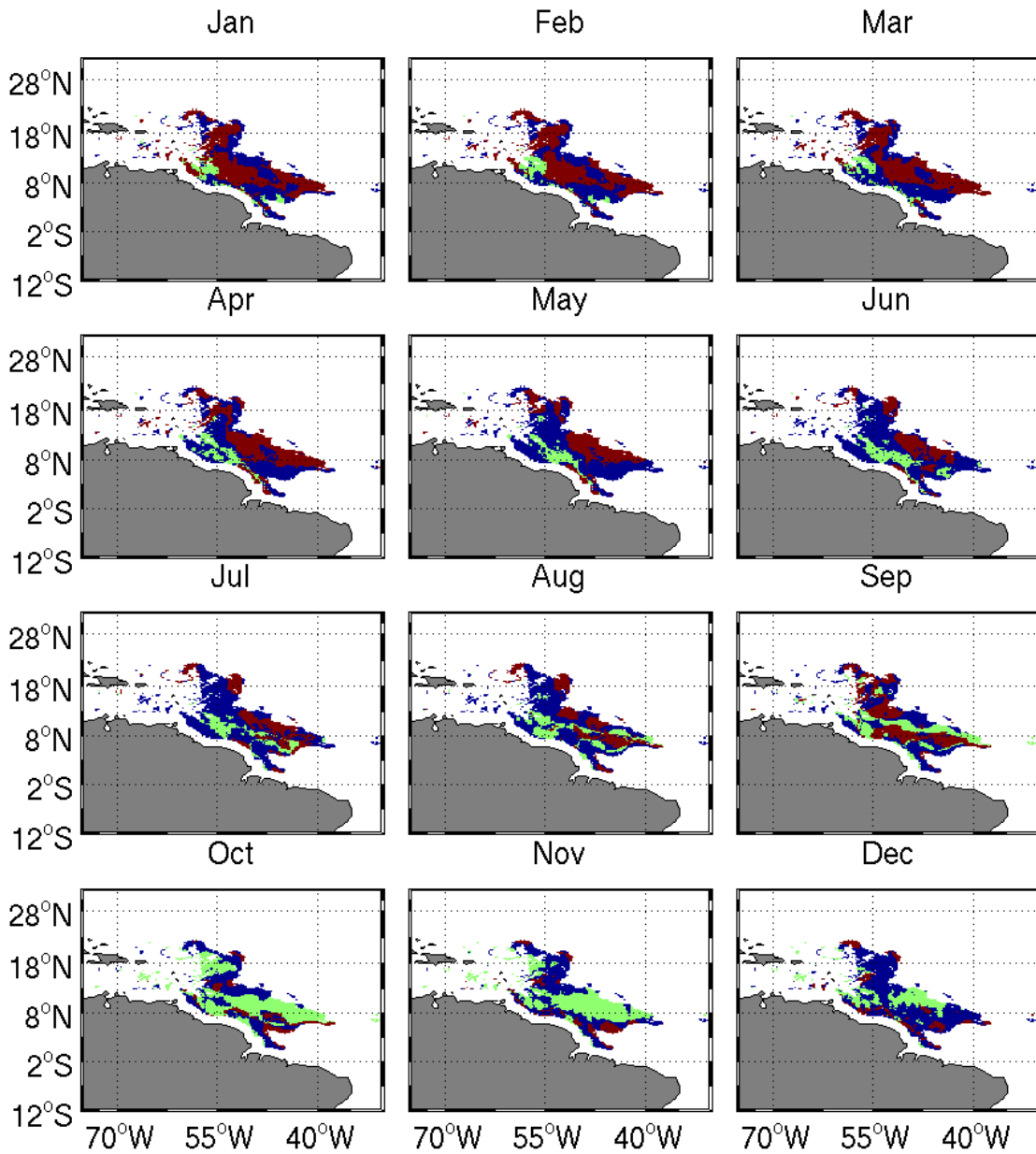


Figure 5.12: 2010 monthly maps of the best SSS retrieval method in terms of lower differences with SMOS SSS (blue for our method, red for Molleri et al. [2010] method and green for Del Vecchio and Subramaniam [2004] method).

5.5 Validation

The retrieved SSS from our model and from [Molleri et al. \[2010\]](#) and [Del Vecchio and Subramaniam \[2004\]](#) models are validated against *in situ* and SMOS data over 2010-2012 (TSG, Argo, CTD and drifters).

5.5.1 Over 2010-2012

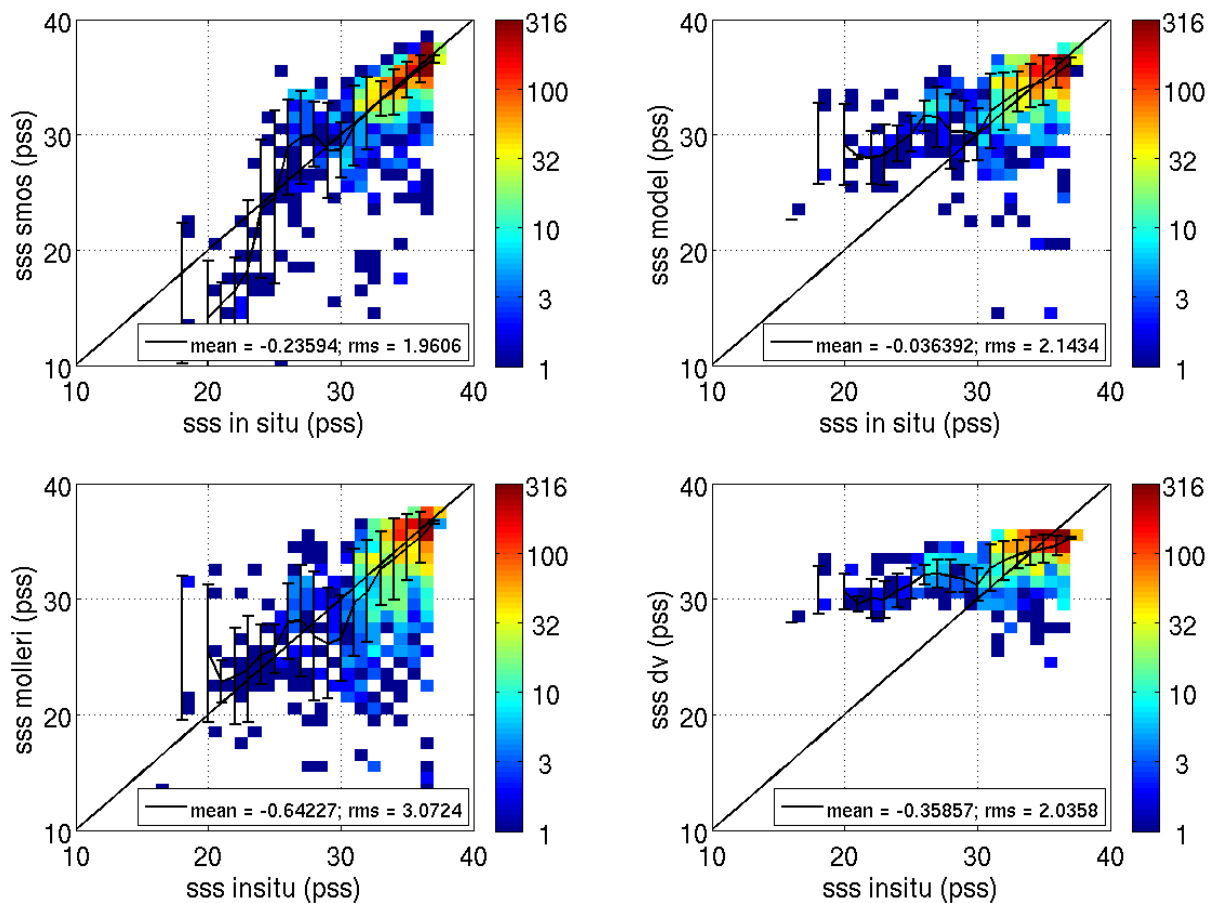


Figure 5.13: Mean (top left) SMOS SSS, (top right) retrieved SSS from our model, (bottom left) retrieved SSS using the [Molleri et al. \[2010\]](#) model and (bottom right) retrieved SSS using the [Del Vecchio and Subramaniam \[2004\]](#) model per bin of 1 pss of *in situ* SSS \pm 1 standard deviation. In z-axis is represented the number of data per bin of 1x1 pss.

Figure 5.13 represents the mean SSS retrieved from our model, from the [Molleri et al. \[2010\]](#) model and from the [Del Vecchio and Subramaniam \[2004\]](#) model (from left to right) per bin of 1 pss *in situ* SSS \pm 1 standard deviation. At low salinity (SSS<30 pss), in

5.5. Validation

the coastal area, our model and [Del Vecchio and Subramaniam \[2004\]](#) one tend to overestimate SSS. No offset on the retrieval using [Molleri et al. \[2010\]](#) model is obvious but the discrepancy between *in situ* and retrieved SSS is more important. [Del Vecchio and Subramaniam \[2004\]](#) model tends to underestimate SSS at high SSS values. The RMS of the differences between *in situ* and retrieved SSS using our model (around 2.1) is higher than the one between SMOS data (around 1.7, not shown here) and it is comparable to the one between *in situ* and [Del Vecchio and Subramaniam \[2004\]](#) (2). However it is lower than the one between *in situ* and [Molleri et al. \[2010\]](#) (3.1).

5.5.2 Along TSG tracks

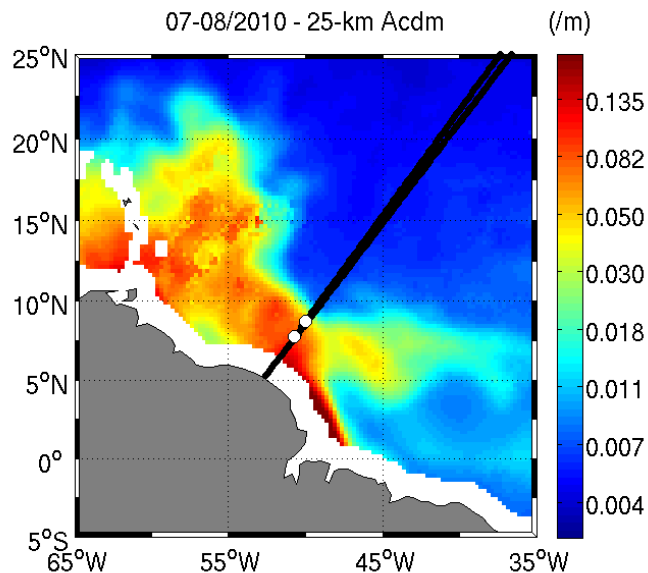


Figure 5.14: Average July-August 2010 a_{cdm} map on top of which are represented as solid black lines, three TSG transects. The white dots mark the locations [7.75°N 50.75°W] and [8.75°N 50°W].

Retrieved SSS are then validated against TSG transects in the Amazon plume. We particularly show the evolution of SSS along three different TSG tracks carried out in July and August 2010. Figure 5.14 represents the average July-August 2010 a_{cdm} and on top of this map is represented the TSG tracks crossing the Amazon plume, an area of strong SSS gradients. The retrieved SSS using our model, [Molleri et al. \[2010\]](#) and [Del Vecchio and Subramaniam \[2004\]](#) models, SMOS SSS and *in situ* SSS along the three TSG tracks are represented as functions of the latitude in figure 5.15. The strong SSS gradients, obtained when the ships cross the plume, are well-retrieved by our model. Once again, we can see that [Del Vecchio and Subramaniam \[2004\]](#) model tends to underestimate high

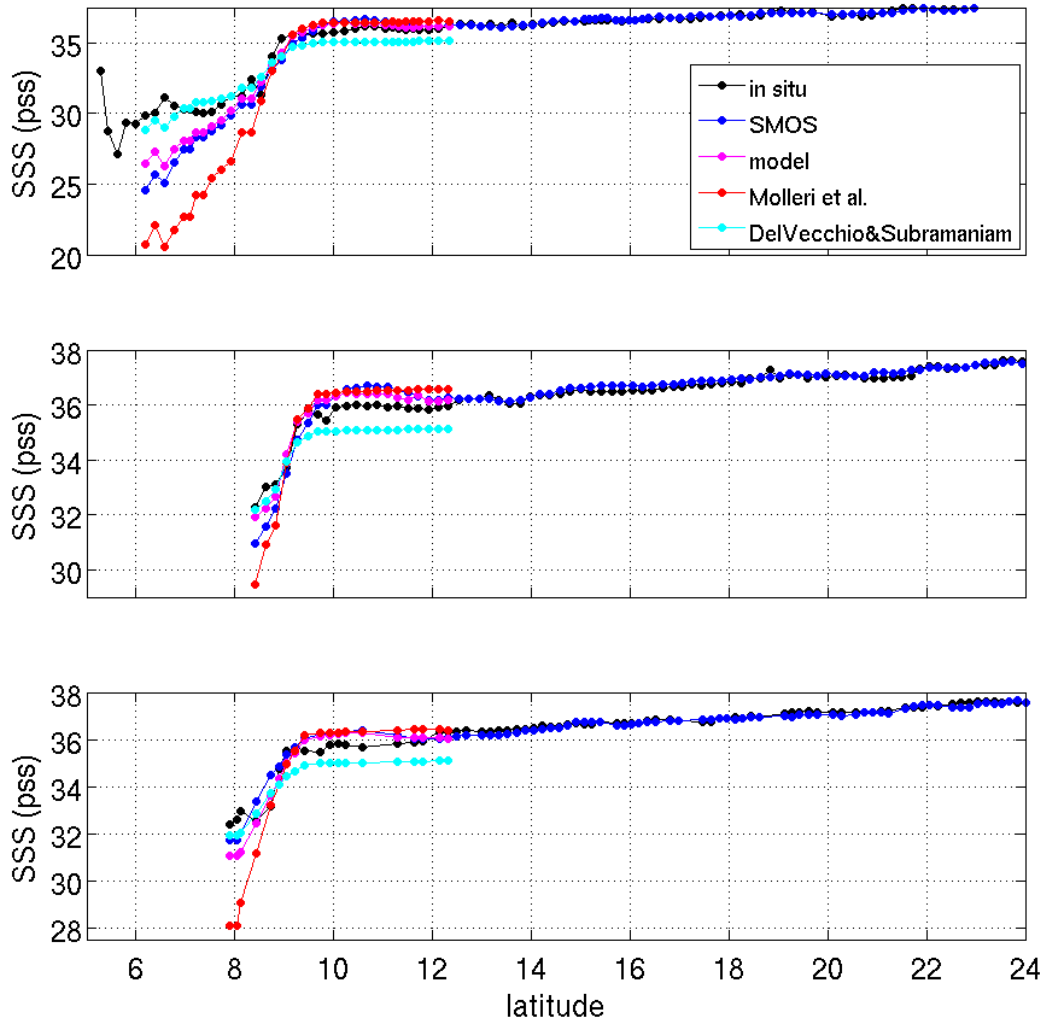


Figure 5.15: Time series of sea surface salinity from SMOS (blue dots), retrieved SSS using our model (magenta dots), using [Del Vecchio and Subramaniam \[2004\]](#) model (cyan dots) and using [Molleri et al. \[2010\]](#) model (red dots) and TSG SSS measurements (black dots) along 3 TSG transects in July and August 2010.

SSS whereas [Molleri et al. \[2010\]](#) model tends to underestimate low SSS.

At locations [7.75°N 50.75°W] and [8.75°N 50°W], marked by white dots in figure 5.14, 1998-2013 time series of a_{cdm} , SMOS and retrieved SSS are shown in figure 5.16. At these 2 locations, *in situ* SSS data from Colibri and Toucan vessels are available from 2002 to 2013, they are superposed as red dots on the time series. As previously reported, sea surface salinity higher than 35 psu are not well-retrieved compared to *in situ* data, they tend to be underestimated.

5.6. Discussion & Conclusions

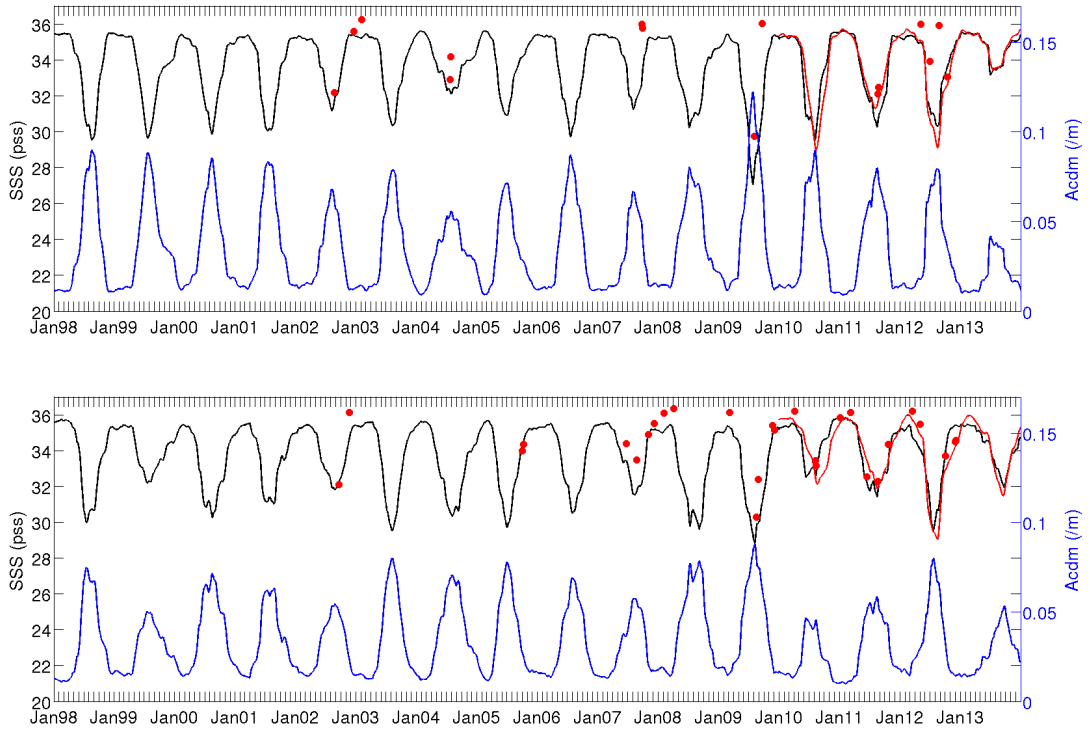


Figure 5.16: 1998-2013 time series of a_{cdm} (blue) and retrieved SSS (black) at locations [7.75°N 50.75°W] and [8.75°N 50°W], marked by white dots in figure 5.14. As a magenta solid line is represented the 2010-2013 time serie of SMOS SSS. The red dots represent *in situ* data available.

5.6 Discussion & Conclusions

Once the conservative mixing relationships were established robustly in the chapter 4, they were used to retrieve a daily ± 45 days 25-km SSS product based on Ocean Color data. This product was validated against SMOS and *in situ* SSS and compared to the SSS retrieved using the Molleri et al. [2010] and Del Vecchio and Subramaniam [2004] models. Compared to SMOS and *in situ* SSS, our model retrieves well strong SSS fronts and gradients in the Amazon plume. Overall, our model gives good results especially for $SSS > 30$ pss. At low SSS ($SSS < 30$ pss), our model tends to overestimate SSS.

Different sources of error can interfere in the retrieval of SSS based on Ocean Color products and on the conservative mixing.

We have seen in section 2.1.3.4 that different sources of errors can affect SMOS data especially near the coast, at low SSS values. As our model is based on SMOS data, this can affect the SSS retrieval.

Near the coast, where turbid waters are present, a_{cdm} retrieval algorithms are not precise

Chapter 5. Application : Sea Surface Salinity retrieval from Ocean Color in the Amazon Plume

enough, inducing the introduction of additional errors in our model also based on ocean color data.

The validation against *in situ* data is based on a comparison between data acquired at a precise time and location and data averaged at 25 km and 90 days. This spatial and temporal differences can have an important impact on the validation especially in the Amazon plume where an important variability in time and space is noticed.

Moreover, *in situ* data are often measured at around 3 or 5 meters deep against few micrometers deep concerning satellite data. In the Amazon plume area, vertical SSS gradients, as seen in the section 2.1.3.4, can be large.

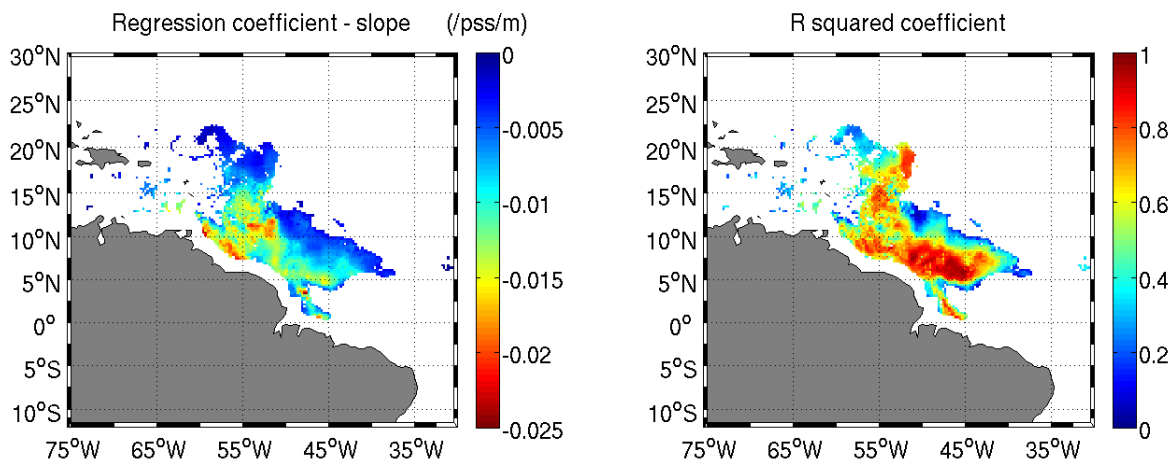


Figure 5.17: Slope (left) and R squared coefficient (right) of the linear regression between the time series of filtered corrected SMOS SSS and a_{cdm} for each $0.25 \times 0.25^\circ$ pixel over 2010-2013, data between May and July 2010 are not considered in the computation. Only pixels in the plume for which the p-value (significance of the SSS/ a_{cdm} correlation) is below 0.01 and time lag between the SSS minimum and a_{cdm} maximum is zero are shown.

Deviations from the conservative mixing can occur due to biogeochemical processes such as primary production and removal processes (photobleaching, flocculation...) especially at the edge and in the northwestern part of the plume where SSS and a_{cdm} are poorly linearly correlated (see the bottom of figure 5.2).

Primary productivity could represent another source of cdm than a terrestrial source and affect the conservative mixing. Indeed, in late summer, the arrival of the Amazon river nutrient-rich (silicates, phosphore, nitrogen) waters stimulates the primary production and thus, induces an increase of dissolved matter next to the Caribbean Sea (Beers et al. [1968]). In summer, from May to July, the biological activity increases in the northwestern part of the plume, which is seen in monthly maps of primary productivity (not shown

5.6. Discussion & Conclusions

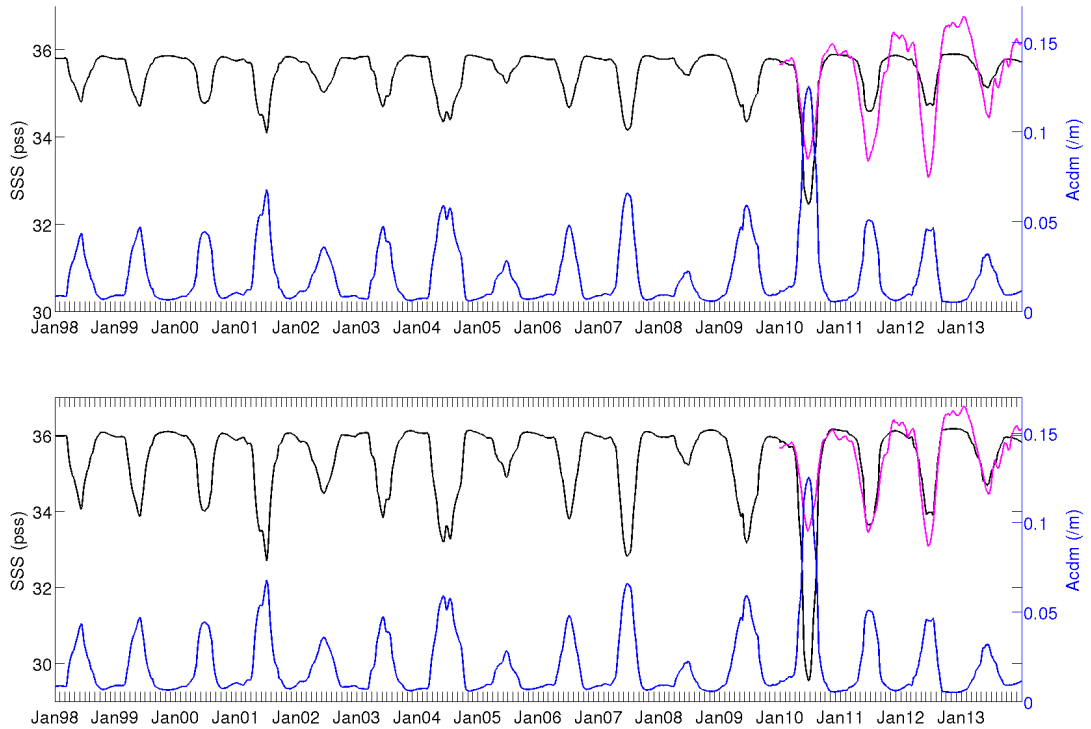


Figure 5.18: 1998-2013 time series of a_{cdm} (blue) at location $[14^{\circ}\text{N } 55^{\circ}\text{W}]$, shown by the blue dot on figure 5.8. As a magenta solid line is represented the 2010-2013 time series of SMOS SSS. As a black solid line is represented the time series of retrieved SSS based on the model using the whole dataset (top panel) and the one putting aside summer 2010 data.

here). Thus, errors may have been introduced computing the conservative mixing in each pixel over the years 2010 to 2013.

Photobleaching (degradation of cdm mainly due to the availability of light) is one of the possible removal processes which can affect the conservative mixing. Indeed, during boreal summer, especially at the edges of the plume, where the riverine materials become less and less important, light is more available in the first meters of the surface layer.

We have identified a possible non conservative process in the northwestern part of the Amazon plume from May through July 2010. To get rid of the errors associated with that phenomenon, which possibly affect the SSS retrieval, we ran our model we computed putting aside SSS and a_{cdm} data between the 1st of May and the 31st of July 2010. We compute thus the slope and endmember values of the linear regression in each $0.25 \times 0.25^{\circ}$ pixel (see figure 5.17 on the right). Figure 5.17, on the left represents the map of the linear regression R-squared coefficient. Comparing this R-squared map to the one obtained considering the whole dataset over 2010-2013 (see figure 5.2), we can notice that the R-squared values are higher when summer 2010 data are discarded. At locations

Chapter 5. Application : Sea Surface Salinity retrieval from Ocean Color in the Amazon Plume

[6.5°N 46°W] and [19°N 51.5°W] (not shown here), the retrieval SSS is identical to the SSS retrieved considering the whole data range (see figure 5.7 on top and bottom panels). Putting aside summer 2010 data doesn't affect the retrieval algorithms anywhere in the Amazon plume except in the northwestern part. On figure 5.18 are represented the time series of a_{cdm} , SMOS and retrieved SSS at the location pointed out in the figure 5.8 by a blue dot using both models (putting aside and not, summer 2010 data). At that location ([14°N 55°W]), in the northwestern part of the plume, the retrieved SSS considering or not summer 2010 data are different (see figure 5.18). When summer 2010 data are discarded, the SSS minima are better-retrieved in 2011, 2012 and 2013. In 2010, comparing with SMOS data, the retrieved SSS is too low (4 pss difference with SMOS in July 2010). Indeed, due to a possible non conservative behaviour such as primary production, in summer 2010, the a_{cdm} value is abnormally high. Thus, as the SSS retrieval is based on a_{cdm} , the retrieved SSS is, as a consequence, abnormally low.

We have just demonstrated that non conservative process occurring at precise time and location can largely affect the SSS/ a_{cdm} relationship. Thus, these processes have to be taken into account for any attempt of SSS retrieval based on the conservative mixing and ocean color data.

Chapter 6

A Lagrangian Approach of the Relationship between Sea Surface Salinity and Light Absorption in the Amazon Plume

6.1 Introduction

In this thesis work, the relationship between sea surface salinity (SSS) and optical properties, also called conservative mixing, in the Amazon-Orinoco river plume was analyzed in terms of correlations between SSS and optical properties measurements. We relied on SSS data and absorption coefficient of colored detrital matter (a_{cdm}) at 443 nm measurements within the plume waters, estimated from spaceborne sensors. Clear negative correlations between SSS and these optical parameters were well evidenced and the regional and local conservative mixing relationships were established.

These two different approaches of the conservative mixing in the Amazon plume, explored in the chapter 4, are based on an Eulerian analysis. Freshwater masses discharged from the Amazon mouth have initial characteristics which may depend on the Amazon and its tributaries discharge cycles, and thus, on the period of the year. As they mix from the mouth to the open ocean, fresh waters may undergo many different physical and biogeochemical processes which might affect the conservative mixing. Moreover, as water masses can travel for several months in the river plume before getting to the open ocean, others can travel for a few weeks only. Computing a relationship between sea surface salinity and optical properties based on an Eulerian approach means to consider together different water masses discharged at different periods of the year with different initial characteristics and which undergo different processes as they mix into the open ocean. A more intuitive approach would be based on a Lagrangian analysis of the conservative mixing, which consists in following a particle from the mouth of the river to the open ocean and studying its mixing process along its trajectory.

In this chapter, we attempt to explore the conservative mixing based on a Lagrangian analysis. After explaining the methodology of our Lagrangian analysis of the conservative mixing, we show few examples of drifters launched at the mouth of the river and followed to the open ocean as they mix. Finally, we show the statistical Lagrangian analysis of

Chapter 6. A Lagrangian Approach of the Relationship between Sea Surface Salinity and Light Absorption in the Amazon Plume

the conservative mixing based on all the drifters launched at different periods of the year at the Amazon mouth. We then attempt to compute a conservative mixing relationship based on this analysis.

6.2 Methodology

Virtual drifters are dropped everyday at the mouth of the Amazon river and are followed during 366 days along their trajectories computed using the altimetric currents from OSCAR (see figure 3.5 for the monthly average current speed from OSCAR over 2010). On figure 3.5, we clearly see that during the low flow (December-January), currents trap the Amazon waters next to the mouth of the river. Then, waters are carried by the northwestward current along the Brazilian shelf (North Brazilian Current). Around June, the North Equatorial Counter Current reverses, becomes stronger and carries the Amazon waters eastwards through the NBC retroflexion. According to the OSCAR currents, and as often reported, two principal pathways for the Amazon waters are thus highlighted.

Everyday from January, the 1st of 2010 to December, the 31st of 2012, drifters are dropped in each $0.25 \times 0.25^\circ$ pixel of the box $[49.5^\circ\text{W } 45^\circ\text{W } 0.5^\circ\text{N } 6^\circ\text{N}]$. At this initial position, each virtual drifter has a value of a_{cdm} , sea surface salinity and eastward and northward horizontal velocities (u and v , respectively). From altimetric u and v , the position of each drifter on the following day can be estimated using a spline interpolation. Then, based on the new position of the drifter, values of SSS and a_{cdm} for this following day are computed as the values of the closest pixel of the a_{cdm} and SSS grids. So on, the positions of the drifters are estimated everyday using altimetric currents and SSS and a_{cdm} values are computed everyday along the drifter trajectory for 366 days.

As we are interested in the mixing of particles from the mouth of the river to the open ocean, only the virtual drifters having an initial SSS value lower than 32 pss are stored. Finally, we obtain 35764 drifters launched over 2010-2012. Looking at the density of drifters launched per month (not shown here), all year long, drifters are launched in the area very closed to the mouth, an area where SSS are below 32 pss all along the year. From April, more drifters are launched northwestward and from July, eastward, when the NBC retroflexion appears. Accordingly, the number of drifters launched in spring-early summer is higher than during other periods of the year (see figure 6.1). In spring-summer 2011, this number is higher than during other years, the area where SSS are below 32 pss might be larger in spring-summer.

6.2. Methodology

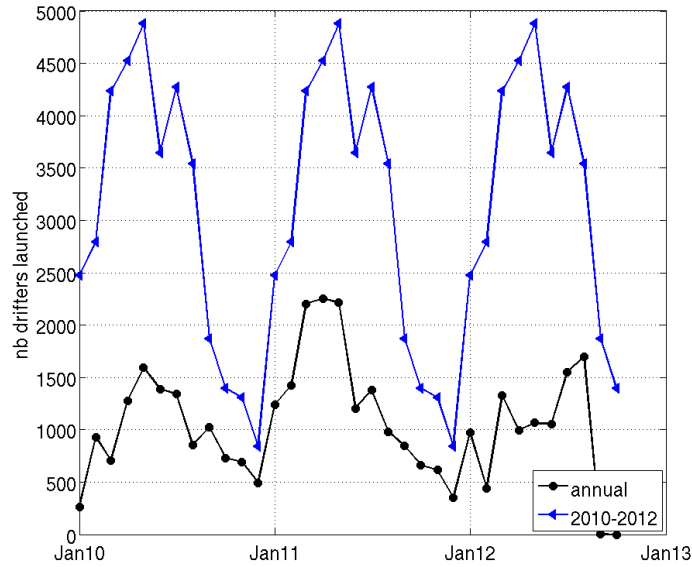


Figure 6.1: Number of drifters launched each month from 2010 to 2012 (black) and the monthly average number of drifters launched each month over 2010-2012.

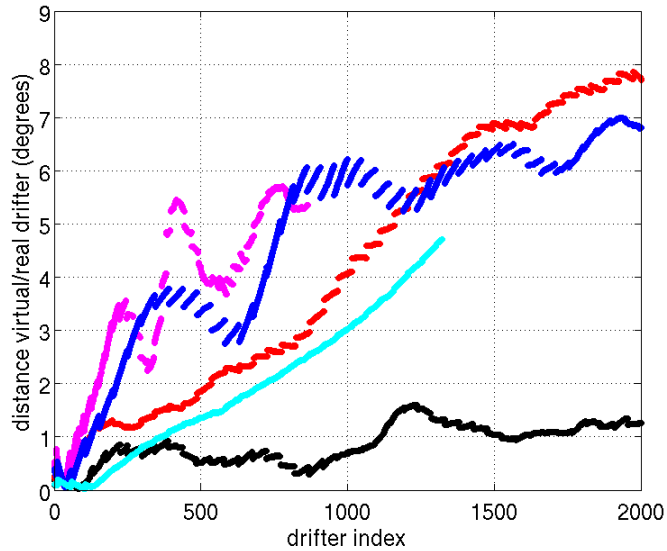


Figure 6.2: Distance between the real and the virtual drifters along the trajectory of 5 drifters. The drifter index representing and index of the time from the drifter launch.

To validate this method, we used *in situ* observations acquired thanks to several drifters launched in this region over the period 2010-2012. 5 drifters have been launched over this period in the northwestern tropical Atlantic ocean. Virtual drifters have been launched at

Chapter 6. A Lagrangian Approach of the Relationship between Sea Surface Salinity and Light Absorption in the Amazon Plume

the same initial dates and positions and then, the virtual trajectories are compared with the effective trajectories of the real drifters. In figure 6.2 are represented the distance between the virtual and real drifters along their trajectories. Altimetric currents are sampled about every 10 days at approximately 100 km of spatial resolution. Consequently, comparing the drifter trajectories based on these altimetric currents with *in situ* drifters must bring up differences in the trajectories. In all the examples, the trajectories during the first days seem to be coherent before deviating from each other.

6.3 Virtual Drifters Examples

In this section, we show examples of several virtual drifters dropped at the mouth of the Amazon river at different periods of the year. In figure 6.3, on the left panel, we can see the trajectory of each drifter followed during one year, and on the right panel, the evolution of SSS and a_{cdm} values along the trajectory of each drifter from the mouth to the open ocean is represented.

For most of the drifters, two different periods can be distinguished. First, the particle mixes with different water masses and its salinity tends to increase or decrease depending on the water masses met. After this mixing or turbulent period, the salinity and a_{cdm} , respectively, slowly and regularly increases and decreases, respectively, until it reaches the open ocean.

The drifter launched on the 18th of February 2010 (figure 6.3, first row), travelled north-westward along the Brazilian shelf up to the open ocean. The turbulent period seems to last around 4-5 months, until July 2010. The other drifter, launched in late spring-summer (on the 26th of June 2010) travelled eastward along the North Equatorial Counter Current. The turbulent period lasts around 3 months (see figure 6.3, second row).

6.4. Statistical Analysis

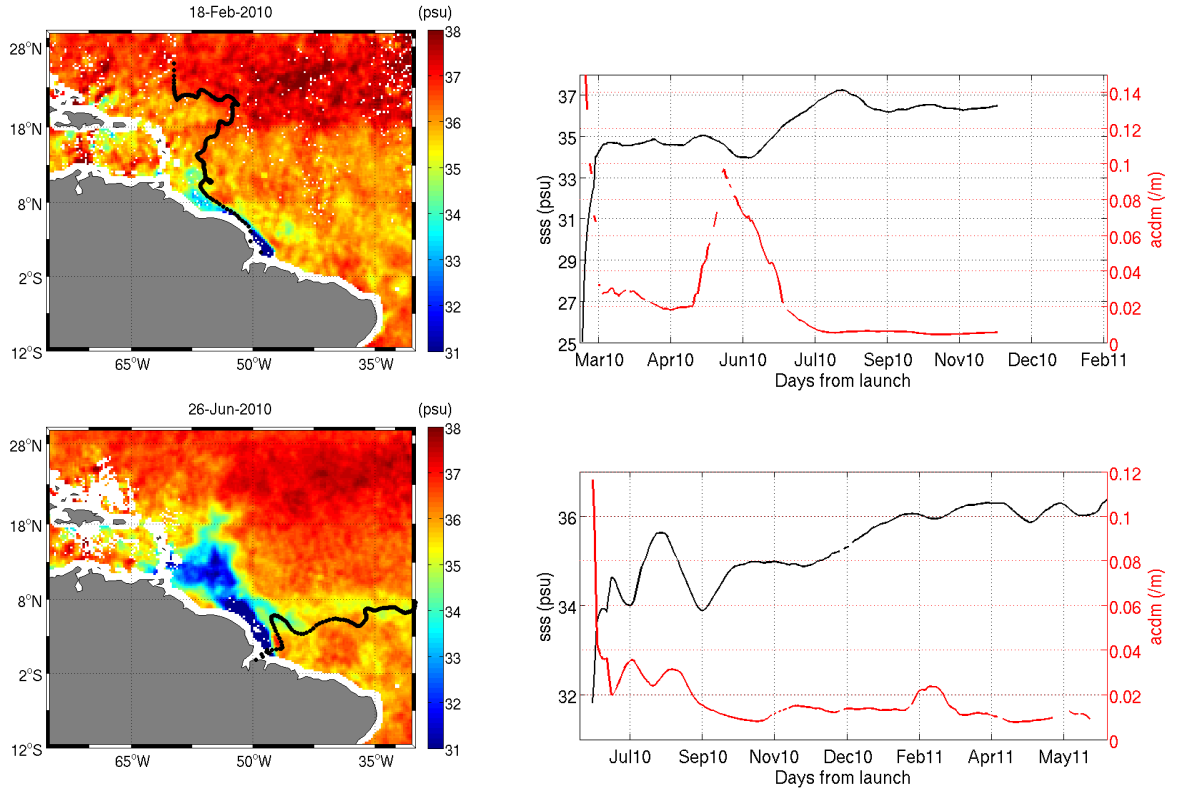


Figure 6.3: (left panel) Average SMOS SSS on the drifter initial day on top of which is represented the drifter trajectory. (right panel) SSS and a_{cdm} value in each of the drifter positions along its trajectory.

6.4 Statistical Analysis

6.4.1 Mixing and relaxation behaviours along the trajectory

We have seen on few examples of drifters launched in 2010 that 2 different behaviours are noticeable along the drifter's trajectory : a mixing behaviour during the first weeks/months and a relaxation behaviour until the drifter reaches the open ocean. We first try to compute the time for which the mixing is over (t_1) and the time for which the drifter reaches the open ocean (t_2). t_1 and t_2 are computed considering all the drifters launched over 2010-2012.

Over the whole period 2010-2012, considering all the drifters launched, we compute the average SSS, a_{cdm} and current speed values as a function of the days from the launch of the drifters (see figure 6.4). Along the average trajectory, as expected, the mean SSS tends to increase as fresh waters from the Amazon river mix into the open ocean, and the mean a_{cdm} tends to decrease. Furthermore, the mean current speed along the average trajectory tends to decrease proportionally with SSS. This shows that the current is a

Chapter 6. A Lagrangian Approach of the Relationship between Sea Surface Salinity and Light Absorption in the Amazon Plume

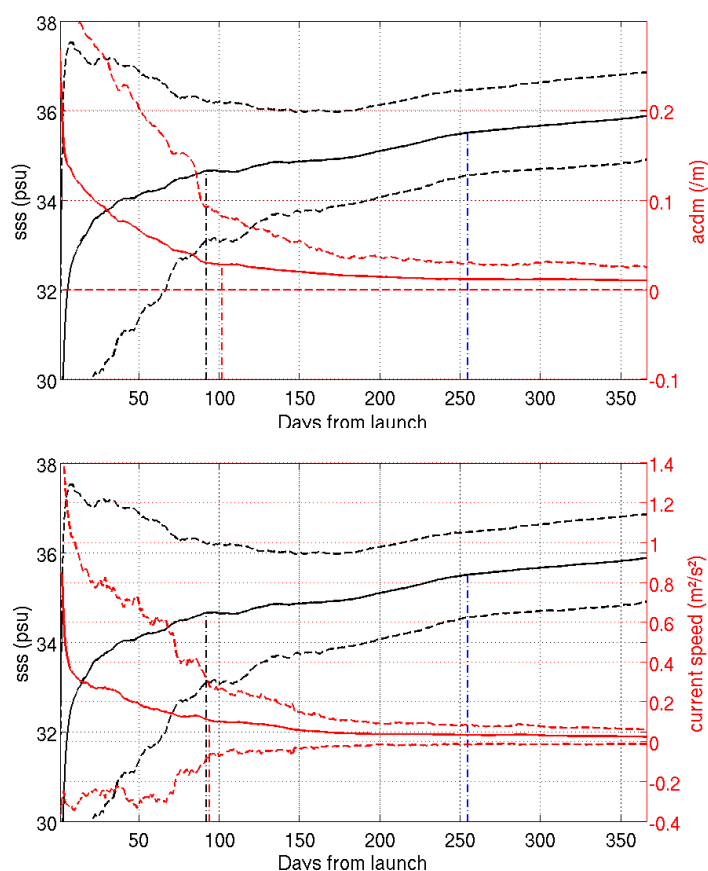


Figure 6.4: (top) : Average SSS (black) and a_{cdm} (red) per bin of day from the drifter launch for all the drifters launched during the period 2010-2012 ± 1 standard deviation. The vertical black dotted line represents t1 computed based on the SSS signal. The red dotted line represents t1 computed based on the a_{cdm} signal and the blue one represents t2. (bottom) : Average SSS (black) and current speed (red) per bin of day from the drifter launch for all the drifters launched during the period 2010-2012 ± 1 standard deviation. The vertical black dotted line represents t1 computed based on the SSS signal. The red dotted line represents t1 computed based on the current speed signal and the blue one represents t2.

major parameter affecting the fresh waters' mixing along the trajectory of the drifters. The standard deviation is also represented on figure 6.4. We can distinguish the 2 different behaviours discussed above. Just after the drifter launch, the standard deviation of each parameter is quite high, all the drifters have various behaviours, this is the mixing period. Some of them go out of the plume quite quickly (SSS reaches 35.5 pss), others are trapped in rings and are mixed with "younger" water masses during a longer time before getting out of the plume. After few months (around 100 days here), the standard deviation stabilizes and the SSS and a_{cdm} tend to increase and decrease, respectively, slowly and constantly, t1 has been reached and we enter in the relaxation period. Finally, the SSS along the average trajectory reaches 35.5 pss, the plume limit, the drifter reaches the open ocean, t2 is then reached. As mean SSS, a_{cdm} and current speed values, respective

6.4. Statistical Analysis

standard deviations are coherent along the average trajectory, especially the SSS and current speed standard deviations.

To compute t_1 and t_2 , we consider a criteria on the SSS, a_{cdm} and current speed standard deviation along the trajectory. For SSS, t_1 is the time for which the mean SSS reaches the average SSS standard deviation along the average trajectory. t_2 is the time for which, the mean SSS reaches 35.5 pss (see figure 6.4). Considering a_{cdm} and current speed, t_1 is computed in an equivalent way. t_1 for SSS and for current speed are almost identical, SSS and current speed standard deviations evolve in a coherent way which may imply that currents directly affect the mixing period. t_2 is also computed for a_{cdm} , it corresponds to the time for which the mean a_{cdm} plume limit value is reached. This value is computed as the mean a_{cdm} value of the pixels corresponding to a SSS of 35.5 pss, over 2010-2012. This value is 0.0144 /s.

6.4.2 The conservative mixing along the drifter trajectory

Our goal here is to study the conservative mixing, the relationship between SSS and a_{cdm} , based on a Lagrangian analysis. We will thus compute the relationship between the average SSS and a_{cdm} along the average drifters trajectory from the drifters' launch. We have seen in the previous section that drifters can have different behaviours, different mixing and relaxation period lengths. To free ourselves from this, we normalize each drifter from the launch to t_1 and from t_1 to t_2 . t_1 and t_2 being the maximum times between SSS and a_{cdm} t_1 and t_2 , respectively.

In figure 6.5, are represented the mean SSS, current speed and a_{cdm} values per bin of days from the drifter's launch, normalized by the t_1 and t_2 computed over 2010-2012. From 0 to 1, this is the mixing period, the standard deviation is higher, then, from 1 to 2, it stabilizes, this is the relaxation period. Around t_2 , drifters reach the open ocean.

Then, we studied the average SSS/ a_{cdm} relationship along the drifters trajectories, from the normalized trajectories computed in the previous section. In figure 6.6, the average a_{cdm} values along the drifters trajectories are plotted against the average SSS values, the day from the launch is represented on the z-axis. This relationship is compared to the 2010-2012 average global Eulerian relationship found in the first part of the chapter 4. The Lagrangian relationship is linearly interpolated from t_1 to t_2 . In the Lagrangian relationship over 2010-2012, we can distinguish the 2 behaviours by a breaking in the slope

Chapter 6. A Lagrangian Approach of the Relationship between Sea Surface Salinity and Light Absorption in the Amazon Plume

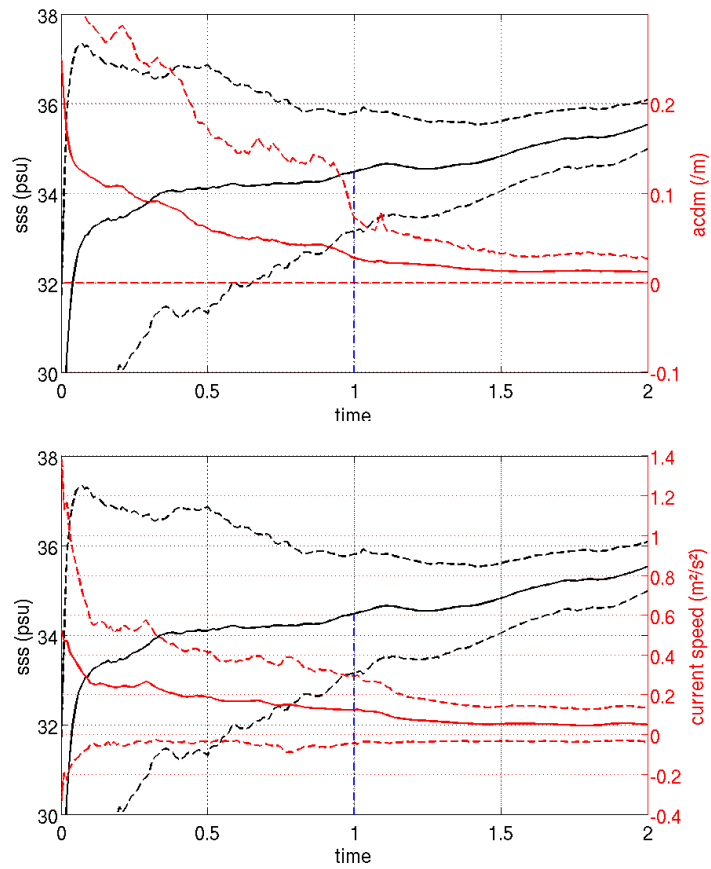


Figure 6.5: Average (top) SSS and a_{cdm} and (bottom) SSS and current speed per bin of day from the drifter launch for all the drifters launched in the period 2010-2012 which have been normalized. The blue dotted lines represents t_1 .

of the relationship. From the launch to t_1 (marked by the black circle in figure 6.6), the slope is large and higher than the one of the 2010-2012 Eulerian relationship. Then, from t_1 to t_2 , the slope decreases and is consistent with the slope of the Eulerian relationship.

6.5. Conclusions

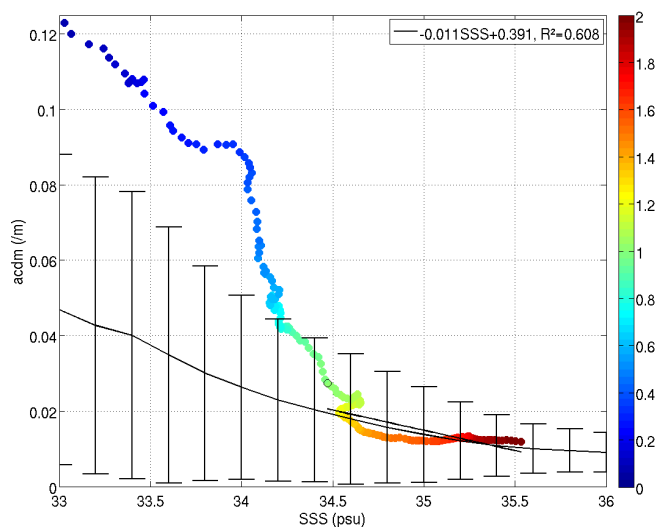


Figure 6.6: $A_{cdm}(t)$ as a function of $SSS(t)$ along the mean drifter trajectory from the launch day, binned per day from the day of launch. The black circle marks t_1 . As a black line is represented the interpolation of the Lagrangian relationship from t_1 to t_2 . The black errorbar represents the 2010-2012 regional Eulerian SSS/a_{cdm} relationship ± 1 standard deviation.

6.5 Conclusions

In this chapter, we explored a new approach of the conservative mixing relationship between sea surface salinity and absorption coefficient of colored detrital matter at 443 nm in the Amazon plume, based on a Lagrangian analysis. We attempted to study the dilution process of the Amazon freshwater masses from the mouth to the open ocean along their trajectory. Indeed, each river freshwater mass mixing from the river mouth to the open ocean, has its own initial biological characteristics depending on the Amazon discharge, can encounter different water masses along its mixing and flow along its own advection pathway depending on the seasonal currents and winds. All these phenomena can affect the dilution process of these water masses and have to be taken into account in the attempt to compute a conservative mixing relationship in river plumes. Considering a Lagrangian analysis is the only way to take into account all these aspects.

In this analysis, we highlighted two behaviours along the drifters trajectories, whatever their date of launch. During the first few weeks/months, we highlighted a mixing behaviour, the water masses encounter other fresher or saltier water masses in the river plume, depending on each water mass trajectory. SSS tends to drop or increase depending on the water mass encountered and a_{cdm} tends to increase or drop, respectively. The mixing period duration is different for each virtual drifter launched and depends on the

Chapter 6. A Lagrangian Approach of the Relationship between Sea Surface Salinity and Light Absorption in the Amazon Plume

trajectory taken by the drifter and thus on the season of launch.

After this mixing behaviour, drifters SSS and a_{cdm} values tend to relax increasing and decreasing, respectively, slowly and continuously to reach the open ocean SSS and a_{cdm} values, respectively.

These 2 behaviours are clearly noticeable in the computation of the conservative mixing relationship by a break in the slope of the relationship.

This Lagrangian analysis needs to be deeply explored in the future. We could, for example, envisage to normalize the SSS and a_{cdm} values with respect to SSS and a_{cdm} values at the mouth of the river. This may decrease the standard deviation values in the figures 6.4 and 6.5.

Conclusions & Perspectives

Conclusions

In the frame of this PhD work, we focused on the northwestern tropical Atlantic ocean area. This region is subject to many major forcing processes. The Amazon river, a main player of the land/sea interactions, discharges large amounts of fresh waters highly concentrated in dissolved and suspended organic matter in the ocean. This can have an important impact on the local biogeochemistry and physics. The area is also subject to local and tidal currents, trade winds and precipitations, all being physical forcings having an important impact on the local area.

We attempted to use a synergetic approach based on many different sensors measuring among others sea surface salinity, optical properties, wind speed, current speed to study this region.

We first showed that the forcings influencing the Amazon plume region have a seasonal variability which affects the dispersal of Amazon fresh waters. Comparing the seasonal evolution of the Amazon waters dispersal to the seasonal cycle of the different forcings influencing the region, we demonstrated for the first time that the Amazon discharge is the main player in its plume extension. Indeed, there is a linear relationship between the Amazon discharge levels and the plume extension considering a 3-month lag. Moreover, it has been shown that the seasonal cycle of trade winds affecting the region can be related to the seasonal variability of the Amazon plume extension.

Using these sensors, we then documented the well-known relationship between sea surface salinity and optical parameters using spaceborne SSS and Ocean Color data in the Amazon plume, for the first time. Thus, we demonstrated the consistency between a microwave instrument and optical instruments. Thanks to remote sensing, this represents a new approach of the SSS/α_{cdm} relationship with a largely improved spatio-temporal monitoring.

We studied the conservative mixing using different approaches. The first one, based on a regional approach of the conservative mixing, is similar to the ones carried on by several authors in river plume areas. Thanks to the spaceborne measurements of sea surface salinity, we were able to study for the first time the regional conservative mixing with improved spatial and temporal resolutions. A clear seasonal cycle in the relationship's slope has been highlighted and related to the Amazon river discharge cycle whereas no spatial variability in the relationship could be inferred from this analysis. At the end,

any noticeable possible spatial or interannual variability in the relationship was related to non conservative processes affecting the relationship between SSS and a_{cdm} , especially during the 2010 high flow period.

As this method doesn't seem to be appropriate to follow the dilution process of water masses from the Amazon mouth to the open ocean, a local approach is envisaged. SSS and a_{cdm} are significantly negatively correlated in the whole plume area. All year long, the Amazon waters are advected from the mouth to the open ocean and mixed with the surrounding water masses, locally. Amazon waters reach each region of the plume gradually after flowing through different advection pathways and after encountering different water masses. Thus, we chose to consider the conservative mixing locally for each $0.25 \times 0.25^\circ$ pixel in the plume area. Accordingly, one conservative mixing relationship was established per pixel and it was then shown that the slope and endmember values vary from a region to another. The conservative mixing relationship thus evolves as a space-time mapping of the seasonal circulation.

Whatever the approach of the conservative mixing considered, SSS and ocean color properties are spatially and temporally coherent in the Amazon plume. Moreover, all these conclusions call into question the previous studies in which *in situ* data collected at precise locations and dates are used to establish the conservative mixing.

Finally, we attempted to explore a new approach of the conservative mixing relationship between sea surface salinity and absorption coefficient of colored detrital matter at 443 nm in the Amazon plume, based on a lagrangian analysis. We studied the dilution process of the Amazon freshwater masses from the mouth to the open ocean along their trajectory. Indeed, each river freshwater mass mixing from the river mouth to the open ocean, has its own initial biological characteristics depending on the Amazon discharge, and can encounter different water masses along its mixing and flows along its own advection pathway depending on the seasonal currents and winds. All these phenomena can affect the dilution process of these water masses and have to be taken into account in the attempt to compute a conservative mixing relationship in river plumes. Considering a lagrangian analysis is the only way to take into account all these aspects.

During the first few weeks/months after the launch, we highlighted a mixing behaviour, the water masses encounter other fresher or saltier water masses in the river plume, depending on each water mass trajectory. The mixing period duration is different for each virtual drifter launched and depends on the trajectory taken by the drifter and thus on the launch season. After this mixing behaviour, drifters SSS and a_{cdm} values tend to

relaxe and increase or decrease, respectively, slowly and continuously to reach the open ocean SSS and a_{cdm} values. These 2 behaviours are clearly noticeable in the computation of the conservative mixing relationship by a break in the slope of the relationship.

Once the conservative mixing relationships were established robustly using the local approach (the second approach presented here), they are used to retrieve a daily ± 45 days 25-km SSS product based on Ocean Color data. This product is validated against SMOS and *in situ* SSS. Compared to SMOS and *in situ* SSS, our model well-retrieve strong SSS fronts and gradients in the Amazon plume. As an overall, our model gives good results especially for $SSS > 30$ pss. At low SSS ($SSS < 30$ pss), our model tends to overestimate SSS.

Perspectives

First of all, regarding the method, the main limitation in this analysis is the precision and quality of the ocean color products. A local algorithm dedicated to the northwestern tropical Atlantic ocean should improve the precision and quality of those data in this area.

Moreover, in the chapter 6, we explored a new approach of the conservative mixing, a lagrangian method. This method needs to be deeply explored in the future and improved.

Finally, a SSS retrieval algorithm from ocean color properties and based on the conservative mixing was established in the frame of this work. Improvements in the SSS retrieval algorithm could be done.

First, as we have seen that several non conservative behaviours, such as the primary productivity, can affect the SSS/a_{cdm} relationship established, net primary production data could be added to the algorithm to retrieve better sea surface salinity in the Amazon plume. Generally, non conservative behaviours (biogeochemical & physical) could be integrated into the algorithm.

Moreover, AMSR-E brightness temperature data could be added to the SMOS and a_{cdm} data to improve the SSS retrieval algorithm. Indeed, as demonstrated by Reul et al. [2009], it is possible to retrieve a SSS signal in the Amazon plume from the AMSR-E radiometer brightness temperatures from the C and X bands, in particular from the difference between the C (6.9 GHz) and X (10.7 GHz) bands brightness temperatures ($\Delta T_b = T_{bv}^{6.9} - T_{bv}^{10.7}$). More details on this assertion are shown in the appendix B. In this ap-

pendix, we also show some results of the attempts to retrieve a SSS product based on C and X bands of the AMSR-E radiometer. In figure 7.1, are represented the 1998-2013 a_{cdm} and retrieved SSS using our model at location $[6.5^{\circ}\text{N } 46^{\circ}\text{W}]$ pointed out by a black dot in figure 4.41. As a magenta solid line is represented the 2010-2013 SMOS SSS time serie. As a red solid line is represented the 2003-2010 time serie of AMSR-E ΔT_b rescaled to match the SSS scale. AMSR-E ΔT_b represents indeed a good proxy for the SSS fronts and strong gradients. As it seems to perfectly retrieve the SSS drops and a_{cdm} increases when the plume waters reach the area, it seems to detect later the SSS increases or a_{cdm} drops. Generally, ΔT_b begins to drop at the same time as a_{cdm} begins to increase but the increase of ΔT_b takes more time than the a_{cdm} decrease. As the SSS fronts are well-detected by AMSR-E, the amplitude of the signal seems poorly detected. Over 2003-2010, our model and ocean color sensors detect an interannual variability in the amplitude of the SSS decreases and increases which is not detected by AMSR-E.

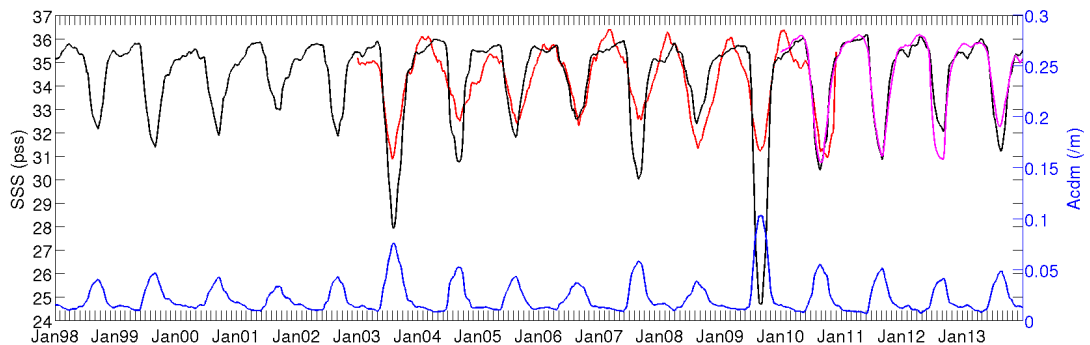


Figure 7.1: 1998-2013 time series of a_{cdm} (blue) and retrieved SSS (black) at location $[6.5^{\circ}\text{N } 46^{\circ}\text{W}]$, marked by a black dot in figure 4.41. As a magenta solid line is represented the 2010-2013 time serie of SMOS SSS and as a red solid line is represented the 2003-2010 time serie of AMSR-E ΔT_b .

In the future, other spaceborne SSS measurement should be considered in this study. Higher-level data products such as blended satellite and *in situ* data fields, blended Aquarius-SMOS analyses and data assimilation products could be a way to compensate for the bias seen in SMOS data at low sea surface salinity. Now that spaceborne L-band instruments proved themselves, future missions carrying L-band radiometers are planned. The NASA Soil Moisture Active Passive (SMAP) mission, planned to be launched in 2014, will carry a radiometer and a synthetic aperture radar operating at L-band.

Regarding the applications of this method, we haven't deeply explored the use of this conservative mixing relationship to study the deviations from the conservative mixing and

their eventual sources. Deviations could occur due to biogeochemical processes such as net primary productivity, photobleaching, flocculation. The non conservative behaviours in the relationship due to primary production have been briefly explored in this work but much needs to be done. Deviations could also occur because of physical processes such as tropical rivers discharges, precipitation/evaporation fluxes, air/sea interactions (hurricanes), advection...

Finally, several geophysical applications back in time from 1998 can now be explored regarding among other the plume extension variability, air/sea interactions, biogeochemistry, land/sea interactions.

Synthetic profiles could, for example, be deduced from sea surface salinity to get an information on the depth of the surface layer containing Amazon plume fresh waters. From this, we could get an information on the 3 dimensional dispersal of the Amazon waters. Another topic of research which could be explored is the study of rings shedding off the North Brazilian Current using sea surface salinity observations. On June the 29th, 2010, a ring shed off the NBC retroflection and had a clear SSS signature (see figure 7.2 on the left). Freshwater masses from the Amazon plume were carried northwestward by the ring on its external part. On the hovmueller graph on figure 7.2 on the right, the track of this ring is clearly noticeable, the ring being fresh on its external part and salty in its core.

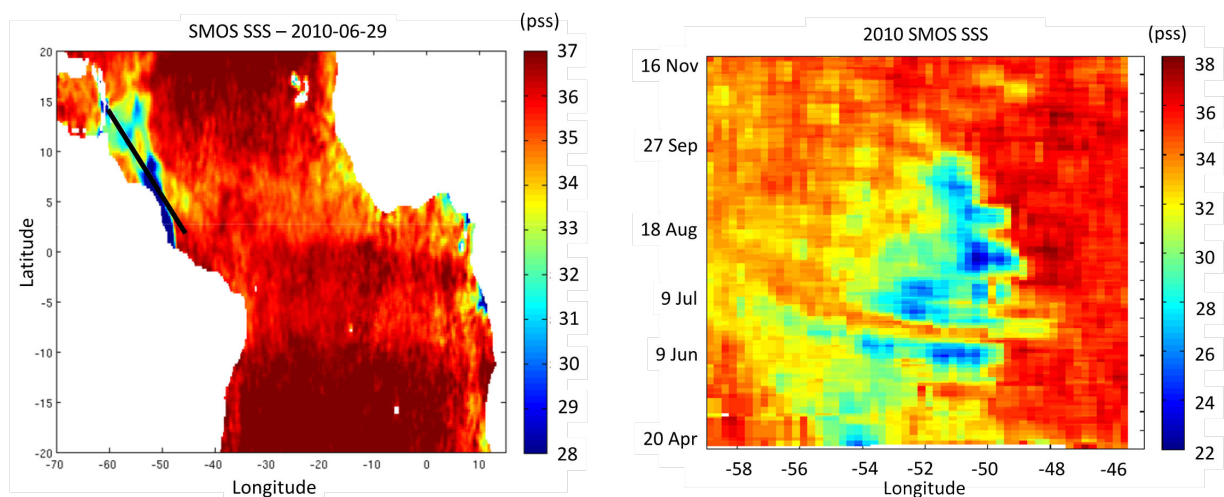


Figure 7.2: (Left) SMOS SSS maps on the 29th of June 2010 on top of which is represented the hovmueller position as a black solid line. (Right) SMOS SSS hovmueller graph in 2010 along the transect.

Appendix A

The Northwestern Tropical Atlantic Ocean

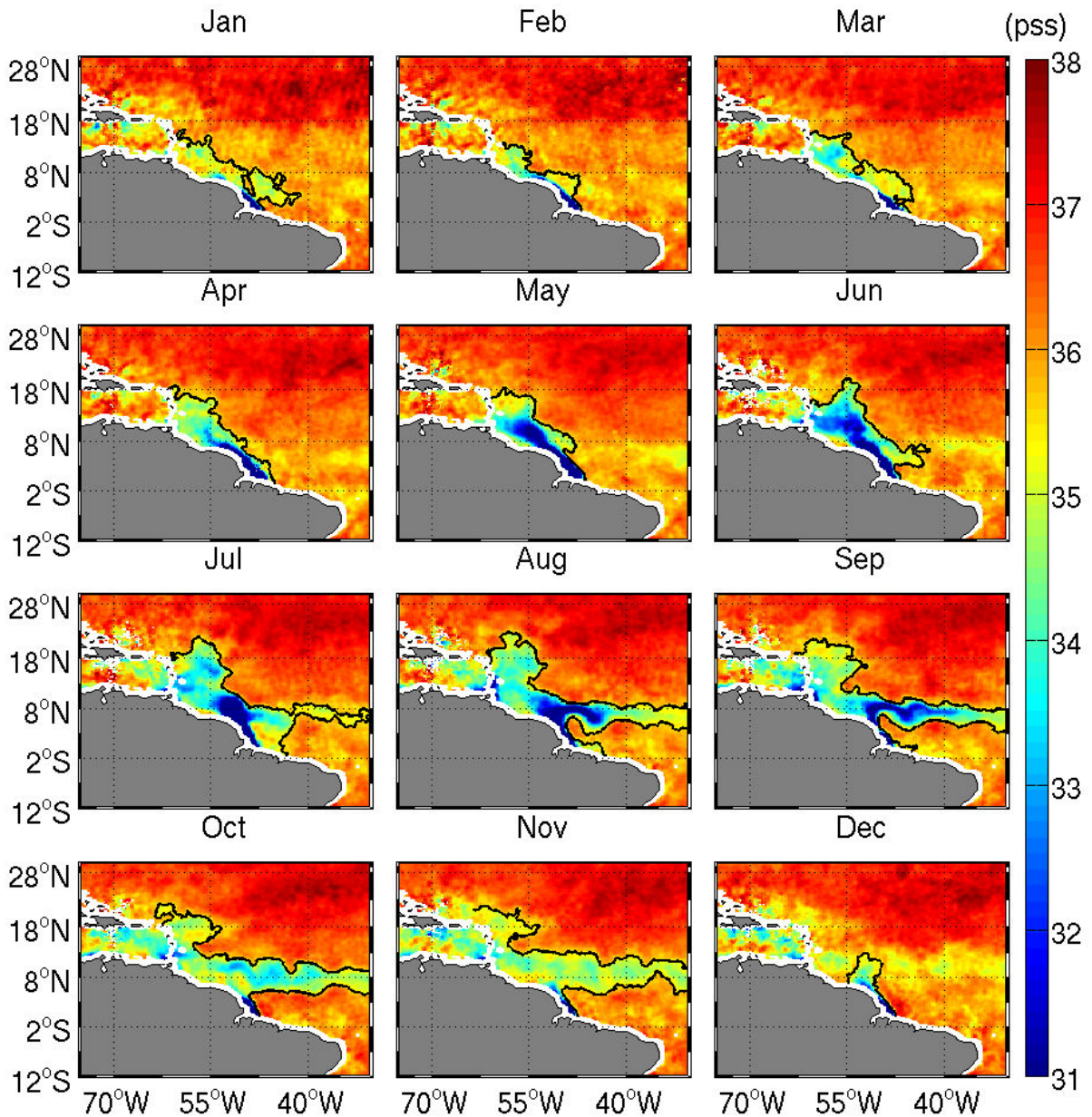


Figure A.1: Monthly SMOS sea surface salinity from January to December 2010, on top of which is represented the 2010 monthly 35.5 pss contour.

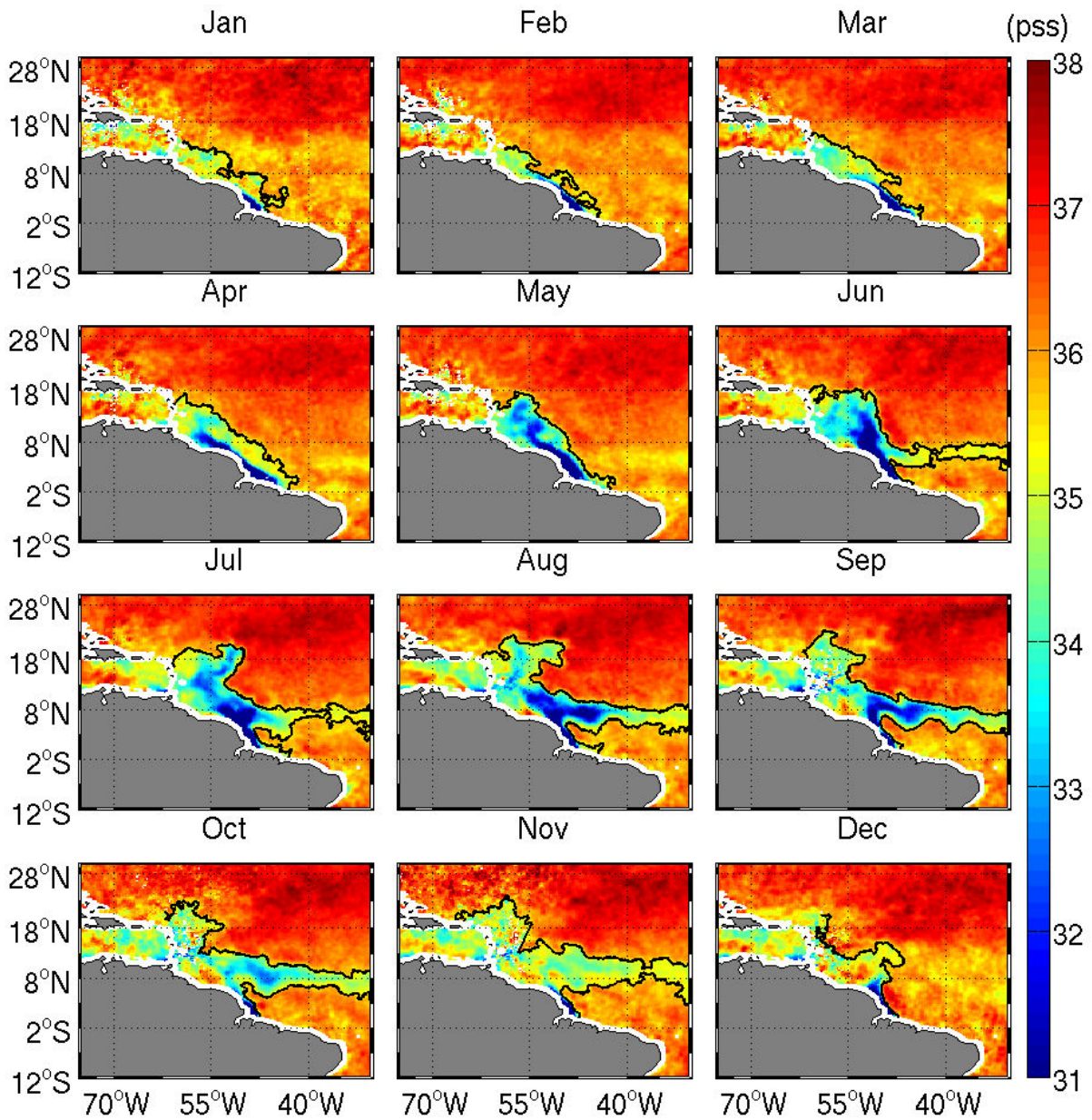


Figure A.2: Monthly SMOS sea surface salinity from January to December 2011, on top of which is represented the 2011 monthly 35.5 pss contour.

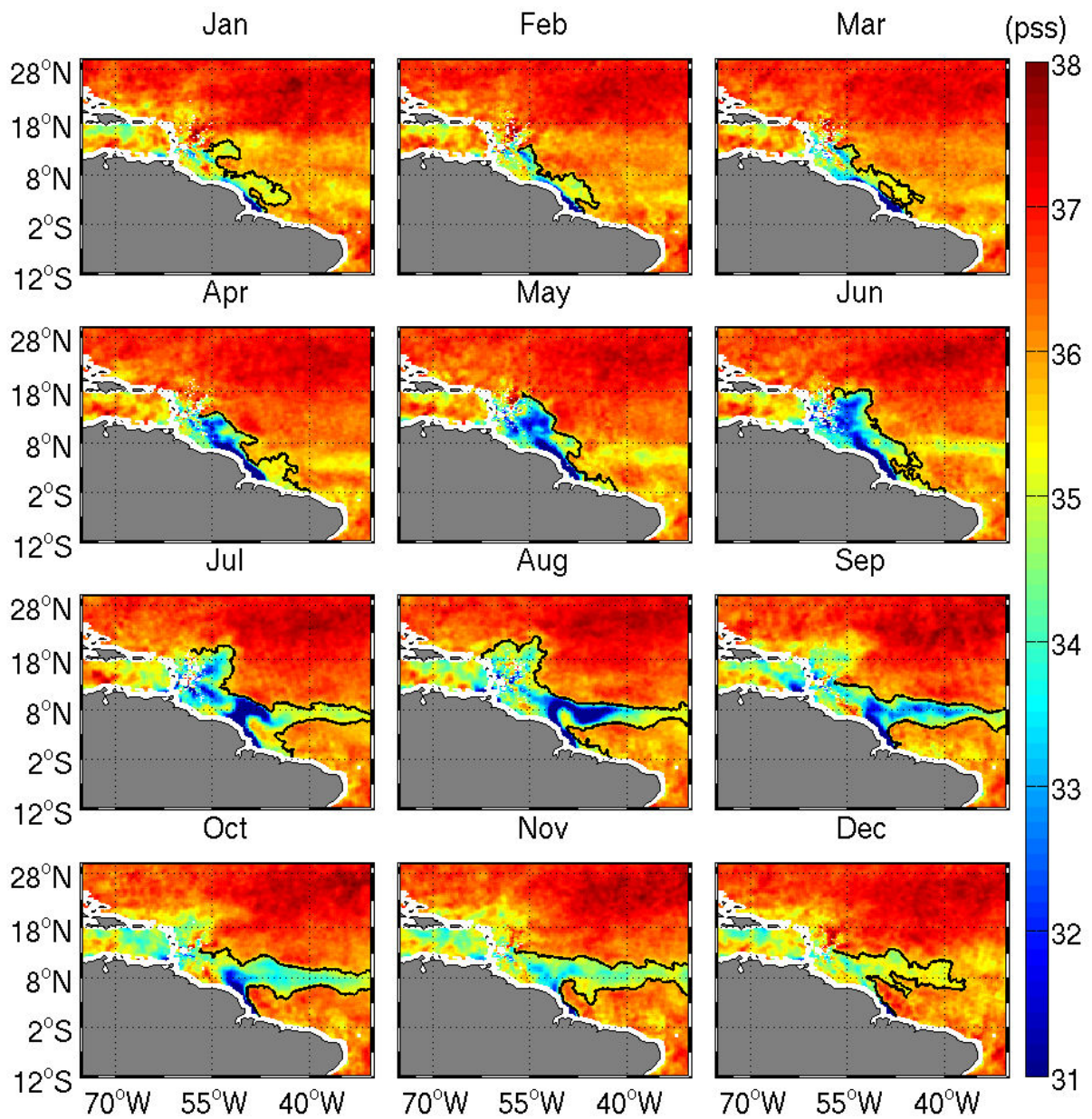


Figure A.3: Monthly SMOS sea surface salinity from January to December 2012, on top of which is represented the 2012 monthly 35.5 pss contour.

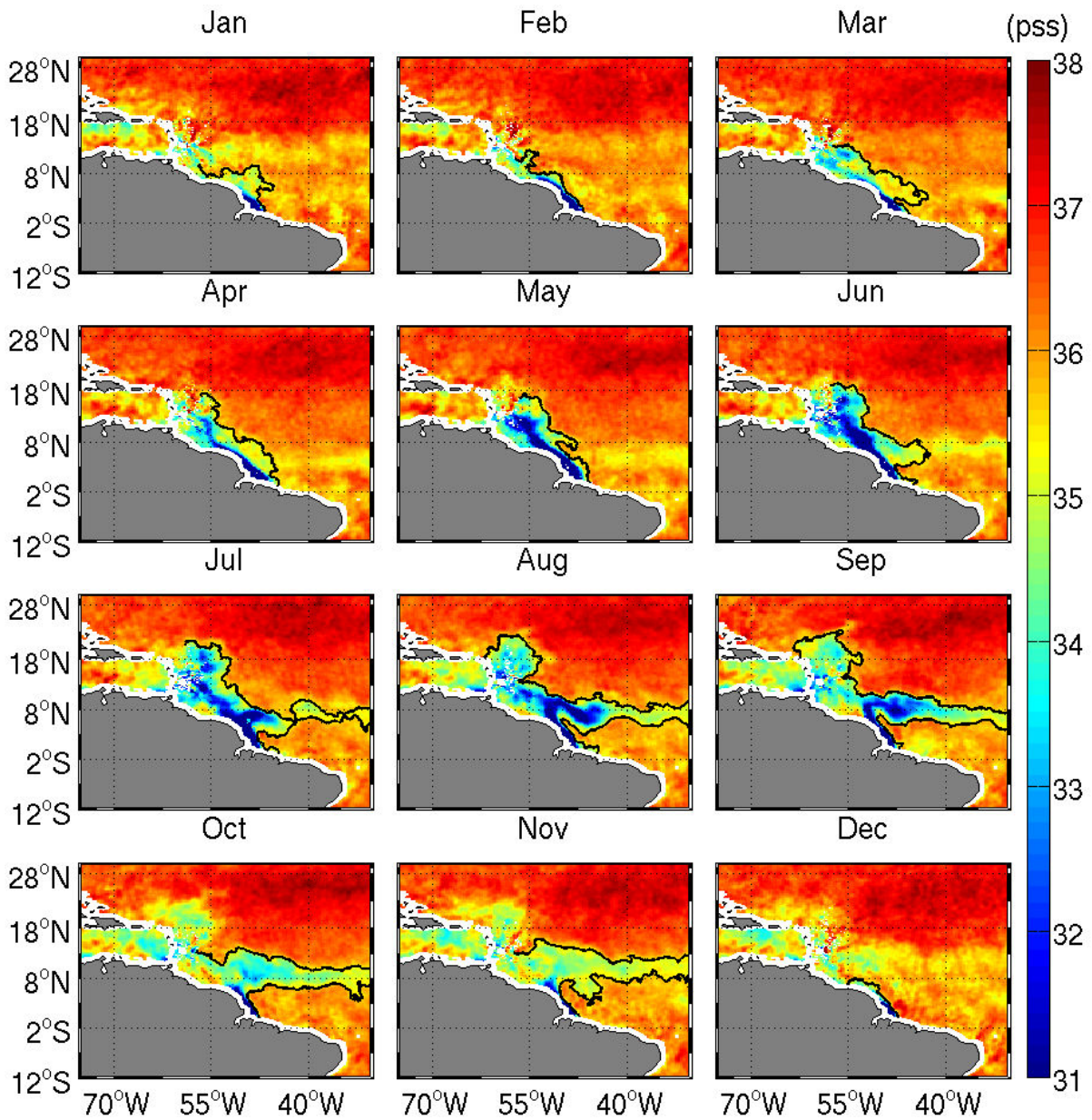


Figure A.4: Monthly SMOS sea surface salinity from January to December 2013, on top of which is represented the 2013 monthly 35.5 pss contour.

Appendix B

Amazon river plume signatures in AMSR-E low-frequency brightness temperature data

We enter now in a new era of global sea surface salinity observing systems from space with the recent successful launches of the ESA Soil Moisture and Ocean Salinity, and the NASA Aquarius/SAC-D missions. Thanks to these new satellite SSS observing systems, sea surface salinity measurements with unprecedented spatial and temporal resolutions are now available, since 2010. Until then, SSS was only measured by an increased number of devices deployed in situ, a number still insufficient to monitor phenomena with a high spatial and temporal resolutions. Thus, some attempts have been made to retrieve a sea surface salinity signal from observations made by undedicated instruments launched before 2010. [Reul et al. \[2009\]](#) and [Salisbury et al. \[2011\]](#) worked on a SSS retrieval algorithm over the Amazon freshwater pool using the radiometer AMSR-E onboard the platform AQUA.

B.1 Radiative Transfer Model

Radiative transfer theory provides the relationship between the Earth's brightness temperature T_B and geophysical parameters such as wind speed, sea surface temperature, sea surface salinity. Physical retrieval algorithms for environmental data records, such as the sea surface temperature, sea surface wind speed, columnar water vapor, columnar liquid cloud water are derived from a radiative transfer model (RTM), which computes the brightness temperatures that are measured by the satellite as a function of these environmental data records. The RTM is based on a model for the sea surface emissivity and the theory of microwave absorption in the Earth's atmosphere.

The brightness temperature at the top of the atmosphere measured by an instrument onboard a satellite platform at a specific frequency and polarization, is given by the radiative transfer model (RTM) described by [Wentz and Meissner \[2000\]](#) and represented in figure B.1 :

$$T_B = T_{BU} + \tau E SST + \tau R [T_{BD} + \tau T_C] + \tau T_{Bscat} \quad (\text{B.1})$$

with :

Appendix B. Amazon river plume signatures in AMSR-E low-frequency brightness temperature data

- R : the sea surface reflectivity
- $E = 1-R$: the sea surface emissivity
- τ : the atmosphere transmittance
- SST : the sea surface temperature
- T_{BU} : the upwelling atmosphere emission
- T_{BD} : the downwelling atmosphere emission reflected at the ocean surface
- T_C : the effective cold space temperature

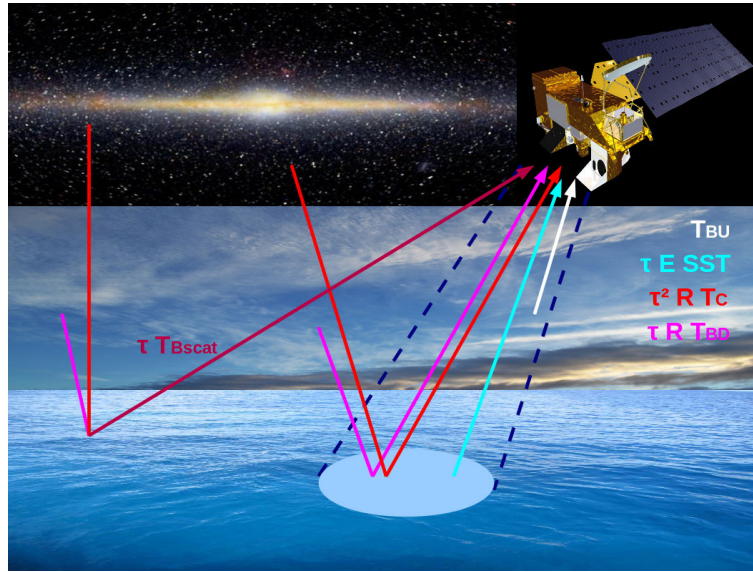


Figure B.1: Scheme of the radiative transfer model.

The term $E \cdot SST$ or $(1-R)SST$ represents the radiation directly emitted from the sea surface. The term τT_{Bscat} accounts for downwelling atmospheric and cold space radiation scattered at the ocean surface from directions other than the incident one.

$T_C = 2.7 \text{ }^\circ\text{C}$ and to compute T_{BU} , T_{BD} and τ , models can be used. T_{Bscat} is a function of the atmosphere transmittance τ , the downwelling atmosphere emission T_{BD} , the radiation coming from cold space T_C and a term dependant on wind speed and atmosphere transmittance.

Thus, from the equation B.1, given the SST and the brightness temperature measurement T_B , the sea surface brightness temperature can be deduced, for several channels and polarizations. This brightness temperature depends on some geophysical parameters, via the sea surface emissivity, which can then be extracted. Here, we are interested in retrieving a SSS signal. In radiometry, the L band (around 1.4-1.5 GHz) is the most sensitive to sea surface salinity (SSS) variations. However, it has been demonstrated by [Reul et al. \[2009\]](#) that SSS variations can, above all, be retrieved using the X and C bands of a radiometer, in warm seas.

B.1. Radiative Transfer Model

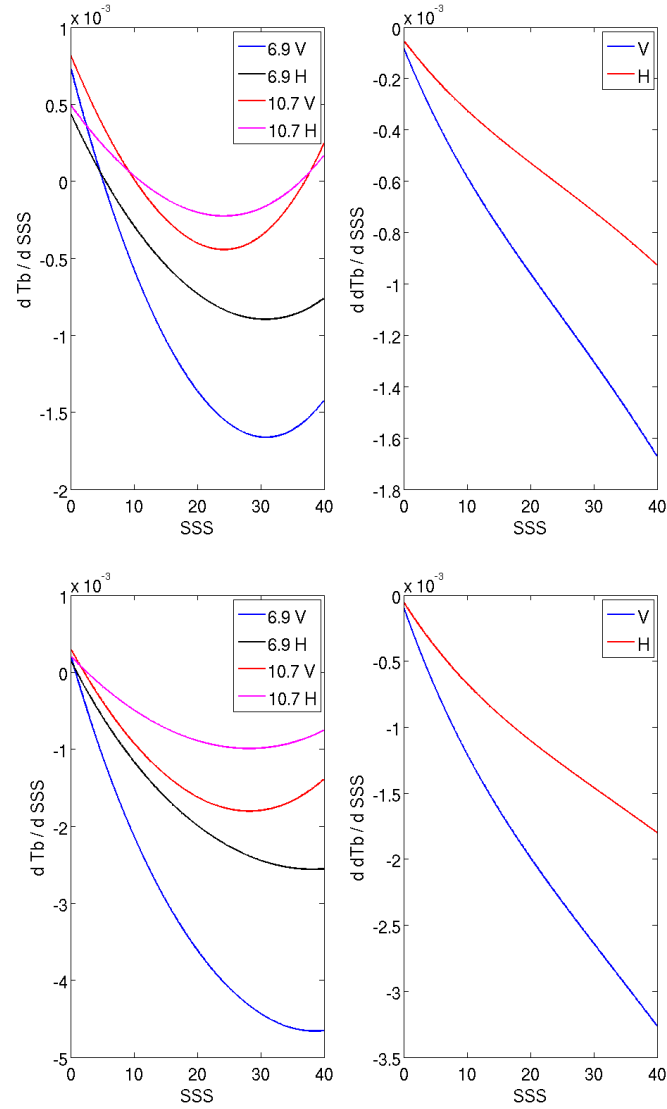


Figure B.2: Variations of Klein and Swift [1977] predictions of brightness temperatures and vertically polarized sea surface microwave emission difference between the C and X bands (ΔT_b^v) with sea surface salinity function of sea surface salinity for a sea surface temperature of 20° (top) and 34.25° (bottom).

In the following, we study the theoretical dependance of brightness temperatures in X and C bands at different polarizations with geophysical parameters. Sea surface brightness temperature is a function of SST and dielectric constant of sea water via the emissivity. The model developed by Klein and Swift [1977] computes a complex dielectric constant of sea water given sea surface salinity and sea surface temperature, at a specific electromagnetic frequency. In the following, the Klein and Swift [1977] model is used to compute a theoretical brightness temperature to explain the sensitivities of brightness temperatures with several geophysical parameters and with frequency.

Appendix B. Amazon river plume signatures in AMSR-E low-frequency brightness temperature data

From figure B.2, we can see that, whatever the sea surface temperature but especially at high SST, the C band is sensitive to the sea surface salinity particularly in the vertical polarization. Indeed, in this case, at high SST, the maximum brightness temperature variations with the salinity is about $5 \cdot 10^{-3}$ K instead of $2.5 \cdot 10^{-3}$ K in the horizontal polarization or, in the X band, about $2 \cdot 10^{-3}$ K in the horizontal polarization and $1 \cdot 10^{-3}$ K in the vertical one.

Moreover, the vertically polarized sea surface microwave emission difference between the C and X bands (ΔT_b^v) is strongly sensitive to salinity. At high SST, the maximum ΔT_b^v variations are about $3.5 \cdot 10^{-3}$ K instead of less than $2 \cdot 10^{-3}$ K for the horizontal polarization.

From figure B.3, we can see that, whatever the salinity value, the vertical polarization is the most sensitive to sea surface temperature, particularly in the C band. Indeed, in this case, at low SSS, the maximum brightness temperature variation with the SST is about $3.5 \cdot 10^{-2}$ K instead of $3 \cdot 10^{-2}$ K in the X band in horizontal polarization and only $1.5 \cdot 10^{-2}$ K in the horizontal polarization.

Moreover, the difference of brightness temperatures in the two bands for the vertical polarization is strongly sensitive to sea surface temperature. Indeed, at low SSS, the maximum ΔT_b^v variation is about $5 \cdot 10^{-3}$ K instead of $3 \cdot 10^{-3}$ K in the horizontal polarization.

SSS signatures can thus be isolated by estimating the vertically polarized sea surface microwave emission difference between the C and X bands (ΔT_b^v). In warm seas, the variability of that surface emission quantity turns out to be dominated by changes in SSS and SST variations and, to a lesser extent, by sea surface roughness impacts. Indeed, this difference permits to isolate the SSS signal from the C band by differentiating out common residual error.

Thus, in theory, it is possible to retrieve SSS from brightness temperature measured by radiometric instruments, but the precision needed is very high.

B.2. Sea surface salinity signal from the AMSR-E

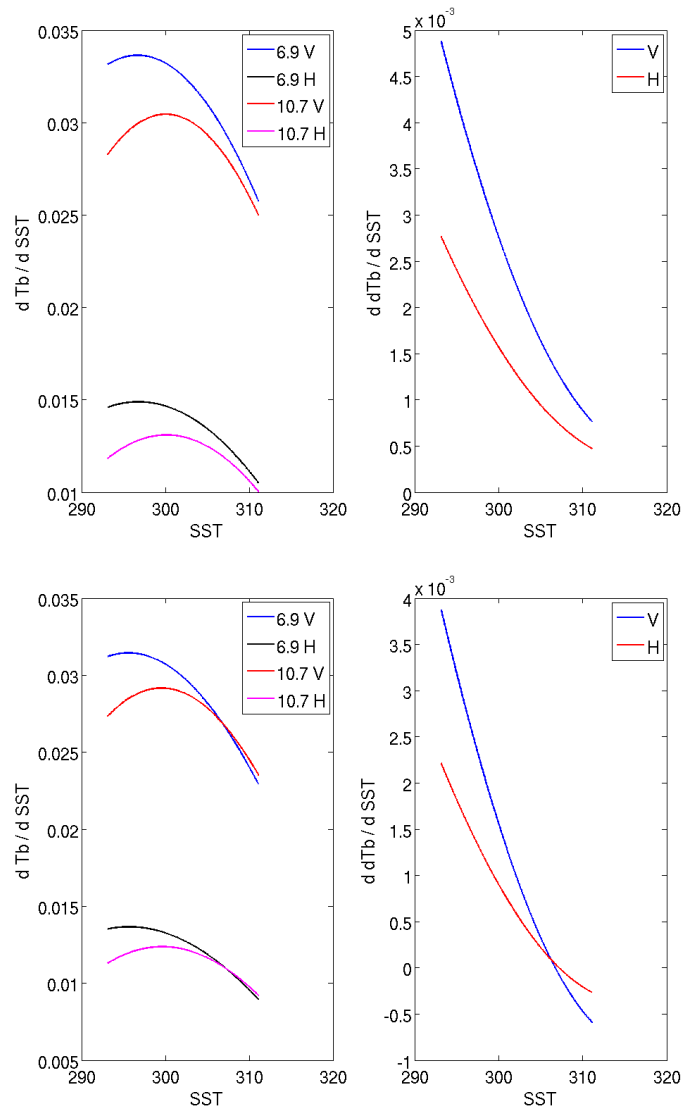


Figure B.3: Variations of Klein and Swift [1977] predictions of brightness temperatures and anomalies with sea surface temperature function of sea surface temperature for a sea surface salinity of 24.95 pss (left) and 38.7 pss (right).

B.2 Sea surface salinity signal from the AMSR-E

Reul et al. [2009] demonstrated that SSS variations can be retrieved from the C band of the radiometer AMSR-E, in warm seas. AMSR-E, the Advanced Microwave Scanning Radiometer, is one of the six instruments onboard AQUA satellite. It measures brightness temperatures at 6.925 GHz (C band), 10.65 GHz (X band) and also 18.7, 23.8, 36.5, and 89.0 GHz, at vertical and horizontal polarizations. Since 2002, it measures :

- precipitation rate
- cloud water (18.7 GHz, 23.8 GHz, and 36.5 GHz)

Appendix B. Amazon river plume signatures in AMSR-E low-frequency brightness temperature data

- water vapor (18.7 GHz, 23.8 GHz, and 36.5 GHz)
- sea surface winds (10.7 through 36.5 GHz)
- sea surface temperature (6.9 through 36.5 GHz)
- ice (89 GHz)
- snow (18.7 GHz and 36.5 GHz)
- soil moisture (6.9 GHz, 10.7 GHz, and 36.5 GHz)

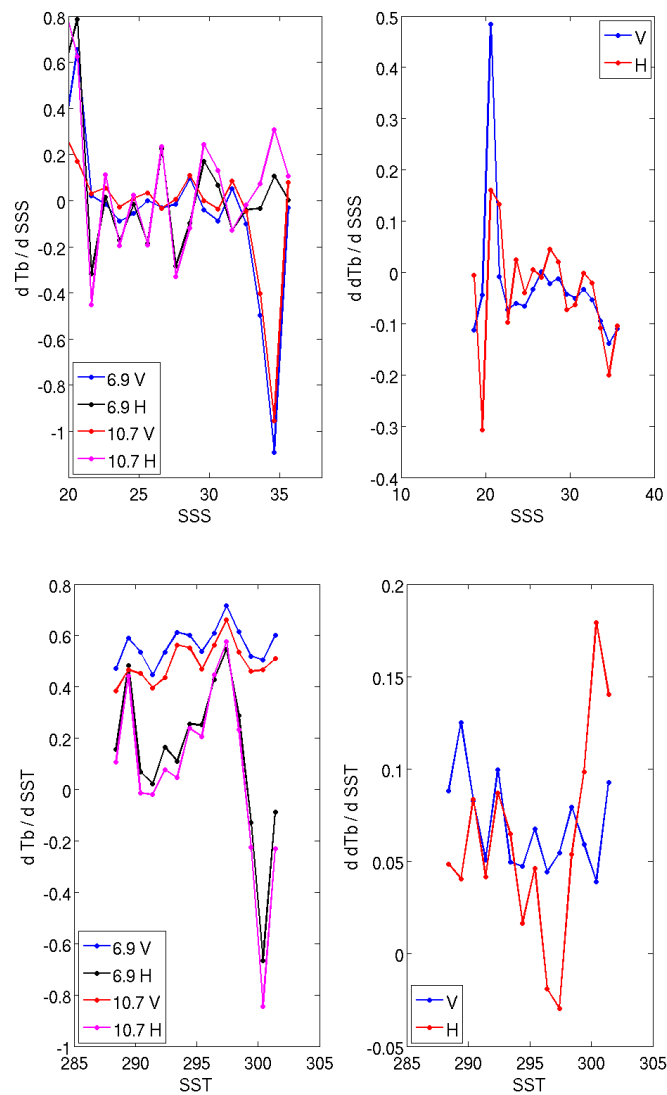


Figure B.4: Variations of AMSR-E brightness temperatures and anomalies with the SSS climatology (left) and the Reynolds et al. [2002] SST (right).

Effects of sea surface salinity and sea surface temperature on AMSR-E brightness temperatures are not as clear as in theory. The figure B.4 on the right shows that the vertical

B.2. Sea surface salinity signal from the AMSR-E

polarization is the most sensitive to SST, especially in the C band.

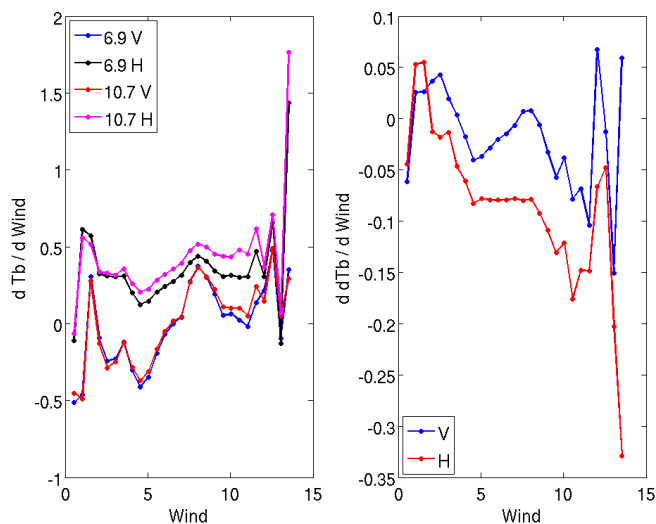


Figure B.5: Variations of AMSR-E brightness temperatures (left) and anomalies (right) with the wind as a function of the wind.

From figure B.5, we can see that, whatever the band, the horizontal polarization is the most sensitive to the wind. Indeed, in this case, the maximum brightness temperature variation with the wind is about 0.6 K instead of less than 0.4 K in the vertical polarization whatever the band.

What is more interesting is that variations of brightness temperatures in each polarization for both channels are very close. Thus, the difference of brightness temperatures in the two bands for each polarization is minimized (less than 0.1 K).

Considering the variations of brightness temperatures with water vapor and cloud liquid water, the figure B.6 shows that the vertical polarization is the most sensitive to water vapor and cloud liquid water. As previously, in both case, variations in each polarization are very close. Thus, the difference of brightness temperatures in the two bands for each polarization is minimized.

Computing the difference between the two channels in the vertical polarization minimizes the effects of the wind, the water vapor and the cloud liquid water. However, regarding the precision we are looking for, it might be insufficient.

Thus, from the equation B.1, using the [Reynolds et al. \[2002\]](#) SST product, the sea surface reflectivity can be computed to obtain the sea surface brightness temperature, for each channel and each polarization. The resulting surface reflectivities at each frequency are

Appendix B. Amazon river plume signatures in AMSR-E low-frequency brightness temperature data

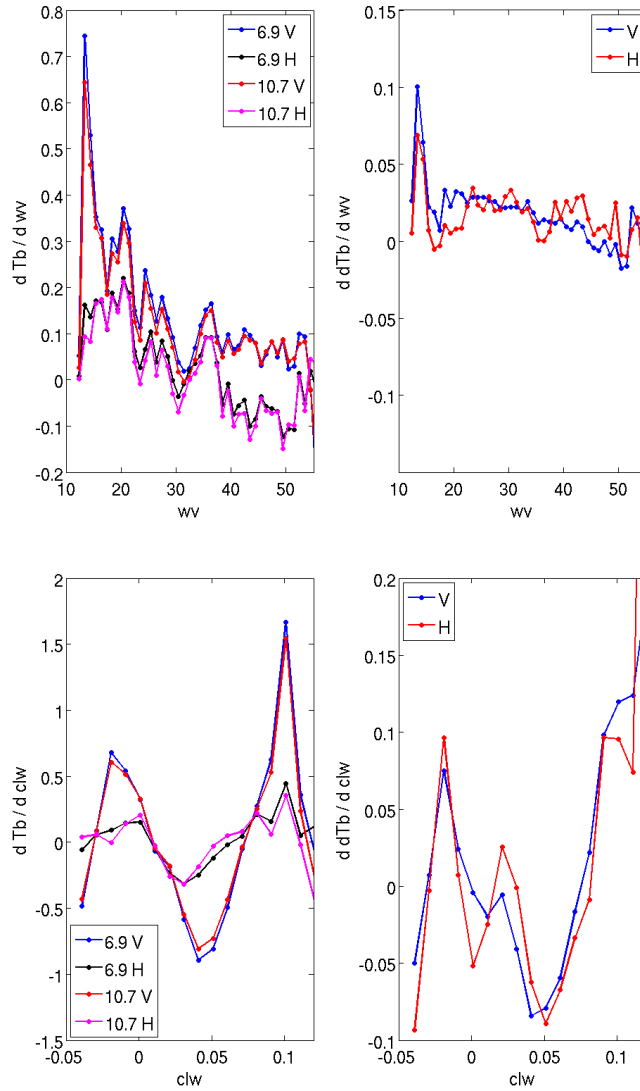


Figure B.6: Variations of AMSR-E brightness temperatures and anomalies with the water vapor (left) and the cloud liquid vapor (right).

then combined to estimate the difference in surface brightness temperature between 6.9 and 10.7 GHz vertical polarization channels ($\Delta T_b = T_{bv}^{6.9} - T_{bv}^{10.7}$).

As to retrieve AMSR-E sea surface temperature (SST), a sea surface salinity model is used, an independent SST dataset is preferable in this work. Moreover, the [Reynolds et al. \[2002\]](#) dataset is performing as it is based on infrared (mostly Advanced Very High Resolution Radiometer (AVHRR)) and microwave measurements. Infrared measurements are not sensitive to roughness but are disturbed by clouds. On the contrary, microwave measurements are not disturbed by clouds but they are sensitive to roughness. However, the bias due to sea state is corrected in the [Reynolds et al. \[2002\]](#) dataset.

B.3. Initial empirical SSS retrieval methodology

The ΔT_b^v quantity is then used to attempt to retrieve a sea surface salinity signal in the Earth's surface emission captured by AMSR-E.

B.3 Initial empirical SSS retrieval methodology

[Reul et al. \[2009\]](#) worked on the retrieval of a sea surface salinity product from the AMSR-E radiometer via the difference between the brightness temperatures at 6.9 GHz and 10.7 GHz, vertically polarized. The ΔT_b^v quantity includes the sum of two contributions. The first one is the difference in the smooth surface ocean reflectivity between the two channels (Δr_{flat}) which only depends on the sea surface temperature and salinity through the differing dielectric constant at the two frequencies. The second term is due to a possibly differing surface roughness impact on the reflectivity (Δr_{rough}) at the two frequencies.

In the northwestern tropical Atlantic, [Reul et al. \[2009\]](#) found that $\Delta r_{rough} \simeq 0$ in the dominant wind conditions between $\sim 4 \text{ m.s}^{-1}$ and $\sim 10 \text{ m.s}^{-1}$. An initial SSS retrieval methodology from the estimated ΔT_b^v thus follows (see [Reul et al. \[2009\]](#)). In their work, model predictions of Δr_{flat} were estimated using a low microwave frequency dielectric constant model, the [Klein and Swift \[1977\]](#) model, applied to the SST fields and for arbitrary salinity values ranging from 0 to 40 pss. The retrieved SSS along swath was then determined by minimizing the difference between the [Klein and Swift \[1977\]](#) model prediction and the AMSR-E ΔT_b^v s, assuming a negligible roughness impact on ΔT_b^v .

As illustrated in figure B.7.b, binning the differences between [Klein and Swift \[1977\]](#) predictions and AMSR-E estimates of ΔT_b^v as a function of SST reveals a clear residual SST dependent bias in this model.

Thus, in a following unpublished work, Reul et al. developed an improved empirical methodology based on the initial methodology to retrieve the sea surface salinity from the estimated ΔT_b^v and from the relationship between the collected ΔT_b^v , SST and SSS data. This empirical SSS retrieval algorithm is based on the monthly relationship between the collected AMSR-E ΔT_b^v , SST and SSS climatology data. For these purposes, [Reverdin et al. \[2007\]](#) monthly SSS climatology data is thus binned as a function of the monthly climatology of AMSR-E ΔT_b^v and [Reynolds et al. \[2002\]](#) SST. The results are illustrated in figure B.8.a, which shows clear dependencies between ΔT_b^v , SST and SSS. We recall here that $\Delta T_b^v = SST \cdot \Delta r_v$ where Δr_v is the difference in ocean surface reflectivity between X and C-band frequencies. Based on the previously established relationships, a simple empirical model to retrieve SSS as function of AMSR-E Δr_v and [Reynolds et al. \[2002\]](#)

Appendix B. Amazon river plume signatures in AMSR-E low-frequency brightness temperature data

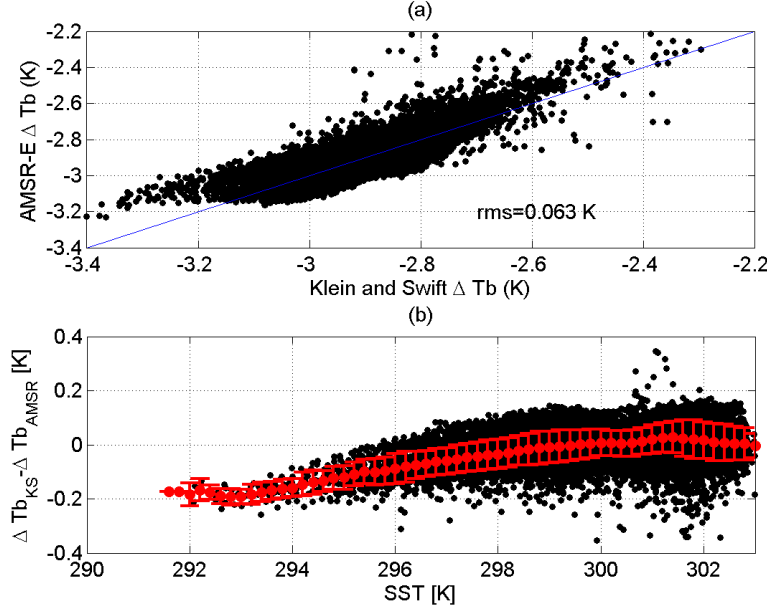


Figure B.7: (a) Comparison between monthly climatologies of AMSR-E and Klein and Swift [1977] predictions of ΔT_b^v . (b) Binned-averaged differences between both products as function of Reynolds et al. [2002] SST.

SST fields (see figure B.8.b) was derived using a two-dimensional polynomial fit :

$$SSS_{AMSR} = a_3(\Delta r_v)^3 + a_2(\Delta r_v)^2 + a_1\Delta r_v + a_o \quad (\text{B.2})$$

where $(a_i)_{i=1,3}$ coefficients are polynomial functions of SST.

In practice, AMSR-E SSS fields are then generated applying Equation B.2 for each coupled value of AMSR-E ΔT_b^v and Reynolds et al. [2002] SST for each $0.25^\circ \times 0.25^\circ$ pixel. Two examples of monthly fields for August 2004 and March 2008 are given in figure B.9. Clear low SSS signatures below 35.5 pss can be seen on these fields corresponding to the Orinoco, Amazon, Congo plumes, as well as freshwater pools induced by the river discharges of Guinea-Bissau and Biafra Bight.

B.4. AMSR-E ΔT_b^v algorithm improvement

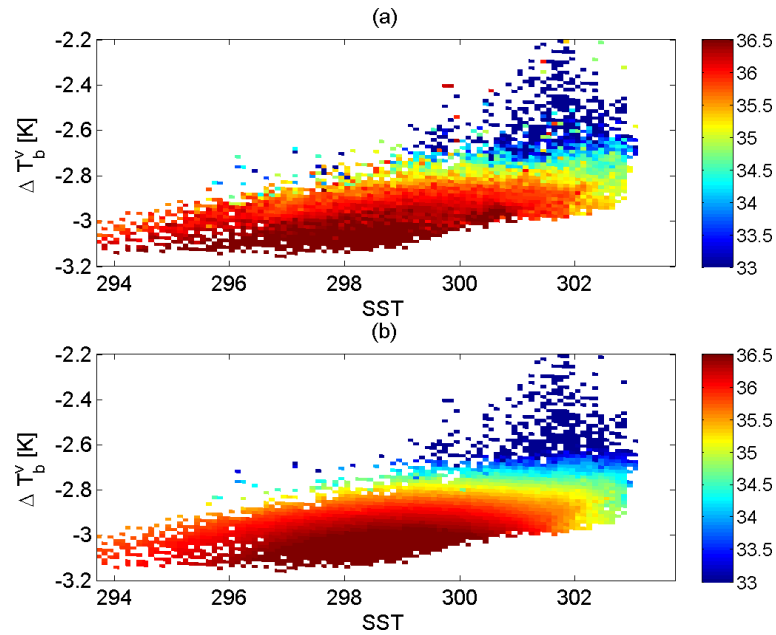


Figure B.8: (a) Monthly SSS climatology of Reverdin et al. [2007] bin-averaged as function of corresponding climatologies of ΔT_b^v and Reynolds et al. [2002] SST. (b) Empirical Model.

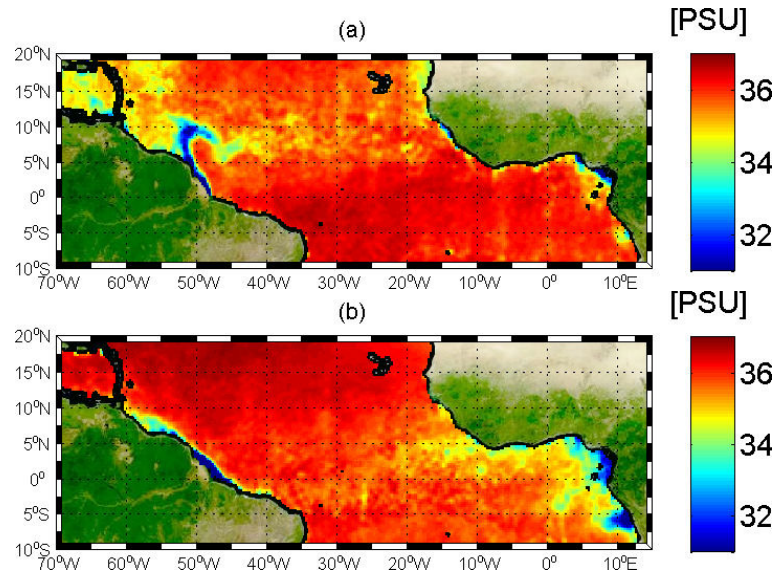


Figure B.9: Examples of Monthly AMSR-E SSS data grouped in 0.25° square bins in latitude x longitude. (a) August 2004 and (b) March 2008.

B.4 AMSR-E ΔT_b^v algorithm improvement

B.4.1 Atmospheric corrections improvement

AMSR-E measures Earth's brightness temperatures on which atmospheric and surface corrections are applied to retrieve sea surface brightness temperatures, as we have seen

Appendix B. Amazon river plume signatures in AMSR-E low-frequency brightness temperature data

in a previous section. At the beginning of AQUA mission, atmospheric corrections' algorithms were based on many years of previous observations from SSM/I (Special Sensor Microwave Imager carried aboard Defense Meteorological Satellite Program (DMSP)), TMI (Tropical Rainfall Measuring Mission's (TRMM) Microwave Imager) and collocated buoy observations.

To validate the AMSR-E ΔT_b^v obtained, they are compared to a prediction of AMSR-E ΔT_b^v , based on the Klein and Swift [1977] model. To Reverdin et al. [2007] SSS climatology data (1970-2002) and to Reynolds et al. [2002] SST model (2003-2010), the Klein and Swift [1977] dielectric constant model is applied and then, predictions of the brightness temperature anomalies are deduced.

In figure B.7b., we observe a residual bias which clearly depends on SST, it increases when SST decreases. This bias would be due to errors in atmospheric corrections and/or errors in the dielectric constant model. In early 2011, new atmospheric corrections were developed by Meissner and Wentz [2012] based on WindSat and still SSM/I measurements.

Even if the new Meissner and Wentz [2012] algorithm is applied on AMSR-E data, there are still residual biases dependent on SST, cloud liquid water, water vapor and wind (see figure B.10). Most of them are lower than 0.05 K in absolute value, corresponding to 1 pss for a SST around 28°C, which is still important given the precision needed here. Compared to other parameters, the bias dependent on water vapor is much greater than the others.

In order to improve those results and to overcome this residual biases issue (especially the biases dependent on cloud liquid water and water vapor), we decided to use a very restrictive cloud mask to be in clear sky conditions. To do that, a cloud mask from the MODIS instrument is computed. The Moderate Resolution Imaging Spectroradiometer (MODIS) is an instrument onboard AQUA, the same platform onboard which AMSR-E is. The two instruments follow each other few minutes only, which is ideal to study clouds, a parameter with an important spatio-temporal variability. Moreover, MODIS and AMSR-E are two independant instruments.

B.4. AMSR-E ΔT_b^v algorithm improvement

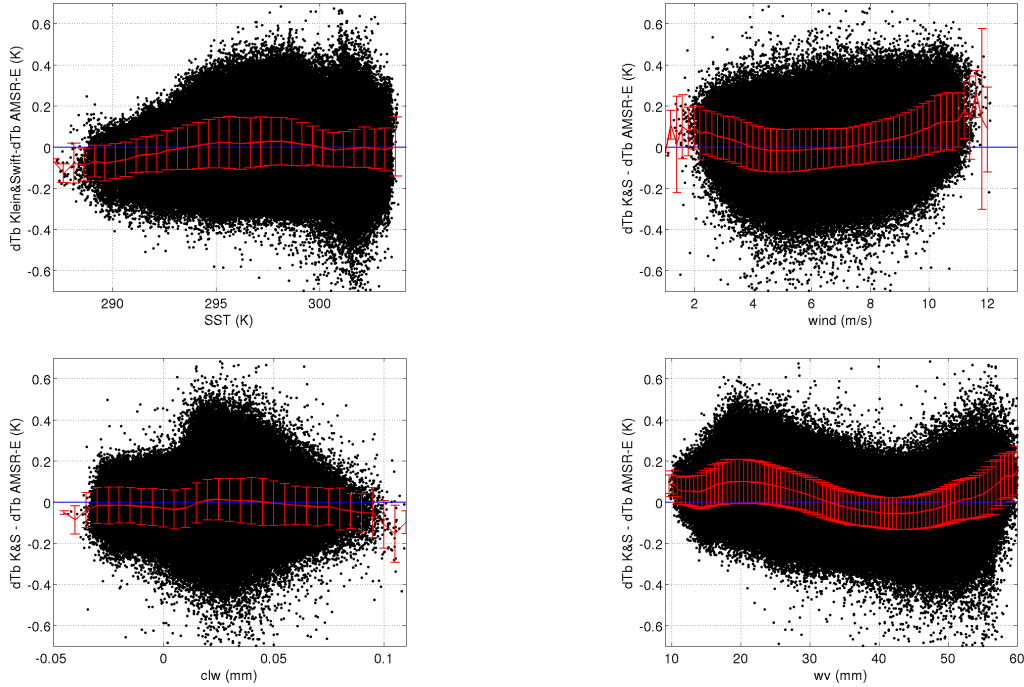


Figure B.10: Differences between AMSR-E and Klein and Swift [1977] predictions of ΔT_b^v (black dots) binned-averaged differences (red) plotted as a function of SST (top left), wind (top right), cloud liquid water (bottom left) and water vapor (bottom right).

B.4.2 Residual biases corrections

As we have seen previously, many residual biases are still affecting AMSR-E data, especially biases due to cloud liquid water and water vapor. In order to overcome these effects, a clear sky situation is needed. To do that, we compute a very restrictive cloud mask selecting AMSR-E data during clear sky conditions only. The Moderate Resolution Imaging Spectroradiometer (MODIS) instrument, as the AMSR-E one, is onboard the platform AQUA. Thus, it scans the oceans 15 minutes only after AMSR-E does, which permits to have same environmental conditions.

Considering clear sky conditions, we, once again, study residual biases with the different parameters (see figure B.11). We can observe that the bias with roughness (wind) is more important than in figure B.10. As we are in clear sky conditions, effects of cloud liquid water in the wind restitution are removed, this is thus the "real" roughness. So, it is now possible to correct from this roughness effect which is "cloud liquid water free".

Considering the residual bias with the water vapor, it has not changed so much. Thus, water vapor residue does not depend on the cloud liquid water parameter. It can now be corrected.

However, a bias with cloud liquid water still exists. As we are in clear sky conditions,

Appendix B. Amazon river plume signatures in AMSR-E low-frequency brightness temperature data

that is to say, there is no more cloud liquid water, this bias has to be due to another parameter such as the wind. Although we are in clear sky conditions, the cloud liquid water distribution has not really changed and the maximum did not translate to low values as expected.

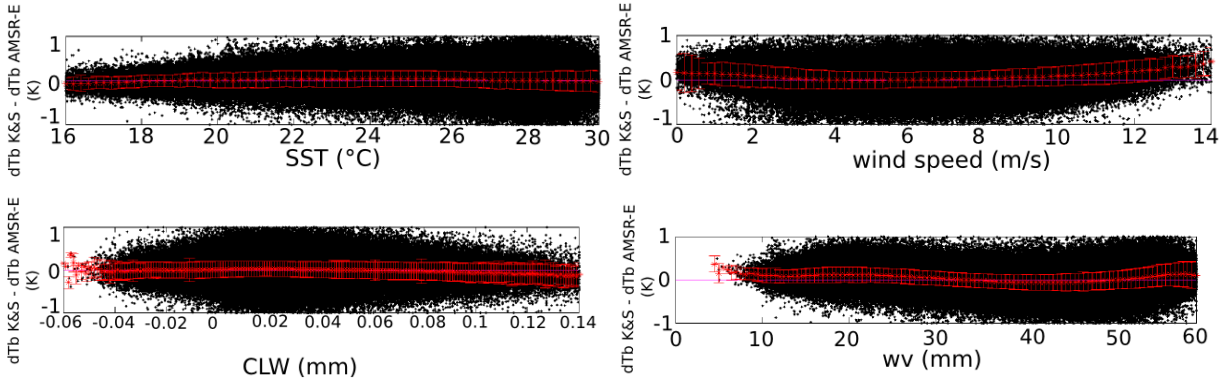


Figure B.11: Differences between cloud free AMSR-E and Klein and Swift [1977] predictions of ΔT_b^v (black dots) and binned-averaged differences (red) plotted as a function of SST (top left), wind (top right), cloud liquid water (bottom left) and water vapor (bottom right).

According to figure B.11, even in "clear sky conditions", there is still biases particularly dependent on water vapor and wind. From this, wind and water vapor corrections are computed and applied to AMSR-E data. Thus, the binned averaged differences residual between AMSR-E and Klein and Swift [1977] predictions of ΔT_b^v as a function of wind is interpolated using a degree 1-polynomial for a wind lower than 2 m/s, a degree 4-polynomial for wind values from 2 to 10.5 m/s and a degree 3-polynomial for wind values higher than 10.5 m/s (see figure B.12 on the left). This correction applied on AMSR-E data flagged by MODIS cloudflag, the residual binned averaged differences between AMSR-E and Klein and Swift [1977] predictions of ΔT_b^v as a function of water vapor is interpolated using a degree 6-polynomial for water vapor values lower than 55 mm and a degree 1-polynomial for water vapor values higher than 55 mm (see figure B.12 on the right).

At this point, these 2 corrections are applied on all AMSR-E data and SSS retrieval method can now be applied to AMSR-E data.

B.5. New SSS retrieval methodologies

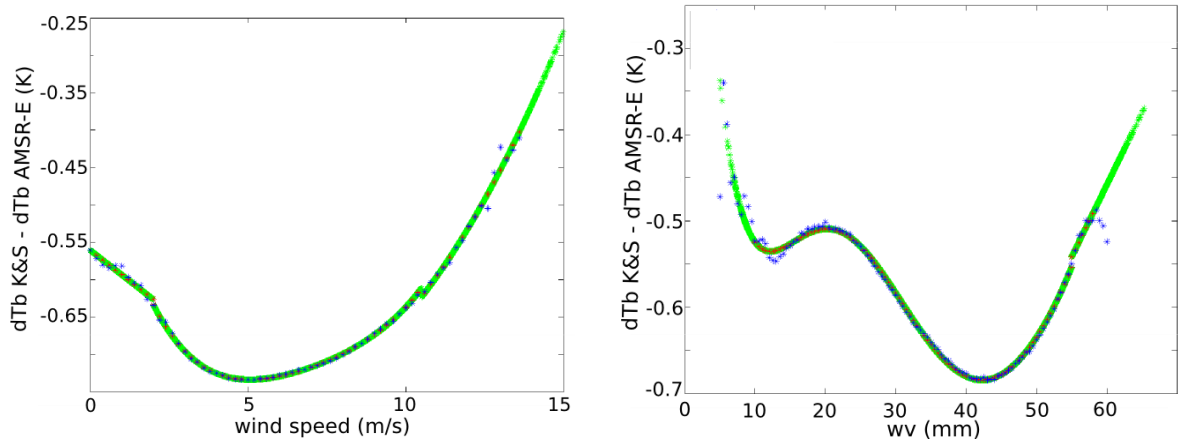


Figure B.12: Wind and water vapor corrections computed on AMSR-E data flagged by MODIS cloud-flag.

B.5 New SSS retrieval methodologies

B.5.1 Empirical model

As did by Reul et al. in an unpublished work, the method consists in retrieving sea surface salinity using an polynomial empirical model based on the relationship between AMSR-E ΔT_b^v , SST and SSS. This method is applied on all AMSR-E data, corrected as we have seen above, using the wind and then the water vapor corrections.

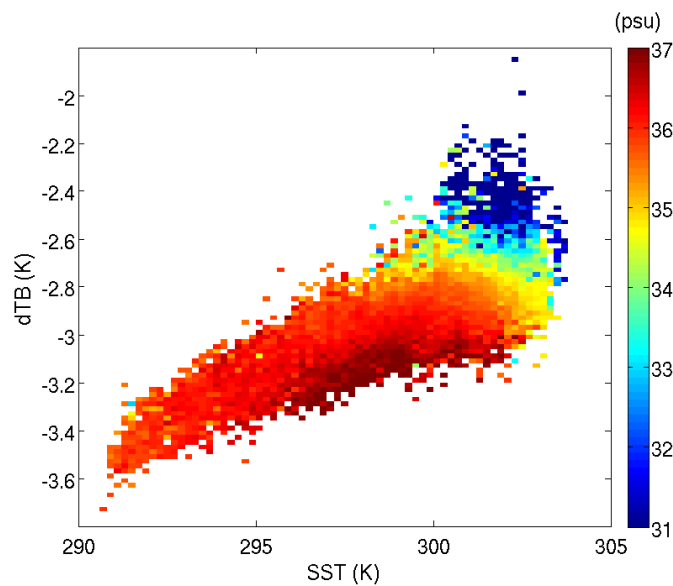


Figure B.13: Monthly SSS bin-averaged as function of corresponding climatologies of ΔT_b^v and Reynolds et al. [2002] SST, using AMSR-E ΔT_b^v collected from 2003 to 2008 and *in situ* SSS.

Appendix B. Amazon river plume signatures in AMSR-E low-frequency brightness temperature data

From the correlation established in figure B.13 between ΔT_b^v , Reynolds et al. [2002] SST and *in situ* SSS from 2003 to 2008, an empirical model is computed using a degree 3 polynomial interpolation (see figure B.14). Thus, for a value of SST and a value of ΔT_b^v , an AMSR-E SSS value can be retrieved.

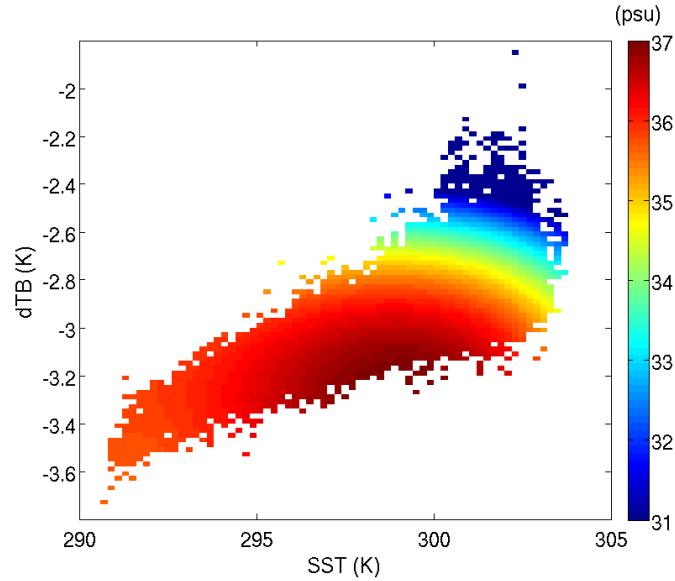


Figure B.14: Empirical Model : a third third degree polynomial interpolation of the relationship seen in figure B.13.

B.5.2 Neural network model

Another more complex method to retrieve AMSR-E SSS, using a neural network, is considered. Indeed, other parameters, such as wind, could influence the polynomial relationship seen above. Furthermore, the previous global algorithm is applied in the whole north-western Atlantic ocean area whereas the algorithm could be different locally. Thus, in this new approach, the wind speed is taken into account and also the localisation (latitude and longitude of each pixel).

The Neural Network Matlab toolbox is used and the network built contains 2 hidden layers, 15 hidden neurons and 70% of data is used for the training, 15% for the validation and 15% for the test. The training is done on the *in situ* SSS from 2003 to 2010. The neural network inputs AMSR-E ΔT_b^v , wind and SST, are connected to the first layer and latitudes and longitudes are only connected to the second layer.

B.5. New SSS retrieval methodologies

B.5.3 AMSR-E SSS Validation

To validate the two SSS products retrieved from AMSR-E data using first an empirical method and then a neural network method, *in situ* data from Argo, TSG and Pirata buoys are used.

Monthly maps of the neural network AMSR-E SSS are computed and compared to the monthly SMOS and *in situ* SSS maps, especially in August and November 2010 and September 2003. In figures B.15 and B.16, we can observe the good coherence between both SSS signals from SMOS and AMSR-E in the Amazon Plume. AMSR-E SSS tends to be underestimated in the open ocean and in the Caribbean Sea. AMSR-E provides SSS in the Congo-Niger area where SMOS signal undergoes interferences.

Furthermore, AMSR-E provides SSS measurements before 2010 (see figure B.17) when only *in situ* data were available, that is to say, very few measurements. Looking particularly at the maps of September 2003 (see figure B.17), we can observe that AMSR-E permits to well retrieve the plume SSS fronts and the structures such as rings.

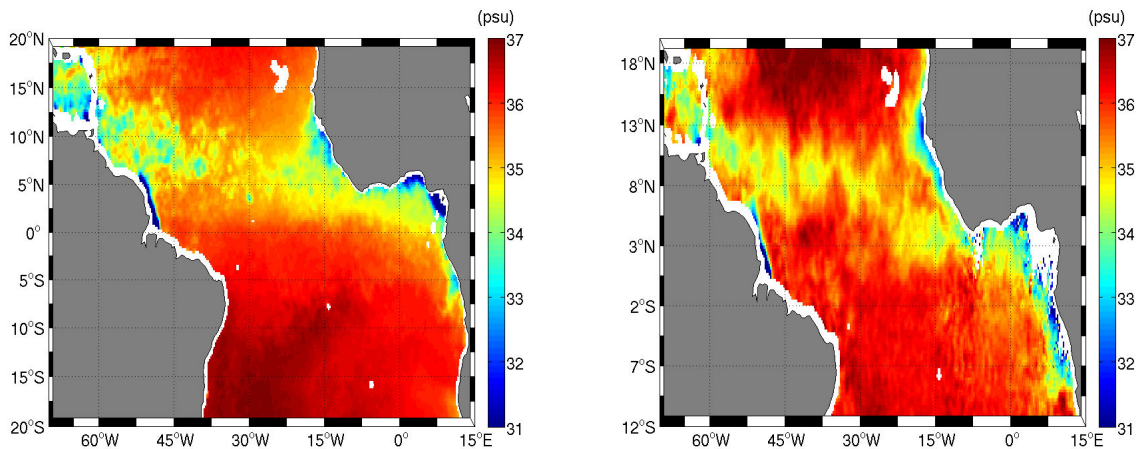


Figure B.15: 0.25° maps of November 2010 SSS from AMSR-E (left) and SMOS (right).

Computing the global RMS map between *in situ* data and both AMSR-E SSS products, for the period 2003-2010 (see figure B.18), it can be shown that RMS values, considering both methods, are higher in the northwestern part of the Amazon plume. Globally, it appears that RMS values are lower considering the empirical retrieval method.

Then, the retrieved AMSR-E SSS from both methods is plotted against *in situ* SSS from Argo, TSG and Pirata buoys (see figure B.19). The mean difference between empirical AMSR-E and *in situ* SSS is about 0.07 pss and the root mean square (RMS) is about 0.98 pss. Considering the neural network method, the mean is about 0.11 pss and the RMS is

Appendix B. Amazon river plume signatures in AMSR-E low-frequency brightness temperature data

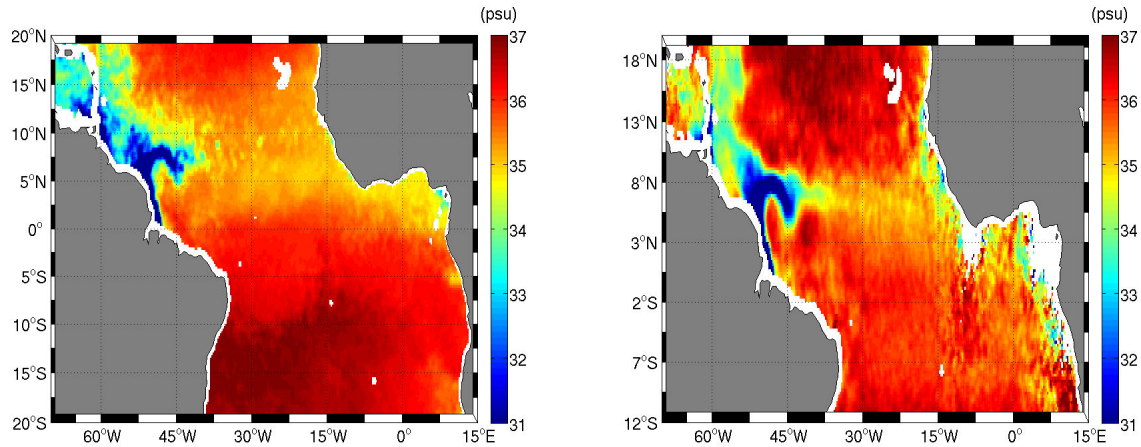


Figure B.16: 0.25° maps of August 2010 SSS from AMSR-E (left) and SMOS (right).

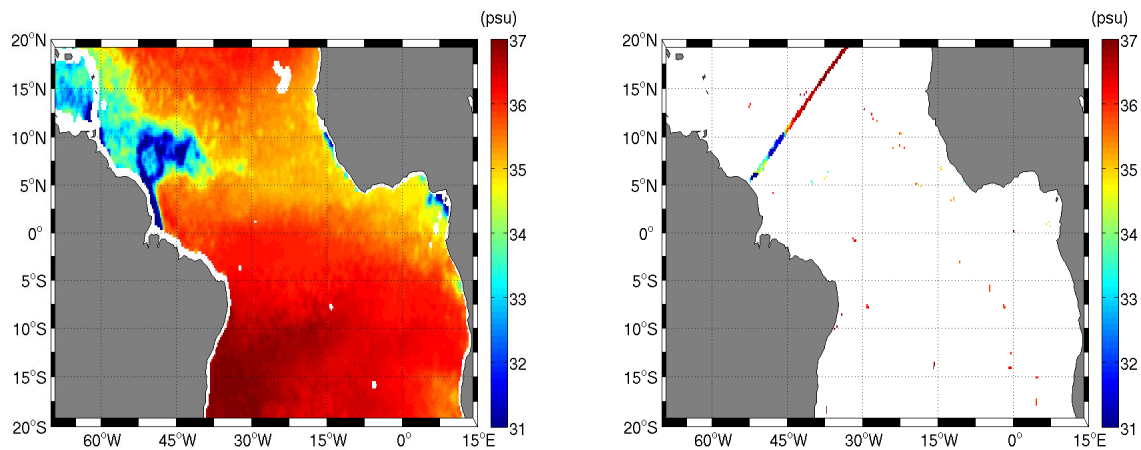


Figure B.17: 0.25° maps of September 2003 SSS from AMSR-E (left) and *in situ* (Argo, TSG and Pirata) (right).

about 1 psu. The figure B.19 highlights the fact that both algorithms tend to overestimate the retrieved SSS below 30 psu. Furthermore, the validation with some Pirata buoys seems to not work well in salt water, the methods underestimating the retrieved SSS.

In the following, to carry on the validation of the AMSR-E retrieved SSS products, AMSR-E SSS is colocated with different Pirata buoys located in the tropical Atlantic ocean (see figure B.20). Each of the sea surface salinity time series from 2003 to 2010 are represented in figures B.21 to B.22.

Above 12°N and below 10°S none of the retrieval methods seem to work efficiently.

At 12°N , the seasonal cycle of AMSR-E retrieved SSS is coherent with Pirata SSS but drops in salinity happen few months too late.

In the plume (at location $[8^\circ\text{N } 38^\circ\text{W}]$), the comparison between the neural network, Pirata

B.5. New SSS retrieval methodologies

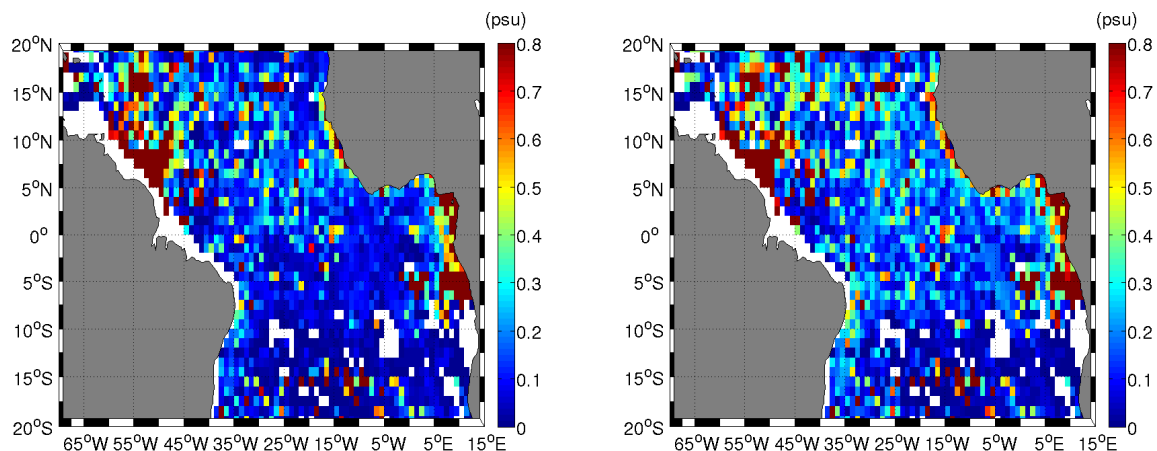


Figure B.18: 1° maps of the total RMS of the differences between empirical (left) or neural network (right) AMSR-E and *in situ* SSS from Argo, TSG and Pirata, over 2003-2010.

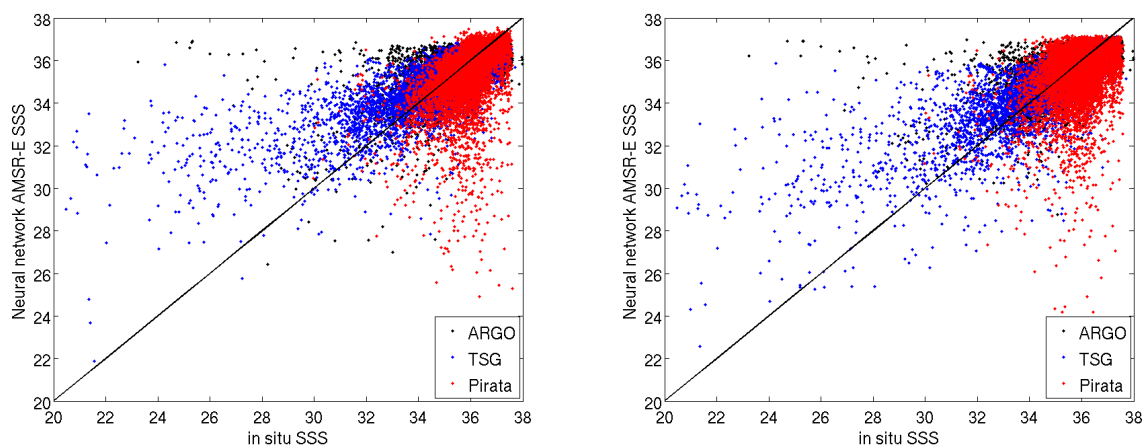


Figure B.19: AMSR-E SSS from the empirical method (left) and from the neural network method (right) as a function of *in situ* SSS (Argo, TSG and Pirata) over 2003-2010.

and SMOS SSS is quite good. However, just below the plume, at $[4^\circ\text{N } 38^\circ\text{W}]$, signals from Pirata, AMSR-E and SMOS are not coherent.

Next to the mouths of the Congo river ($[0^\circ 0^\circ]$ and $[0^\circ 10^\circ\text{W}]$) and the Niger river ($[6^\circ\text{S } 8^\circ\text{E}]$), the SSS signal retrieved from AMSR-E by the neural network and the empirical methods are very coherent with the Pirata SSS, especially the neural network SSS.

The figure B.23 shows statistics of the comparison between AMSR-E SSS products with *in situ* data from Argo (in black), TSG (in blue) and Pirata buoys (in red). On the left-hand figure, RMS of the differences between AMSR-E SSS and *in situ* SSS using the empirical and neural network SSS retrieval methods is plotted. Total RMS over 2003-2010 was computed but also RMS over the single year 2010 and then, the monthly RMS climatologies over 2003-2010. RMS is lower considering the neural network SSS retrieving

Appendix B. Amazon river plume signatures in AMSR-E low-frequency brightness temperature data

method.

On the right-hand figure, the total RMS of the differences between AMSR-E and *in situ* SSS per bin of 0.5 pss is represented. As expected, RMS is lower for higher SSS values and almost the same considering both methods. For low SSS values, comparisons with TSG data lead to lower RMS values than the comparisons with Argo floats data. Furthermore, compared to the neural network AMSR-E SSS product, the empirical method seems to more efficiently work.

B.5. New SSS retrieval methodologies

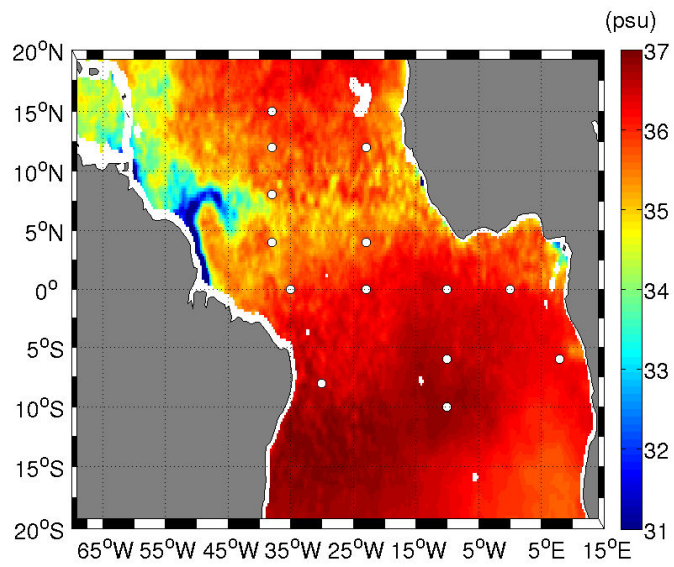


Figure B.20: August 2010 AMSR-E empirical SSS on top of which are the Pirata buoys positions.

Appendix B. Amazon river plume signatures in AMSR-E low-frequency brightness temperature data

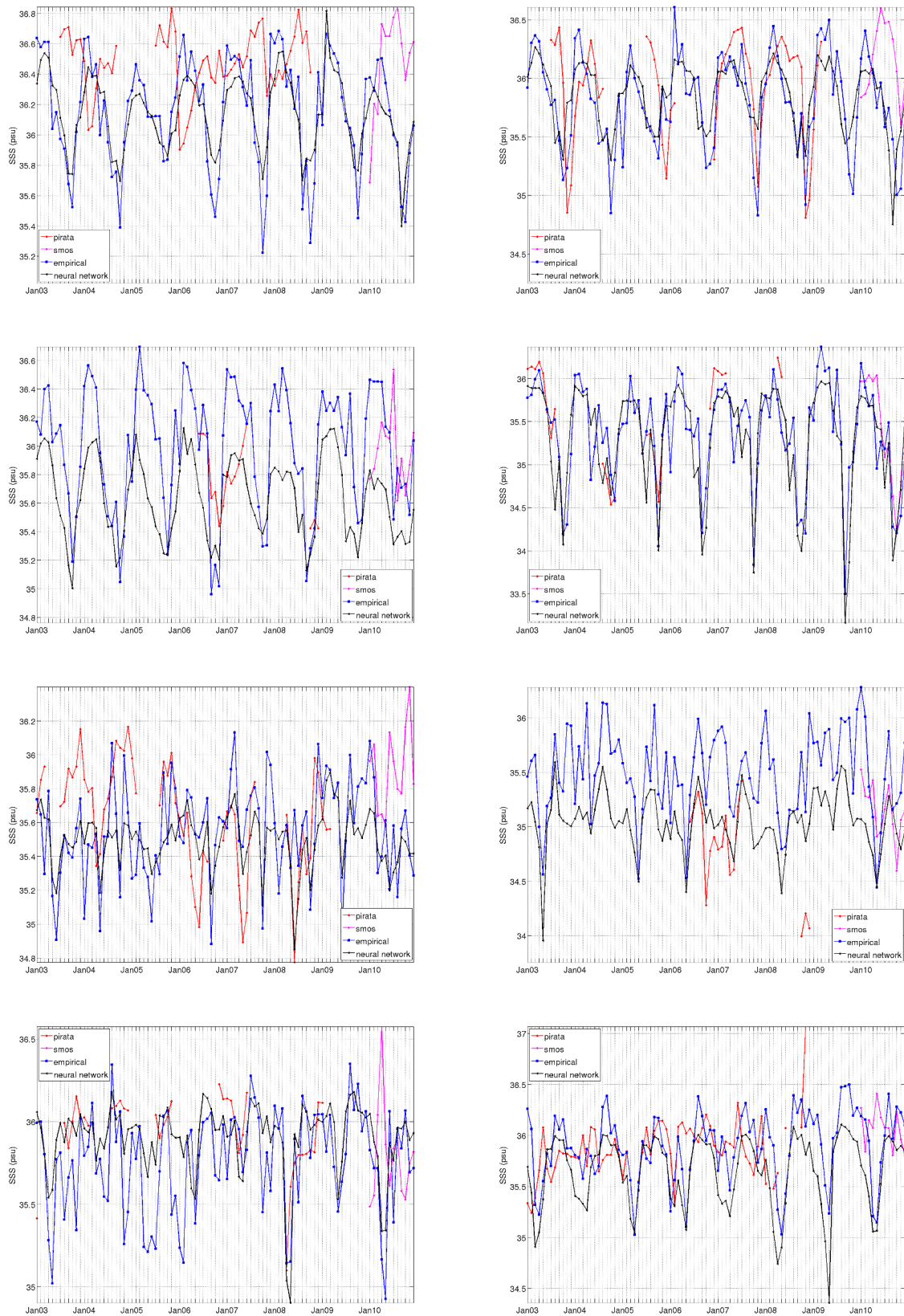


Figure B.21: Pirata (red), empirical (blue), neural network (black) AMSR-E and SMOS (magenta) SSS at, from left to right, top to bottom, $[15^{\circ}\text{N } 38^{\circ}\text{W}]$, $[12^{\circ}\text{N } 38^{\circ}\text{W}]$, $[12^{\circ}\text{N } 23^{\circ}\text{W}]$, $[8^{\circ}\text{N } 38^{\circ}\text{W}]$, $[4^{\circ}\text{N } 38^{\circ}\text{W}]$, $[4^{\circ}\text{N } 23^{\circ}\text{W}]$, $[0^{\circ} 35^{\circ}\text{W}]$ and $[0^{\circ} 23^{\circ}\text{W}]$. **178**

B.5. New SSS retrieval methodologies

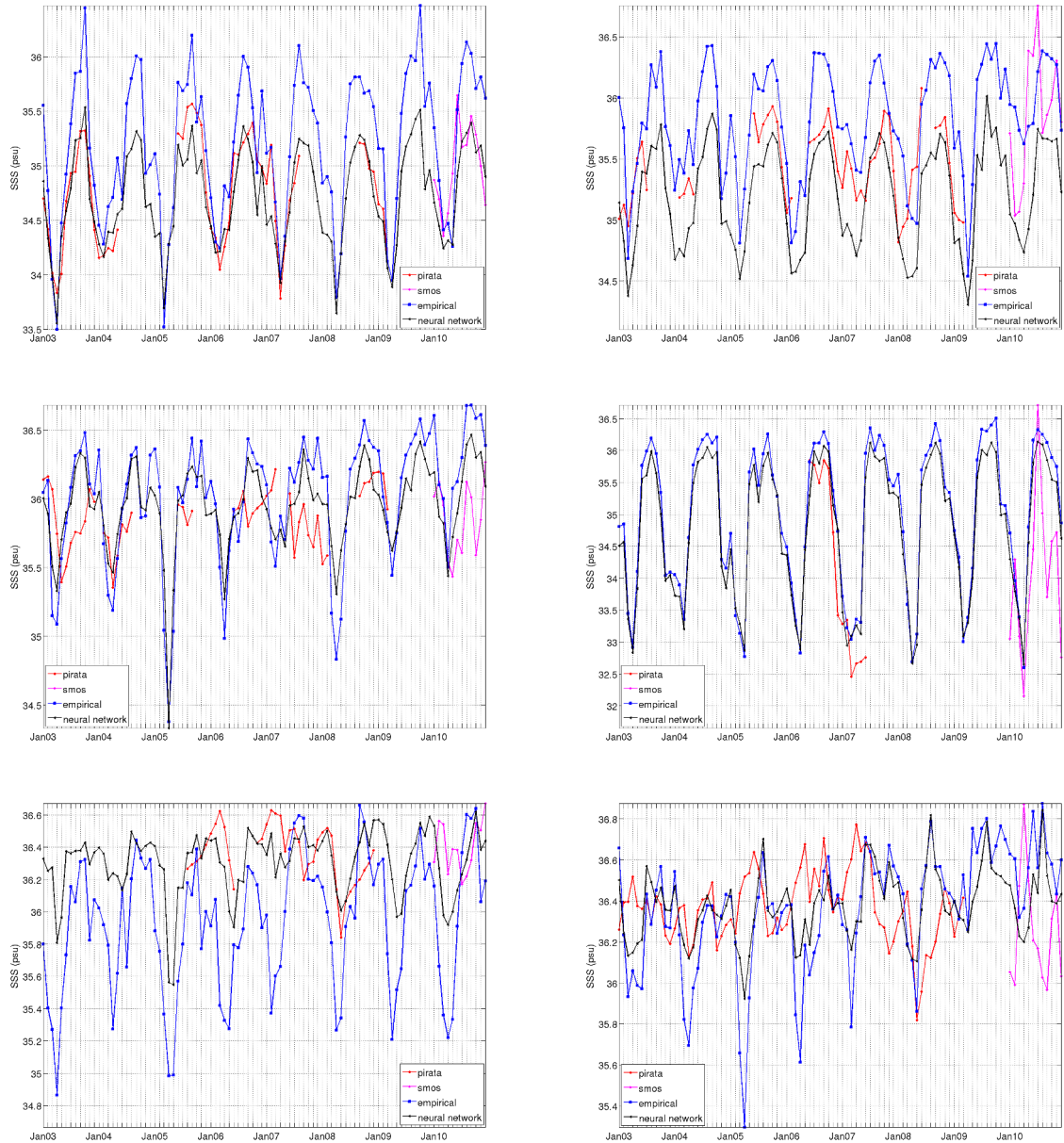


Figure B.22: Pirata, empirical AMSR-E and neural network AMSR-E sea surface salinity at, from left to right, top to bottom, $[0^\circ 0^\circ]$, $[0^\circ 10^\circ\text{W}]$, $[6^\circ\text{S } 10^\circ\text{W}]$, $[6^\circ\text{S } 8^\circ\text{E}]$, $[8^\circ\text{N } 30^\circ\text{W}]$ and $[10^\circ\text{S } 10^\circ\text{W}]$.

Appendix B. Amazon river plume signatures in AMSR-E low-frequency brightness temperature data

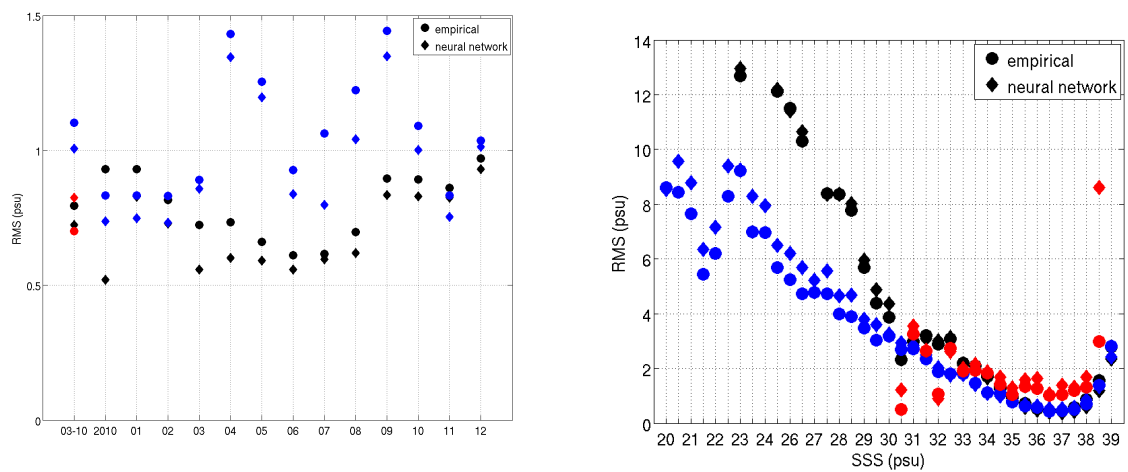


Figure B.23: Total RMS of the differences between AMSR-E SSS and Argo (black), TSG (blue) and Pirata (red) SSS using the different SSS retrieval methods, over 2003-2010, for 2010 and monthly over 2003-2010 (left) and as a function of 0.5 pss SSS bins (right).

B.6 Conclusion

At the end, it seems obvious that from AMSR-E, it is possible to retrieve a sea surface salinity signal. Here, we tried different approach to achieve that. First, an empirical approach, based on an unpublished work of Reul et al, has been considered. This method is based on the retrieval of SSS using the polynomial relationship between AMSR-E ΔT_b^v , SST and SSS. Then, in order to also take into account the wind and the localisation, a neural network method is developed. Comparing these new SSS products with *in situ* data, both methods retrieve a SSS signal and the Amazon plume fronts in terms of SSS. However, the precision of these products is not better than 0.8-1 pss. This might be due to an important signal-to-noise ratio of the brightness temperature measurements at 6.9 GHz and to the importance of atmospheric and roughness corrections.

Moreover, on some Pirata time series, a seasonal cycle in the neural network AMSR-E SSS appears whereas it doesn't seem to be related with a Pirata SSS seasonal signal. AMSR-E retrieved SSS signal may not be dominated by sea surface salinity. In order to attempt to understand this effect, we try to decompose our neural network AMSR-E SSS signal using the principal component analysis (PCA). The AMSR-E retrieved SSS seems to be mainly dominated by the sea surface temperature (see figure B.24).

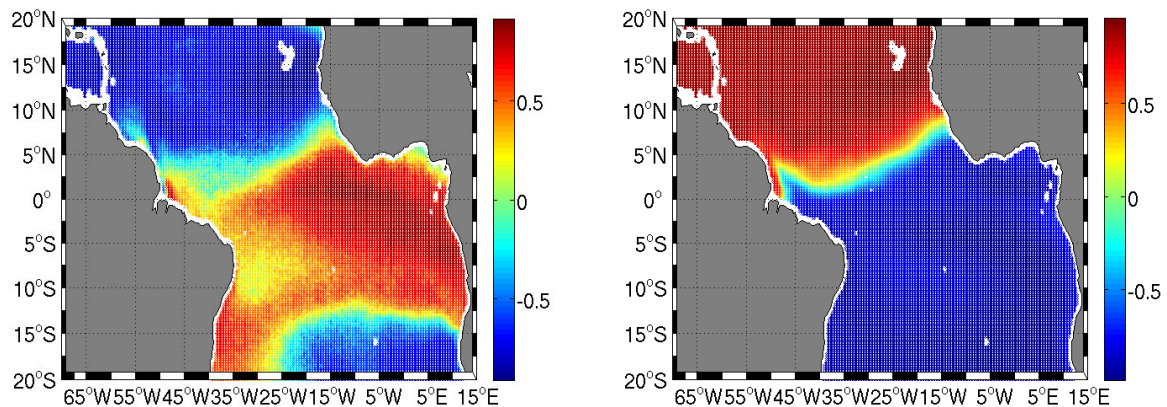


Figure B.24: 1st principal component homogeneous correlation map for AMSR-E SSS (top left) and Reynolds et al. [2002] SST (top left).

References

- Anderson, S. P., Weller, R. A., and Lukas, R. B. (1996). Surface buoyancy forcing and the mixed layer of the western Pacific warm pool: Observations and 1D model results. *Journal of Climate*, 9(12):3056–3085. 5
- Antonov, J. I., Locarnini, R., Boyer, T., Mishonov, A., Garcia, H., Levitus, S., et al. (2006). World ocean atlas 2005 volume 2: Salinity. *NOAA Atlas NESDIS*, 62(2). 13
- Bai, Y., Pan, D., Cai, W.-J., He, X., Wang, D., Tao, B., and Zhu, Q. (2013). Remote sensing of salinity from satellite-derived CDOM in the Changjiang river dominated east China sea. *Journal of Geophysical Research: Oceans*, 118(1):227–243. 11, 116
- Balaguru, K., Chang, P., Saravanan, R., Leung, L. R., Xu, Z., Li, M., and Hsieh, J.-S. (2012). Ocean barrier layers’ effect on tropical cyclone intensification. *Proceedings of the National Academy of Sciences*, 109(36):14343–14347. 6
- Battin, T. J. (1998). Dissolved organic matter and its optical properties in a blackwater tributary of the upper Orinoco river, Venezuela. *Organic Geochemistry*, 28(9-10):561–569. 11
- Baumgartner, A. and Reichel, E. (1975). *The World Water Balance*. Elsevier. 47
- Beers, J. R., Steven, D. M., and Lewis, J. B. (1968). Primary productivity in the Caribbean sea off Jamaica and the tropical north Atlantic off Barbados. *Bulletin of Marine Science*, 18(1):86–104. 84, 134
- Berger, M., Camps, A., Font, J., Kerr, Y., Miller, J., Johannessen, J., Boutin, J., Drinkwater, M., Skou, N., Floury, N., et al. (2002). Measuring ocean salinity with ESA’s SMOS mission. *ESA Bull*, 111(113f):113–121. 17
- Bianchi, T. S. and Allison, M. A. (2009). Large-river delta-front estuaries as natural ‘recorders’ of global environmental change. *Proceedings of the National Academy of Sciences*, 106(20):8085–8092. 4
- Binding, C. and Bowers, D. (2003). Measuring the salinity of the Clyde sea from remotely sensed ocean colour. *Estuarine, Coastal and Shelf Science*, 57(4):605–611. 11, 116
- Blough, N. and Del Vecchio, R. (2002). Chromophoric DOM in the coastal environment. In Hansell, D. e. a. E., editor, *Biogeochemistry of marine dissolved organic matter*, pages 509–546. 8, 9, 11, 12

- Bonjean, F. and Lagerloef, G. S. E. (2002). Diagnostic model and analysis of the surface currents in the tropical Pacific ocean. *J. Phys. Oceanogr.*, 32. 46
- Bowers, D. and Brett, H. (2008). The relationship between CDOM and salinity in estuaries: An analytical and graphical solution. *Journal of Marine Systems*, 73(1-2):1–7. 11
- Boyer, T., Levitus, S., Garcia, H., Locarnini, R. A., Stephens, C., and Antonov, J. (2005). Objective analyses of annual, seasonal, and monthly temperature and salinity for the world ocean on a 0.25 grid. *International Journal of Climatology*, 25(7):931–945. 13
- Boyle, E., Collier, R., Dengler, A., Edmond, J., Ng, A., and Stallard, R. (1974). On the chemical mass-balance in estuaries. *Geochimica et Cosmochimica Acta*, 38(11):1719–1728. 10
- Bricaud, A., Morel, A., Prieur, L., et al. (1981). Absorption by dissolved organic matter of the sea (yellow substance) in the UV and visible domains. *Limnol. Oceanogr*, 26(1):43–53. 7
- Carton, J. A. (1991). Effect of seasonal surface freshwater flux on sea surface temperature in the tropical Atlantic ocean. *Journal of Geophysical Research: Oceans (1978–2012)*, 96(C7):12593–12598. 5
- Chen, Z., Hu, C., Conmy, R. N., Muller-Karger, F., and Swarzenski, P. (2007). Colored dissolved organic matter in Tampa bay, Florida. *Marine Chemistry*, 104(1-2):98–109. 11
- Coble, P., Hu, C., Gould Jr, R. W., Chang, G., and Wood, A. M. (2004). Colored dissolved organic matter in the coastal ocean: An optical tool for coastal zone environmental assessment & management. Technical report. 7, 9, 34
- Coble, P. G. (2007). Marine optical biogeochemistry: the chemistry of ocean color. *Chemical reviews*, 107(2):402–418. 8
- Coble, P. G., Del Castillo, C. E., and Avril, B. (1998). Distribution and optical properties of CDOM in the Arabian sea during the 1995 southwest monsoon. *Deep-Sea Research Part II*, 45(10-11):2195–2223. 8
- Da Silva, A. C. (2007). Seasonal variability of the Amazon river plume during REVIZEE program. 58

References

- Dai, A., Qian, T., Trenberth, K. E., and Milliman, J. D. (2009). Changes in continental freshwater discharge from 1948 to 2004. *Journal of Climate*, 22(10):2773–2792. 5
- Dai, A. and Trenberth, K. E. (2002). Estimates of freshwater discharge from continents: Latitudinal and seasonal variations. *Journal of hydrometeorology*, 3(6):660–687. 5
- Del Castillo, C. E., Coble, P. G., Morell, J. M., López, J. M., and Corredor, J. E. (1999). Analysis of the optical properties of the Orinoco river plume by absorption and fluorescence spectroscopy. *Marine Chemistry*, 66(1):35–51. 9
- Del Castillo, C. E. and Miller, R. L. (2008). On the use of ocean color remote sensing to measure the transport of dissolved organic carbon by the Mississippi river plume. *Remote Sensing of Environment*, 112(3):836–844. 11, 116
- Del Vecchio, R. and Subramaniam, A. (2004). Influence of the Amazon river on the surface optical properties of the western tropical north Atlantic ocean. *Journal of Geophysical Research: Oceans*, 109(C11). 5, 66, 67, 68, 70, 71, 116, 117, 126, 128, 129, 130, 131, 132, 133
- Donlon, C. J., Martin, M., Stark, J., Roberts-Jones, J., Fiedler, E., and Wimmer, W. (2012). The operational sea surface temperature and sea ice analysis (OSTIA) system. *Remote Sensing of Environment*, 116:140–158. 45
- Duce, R. A. and Duursma, E. K. (1977). Inputs of organic matter to the ocean. *Marine Chemistry*, 5(4-6):317–339. 7
- Dyer, K. (1973). *Estuaries: a physical introduction*. John Wiley. 10
- Ertel, J. R., Hedges, J. I., Devol, A. H., Richey, J. E., de Nazare Goes Ribeiro, M., and Ribeiro, G. (1986). Dissolved humic substances of the Amazon river system. *Limnology and Oceanography*, 31(4):739–754. 7
- Ferrari, G. and Dowell, M. (1998). CDOM absorption characteristics with relation to fluorescence and salinity in coastal areas of the southern Baltic sea. *Estuarine, Coastal and Shelf Science*, 47(1):91–105. 11
- Ferry, N. and Reverdin, G. (2004). Sea surface salinity interannual variability in the western tropical Atlantic: An ocean general circulation model study. *Journal of Geophysical Research: Oceans*, 109(C5). 5

- Ffield, A. (2005). North Brazil current rings viewed by TRMM microwave imager SST and the influence of the Amazon plume. *Deep Sea Research Part I: Oceanographic Research Papers*, 52(1):137–160. 50
- Ffield, A. (2007). Amazon and Orinoco river plumes and NBC rings: Bystanders or participants in hurricane events ? *Journal of Climate*, 20(2). 5
- Foltz, G. R. and McPhaden, M. J. (2009). Impact of barrier layer thickness on SST in the central tropical north Atlantic*. *Journal of Climate*, 22(2):285–299. 5
- Font, J., Camps, A., Borges, A., Martin-Neira, M., Boutin, J., Reul, N., Kerr, Y., Hahne, A., and Mecklenburg, S. (2010). SMOS: The challenging sea surface salinity measurement from space. *Proceedings of the IEEE*, 98(5):649–665. 17
- Font, J., Lagerloef, G. S., Le Vine, D. M., Camps, A., and Zanife, O.-Z. (2004). The determination of surface salinity with the european smos space mission. *Geoscience and Remote Sensing, IEEE Transactions on*, 42(10):2196–2205. 18
- Fratantoni, D. M. and Glickson, D. A. (2002). North Brazil current ring generation and evolution observed with SeaWiFS. *Journal of Physical Oceanography*, 32(3):1058–1074. 5, 50
- Garver, S. A. and Siegel, D. A. (1997). Inherent optical property inversion of ocean color spectra and its biogeochemical interpretation 1, time series from the Sargasso sea. *Journal of Geophysical Research*, 102(C8):18607–18. 38
- Garzoli, S. L. and Katz, E. J. (1983). The forced annual reversal of the Atlantic north equatorial countercurrent. *Journal of Physical Oceanography*, 13(11):2082–2090. 50
- Geyer, W. R., Beardsley, R. C., Lentz, S. J., Candela, J., Limeburner, R., Johns, W. E., Castro, B. M., and Soares, I. D. (1996). Physical oceanography of the Amazon shelf. *Continental Shelf Research*, 16(5-6):575–616. 47, 52, 64
- Gibbs, R. J. (1982). Currents on the shelf of north-eastern south America. *Estuarine, Coastal and Shelf Science*, 14(3):283–299. 50
- Goni, G. J. and Johns, W. E. (2003). Synoptic study of warm rings in the north Brazil current retroreflection region using satellite altimetry. *Elsevier Oceanography Series*, 68:335–356. 50

References

- Gordon, H. R. (1997). Atmospheric correction of ocean color imagery in the earth observing system era. *Journal of Geophysical Research: Atmospheres (1984–2012)*, 102(D14):17081–17106. 35, 38
- Gordon, H. R. and Morel, A. Y. (1983). *Remote assessment of ocean color for interpretation of satellite visible imagery: A review*, volume 4. American Geophysical Union. 9
- Granskog, M. A., Macdonald, R. W., Mundy, C.-J., and Barber, D. G. (2007). Distribution, characteristics and potential impacts of chromophoric dissolved organic matter (CDOM) in Hudson strait and Hudson bay, Canada. *Continental Shelf Research*, 27(15):2032–2050. 11
- Green, S. A. and Blough, N. V. (1994). Optical absorption and fluorescence properties of chromophoric dissolved organic matter in natural waters. *Limnology and Oceanography*, 39(8):1903–1916. 7
- Grodsky, S. A., Reverdin, G., Carton, J. A., and Coles, V. J. (2014). Year-to-year salinity changes in the amazon plume: Contrasting 2011 and 2012 {A}quarius/{SACD} and {SMOS} satellite data. *Remote Sensing of Environment*, 140(0):14–22. 97, 99
- Hickey, B. M., Kudela, R. M., Nash, J. D., Bruland, K. W., Peterson, W. T., MacCready, P., Lessard, E. J., Jay, D. A., Banas, N. S., Baptista, A. M., Dever, E. P., Kosro, P. M., Kilcher, L. K., Horner-Devine, A. R., Zaron, E. D., McCabe, R. M., Peterson, J. O., Orton, P. M., Pan, J., and Lohan, M. C. (2010). River influences on shelf ecosystems: Introduction and synthesis. *Journal of Geophysical Research: Oceans*, 115(C2). 4
- Hu, C., Montgomery, E. T., Schmitt, R. W., and Muller-Karger, F. E. (2004). The dispersal of the Amazon and Orinoco River water in the tropical Atlantic and Caribbean Sea: Observation from space and S-PALACE floats. *Deep-sea Research Part II-topical Studies in Oceanography*, 51:1151–1171. 5, 9, 40, 48, 64, 66, 68
- Hu, C., Muller-Karger, F. E., Biggs, D. C., Carder, K. L., Nababan, B., Nadeau, D., and Vanderbloemen, J. (2003). Comparison of ship and satellite bio-optical measurements on the continental margin of the NE gulf of Mexico. *International Journal of Remote Sensing*, 24(13):2597–2612. 9, 11, 99
- Huang, W. and Chen, R. F. (2009). Sources and transformations of chromophoric dissolved organic matter in the Neponset river watershed. *Journal of Geophysical Research: Biogeosciences*, 114(G4). 11

- Johns, W. E., Zantopp, R. J., and Goni, G. (2003). Cross-gyre transport by north Brazil current rings. In Goni, G. and Malanotte-Rizzoli, P., editors, *Interhemispheric Water Exchange in the Atlantic Ocean*, volume 68 of *Elsevier Oceanography Series*, pages 411–441. Elsevier. 50
- Johnson, G. C. and Lyman, J. M. (2008). Global oceans : Sea surface salinity. In Levinson, D. and Lawrimore, J., editors, *State of the Climate in 2007*, volume 89, pages S45–S47. Eds. Bulletin of the American Meteorological Society. 13
- Kerr, Y., Waldteufel, P., Wigneron, J.-P., Delwart, S., Cabot, F., Boutin, J., Escorihuela, M.-J., Font, J., Reul, N., Gruhier, C., Juglea, S., Drinkwater, M., Hahne, A., Martin-Neira, M., and Mecklenburg, S. (2010). The SMOS mission: New tool for monitoring key elements of the global water cycle. *Proceedings of the IEEE*, 98(5):666–687. 17
- Kerr, Y. H., Font, J., Waldteufel, P., and Berger, M. (2000). The soil moisture and ocean salinity mission: SMOS. *ESA Earth Observation Quarterly*, 66:18–25. 17
- Klein, L. and Swift, C. (1977). An improved model for the dielectric constant of sea water at microwave frequencies. *Antennas and Propagation, IEEE Transactions on*, 25(1):104–111. 32, 159, 161, 165, 166, 168, 169, 170
- Körtzinger, A. (2003). A significant CO₂ sink in the tropical Atlantic ocean associated with the Amazon river plume. *Geophysical Research Letters*, 30(24). 4
- Lagerloef, G., Colomb, F., Le Vine, D., Wentz, F., Yueh, S., Ruf, C., Lilly, J., Gunn, J., Chao, Y., deCharon, A., Feldman, G., and Swift, C. (2008). The AQUARIUS/SAC-D mission: Designed to meet the salinity remote-sensing challenge. *Oceanography*, pages 68–81. 18
- Le Vine, D. M., Lagerloef, G. S., Colomb, F. R., Yueh, S. H., and Pellerano, F. A. (2007). Aquarius: An instrument to monitor sea surface salinity from space. *Geoscience and Remote Sensing, IEEE Transactions on*, 45(7):2040–2050. 18
- Lefèvre, N., Urbano, D. F., Gallois, F., and Diverrès, D. (2014). Impact of physical processes on the seasonal distribution of the fugacity of CO₂ in the western tropical Atlantic. *Journal of Geophysical Research: Oceans*. 4
- Lentz, S. J. (1995). Seasonal variations in the horizontal structure of the Amazon plume inferred from historical hydrographic data. *Journal of Geophysical Research: Oceans*, 100(C2):2391–2400. 48

References

- Lentz, S. J. and Limeburner, R. (1995). The Amazon river plume during AMASSEDS: Spatial characteristics and salinity variability. *Journal of Geophysical Research: Oceans*, 100(C2):2355–2375. 5, 26, 57
- Loder, T. C. and Reichard, R. P. (1981). The dynamics of conservative mixing in estuaries. *Estuaries*, 4(1):64–69. 10, 11
- Longhurst, A. (1993). Seasonal cooling and blooming in tropical oceans. *Deep Sea Research Part I: Oceanographic Research Papers*, 40(11-12):2145–2165. 114
- Longhurst, A. (1995). Interpreting CZCS images of the Amazon plume : Reply. *Deep Sea Research Part I: Oceanographic Research Papers*, 42(11-12):2139–2141. 5
- Lumpkin, R. and Garzoli, S. L. (2005). Near-surface circulation in the tropical Atlantic ocean. *Deep Sea Research Part I: Oceanographic Research Papers*, 52(3):495–518. 49, 50
- Maritorena, S., Siegel, D. A., and Peterson, A. R. (2002). Optimization of a semianalytical ocean color model for global-scale applications. *Applied Optics*, 41(15):2705–2714. 34, 38, 42
- Masson, S. and Delecluse, P. (2001). Influence of the Amazon river runoff on the tropical Atlantic. *Physics and Chemistry of the Earth, Part B: Hydrology, Oceans and Atmosphere*, 26(2):137–142. 5, 48
- McKee, B., Aller, R., Allison, M., Bianchi, T., and Kineke, G. (2004). Transport and transformation of dissolved and particulate materials on continental margins influenced by major rivers: benthic boundary layer and seabed processes. *Continental Shelf Research*, 24(7-8):899–926. 4
- Meissner, T. and Wentz, F. (2012). The emissivity of the ocean surface between 6 and 90 GHz over a large range of wind speeds and earth incidence angles. *Geoscience and Remote Sensing, IEEE Transactions on*, 50(8):3004–3026. 168
- Meybeck, M. (2003). Global analysis of river systems: from Earth system controls to anthropocene syndromes. *Philosophical Transactions of the Royal Society of London. Series B: Biological Sciences*, 358(1440):1935–1955. 4
- Meybeck, M. and Ragu, A. (1997). *River discharges to the oceans: An assessment of suspended solids, major ions, and nutrients*. IASH Publ. 48

- Meybeck, M. and Vörösmarty, C. (2005). Fluvial filtering of land-to-ocean fluxes: from natural holocene variations to anthropocene. *Comptes Rendus Geoscience*, 337(1-2):107–123. 4
- Mignot, J., Lazar, A., and Lacarra, M. (2012). On the formation of barrier layers and associated vertical temperature inversions: A focus on the northwestern tropical Atlantic. *Journal of Geophysical Research: Oceans*, 117(C2). 5, 6
- Miller, W. L. and Zepp, R. G. (1995). Photochemical production of dissolved inorganic carbon from terrestrial organic matter: Significance to the oceanic organic carbon cycle. *Geophysical Research Letters*, 22(4):417–420. 12
- Milliman, J., Farnsworth, K., Jones, P., Xu, K., and Smith, L. (2008). Climatic and anthropogenic factors affecting river discharge to the global ocean, 1951–2000. *Global and Planetary Change*, 62(3):187–194. 4
- Moller, G. S., de M. Novo, E. M., and Kampel, M. (2010). Space-time variability of the Amazon river plume based on satellite ocean color. *Continental Shelf Research*, 30(3–4):342–352. 66, 67, 68, 70, 71, 76, 79, 107, 108, 116, 117, 126, 127, 129, 130, 131, 132, 133
- Moran, M., Sheldon, W., and Sheldon, J. (1999). Biodegradation of riverine dissolved organic carbon in five estuaries of the southeastern United States. *Estuaries*, 22(1):55–64. 12
- Morel, A. and Prieur, L. (1977). Analysis of variations in ocean color. *Limnology and Oceanography*, 22(4):709–722. 9
- Muller-Karger, F., McClain, C., and Richardson, P. (1988). The dispersal of the Amazon’s water. *Nature*, 333(6168):56–59. 5, 9, 58, 64, 104
- Muller-Karger, F., Richardson, P., and McGillicuddy, D. (1995). On the offshore dispersal of the Amazon’s plume in the north Atlantic: Comments on the paper by A. Longhurst, ”Seasonal cooling and blooming in tropical oceans”. *Deep Sea Research Part I: Oceanographic Research Papers*, 42(11–12):2127–2137. 5, 58, 104, 114
- Nelson, N., Siegel, D., and Michaels, A. (1998). Seasonal dynamics of colored dissolved material in the Sargasso sea. *Deep Sea Research Part I: Oceanographic Research Papers*, 45(6):931–957. 8

References

- Obernosterer, I. and Herndl, G. J. (2000). Differences in the optical and biological reactivity of the humic and non-humic DOC component in two contrasting coastal marine environments. *Limnol. Oceanogr.*, 45:1120–1129. 12
- Oki, T. and Kanae, S. (2006). Global hydrological cycles and world water resources. *Science*, 313(5790):1068–1072. 4
- Pailler, K., Bourlès, B., and Gouriou, Y. (1999). The barrier layer in the western tropical Atlantic ocean. *Geophysical Research Letters*, 26(14):2069–2072. 5, 48
- Paluszkiwicz, T., Curtin, T., and Chao, S.-Y. (1995). Wind-driven variability of the Amazon river plume on the continental shelf during the peak outflow season. *Geo-Marine Letters*, 15(3-4):179–184. 58
- Pawlowicz, R. (2013). Key physical variables in the ocean: Temperature, salinity, and density. *Nature Education Knowledge*, 4(4):13. 6
- Reul, N., Fournier, S., Boutin, J., Hernandez, O., Maes, C., Chapron, B., Alory, G., Quilfen, Y., Tenerelli, J., Morisset, S., Kerr, Y., Mecklenburg, S., and Delwart, S. (2013). Sea surface salinity observations from space with the SMOS satellite: A new means to monitor the marine branch of the water cycle. *Surveys in Geophysics*, pages 1–42. 73, 80
- Reul, N., Saux-Picart, S., Chapron, B., Vandemark, D., Tournadre, J., and Salisbury, J. (2009). Demonstration of ocean surface salinity microwave measurements from space using AMSR-E data over the Amazon plume. *Geophysical Research Letters*, 36(13). 67, 149, 157, 158, 161, 165
- Reul, N. and Tenerelli, J. (2011). SMOS level 3 SSS research products - products validation document - reprocessed year 2010. *CECOS/CNES/IFREMER/CATDS Techn Doc*. 19
- Reverdin, G., Kestenare, E., Frankignoul, C., and Delcroix, T. (2007). Observing and modelling ocean heat and freshwater budgets and transports. 16, 26, 58, 59, 60, 61, 165, 167, 168
- Reynolds, R. W., Raynar, N. A., Smith, T. M., Stokes, D. C., and Wanqiu, W. (2002). An improved in situ satellite SST analysis for climate. *Journal of Climate*, 15(13):1609–1625. 45, 162, 163, 164, 165, 166, 167, 168, 171, 172, 181
- Richardson, P. and Reverdin, G. (1987). Seasonal cycle of velocity in the Atlantic north equatorial countercurrent as measured by surface drifters, current meters, and ship drifts. *Journal of Geophysical Research: Oceans (1978–2012)*, 92(C4):3691–3708. 50

- Richardson, P. L. and Walsh, D. (1986). Mapping climatological seasonal variations of surface currents in the tropical Atlantic using ship drifts. *Journal of Geophysical Research: Oceans (1978–2012)*, 91(C9):10537–10550. 50
- Riser, S., ReN, L., and Wong, A. (2008). Salinity in argo. *Oceanography*, 21(1):56. 13
- Robinson, I. S. (2004). *Measuring the oceans from space: the principles and methods of satellite oceanography*. Springer. 11, 33, 34
- Salisbury, J., Vandemark, D., Campbell, J., Hunt, C., Wisser, D., Reul, N., and Chapron, B. (2011). Spatial and temporal coherence between Amazon river discharge, salinity, and light absorption by colored organic carbon in western tropical Atlantic surface waters. *Journal of Geophysical Research: Oceans*, 116(C7). 66, 68, 73, 157
- Salisbury, J. E. (2003). *Satellite indices of fluvial influence in coastal waters*. PhD thesis, University of New Hampshire, National Resources and Earth System Science. 11
- Salisbury, J. E., Vandemark, D., Hunt, C. W., Campbell, J. W., McGillis, W. R., and McDowell, W. H. (2008). Seasonal observations of surface waters in two Gulf of Maine estuary-plume systems: Relationships between watershed attributes, optical measurements and surface pCO₂. *Estuarine, Coastal and Shelf Science*, 77(2):245–252. 11
- Schanze, J. J., Schmitt, R. W., and Yu, L. (2010). The global oceanic freshwater cycle: A state-of-the-art quantification. *Journal of Marine Research*, 68(3–4):3–4. 4, 5
- Sharkov, E. A. (2003). *Passive Microwave Remote Sensing of the Earth*, volume XXVI. Praxis Publishing. 16
- Sverdrup, H. U., Johnson, M. W., Fleming, R. H., et al. (1942). *The oceans: their physics, chemistry, and general biology*, volume 7. Prentice-Hall New York. 6
- Syvitski, J. P., Vörösmarty, C. J., Kettner, A. J., and Green, P. (2005). Impact of humans on the flux of terrestrial sediment to the global coastal ocean. *Science*, 308(5720):376–380. 4
- Tomczak, M. (1999). Some historical, theoretical and applied aspects of quantitative water mass analysis. *Journal of Marine Research*, 57(2):275–303. 6, 7
- Trenberth, K. E. (1999). Conceptual framework for changes of extremes of the hydrological cycle with climate change. In *Weather and Climate Extremes*, pages 327–339. Springer. 4

References

- Trenberth, K. E., Smith, L., Qian, T., Dai, A., and Fasullo, J. (2007). Estimates of the global water budget and its annual cycle using observational and model data. *Journal of Hydrometeorology*, 8(4):758–769. 4
- Twardowski, M. S. and Donaghay, P. L. (2001). Separating in situ and terrigenous sources of absorption by dissolved materials in coastal waters. *Journal of Geophysical Research: Oceans*, 106(C2):2545–2560. 12
- Urquhart, E. A., Zaitchik, B. F., Hoffman, M. J., Guikema, S. D., and Geiger, E. F. (2012). Remotely sensed estimates of surface salinity in the Chesapeake bay: A statistical approach. *Remote Sensing of Environment*, 123(0):522–531. 11, 116
- Vialard, J. and Delecluse, P. (1998a). An OGCM study for the TOGA decade. part I: Role of salinity in the physics of the western Pacific fresh pool. *Journal of Physical Oceanography*, 28(6):1071–1088. 5
- Vialard, J. and Delecluse, P. (1998b). An OGCM study for the TOGA decade. part II: Barrier-layer formation and variability. *Journal of physical oceanography*, 28(6):1089–1106. 5
- Vörösmarty, C., Fekete, B., Meybeck, M., and Lammers, R. (2000). Global system of rivers: Its role in organizing continental land mass and defining land-to-ocean linkages. *Global Biogeochemical Cycles*, 14(2):599–621. 4
- Wentz, F. and Meissner, T. (2000). AMSR-E ocean algorithm, algorithm theoretical basis document, version 2. *Santa Rosa, California USA: Remote Sensing Systems*. 157
- Westberry, T., Behrenfeld, M. J., Siegel, D. A., and Boss, E. (2008). Carbon-based primary productivity modeling with vertically resolved photoacclimation. *Global Biogeochemical Cycles*, 22(2). 44
- Yamashita, Y. and Tanoue, E. (2004). In situ production of chromophoric dissolved organic matter in coastal environments. *Geophysical Research Letters*, 31(14). 12

Publications & Conferences

PUBLICATIONS :

Sea Surface Salinity observations from Space with the SMOS satellite : A new means to monitor the marine branch of the water cycle

Reul N., Fournier S., Boutin J., Hernandez O., Maes C., Chapron B., Alory G., Quilfen Y., Tenerelli J., Morisset S., Kerr Y., Mecklenburg S. and Delwart S.
Surveys in Geophysics, 2013

Spatio-temporal analysis of the conservative mixing between spaceborne measurements of Sea Surface Salinity and Optical Properties in the Amazon plume

Fournier S., Chapron B., Salisbury J., Vandemark D., Reul N.
Journal of Geophysical Research, 2014, submitted

Multi-Sensor Observations of the Amazon-Orinoco River Plume Interactions with Hurricanes

Chapron B., Reul N., Quilfen Y., Fournier S., Sabia R.
Journal of Geophysical Research, 2014, submitted

PROCEEDINGS :

Spatio-temporal coherence between spaceborne measurements of Salinity and Light Absorption in the Amazon plume region

Fournier S., Reul N., Charpon B., Tenerelli J.
ESA-SOLAS, Earth Observation for Ocean Atmosphere Interaction Science, 29th November-2nd December 2011, ESRIN, Frascati, Italy

Sea Surface Salinity observations from Space : A new tool to monitor the oceanic freshwater cycle as well as ocean/land and ocean/atmosphere interactions

Reul N., Chapron B., Tenerelli J., Fournier S., Quilfen Y.
EGU General Assembly, 2012

Linking the continental landmass to biogeochemical variability in the coastal ocean: the role of hydrological models and new satellite ocean color and salinity sensors

Salisbury J., Vandemark D., Fournier S., Reul N., Chapron B., Mannino A., Wollheim W.M.

AGU Fall Meeting, 2012

ORAL PRESENTATIONS :

Spatio-temporal coherence between spaceborne measurements of Salinity and Light Absorption in the Amazon plume region

Fournier S., Reul N., Charpon B., Tenerelli J.

ESA-SOLAS, Earth Observation for Ocean Atmosphere Interaction Science, 29th November-2nd December 2011, ESRIN, Frascati, Italy

Spatio-temporal coherence between spaceborne measurements of Salinity and Light Absorption in the Amazon plume region

Fournier S., Reul N.

India EU Workshop on Marine Primary Production, 12th-15th March 2013, Kochi, India

Large tropical river plume monitoring with SMOS to better estimate land-sea freshwater fluxes

Fournier S., Reul N., Chapron B., Salisbury J., Vandemark D.

ESA-EGU-SOLAS, Air-Sea Gas Flux Climatology, Progress and Future Prospect, 24th-27th September 2013, Ifremer, Brest, France

POSTERS :

Spatial and temporal coherence between spaceborne measurements of Salinity and Light Absorption in the Amazon plume region

Fournier S., Reul N.

ESA Living Planet Symposium, 9th-13th September 2013, Edinburgh, Scotland

Spatio-Temporal Coherence between Spaceborne Measurements of Salinity and Optical Properties in the Amazon-Orinoco Plume Region

Abstract :

We enter now in a new era of global Sea Surface Salinity (SSS) observing systems from Space with the recent successful launches of the ESA Soil Moisture and Ocean Salinity (SMOS) mission and the NASA Aquarius/SAC-D mission. These new satellite SSS observing systems are as well complemented by an increased number of devices deployed *in situ*. Finally, ocean color products can be used as well for tracking salinity via semi-conservative tracers such as dissolved organic matter absorption coefficient at 443 nm (acdm), light attenuation at 490 nm and chlorophyll concentration. With these new methods, we are now in an excellent position to revisit the SSS observed in the warm seas of the tropical Atlantic with multi-year time series of excellent remote sensing and concurrent *in situ* observations. The seasonal cycles in the spatial extent of low surface salinity waters of the major river plumes and freshwater pools of the tropical Atlantic oceans as the Amazon and Orinoco rivers can thus be analyzed in a new and original manner. In particular, the correlation between SSS and bio-optical properties measured from Space in the plume waters can now be established and analyzed over large spatial scales. In the frame of this PhD work, different major research topics were studied. First the correlations between sea surface salinity and absorption coefficient of colored detrital matter at 443 nm in the Amazon-Orinoco plume over 2010-2013 are studied. Then the conservative mixing relationship is robustly established based on two different approaches, a regional one over the whole Amazon plume and a local one. Once the SSS/acdm relationship established, it is used to retrieve a SSS product from 1998 to 2013 based on Ocean Color data. Finally, we attempt to explore the conservative mixing using a lagrangian approach.

Keywords : satellite, plume, optical properties, salinity.

Signature du Panache des Fleuves Amazone et Orénoque à la Surface des Océans : Corrélation entre Salinité et Propriétés Optiques déduites de Mesures Satellite

Résumé :

Avec les lancements réussis des missions ESA Soil Moisture and Ocean Salinity (SMOS) et NASA Aquarius/SAC-D, la salinité de surface des océans peut maintenant être déduite. De plus, les produits de couleur de l'eau, tels que les mesures d'absorption et d'atténuation de la lumière et de concentration en chlorophylle, peuvent être utilisés comme traceurs de la salinité. Les signatures des panaches des grands fleuves tropicaux tels que l'Amazone et l'Orénoque peuvent être étudiées en détail grâce à ces nouvelles méthodes. En particulier, les relations de corrélations entre SSS et propriétés optiques également déduites de mesures satellites peuvent maintenant être établies et analysées sur des échelles spatiales beaucoup plus grandes. Différents efforts de recherche sont envisagés dans le cadre de ce travail de thèse. Tout d'abord, nous étudions les corrélations entre salinité de surface et propriétés optiques dans le panache de l'Amazone durant la période 2010-2013. Ensuite, la relation de mélange est établie de façon robuste selon tout d'abord une approche régionale, puis selon une approche locale. Ensuite, une fois cette loi de dilution établie de façon robuste, nous l'utilisons pour estimer un produit de salinité de surface à partir des produits couleur de l'eau sur la période 1998-2013. Enfin, nous tentons d'envisager la relation de dilution suivant une approche lagrangienne.

Mots clés : satellite, panache, propriétés optiques, salinité